Surface-tension-driven coalescence

Alice B. Thompson

Thesis submitted to the University of Nottingham
for the degree of Doctor of Philosophy

January 2012

Abstract

When fluid droplets coalesce, the flow is initially controlled by a balance between surface tension and viscosity. For low viscosity fluids such as water, the viscous lengthscale is quickly reached, yielding a new balance between surface tension and inertia. Numerical and asymptotic calculations have shown that there is no simply connected solution for the coalescence of inviscid fluid drops surrounded by a void, as large amplitude capillary waves cause the free surface to pinch off. We analyse in detail a linearised version of this free boundary problem.

For zero density surrounding fluid, we find asymptotic solutions to the leading order linear problem for small and large contact point displacement. In both cases, this requires the solution of a mixed type boundary value problem via complex variable methods. For the large displacement solution, we match this to a WKB analysis for capillary waves away from the contact point. The composite solution shows that the interface position becomes self intersecting for sufficiently large contact point displacement.

We identify a distinguished density ratio for which flows in the coalescing drops and surrounding fluid are equally important in determining the interface shape. We find a large displacement solution to the leading order two-fluid problem with a multiple-scales analysis, using a spectral method to solve the leading order periodic oscillator problem for capillary waves. This is matched to a single-parameter inner problem, which we solve numerically to obtain the correct boundary conditions for the secularity equations. We find that the composite solution for the two-fluid problem is simply connected for arbitrarily large contact-point displacement, and so zero density surrounding fluid is a singular limit.

Acknowledgements

I would like to thank my supervisors, John Billingham and Richard Tew, for their helpful advice throughout my Ph.D. studies. I would also like to thank my colleagues at both the University of Nottingham and other institutions for a number of interesting discussions. This work was funded by the Engineering and Physical Sciences Research Council, via a doctoral training award.

During my Ph.D., I was also able to undertake an industrial mathematics internship with Airbus, organised by the KTN for Industrial Mathematics (managed by the Smith Institute for Industrial Mathematics and System Engineering). I am very grateful for this opportunity to spend time at Airbus and would like to thank my colleagues at Airbus for making this such an enjoyable and stimulating experience.

This thesis would not have been possible without the support and encouragement of my family, friends and my partner, Chris.

Contents

List of Figures

Chapter 1

Introduction

1.1 Coalescence

Coalescence and pinch-off problems represent a class of fluid flows where separate bodies of fluid merge or split. At the moment of coalescence, the bodies touch only at a single point. In the earliest stages of coalescence, surface tension forces due to the highly curved meniscus between the two bodies are balanced by viscosity. However, for low viscosity fluids, viscous forces soon become negligible compared to the inertia of this rapid recoiling flow, and so examining the surface tension driven coalescence of an inviscid fluid has physical relevance. Near the contact point, the far field geometry is perceived as a wedge or cone, and the flow can be self similar.

Experiments and time dependent simulations of the coalescence of fluid droplets show qualitatively different behaviour depending on the density and viscosity ratios between the fluid drop and any surrounding fluid. In particular, there is no simply connected time dependent solution for the inviscid coalescence of drops surrounded by a vacuum, in contrast to the converse configuration where two bubbles coalesce surrounded by a much denser fluid, for which the solution is simply connected.

In agreement with the non-existence of simply connected time dependent solutions for inviscid coalescence, it can be shown that no self similar solutions exist for dense drops surrounded by a vacuum, though they do exist for bubbles merging. However, for an intermediate density ratio, as perhaps for water drops coalescing surrounded by air, the surrounding fluid may prevent the excited capillary waves from self intersecting or pinching off, so that a valid similarity solution and corresponding time dependent solution may be obtained.

The two main problems investigated in this thesis consider self similar solutions to recoil of 'very fat' two dimensional fluid wedges, which allows certain approximations to be made to the self similar equations. Under the contact angle conditions imposed in these two problems, the flow domain for the coalescing fluid can be approximated by a half plane, with an effectively one dimensional flow driven in the slender gap between the coalescing drops. These two simplifications make the flow analysis significantly more tractable, and we derive various asymptotic solutions to the resulting system, for the case of 'large' and 'small' free surface displacement within appropriate limits. The two problems considered correspond to recoil of an inviscid fluid surrounded by a vacuum, and by a low density fluid. For these linearised problems, we find that zero density surrounding fluid is a singular limit.

1.2 Literature review

Coalescence and pinch off problems have been the subject of investigation in some form since the 19th century [Thomson and Newall, 1885]. As well as their intrinsic mathematical appeal, such processes have important applications to multiphase flow, microfluidics, printing processes, control of emulsions, sintering and even the size distribution of raindrops [Aarts et al., 2005].

The coalescence of two spherical drops into a single drop of the same total volume reduces the total surface energy of the system, and so should be energetically favourable. However, drops can sometimes spend considerable time in near contact before coalescence is initiated [Yao et al., 2005], even for periods of up to several hours. The phenomenon of non-coalescence is a field of study in its own right. For the purposes of this discussion, we will assume that coalescence has already been initiated by the formation of a meniscus between the two droplets. Possible mechanisms for the formation of such a meniscus include molecular forces, surface diffusion, and intrinsic dynamic roughness.

Once a neck or meniscus has formed between the bodies, the evolution of the interface shape and flow within the drops is determined by viscous, inertial and surface tension forces. At very early times, the dominant balance is always between viscosity and surface

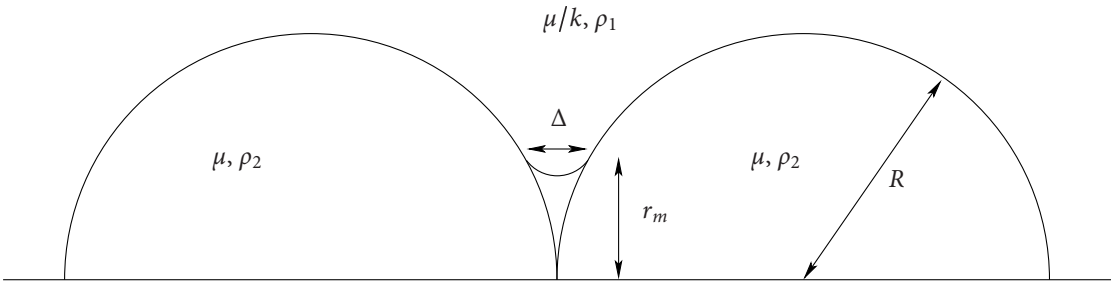

Figure 1.1: Coalescence of two identical spherical fluid drops. The drops both have viscosity μ, density $\rho_2 = \rho$ and initial radius R. The external fluid has viscosity μ/k and density ρ_1. A meniscus forms between the drops of radius $r_m(t)$ and width $\Delta(t)$. After Eggers et al. [1999].

tension. The Reynolds number of the flow can be estimated as

$$\mathrm{Re} = \frac{\gamma r_m}{\rho \nu^2}, \tag{1.1}$$

where γ is the coefficient of surface tension, ρ is the fluid density and $\nu = \mu/\rho$ is the kinematic viscosity of the fluid. The flow velocity is proportional to the capillary speed, and the flow lengthscale is based on the meniscus radius $r_m(t)$ (figure 1.1). Thus regardless of the physical properties of the fluid, the Reynolds number will be small during the earliest stages of coalescence. The first regime after initial meniscus formation is therefore Stokes flow, and the meniscus radius r_m is proportional to t. However, once the radius of the meniscus reaches the viscous lengthscale, given by

$$l_\nu = \frac{\rho \nu^2}{\gamma}, \tag{1.2}$$

then $\mathrm{Re} = O(1)$ and inertia can no longer be neglected. For low viscosity fluids with strong surface tension, the viscous lengthscale can be much smaller than typical drop sizes, with $l_\nu \approx 10^{-9}$ m for water. If r_m is much greater than the viscous lengthscale, the Reynolds number is very large, and so inertia dominates viscosity in resisting the recoil of the drop. We therefore find that inviscid surface tension driven coalescence is relevant to the later stages of water droplet coalescence.

The subsequent sections of this literature review describe a variety of analytical, experimental and numerical investigations of droplet coalescence, for viscous and inviscid fluid, with an emphasis on how results for the interface shape and speed vary with the density and viscosity ratios between the drop and surrounding fluid.

In section 1.2.1, we summarise theoretical and numerical results for the coalescence of spherical droplets, for flows with surface tension and viscosity only [Hopper, 1990, Eggers et al., 1999] and for flows with surface tension and inertia only [Duchemin et al., 2003]. We discuss experimental observations of coalescence in section 1.2.2.

If the meniscus radius r_m is much smaller than the drop radius R, the interface shape is related to that for a recoiling semi infinite fluid wedge due to a sudden change of wedge angle (figure 1.7). This recoiling wedge has no imposed lengthscales, and on dimensional grounds, solutions must be self similar for flows with surface tension and viscosity only [Miksis and Vanden-Broeck, 1999], and for flows with surface tension and inertia only [Keller and Miksis, 1983]. In section 1.2.3, we discuss numerical and analytical investigations of the self similar equations for inviscid wedge recoil, for wedge angles appropriate for the coalescence of droplets and bubbles. In section 1.2.4, we discuss self similar and time dependent solutions for the surface tension driven recoil of a wedge of viscous fluid.

Self similar flow in wedge and cone based geometries also has applications to the pinch-off of fluid droplets, which we discuss in section 1.2.5, and as an inviscid model of contact line motion, which we discuss in section 1.2.6.

1.2.1 Theoretical analysis of coalescence

Hopper [1990] used complex variable techniques to obtain an exact solution for the zero Reynolds number coalescence of cylinders, for viscous drops with an inviscid or absent surrounding fluid. The exact solution shows that the interface evolves smoothly away from its singular initial condition, with no accumulation of fluid at the meniscus or waves on the free surface. A selection of interface positions for this solution are shown in figure 1.2(a). The meniscus radius for this solution is $O(t \log t)$ for early times.

Eggers et al. [1999] conducted a numerical and asymptotic investigation of the time dependent evolution of spherical drops coalescing in Stokes flow, in the presence of a surrounding fluid with comparable viscosity. In their analysis, molecular forces were assumed to be responsible for the formation of a meniscus between the drops, which was taken as an initial condition. The initial focus of their study was the coalescence of three-dimensional spheres, but they showed that the meniscus width Δ is much smaller

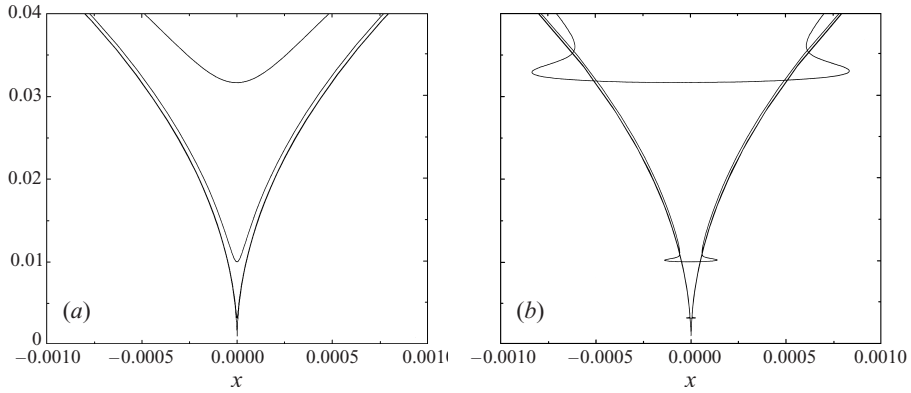

(a) Exact result from Hopper [1990] for zero viscosity surrounding fluid.

(b) Numerical result from Eggers et al. for equal viscosity surrounding fluid.

Figure 1.2: From Eggers et al. [1999]. Interface shapes for coalescence of two cylinders in Stokes flow. For both plots, interface profiles are shown for $r_m = 10^{-3}, 10^{-2.5}, 10^{-2}, 10^{-1.5}$. Note the different scales in the x and y directions.

than the meniscus radius r_m, so that the two-dimensional curvature is much larger than that arising from the rotational symmetry of the surface, and hence coalescence of spheres and cylinders are equivalent at leading order.

The numerical solutions were concentrated on the case where the two fluids have equal dynamic viscosity, as in this case the boundary integral equation is significantly simpler. Numerically calculated interface positions for the equal viscosity case are shown in figure 1.2(b). Their analysis showed that for this two-fluid problem, the capillary pressure at the meniscus is insufficient to force the surrounding fluid out of the narrow gap between the drops, so that a widening bubble accumulates at the meniscus, connected to the exterior fluid by a long neck region, shown here in figure 1.3.

Eggers et al. used scaling methods to examine the structure of this bubble and neck region. They argued that near the meniscus, the interfaces of the two drops are nearly parallel. The leading order force at the meniscus is surface tension on each interface pulling radially outwards, forming a ring force with constant nondimensional strength '2', applied at a radius r_m and spread over a distance Δ. The leading order velocity field is then obtained by integrating over the force distribution. The integral is dominated by the region $\Delta \ll |\mathbf{x} - \mathbf{x}'| \ll r_m$, and hence

$$\mathbf{u}(r_m) = \dot{r}_m(t)\mathbf{e}_r = -\frac{1}{2\pi}\log\left(\frac{\Delta}{r_m}\right)\mathbf{e}_r. \tag{1.3}$$

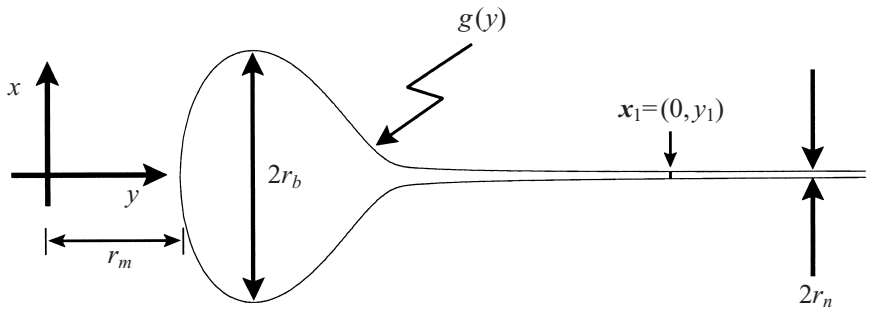

Figure 1.3: From Eggers et al. [1999]. A sketch of the structure of the local solution close to the meniscus, which resembles a bubble connected to a thin neck. The radius of the bubble is r_b and the minimum radius of the neck is r_n. The distance from the origin to the front of the bubble is r_m, which is not drawn to scale here.

If the lengthscale Δ is known, then this equation can be integrated to give the meniscus radius $r_m(t)$.

If a finite proportion of the fluid initially occupying the slender gap between the spherical drops is accumulated at the meniscus as the meniscus moves outwards, we can determine the toroidal bubble height Δ as a function of r_m. The area of the viscous fluid contained between the two spheres in $r < r_m$ is $O(r_m^3)$. Eggers et al. proposed that a finite proportion of this fluid forms a bubble of radius r_b, as shown in figure 1.3; by considering the area of this bubble they found that $r_b = O(r_m^{3/2})$. The bubble has approximately constant pressure, and gives an annulus height $\Delta \approx r_b = O(r_m^{3/2})$. For sufficiently small time, Eggers et al. found from (1.3) that

$$r_m(t) \sim -\frac{1}{4\pi} t \log t \quad \text{as} \quad t \to 0. \tag{1.4}$$

The system is non-dimensionalised on the viscosity and radius of the drop, with capillary speeds calculated from the two-fluid surface tension. The surrounding fluid has viscosity μ/k.

The leading order result (1.4) is independent of the viscosity ratio k, provided that k is finite. This is because the force is transmitted by the spherical drops, rather than the thin layer of surrounding fluid. However, in the case $k = \infty$, where surrounding fluid is inviscid, Hopper's solution gives

$$r_m(t) \sim -\frac{1}{\pi} t \log t \quad \text{as} \quad t \to 0. \tag{1.5}$$

This meniscus velocity is four times faster than that predicted by Eggers et al. [1999] if a

viscous outer fluid is present. Comparing (1.5) to (1.3), we note that the meniscus width Δ should scale as $O(r_m^3)$, which is much smaller than both the gap width $w = O(r_m^2)$ and the width $r_b = O(r_m^{3/2})$ of the toroidal bubble, which forms only when the surrounding fluid is viscous.

It is important to note that the ring-force scaling analysis only predicts the leading order meniscus position (1.4). It does not predict the coefficient of the $O(t)$ term, which is expected to vary with the viscosity ratio. To date, no experimental studies have observed logarithmic behaviour for small time.

When the radius of the meniscus has grown beyond the viscous lengthscale given by (1.2), a new balance occurs between surface tension and inertia, with viscous forces now negligible. We assume that the initial velocity profile for the inviscid regime is irrotational, so we now solve for a velocity potential, with $\mathbf{u} = \nabla\phi$. The Bernoulli equation then gives

$$\phi_t + \frac{1}{2}|\nabla\phi|^2 = \frac{\gamma\kappa}{\rho}. \tag{1.6}$$

By assuming that velocities are of order r_m/t, and that the height of the meniscus is proportional to the original gap height $w = r_m^2/R$, Eggers et al. [1999] proposed

$$r_m(t) \propto \left(\frac{\gamma R}{\rho}\right)^{1/4} t^{1/2}, \tag{1.7}$$

as the scaling for meniscus evolution determined by surface tension and inertia.

Duchemin et al. [2003] investigated the inviscid coalescence problem for spherical drops surrounded by a vacuum. Starting from an imposed initial meniscus shape, their numerical solutions show that capillary waves are excited on the free surface. The amplitude of the capillary waves grows with time, until they take up the width of the meniscus and pinch off. Thus there is no simply connected solution for inviscid coalescence of spheres with a zero density external fluid.

In order to allow the numerical solutions of Duchemin et al. to proceed beyond the pinch off of the toroidal bubble, the bubble was extracted from the profile, and the simulation restarted with initial conditions given by the interface position at pinch off and zero velocity everywhere. The numerical solutions show that the velocity field quickly resumes its value from before the pinch off. The time dependent solution consists of a sequence of collapses of the interface, with the contact point moving a short distance

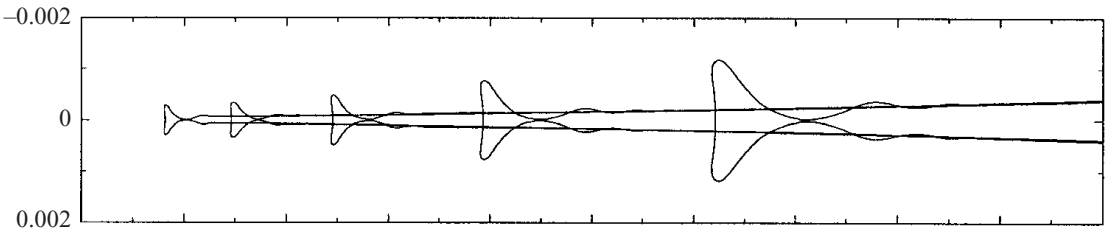

Figure 1.4: From Duchemin et al. [2003]. A sequence of successive entrapment of voids during the coalescence for an initial liquid bridge radius of $r_m = 0.008$. After every reconnection, the void is extracted from the profile and a new computation begins, with a null initial velocity field.

outwards between each event. A sequence of pinching events is shown in figure 1.4. By averaging over these pinching events, they recovered the scaling (1.7) and determined the prefactor numerically to be 1.62.

1.2.2 Experimental Results

Experimental studies of droplet coalescence must contend with a number of difficulties. The most obvious is that the coalescence process is typically very fast, and has interesting features on a very small scale. The development of cameras with high frame-rate has enabled more detailed study of early-time phenomena for low viscosity fluids (Anilkumar et al. [1991], Menchaca-Rocha et al. [2001], Biance et al. [2004], Wu et al. [2004], Yao et al. [2005], Thoroddsen et al. [2005], Aarts et al. [2005] and Thoroddsen et al. [2007]). Another approach was taken by Aarts et al. [2005] and Yao et al. [2005], who used high viscosity silicon oil, or polymer-colloid mixtures with ultralow surface tension, in order to significantly increase the viscous lengthscale given by

$$l_\nu = \frac{\rho \nu^2}{\gamma}. \tag{1.8}$$

As a result, Aarts et al. and Yao et al. were able to obtain viscous lengthscales of up to a few centimetres, in contrast to 10 nm for water.

Theoretical analyses of coalescence problems typically assume droplets are initially spherical, at rest, and free from the influence of gravity. However, each of these assumptions poses difficulties for the experimental setup. A common experimental setup (Menchaca-Rocha et al. [2001], Yao et al. [2005], Biance et al. [2004]) uses planar surfaces to hold almost-spherical drops or spherical caps in place. Another surface or a second drop can then be slowly manoeuvred into position.

In order to make valid comparisons with the various scaling laws for small time, it is important to accurately identify the time at which coalescence begins. The simplest method is to fit images of the bridge radius to some assumed profile, and extrapolate backwards to identify the 'moment' of coalescence. An alternative approach was taken by Menchaca-Rocha et al. [2001] who investigated coalescence of drops of mercury, gently pushed together on a planar surface. A small current was passed through the pushing devices, so that the initiation of coalescence completed a low-current circuit. The current then triggered the photographic sequence. One of the disadvantages of using mercury is that, like water, the viscous lengthscale l_v is very small, and so the viscous-dominated stages of coalescence are too quick and too small to resolve well. However, Menchaca-Rocha et al. [2001] were able to obtain useful images of the coalescence process on the scale of the drop, shown in figure 1.5. These show considerable deformations from spherical shapes.

For low viscosity fluids, experimental results for drop coalescence (Menchaca-Rocha et al. [2001], Wu et al. [2004], Aarts et al. [2005]) agree with the $t^{1/2}$ scalings for meniscus radius predicted by the inviscid coalescence analysis of Duchemin et al. [2003], which found

$$r_m \sim \left(\frac{\gamma R_0}{\rho}\right)^{1/4} \sqrt{t}. \tag{1.9}$$

By averaging over a sequence of pinching events, Duchemin et al. found that the prefactor for this relationship should be 1.62. The experimental investigations found lower prefactors, in the range 1.0–1.2, with some variation for different fluids. The coalescence experiments did not show the free surface pinching off, although capillary waves were observed on the free surface. Thoroddsen et al. [2005] investigated the coalescence of bubbles. Their analysis was consistent with the scaling relationship (1.9) for $r/R_0 < 0.45$; they calculated a prefactor of 1.39 which is higher than those observed experimentally for coalescing drops.

Experimental observations of coalescence in the viscous-dominated regime [Aarts et al., 2005, Yao et al., 2005] typically involve high viscosity, low surface tension fluids. These studies do find support for the scaling

$$r_m \sim \frac{\gamma}{\mu} t, \tag{1.10}$$

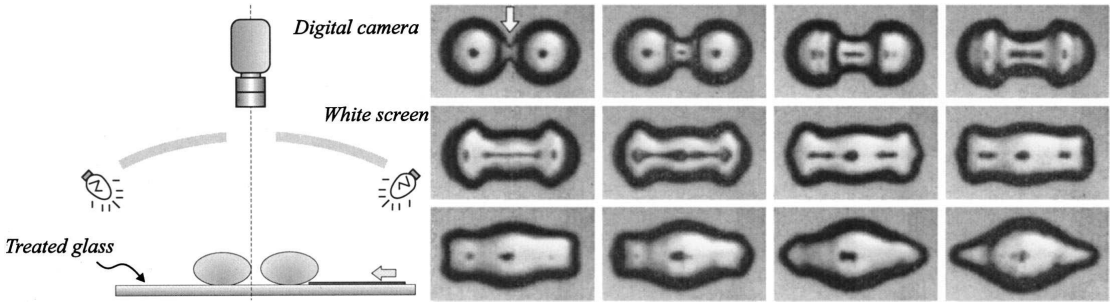

Figure 1.5: From Menchaca-Rocha et al. [2001]. Experimentally observed surface shape evolution of two 1.0-g mercury drops, using the apparatus shown on the left. In the photographs, time runs from left to right, and from top to bottom. The time lapsed between images is Δt = 3.5 ms. The sequence stops near the maximum horizontal stretching.

with prefactors of 0.55 for silicon oil and 0.3–0.4 for various colloid-polymer mixtures. The experimental investigations have not found evidence of the logarithmic behaviour predicted by the calculations of Hopper [1990] and Eggers et al. [1999] and so the experimentally calculated prefactors cannot be directly compared to the theoretical predictions.

The inviscid drop coalescence simulations of Duchemin et al. [2003] predict repeated pinch off processes, leading to the formation of zero-density toroidal bubbles. Toroidal bubbles have not yet been observed in the droplet coalescence. However, isolated bubbles of the surrounding fluid have been observed in some experiments, such as the investigations by Aarts and Lekkerkerker [2008] of coalescence in colloid-polymer mixtures with ultralow surface tension.

1.2.3 Similarity solutions for inviscid coalescence

Self similar scalings for flows with surface tension and inertia alone were first identified by Keller and Miksis [1983]. They considered surface tension driven flow in an initially stationary semi infinite wedge of fluid, so that there are no geometrically imposed lengthscales. At time $t = 0$ the boundary conditions at the tip of the wedge are altered discontinuously and the fluid is released from rest. The only dimensional quantities in the problem are the fluid density ρ, coefficient of surface tension γ and time since release t. On dimensional grounds, only one lengthscale can be constructed from these quantities, giving a self similar solution where all lengths are proportional to

$$L_{inviscid} \equiv \left(\frac{\gamma}{\rho}\right)^{1/3} t^{2/3}. \tag{1.11}$$

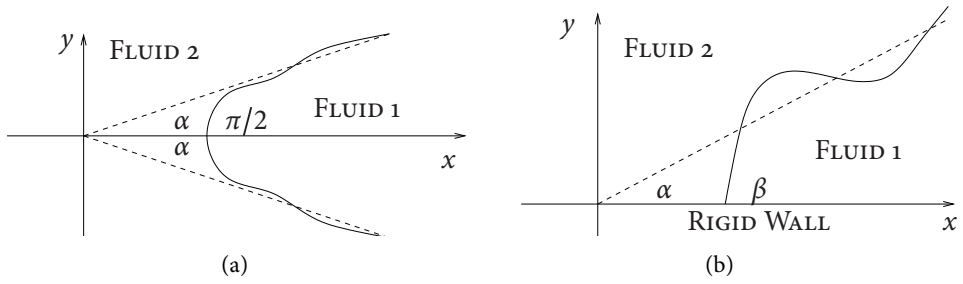

Figure 1.6: The wedge geometries proposed by Keller and Miksis [1983]. (a) Inviscid fluid with density ρ_1 initially lies at rest within a wedge of semi-angle α and fluid of density ρ_2 lies outside this wedge. When $t > 0$ the interface is allowed to recoil under the action of surface tension. The flow is symmetric about the x-axis and the tip of the interface is perpendicular to the x-axis. This configuration describes the merging and splitting of fluid wedges. (b) Inviscid fluid occupies the region $y > 0$, with a rigid wall along $y = 0$. Initially the two fluids are at rest, with fluid 1 filling a wedge of angle α. When $t = 0$ the contact angle at the tip of the wedge is suddenly changed to β. This configuration corresponds to an inviscid model of contact line motion, discussed in section 1.2.6.

Miksis and Vanden-Broeck [1999] considered Stokes flow in an initially wedge shaped domain. Here inertia is negligible and the lengthscale must be constructed from the dynamic viscosity μ and coefficient of surface tension γ. It is again necessary to make use of time since release t in order to construct a lengthscale, which is given by

$$L_{Stokes} \equiv \frac{\gamma}{\mu} t. \tag{1.12}$$

The similarity solutions implied by (1.11) and (1.12) simplify the corresponding free boundary problems significantly by removing the time dependence. The problem must be solved in self similar variables at one instant only and then the solution is known for all time.

Keller and Miksis [1983] suggested two applications for self similar flow in wedges and cones. The first is to fluid pinch off or coalescence. At the moment of pinch off or coalescence, two fluid bodies are in contact only at a single point. Sufficiently near this contact point, the flow is independent of the drop-size geometry, with the macroscale contributing only angles to the flow near the contact point. Just after pinch off or coalescence, the flow interfaces must avoid cusps or other curvature singularities. Instead, the contact angles become $\beta = \pi/2$, as shown in figure 1.6(a). This is consistent with photographic studies of drop pinch off by Peregrine et al. [1990], which show that just before pinch off, the local shape of the drop resembles a cone. A sequence of photographs of drop pinch

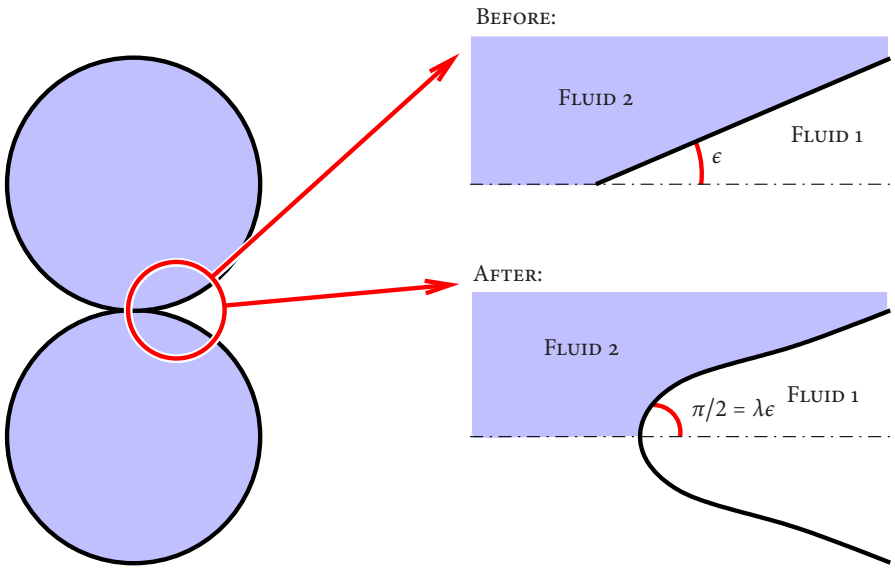

Figure 1.7: Symmetric recoil has $\lambda\epsilon = \pi/2$, with the limit $\epsilon \to 0$ being the coalescence of spherical drops. In chapters 3 and 4 we consider solutions for $1 \ll \lambda \ll \epsilon^{-1}$ so that the domain for fluid 2 can be approximated by a half plane. Throughout this thesis we refer to this configuration, in which fluid 1 surrounds drops of fluid 2 which coalesce.

off is shown here in figure 1.10. Similarly, flow from initially wedge-shaped conditions is relevant to the breaking apart of sheets of fluid.

The second proposed application is as an inviscid model of contact line motion, illustrated in figure 1.6(b), with the axis of symmetry shown by the dash-dotted line in figure 1.6(b) becoming a rigid wall. A wedge of fluid is initially in contact with the rigid wall, with the wedge angle equal to the contact angle, and the system in equilibrium. A second inviscid fluid, or a void, occupies the complementary region between the first fluid and the wall. When time $t = 0$, the contact angle at the tip of the wedge is suddenly changed and the fluid recoils. For this moving contact line problem, the initial wedge angle α and the subsequent contact angle β may lie anywhere in the range $(0, \pi)$.

The coalescence of spherical drops corresponds to a restricted range of initial wedge angle. As sketched in figure 1.7, we find that the appropriate angles for recoil due to coalescence of spherical drops are $\alpha = \epsilon$, $\beta = \pi/2$, with the fluid in the drop (fluid 2) occupying the fat wedge with initial angle $\pi - \epsilon$, and the surrounding fluid (fluid 1) initially occupying the complementary wedge with angle ϵ. The limit $\epsilon \to 0$ corresponds to moving towards the initial rupture location, with $\epsilon = O(r_m/R)$. The evolution of fluid bodies towards and after pinch off involve a different selection of wedge angles, and conical

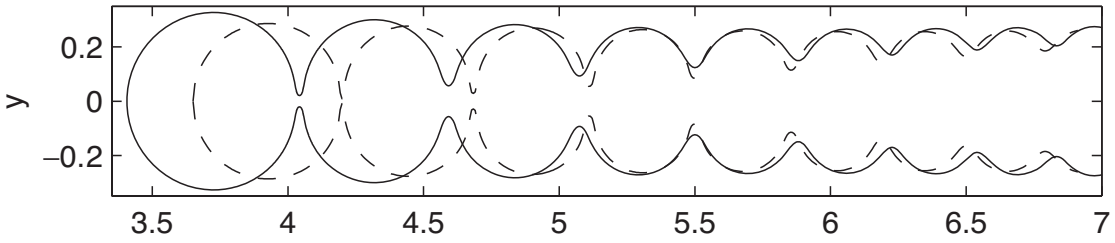

(a) From Billingham [2006]. Self similar recoil of a slender wedge of inviscid fluid. The initial wedge angle is $\epsilon = 2^\circ$, and $\beta = 90^\circ$. The solid line shows the numerical solution to the free-boundary problem. The dashed line shows the asymptotic solution for flow inside a slender wedge for $\epsilon \ll 1$ and $\lambda\epsilon = O(1)$.

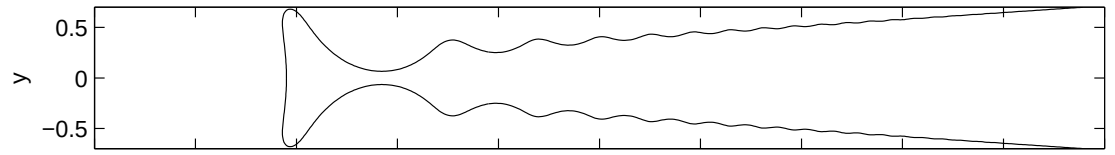

(b) From Billingham and King [2005]. Self similar recoil of inviscid fluid outside a slender void, with $\beta = 90^\circ$ and $\alpha = 4^\circ$.

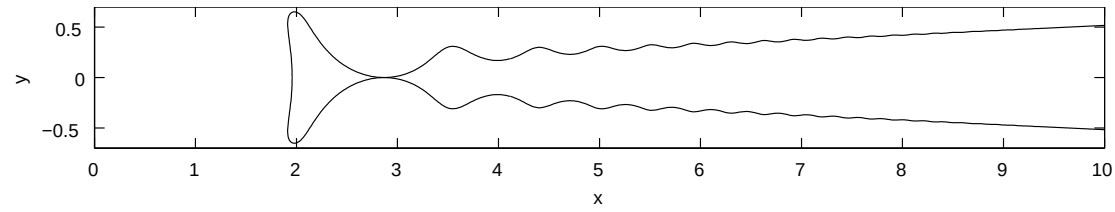

(c) From Billingham and King [2005]. Self similar recoil of inviscid fluid outside a slender void, with $\beta = 90^\circ$ and $\alpha = 2.87^\circ$. There is no solution for $\alpha < 2.87^\circ$ for flow outside a slender wedge.

Figure 1.8: Interface positions for inviscid recoil inside and outside a slender wedge.

curvature can become significant.

For general angles α and β, Keller & Miksis showed that the two-dimensional system for the recoil of a fluid wedge could be written as a nonlinear integro-differential equation involving only properties of the free surface. This integral equation system is then discretised and solved numerically. Keller and Miksis noted the presence of capillary waves on the interface; they use a linearised analysis to calculate these waves, and showed that the waves decay in amplitude and grow in frequency as they propagate away from the contact point. Capillary waves have been observed experimentally for coalescence and pinch-off problems. They are predicted by inviscid surface tension driven models, but do not arise in Stokes flow [Miksis and Vanden-Broeck, 1999].

One of the first analytical investigations of the system posed by Keller & Miksis came from Lawrie [1990], who solved the linearised system that arises when $|\alpha - \beta| \ll 1$. The

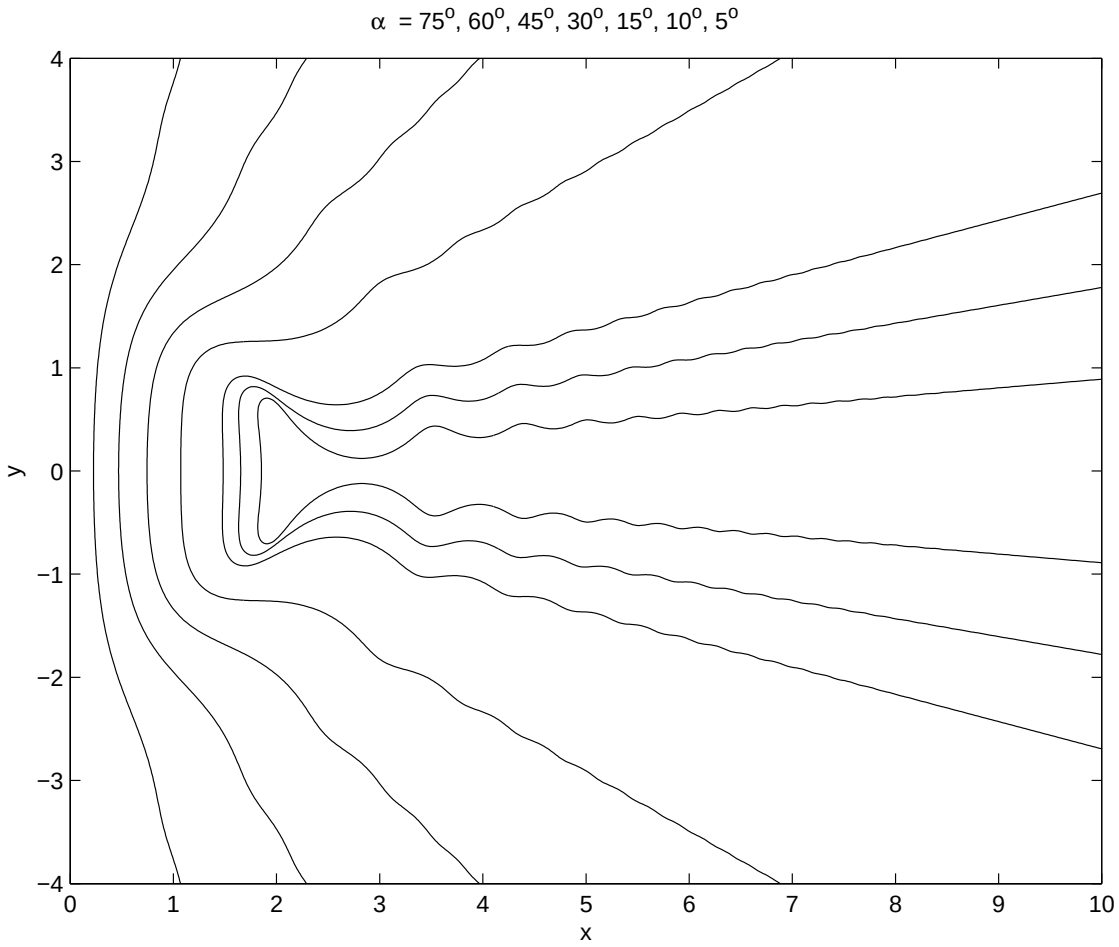

Figure 1.9: From Billingham and King [2005]. Interface position for self similar inviscid flow outside a slender void for a range of $\alpha \geq 5°$, $\beta = \pi/2$. As α decreases, the capillary wave amplitude increases, and at $\alpha = 2.87°$, the two sides of the interface make contact.

domain of solution here is a wedge of angle α, and an analytic solution is available by means of Mellin transforms (see also Lawrie and King [1994]). As is common using such methods, the resulting solution was explicit only for rational wedge angles of the form $\alpha = p\pi/2q$ where p and q have no common factors and p is odd. However, the linearisation assumption fails near the contact point, and so other approximations must be used; Lawrie assumed that the free surface takes the shape of a circular arc in this region.

King [1991] considered the recoil of a slender fluid wedge due to a small change in contact angle, and showed that in contrast to Lawrie's analysis, the leading order system is nonlinear. He examined the case where $\alpha = \epsilon$, $\beta = \lambda\epsilon$ and $\lambda = O(1)$ as $\epsilon \to 0$ so that

the fluid always occupies a slender domain. He showed that as $\epsilon \to 0$, the flow near the wedge tip is predominantly unidirectional, and was able to reduce the system to a pair of coupled nonlinear ODEs for the velocity potential along the free surface and the linearised interface displacement. At larger distances, the wedge is no longer narrow, and so there is a weakly two dimensional flow in the far field. Another difference with Lawrie's analysis is that King's equations allow the contact point to move freely along the rigid wall.

Billingham [2006] extended the analysis of King's nonlinear ODE system by using Kuzmak's method to find an asymptotic solution for $1 \ll \lambda \ll \epsilon^{-1}$. The solution takes the form of a rapid oscillation with slowly varying amplitude and phase. Kuzmak's method is a version of the method of multiple scales which allows for the capillary wave period to vary with amplitude. Billingham derived and solved equations for the leading order periodic oscillator and secularity equations for the slow variation of oscillator parameters. The nonlinear periodic oscillator equations for this analysis have an exact solution in terms of elliptic integrals. The secularity equations can then be written in terms of complete elliptic integrals, and the boundary value problem for the secularity equation system solved numerically to obtain the correct solution. This asymptotic solution is simply connected for $\lambda \to \infty$, although the derivation of the ODE system requires $1 \ll \lambda \ll \epsilon^{-1}$. This asymptotic calculation forms the basis for the two-fluid asymptotic solution discussed here in chapter 4.

Billingham also considered the recoil of a slender wedge for $O(1)$ contact angles. He found valid solutions for all λ, ϵ with $\lambda\epsilon < 90°$ and obtained an asymptotic solution for $\epsilon \to 0$. The asymptotic solution again consists of a sequence of modulated oscillations; however the underlying nonlinear oscillator becomes a nonlinear free boundary problem which has an exact solution. The numerical solution for $\beta = \pi/2$ is shown in figure 1.8(a) for $\epsilon = 2°$ and resembles a sequence of circular 'beads' connected by narrow necks. Decent and King [2008] considered the related problem of recoil of a slender cone of inviscid fluid for $\beta = \pi/2$, which is an inviscid model of the retraction of the 'liquid bridge' just after drop pinch off (figure 1.10). The asymptotic solution found by Decent and King also resembles a string of spherical beads connected by thin neck regions, which are matched to the original cone shape in the far field.

Keller et al. [2000, 2002] discussed various configurations of the inviscid self similar

problem in relation to breaking and merging of fluid bodies, and coalescence with solid surfaces. They found numerical solutions to the nonlinear free boundary problem and explored the relationship between contact-point displacement and the angles governing the problem. They showed that for the coalescence of fat two-dimensional fluid wedges, the free surface pinches off once the wedge semi-angle reaches 87.5°.

Motivated by the prediction by Keller et al. [2002] of a self-intersecting free surface, Billingham and King [2005] calculated interface positions for self similar inviscid flow outside a slender wedge, with $\alpha = \epsilon$, $\beta = \pi/2$ and $\rho_1 = 0$ in figure 1.6(b). Some typical interface positions calculated by Billingham and King [2005] are shown in figure 1.9. We note that the problems considered by Billingham and King and by Keller et al. [2002] are not completely equivalent; the flow analysed by Keller et al. has two distinct free surfaces, while that examined by Billingham and King has only one. The significance of the reflected interface diminishes as the contact point position x_c increases. We further discuss the relationship between these two problems in chapter 5.

Billingham and King showed that for inviscid recoil outside a single slender wedge, there is no solution for $\epsilon < 2.87°$, as the amplitude of the capillary waves causes the interface to self-intersect (figures 1.8(a), 1.8(b)). The shape taken by the interface for small ϵ resembles the interface obtained by Duchemin et al. [2003] for successive reconnections, shown here in figure 1.4. For an external fluid with non-zero density, mass conservation is violated for self similar solutions if the interface pinches off. However, Billingham and King showed that the presence of an external fluid with non-zero density slightly decreases the range of ϵ for which a solution exists, as the narrowing interface drives a fast flow towards the contact point in the slender wedge which sucks the sides of the interface together.

1.2.4 Viscous flow in wedges

Self similar solutions are also available for viscous coalescence [Miksis and Vanden-Broeck, 1999]. In this case the lengthscales grow as $O(t)$. Miksis and Vanden-Broeck found suitable solutions for coalescence with finite density ratio between drops and surrounding fluid, but could not obtain a self similar solution for the coalescence of bubbles surrounded by a viscous fluid. Billingham [2005] investigated the recoil of an

isolated fluid wedge in more detail, and showed that the solution is not self similar, but consists of an inner region with a balance between viscosity and surface tension, and an outer region where viscosity and inertia balance, and surface tension is negligible. This non-self similar solution has wedge tip position $O(t \log t)$, which is consistent with the time dependent analyses from Hopper [1990] and Eggers et al. [1999], in contrast to the self similar Stokes flow solutions which by construction have $r_m = O(t)$.

Billingham [1999] considered the recoil of fat wedges and cones under the action of surface tension, viscosity and inertia, with wedge angles $\alpha = \pi/2 - \epsilon$ and $\beta = \pi/2$. If the fluid is viscous, there is no longer a self similar solution. Billingham showed that viscosity reduces the initial velocity singularity from $O(t^{-1/3})$ to $O(\log(1/t))$. At long times, the solution tends towards the inviscid similarity solution found by Keller and Miksis so long as $r \ll t^{3/4}$. Beyond this distance viscosity damps the high frequency capillary waves – this would be expected as capillary wave curvature grows unbounded for the inviscid solution. Billingham found a very similar asymptotic structure in the case of a recoiling fat wedge and a recoiling fat cone. However, the surface deformations are much smaller in the case of the cone, partly due to the geometrical spreading factor, and partly due to the non-zero curvature of the cone itself.

1.2.5 Pinch-off problems

Self similar flow in wedges and cones also has applications to pinch off problems. Various experimental studies have shown that the pinch off of a droplet from a dripping tap, for example, occurs by formation of a thin liquid bridge connected to the main body of the droplet [Peregrine et al., 1990]. At the moment of pinch off, the liquid bridge and the main droplet body touch at a single point, and form a double-cone structure, with different cone angles for the bridge and the drop. The curvature at the tip of each cone is singular, and so the each fluid cone recoils after pinch off. A sequence of images of a dripping tap is shown in figure 1.10. This shows the formation and recoil of the liquid bridge.

Using similar arguments to that for coalescence, we find that at times very close to pinch off, surface tension and viscous forces form the dominant balance. However, further from the time of pinch-off, whether earlier or later, the inviscid surface tension driven flow is useful for flow of low viscosity fluids.

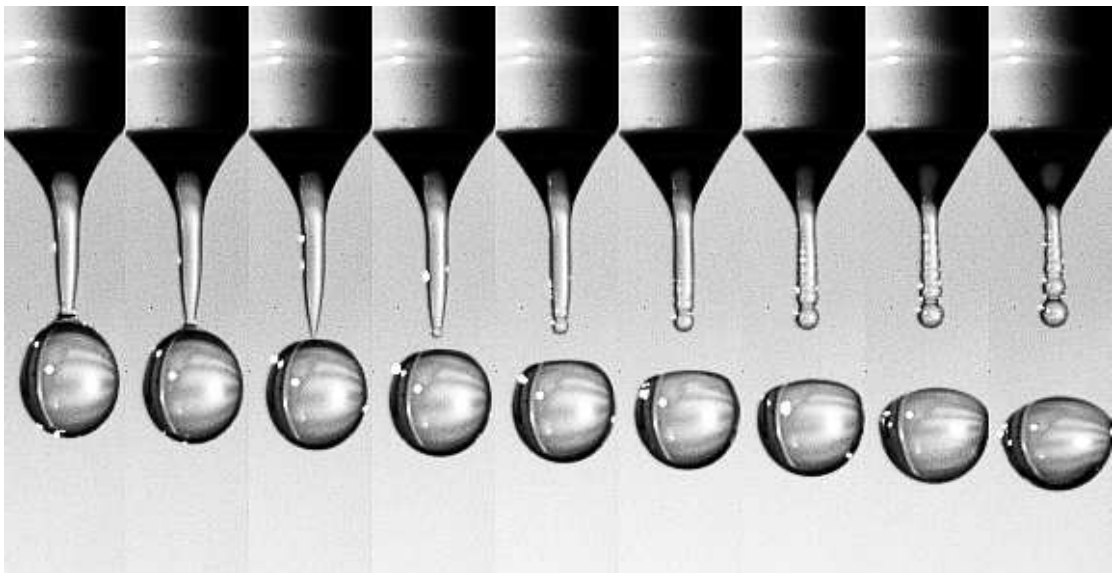

Figure 1.10: Neck formation and pinch off from a dripping tap. This image sequence is filmed at 850 frames per second, and the width of each image is approximately 8 mm. Photo: C.G. Johnson.

Day et al. [1998] conducted a numerical analysis which showed that deformed droplets of inviscid fluid could tend towards a singular double cone structure under the action of surface tension. Starting from drops shaped like a dumbbell, they calculated the time dependent evolution of drops under the action of surface tension and inertia. For those drops which led to finite time singularities, the interface tended towards a self-similar double-cone shape, with lengths proportional to $(t - t^*)^{2/3}$, where t^* is the pinch-off time. This time dependence is also the self similar scaling for surface tension driven, inviscid flow.

Day et al. found that the cone angles at pinch-off were largely independent of the initial configuration of the drop. For the case of a single fluid pinching in a vacuum, the cone angles tended towards 18.1° and 112.8°. An earlier analysis by Chen and Steen [1997] showed computationally that an axisymmetric soap-film sleeve tends towards a double cone structure with angles 12° and 127°. Leppinen and Lister [2003] investigated the variation of evolution towards pinch-off for different density ratios between the drop and the surrounding fluid and showed that the cone angles vary with the density ratio. In all cases, the two cone angles differ, with liquid bridge corresponding to a slender cone, and the pinching drop corresponding to a much fatter cone. The flow in the slender cone

can be predominantly one-dimensional, but flow in the fatter cone will have comparable axial and radial velocities and so requires an analysis in two spatial dimensions. The recoil of the slender liquid bridge has been examined in more detail by Decent and King [2001, 2008], Schulkes [1994], Keller et al. [1995].

A constant-angle cone has non-zero curvature, and so a static cone of fluid cannot be in equilibrium, unlike a two-dimensional wedge of fluid. Therefore, self similar solutions starting from a conical interface must have a non trivial initial velocity. Simulations of flow towards pinch-off can calculate the far field flow as part of the solution. Solutions for flow after pinch-off should take a suitable far field velocity potential as an initial condition.

Sierou and Lister [2004] examined flow after pinch-off from these double cone shape structures. They took as initial conditions the cone angles and velocity profiles calculated by Leppinen and Lister [2003]. The flow is again self similar, with all lengths proportional to $t^{2/3}$. They showed that the self similar recoiling interface position depends strongly on the initial velocity profile. Sierou and Lister found good agreement between recoil of the narrower cones and the asymptotic solution for slender cones found by Decent and King [2001].

1.2.6 Moving contact line models

Moving contact lines in viscous flow have long been a contentious issue. At a contact line between two fluids and a solid, applying the no slip boundary condition along the solid surface together with the full Navier–Stokes equations implies that an infinite force is required to move the contact line [Huh and Scriven, 1971]. A number of theories have been proposed to remove this apparent paradox, but none have been universally accepted. It is well known that the introduction of viscosity is a singular perturbation, and so an inviscid model of contact line motion cannot fully describe the motion of the fluid close to the contact point even for a low viscosity fluid. In justification of our simple inviscid contact line model, we hope that sufficiently far from the contact line itself that we can neglect the detail of the flow in the viscous inner region, and so we are interested in a macroscopic description of contact line motion.

A review of experimental and theoretical results for contact line motion was provided by Dussan V. [1979], who showed that for a given fluid, the contact angle θ is a monotonic

function of the contact line speed U. When the contact line is at rest, the contact angle θ lies within some interval (θ_R, θ_A). When the contact angle, as measured within the fluid, is increased above θ_A, the contact line advances, and when the contact angle is decreased below θ_R, the contact line recedes. Once the contact line is in motion, the contact angle increases as U increases, but tends towards some finite angle.

For inviscid flow the similarity scaling obtained by Keller and Miksis implies that all velocities scale as $t^{-1/3}$, and so the velocity of the contact point is very fast for small times. We therefore assume that the contact angle immediately adopts the limiting value appropriate to infinitely fast contact line motion, and remains at this value for all times.

Self similar scalings for surface tension driven inviscid flow can be applied to flows with a change of contact angle, whether due to coalescence, pinch off, coming into contact with a solid or a sudden change in surface chemistry. Keller et al. [2000, 2002] showed that similarity solutions could be found for the coalescence of a wedge of fluid into a corner, or the coalescence of wedges of fluid along a solid surface. In both cases, the initial geometry is specified entirely by angles. Billingham and King [1995] and King et al. [1999] considered the case of a fluid/fluid interface dragged onto a solid plate, thus creating a contact point where the interface meets the plate. The flow in the far field continues with its original velocity, giving a further dimensional quantity, and so the solution is not self similar. They assumed an explicit dependence of the contact angle θ on the contact point velocity U. The initial formation of the contact line was found to depend strongly on the profile of $\theta(U)$. However, for large times, the contact line moves at the same speed as the far field flow, so the contact angle becomes constant and a similarity solution is obtained.

1.2.7 Conclusion

The initial force balance for coalescing drops is always between surface tension and viscosity. However, the Reynolds number grows as the meniscus widens. For low viscosity fluids such as water, the viscous lengthscale is very small; once the meniscus radius is beyond this lengthscale, inertial effects become important, and a new balance is formed between surface tension forces and inertia.

The merging of two cylinders in Stokes flow with no surrounding fluid has been solved exactly by Hopper [1990]. Eggers et al. [1999] investigated the coalescence of

cylinders with a viscous surrounding fluid and found that a bubble of the surrounding fluid accumulates at the meniscus as it moves outwards, although the drops remain simply connected. These theoretical solutions for viscous coalescence predict that the meniscus radius $r_m = O(t \log t)$ for early time. Experimental observations of coalescence in the Stokes flow regime support the scaling $r_m = O(t)$ but have not yet verified the logarithmic behaviour.

The inviscid surface tension driven coalescence of spheres has been studied numerically by Duchemin et al. [2003]. They found that there is no simply connected solution for the coalescence of spheres with zero density surrounding fluid, as large amplitude capillary waves cause the free surface to pinch off a toroidal bubble. Averaging over a sequence of pinching events gives a solution with $r_m = O(t^{1/2})$ which is in accordance with experimental observations of coalescence of low viscosity fluids, but there is a discrepancy in the prefactor between experimental observations and the calculations of Duchemin et al.

A related problem to coalescence of spheres is the recoil of fat fluid wedges due to a sudden change in wedge tip angle. If there are no geometrically imposed lengthscales, the subsequent fluid flow must be self similar, for flows with surface tension and viscosity alone [Miksis and Vanden-Broeck, 1999] and for flows with surface tension and inertia alone [Keller and Miksis, 1983]. Self similar scalings remove the time dependence of the problem. A number of studies have been made of the viscous and inviscid recoil of wedges and cones, which are also useful for pinch off problems. For coalescence, Billingham and King [2005] showed that there is no simply connected self similar solution for inviscid recoil around a slender void, which is consistent with the collapsing interfaces found in the time dependent coalescence of spheres studied by Duchemin et al. However, analysis of the recoil of a slender wedge [King, 1991, Billingham, 2006] suggests that the inviscid coalescence of bubbles is simply connected.

For two-fluid problems, viscous and inertial effects in the surrounding fluid may have a significant effect on the coalescence flow, particularly in regions where the free surface narrows.

1.3 Thesis outline

The aim of this thesis is to examine the effect of a low density surrounding fluid on the existence and behaviour of self-similar solutions for inviscid coalescence. In order to make the analysis more tractable, we make several simplifications to this time-dependent, nonlinear, free-boundary problem. We consider the coalescence of two-dimensional fluid wedges, rather than spherical fluid drops, so that the flow becomes self-similar, thus removing the time dependence. Symmetric coalescence then corresponds to the coalescence of very fat fluid wedges, with initial wedge angle $\pi - \epsilon$, where $\epsilon \ll 1$, and subsequent wedge angle $\pi/2$. We simplify the problem further by considering the recoil of the system due to a small change in wedge angle, so that the wedge angle changes from $\pi - \epsilon$ to $\pi - \lambda\epsilon$ during coalescence, where $\lambda = O(1)$, as illustrated in figure 1.6(b). In the limit $\lambda = O(1)$ and $\epsilon \ll 1$, the leading order problem is no longer a free-boundary problem; instead the flow in fluid 1 is described by nonlinear ODEs, while the flow in fluid 2 is described by a half-plane problem.

Although this leading order problem does not replicate all the nonlinearities of the full free-boundary problem, we find that the existence of simply-connected solutions corresponds to the known results for the nonlinear problem for single fluid problems. King [1991] and Billingham [2006] have studied the recoil of a slender fluid wedge, which is applicable to the coalescence of bubbles, and showed that in both the $\lambda = O(1)$ and $\lambda\epsilon = O(1)$ cases, solutions remain simply connected as $\epsilon \to 0$. For the coalescence of drops, Billingham and King [2005] have shown that there is no simply connected solution for $\epsilon \ll 1$ with $\lambda\epsilon = O(1)$, with solutions pinching off at a finite value of ϵ for $\lambda\epsilon = \pi/2$. In chapter 3, we consider the linearised version of the problem studied by Billingham and King, for $\lambda = O(1)$ and $\epsilon \ll 1$, and show that pinch-off occurs at a finite value of λ. This linearised half-plane problem for coalescence of fluid drops with no surrounding fluid has not been investigated previously.

In chapter 4, we investigate the behaviour of the two-fluid problem in this linearised limit. We find that a distinguished limit for $\epsilon \ll 1$ occurs when $\rho_1/\rho_2 = O(\epsilon)$, and the problem is further distinguished when $\rho_1/\rho_2 = O(\lambda\epsilon)$. We investigate the solution behaviour for these density ratios, both numerically and asymptotically, and find evidence that the solutions remain simply connected as $\lambda \to \infty$ with $\lambda\epsilon \ll 1$ for both density

regimes. These novel asymptotic results for two-fluid coalescence give support to the theory that a low density surrounding fluid may allow self-similar solutions for the fully nonlinear free-boundary problem to remain simply connected as $\epsilon \to 0$ with $\lambda\epsilon = \pi/2$.

Throughout the thesis, we use a variety of numerical, asymptotic and analytical methods to analyse the half-plane problems, both for single-fluid and two-fluid coalescence. We now give a more detailed description of the work undertaken.

In chapter 3, we consider the behaviour of the 'half plane problem' for $\epsilon \ll 1$ when $\rho_1 = 0$. We use a boundary integral discretisation to find numerical solutions for the free surface displacement and velocity potential. We then find an asymptotic solution for large λ, with $1 \ll \lambda \ll \epsilon^{-1}$. This asymptotic solution takes the form of large amplitude, high frequency, capillary waves on the free surface, which are matched to an inner region near the contact point. The equations in this inner region can be reduced to those for a special case of the 'dock problem', which is a classical problem in wave scattering, and its solution, firstly by the Wiener–Hopf method and secondly by Mellin transforms, is discussed in chapter 2. The dock problem solution completes the asymptotic solution for large λ. We also investigate the small displacement limit of the half plane problem, with $|\lambda - 1| \ll 1$, and solve the resulting leading order problem exactly using Mellin transforms.

Both the numerical solution and the asymptotic solution for large λ found in chapter 3 show that the amplitude of the capillary waves on the free surface increases as λ increases. In fact we find that for $\lambda \gtrapprox 30$, the free surface intersects with the position of the rigid wall. As the leading order equations are linear, this is mathematically but not physically valid. This behaviour is analogous to the nonexistence of self similar solutions for $\beta = \pi/2$ and $\alpha < 2.87°$ when $\rho_1 = 0$ and $\rho_2 = 1$ as found by Billingham and King [2005].

In chapter 4, we consider a two-fluid problem with the same contact angle limits as in chapter 3. We find that $\rho_1/\rho_2 = O(\epsilon)$ is a distinguished limit for $\epsilon \ll 1$ and $\lambda = O(1)$. The leading order system now features a linear half plane problem for the velocity potential in fluid 2 coupled to nonlinear ODEs for the flow in fluid 1. We use a boundary-integral method to reduce the kinematic equations for fluid 2 to a one-dimensional integral equation, and combine this with a relaxation method to find numerical solutions to the two-fluid system. Valid numerical solutions appear to be available for all finite λ with density ratio $\rho_1/\rho_2 = O(\epsilon)$.

In the second half of chapter 4, we pursue a large-displacement asymptotic solution to the two-fluid problem, and find that the strongest coupling between the flows in the two fluids occurs when $\rho_1/\rho_2 = O(\lambda\epsilon)$. For this problem, the governing equations are nonlinear PDEs, so finding the shape and evolution of the capillary waves on the free surface, even away from the contact point, requires multiple scales analysis. We use Kuzmak's method to find nonlinear, nonlocal, periodic oscillator equations for the capillary waves, with oscillator parameters determined by secularity equations. As in the analysis for the large-displacement solution in chapter 3, we find that the solution is critically controlled by an inner region near the contact point, where free surface capillary waves are matched to a two-dimensional flow. For this problem we find that the inner problem is discontinuous, and involves a gradual transition from the periodic capillary waves along the free surface to a half plane problem near the contact point. The inner problem does not seem to be amenable to analytical approaches; its numerical solution is discussed in appendix A.

For the doubly-distinguished density ratio $\rho_1/\rho_2 = O(\lambda\epsilon)$, the large-$\lambda$ asymptotic solution is valid for $\lambda \to \infty$. We consider the behaviour of this asymptotic solution as $\rho_1/\rho_2 \to 0$, and show that this is a singular limit, with the rapid flow in the slender wedge preventing pinch off in this linearised problem, subject to the existence of suitable solutions to the inner problem.

Chapter 2

The dock problem

In chapter 3, we will study the self-similar, surface-tension-driven recoil of a fat wedge of fluid, bounded along one side by a rigid wall, and on the other edge by a free surface, as shown in figure 3.1. The flow recoils due to a sudden change in wedge angle, from $\pi - \epsilon$ to $\pi - \lambda\epsilon$. We consider the behaviour of this system in the limit $\epsilon \ll 1$ with $\lambda = O(1)$, and find that at leading order in ϵ, the flow domain for the fluid in the fat wedge can be approximated by the half-plane $y > 0$. The rigid wall becomes a no-net-flux boundary condition on the negative x-axis, while the free-surface gives linear boundary conditions on the positive x-axis, and so at leading order, we solve a linear half-plane problem with boundary conditions of mixed type on the x-axis. The equations for this half-plane problem are given by the system (3.4). We investigate solutions to this system for different values of λ, and find asymptotic solutions for large λ, described in section 3.4 and for $|\lambda - 1| \ll 1$, described in section 3.5. We find that in both cases, the asymptotic analysis requires the solution of a two-dimensional problem for the velocity potential, with boundary conditions of mixed type. For the large-λ analysis, this two-dimensional problem arises in an inner region, in which the equations reduce to a special case of the dock problem, while for the $|\lambda - 1| \ll 1$ analysis, the leading order problem is a parameter-free half-plane problem which is solvable using Mellin transforms.

In the first half of this chapter, we use the Wiener-Hopf method to derive the unique solution for the dock problem that meets the requirements of the large-λ problem in chapter 3. In the second half of this chapter, we rederive this dock problem solution using Mellin transforms. We do not use the Mellin transform solution found here directly, but the calculation serves as a useful prototype for the asymptotic calculations for $|\lambda - 1| \ll 1$

in chapter 3.

2.1 Introduction

The dock problem is a classical problem in wave scattering. Gravity-inertia waves of the form $\exp(i\mathbf{k}\cdot\mathbf{x} - \omega t)$ along the surface of a body of water occupying the half-space $y < 0$ are incident on a rigid dock located at $y = 0$, $x < 0$. The wave vector $\mathbf{k}$ has component k_x perpendicular and k_z parallel to the dock edge. The line $x = 0$, $y = 0$ represents a sudden jump between the free-surface boundary conditions on $x > 0$, $y = 0$, and rigid wall boundary conditions on $x < 0$, $y = 0$. The problem for a semi-infinite dock has been solved for $k_z = 0$ by Friedrichs and Lewy [1948] and for $k_z \neq 0$ by Heins [1956]. A number of other problems, such as scattering by a finite-length dock, have also been studied.

The inner problem for the large-λ analysis in discussed in section 3.4.2. We find that the equations reduce to those for the dock problem with $k_z = 0$. As the problem considered in chapter 3 is self-similar, the velocity potential itself, as well as its spatial derivatives, appears in the Bernoulli equation (3.4b). However, this term does not appear at leading order in the Bernoulli equation for the inner region; instead we require the velocity potential to be bounded at the contact point in order to yield a finite contact angle. The time-dependent dock problem has bounded velocity potential ϕ only once per cycle, so we can replace the time dependence with a normalisation constraint on ϕ; we find that there is a unique solution to the normalised problem.

In this chapter we derive solutions to this special case of the dock problem using two complex variable methods: the Wiener-Hopf technique, and Mellin transforms. We find that the Wiener-Hopf technique gives a solution in terms of integrals of elementary functions. The Mellin transform method leads to a functional difference equation that we solve in terms of Barnes double Gamma functions. We must then invert the Mellin transform solution.

2.2 Problem statement

The dock problem is a half-plane problem, with boundary conditions of mixed type. The problem has no parameters and all the equations and boundary conditions take simple forms. Throughout this chapter we will use the configuration shown in figure 2.1, in which

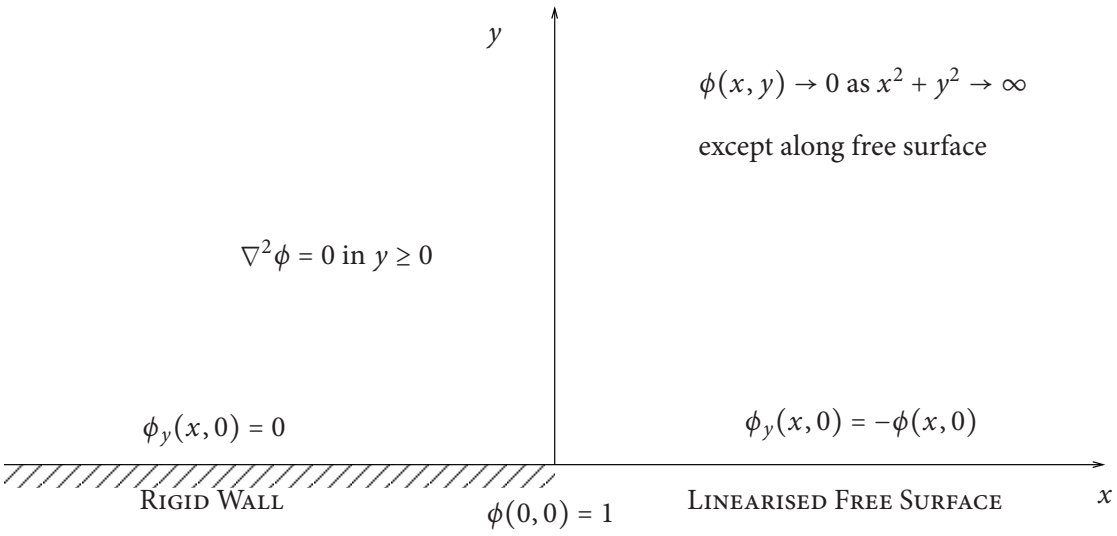

Figure 2.1: Equations and boundary conditions for the dock problem as considered in this chapter.

the fluid occupies the half-plane $y \geq 0$.

The fluid is irrotational and incompressible, so we solve for the velocity potential $\phi(x, y)$ where $\mathbf{u} = \nabla\phi$, with $\phi(x, y)$ satisfying

$$\nabla^2\phi(x, y) = 0 \quad \text{when} \quad y \geq 0. \tag{2.1}$$

The conditions on the boundary of this half plane take three different forms. We have a linearised free surface along the half-line $y = 0$ and $x > 0$, with the boundary condition

$$\phi_y(x, 0) = -\phi(x, 0) \quad \text{when} \quad x > 0. \tag{2.2}$$

A rigid wall is placed along the half-line $y = 0$ and $x < 0$. Here we enforce no normal flow through the wall, so that

$$\phi_y(x, 0) = 0 \quad \text{when} \quad x < 0. \tag{2.3}$$

For convenience we also define polar coordinates (r, θ) so that $x = r\cos\theta$ and $y = r\sin\theta$. On the remaining part of the boundary, we require

$$\phi(r, \theta) \to 0 \quad \text{as} \quad r \to \infty \tag{2.4}$$

when $\theta > 0$. We do not apply this condition on the line $\theta = 0$ because waves of the form

$$\phi(x, y) \propto e^{ix-y} \tag{2.5}$$

satisfy the local boundary condition (2.2) but do not decay with x. Instead we require that $\phi(x, 0)$ be bounded as $x \to +\infty$.

So far the system is homogeneous, and $\phi(x, y) = 0$ is a valid solution. To obtain a non-trivial solution, we choose to impose the normalisation constraint

$$\phi(0, 0) = 1, \tag{2.6}$$

which immediately implies a discontinuity in boundary condition at $x = y = 0$. If there is a solution of the system that meets the far field boundary conditions and also has $\phi(0, 0) = 0$, then we should expect an arbitary multiple of this eigensolution to appear in the general solution to the system. We seek solutions that are bounded everywhere, so discard solutions that are singular at the origin.

In this chapter we will use two methods to find an exact solution for $\phi(x, y)$. The first is based around the Wiener-Hopf technique. Here we take half-range Fourier transforms with respect to a complex variable k to obtain a Wiener-Hopf equation valid in a strip of the complex k-plane. We factorise the equation and use analytic continuation to extend both the Wiener-Hopf equation and its factors to the whole of the complex plane. We define an entire function out of the half-range transforms and the factors we have found. We use Liouville's theorem, together with information about the behaviour of the half-range transforms for large k, to determine that this entire function is a polynomial (in this case a constant). We can then recover the half-range transforms and use Fourier inversion to find $\phi(x, y)$.

We find that the Wiener-Hopf technique requires some modification of our problem in order to obtain a finite-width strip of analyticity. However, it does eventually provide a solution to the original problem in terms of integrals of elementary functions and the amplitude and phase of the wave part $\phi(x, y)$ that propagates along the line $\theta = 0$ emerges easily.

The second method makes use of Mellin transforms, which are often used to solve problems in wedge geometries [Lawrie, 1990]. We convert the problem to polar coordinates and then take Mellin transforms with respect to r. The Mellin transform variable p is again complex. The Mellin transforms of (2.1) and (2.3) take simple forms, and we can solve for the θ dependence of the Mellin transform of ϕ in terms of p. With this θ dependence known, the remaining condition (2.2) leads to a functional difference

equation in the complex p-plane. We can solve this functional difference equation in terms of Gamma functions and Barnes double Gamma functions, up to a multiple of a periodic function. We use our knowledge of the singularities and far-field behaviour of the Mellin transform of ϕ, together with Liouville's theorem, to eventually pin this periodic function down to a constant. We can then use Mellin inversion to find $\phi(r, \theta)$.

Although the Mellin transform method needs no modification to work for this problem, its application suffers from our unfamiliarity with Mellin transforms, functional difference equations and double Gamma functions. It is relatively easy to find an asymptotic expansion for small r, by summing residues from poles. However, it is more difficult to understand the behaviour of ϕ for large r as the wave part of $\phi(x, y)$ is hidden inside the inversion integral.

2.3 Expected behaviour of ϕ

Both of the methods we use require some knowledge of the behaviour of ϕ for small and large r, in order to determine for which k the half-range Fourier transforms

$$\tilde{\phi}^+(k, y) = \int_0^\infty e^{ikx}\phi(x, y)dx, \qquad \tilde{\phi}^-(k, y) = \int_{-\infty}^0 e^{ikx}\phi(x, y)dx \tag{2.7}$$

exist and are analytic, and for which p the Mellin transform

$$\Phi^*(p, \theta) = \int_0^\infty r^{p-1}\Phi(r, \theta)dr \tag{2.8}$$

exists and is analytic. The validity of the Fourier transforms depend on the exponential behaviour of $\phi(x, y)$, while the Mellin transform is concerned with algebraic behaviour.

We require $\phi(0, 0) = 1$. This forces a discontinuity in $\phi_y(x, 0)$ at $x = 0$. For small r, we want

$$\frac{1}{r}\frac{\partial\phi}{\partial\theta} = \begin{cases} -1, & \theta = 0, \\ 0, & \theta = \pi, \end{cases} \tag{2.9}$$

which is solved by the harmonic function

$$\phi(x, y) \sim 1 - \frac{x\log r}{\pi} + y\left(\frac{\theta}{\pi} - 1\right) + ax \tag{2.10}$$

where a is an arbitrary constant. We therefore have $\phi_x(x, 0) = O(\log r)$ as $r \to 0$.

The structure for large r is not forced directly by the boundary conditions. Instead we look for separable modes that satisfy (2.1), (2.2) and (2.3) while decaying as $r \to \infty$. In polar coordinates (2.2) takes the form

$$\phi_\theta(r,0) = -r\phi(r,0), \quad \theta = 0 \tag{2.11}$$

and so on $\theta = 0$, ϕ decays more rapidly with r than ϕ does. For the leading order mode, we have $\phi(r,0) = 0$, and the largest separable mode that satisfies this, as well as (2.1) and (2.3), is

$$\phi(r,\theta) \propto r^{-1/2} \sin(\theta/2). \tag{2.12}$$

Thus we see for large r that $\phi(r,\theta) = O(r^{-1/2})$ when $\theta > 0$ but $\phi = O(r^{-3/2})$ when $\theta = 0$.

As mentioned briefly in section 2.1, we also expect waves of the form

$$\phi \propto e^{ix-y}. \tag{2.13}$$

These are harmonic, so satisfy (2.1) and are solutions to the free surface equation (2.2), but do not meet the condition on the rigid wall (2.3). We therefore expect these waves only in $x > 0$, with the solution near $x = 0$, $y = 0$ stitching together the oscillatory and smooth parts of $\phi(x,y)$.

From this information, we expect that the Mellin transform

$$\Phi^*(p,\theta) = \int_0^\infty r^{-p}\phi(r,\theta)dr \tag{2.14}$$

will be analytic for $0 < \mathrm{Re}\, p < 1/2$ when $0 < \theta \leq \pi$, and for $0 < \mathrm{Re}\, p < 3/2$ when $\theta = 0$.

For the problem as stated above, with (2.1), (2.2) and (2.3), there is no complex k for which both half-range Fourier transforms defined by (2.7) exist when $y = 0$. In order to provide a common strip of analyticity with finite width for the Wiener-Hopf method, we replace (2.1) with

$$\nabla^2\phi(x,y) = \delta^2\phi(x,y), \quad \text{when} \quad y \geq 0, \tag{2.15}$$

where δ is small, positive and real, and consider the limit $\delta \to 0$. We leave the boundary conditions as they are. We still expect constant amplitude oscillations along $y = 0$, $x > 0$ and require $\phi(0,0) = 1$. However, we now expect $\phi(x,0) = O(\exp(\delta x))$ as $x \to -\infty$. This gives $\tilde{\phi}^+(k,y)$ analytic when $\mathrm{Im}\, k > 0$ and $\tilde{\phi}^-(k,y)$ analytic when $\mathrm{Im}\, k < \delta$. Both are analytic in the common strip $0 < \mathrm{Im}\, k < \delta$. We will use the Wiener-Hopf technique to find a solution for $\delta > 0$ and then consider the limit of this solution as $\delta \to 0$.

2.4 Wiener-Hopf approach

2.4.1 An outline of the Wiener-Hopf technique

A Wiener-Hopf equation for complex variable k takes the form

$$A(k)\Phi_+(k) + B(k)\Psi_-(k) + C(k) = 0, \quad \text{for } \tau_- < \mathrm{Im}(\tau) < \tau_+. \tag{2.16}$$

Throughout this chapter we will refer to the real and imaginary parts of k as σ and τ respectively. Here $k \equiv \sigma + i\tau$ is a complex variable, for example the Fourier transform variable. In (2.16), $A(k)$, $B(k)$ and $C(k)$ are known functions of k and are analytic in the strip of analyticity given by $\tau_- < \tau < \tau_+$. The functions to be found, $\Phi_+(k)$ and $\Psi_-(k)$ are known to be analytic for $\tau > \tau_-$ and $\tau < \tau_+$ respectively. We refer to the region $\tau > \tau_-$ as the upper half-plane and the region $\tau < \tau_+$ as the lower half-plane.

We now divide (2.16) by $B(k)$ to obtain the standard Wiener-Hopf form [Noble, 1958]:

$$K(k)\Phi_+(k) + \Psi_-(k) + C(k)/B(k) = 0 \tag{2.17}$$

where $K(k) = A(k)/B(k)$ is the multiplicative kernel. We suppose that we can find functions $K_+(k)$ and $K_-(k)$ such that $K(k) = K_+(k)/K_-(k)$ for all k in the strip $\tau_- < \tau < \tau_+$, with $K_+(k)$ analytic for $\tau > \tau_-$ and $K_-(k)$ analytic for $\tau < \tau_+$. Then multiplying (2.17) through by $K_-(k)$ gives

$$K_+(k)\Phi_+(k) + K_-(k)\Psi_-(k) + C(k)K_-(k)/B(k) = 0. \tag{2.18}$$

Now suppose that we are also able to find functions $C_+(k)$ and $C_-(k)$, analytic in the upper and lower half planes respectively, so that the equality

$$C(k)K_-(k)/B(k) = C_+(k) + C_-(k) \tag{2.19}$$

holds for all k in the strip of analyticity, then we can rearrange (2.18) to give

$$K_+(k)\Phi_+(k) + C_+(k) = -K_-(k)\Psi_-(k) - C_-(k). \tag{2.20}$$

By construction the left hand side of (2.20) is analytic for $\tau > \tau_-$, and the right hand side is analytic for $\tau < \tau_+$. Both sides of (2.20) are equal and analytic across the common strip $\tau_- < \tau < \tau_+$. We can now define an entire function by

$$E(k) \equiv \begin{cases} K_+(k)\Phi_+(k) + C_+(k), & \tau > \tau_-, \\ -K_-(k)\Psi_-(k) - C_-(k), & \tau < \tau_+. \end{cases} \tag{2.21}$$

To proceed beyond this stage we need to determine the entire function $E(k)$. Here Liouville's theorem and its extension are very useful. $K_\pm(k)$ and $C_\pm(k)$ are functions we have determined, and we know how they behave as $k \to \infty$ in their respective half-planes. We also need to know the behaviours of $\Phi_+(k)$ and $\Psi_-(k)$ as $k \to \infty$ in the appropriate half planes (the Abelian theorem on page 39 can be very useful in determining the large-k behaviour of transform functions), so suppose that we know

$$|K_+(k)| < P_+|k|^{\alpha_+}, \quad |C_+(k)| < Q_+|k|^{\beta_+}, \quad |\Phi_+(k)| < R_+|k|^{\gamma_+} \tag{2.22}$$

as $k \to \infty$ in the upper half plane, and

$$|K_-(k)| < P_-|k|^{\alpha_-}, \quad |C_+(k)| < Q_-|k|^{\beta_-}, \quad |\Psi_-(k)| < R_-|k|^{\gamma_-} \tag{2.23}$$

as $k \to \infty$ in the lower half plane. Then the function $E(k)$ is bounded as $k \to \infty$ by

$$|E(k)| < \begin{cases} P_+R_+|k|^{\alpha_+ + \gamma_+} + Q_+|k|^{\beta_+}, & \tau > \tau_- \\ P_-R_-|k|^{\alpha_- + \gamma_-} + Q_-|k|^{\beta_-}, & \tau < \tau_+. \end{cases} \tag{2.24}$$

Then by Liouville's theorem and its extension, $E(k)$ is a polynomial of degree at most N, where N is the integer part of $\max\{\alpha_+ + \gamma_+, \beta_+, \alpha_- + \gamma_-, \beta_-\}$. We shall write $E(k) = P_N(k)$. We can now use the definition of $E(k)$ from (2.21) to write

$$\Phi_+(k) = \frac{P_N(k) - C_+(k)}{K_+(k)}, \quad \tau > \tau_- \tag{2.25}$$

$$\Psi_-(k) = -\frac{P_N(k) + C_-(k)}{K_-(k)}, \quad \tau < \tau_+. \tag{2.26}$$

The $N + 1$ coefficients of $P_N(k)$ are left undetermined by the Wiener-Hopf method. However, in many cases $K_\pm(k)$, $C_\pm(k)$, $\Phi_+(k)$ and $\Psi_-(k)$ all decay to zero as $k \to \infty$ in their respective half planes. Then $E(k)$ tends to zero as $k \to 0$, so $P_N = 0$, and the Wiener-Hopf method gives a unique solution.

2.4.2 Formulation of Wiener-Hopf equation for Dock problem

We would like to apply the Wiener-Hopf technique to find the harmonic function ϕ that satisfies the system

$$\nabla^2\phi = 0 \quad \text{for } y > 0, \tag{2.27a}$$

$$\frac{\partial \phi}{\partial y} = -\phi, \quad \text{for } y = 0, x > 0, \tag{2.27b}$$

$$\frac{\partial \phi}{\partial y} = -\phi, \quad \text{for } y = 0, x < 0, \tag{2.27c}$$

is bounded in $y > 0$, and decays to zero as $r \to \infty$ on $0 < \theta \leq \pi$.

We define half-range Fourier transforms by

$$\tilde{\phi}^+(k, y) = \int_0^\infty e^{ikx}\phi(x, y)dx, \qquad \tilde{\phi}^-(k, y) = \int_{-\infty}^0 e^{ikx}\phi(x, y)dx. \tag{2.28}$$

The Fourier inversion theorem gives

$$\phi(x, y) = \frac{1}{2\pi}\int_{-\infty}^\infty e^{-ikx}\left(\tilde{\phi}^+(k, y) + \tilde{\phi}^-(k, y)\right)dk, \tag{2.29}$$

and for notational convenience we also define the full range transform

$$\tilde{\phi}(k, y) = \tilde{\phi}^+(k, y) + \tilde{\phi}^-(k, y). \tag{2.30}$$

However, the Fourier transform of (2.27a) gives a non-analytic kernel in k-space and so we consider the system (2.27) as the limit as $\delta \to 0$ of

$$\begin{cases} \nabla^2\phi = \delta^2\phi & \text{for } y > 0, \\ \dfrac{\partial \phi}{\partial y} = -\phi & \text{for } y = 0, x > 0, \\ \dfrac{\partial \phi}{\partial y} = 0 & \text{for } y = 0, x < 0. \end{cases} \tag{2.31}$$

The system (2.31) transforms to give

$$\frac{\partial^2 \tilde{\phi}}{\partial y^2} = (\delta^2 + k^2)^{1/2}\tilde{\phi}, \qquad \text{for } y > 0 \tag{2.32a}$$

$$\frac{\partial \tilde{\phi}^+}{\partial y} = -\tilde{\phi}^+, \qquad \text{on } y = 0 \tag{2.32b}$$

$$\frac{\partial \tilde{\phi}^-}{\partial y} = 0, \qquad \text{on } y = 0. \tag{2.32c}$$

The complex Fourier transform variable k has real and imaginary parts $k = \sigma + i\tau$. The far field behaviour for ϕ implies that $\tilde{\phi}^+$ is analytic for $\tau > 0$ and that $\tilde{\phi}^-$ is analytic for $\tau < \delta$. Both are analytic in the common strip of analyticity given by $0 < \tau < \delta$.

We define $\gamma(k) = (k^2 + \delta^2)^{1/2}$. This has branch points at $k = \pm i\delta$. We position the branch cuts along the imaginary axis, extending to $\pm i\infty$ respectively, so that they do

not intersect the strip of analyticity. The branch cuts are shown in bold and the strip of analyticity is shaded in figure 2.2. We choose the branch of $\gamma(k)$ so that the real part of γ is positive in the strip of analyticity. The real part of $\gamma(k)$ is only zero along the branch cuts on the imaginary axis, and so $\gamma(k)$ has positive real part over all the complex plane, excluding the branch cuts. Then (2.32a) has general solution

$$\tilde{\phi} = A(k)e^{-\gamma(k)y} + B(k)e^{\gamma(k)y}. \tag{2.33}$$

However, we seek ϕ that decays as $y \to \infty$ and so we put $B(k) = 0$. Eliminating $A(k)$ from (2.33), we find

$$\frac{\partial \tilde{\phi}}{\partial y} = -\gamma\tilde{\phi}, \tag{2.34}$$

which is equivalent to the statement

$$\frac{\partial \tilde{\phi}^+}{\partial y} + \frac{\partial \tilde{\phi}^-}{\partial y} = -\gamma\left(\tilde{\phi}^+ + \tilde{\phi}^-\right). \tag{2.35}$$

We now evaluate (2.33) at $y = 0$ and substitute the remaining boundary conditions from (2.32b) and (2.32c) to obtain the Wiener-Hopf equation:

$$\tilde{\phi}^+\left(1 - \frac{1}{\gamma}\right) + \tilde{\phi}^- = 0. \tag{2.36}$$

This Wiener-Hopf equation relates the two half range transforms $\tilde{\phi}^+(k,0)$ and $\tilde{\phi}^-(k,0)$. The equation (2.36) itself is valid only in $0 < \tau < \delta$, but we know that $\tilde{\phi}^+(k,y)$ is analytic in $\tau > 0$ and $\tilde{\phi}^-(k,y)$ is analytic in $\tau < \delta$. By factorising this equation, we will be able to use analytic continuation to determine $\tilde{\phi}^+(k,0)$ and $\tilde{\phi}^-(k,0)$ for the whole complex k-plane.

2.4.3 Factorisation using the Cauchy integral formula

The next stage in the application of the Wiener-Hopf method is to find functions $K_\pm(k)$, with $K_+(k)$ analytic in the upper half plane $\tau > 0$ and $K_-(k)$ analytic in the lower half plane $\tau < \delta$, such that the equation

$$K(k) \equiv 1 - \frac{1}{(k^2+\delta^2)^{1/2}} = 1 - \frac{1}{\gamma(k)} = \frac{K_+(k)}{K_-(k)} \tag{2.37}$$

is satisfied for all k in the common strip of analyticity $0 < \tau < \delta$. In the absence of an obvious factorisation by inspection, we proceed with an analysis based around Cauchy's

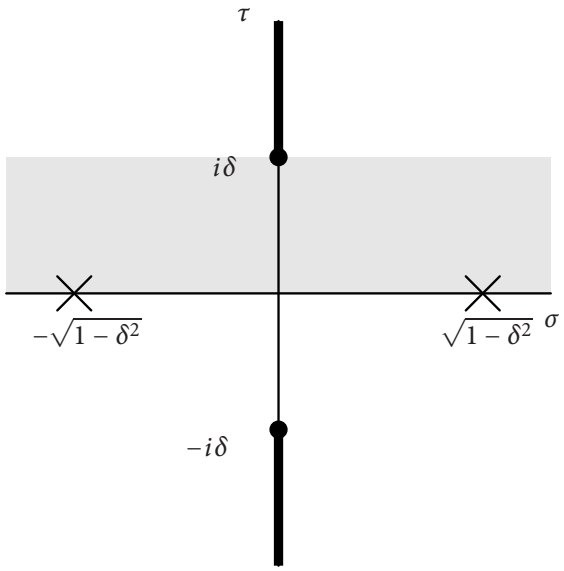

Figure 2.2: The strip of analyticity (shaded), branch cuts (bold) and the location of the zeroes of $K(k)$ (crosses), for the factorisation of $K(k)$. The branch cuts also apply to $\gamma(k) = (k^2 + \delta^2)^{1/2}$.

integral formula. This is a standard method for finding Wiener-Hopf decompositions, and is discussed further by Noble [1958].

We begin by considering the singularities of K. Firstly, $K(k)$ has both branch cuts associated with $\gamma(k)$. $K(k)$ also has two zeroes, occurring at $k = \pm(1 - \delta^2)^{1/2}$. These branch cuts, zeroes and the strip of analyticity for $K(k)$ are illustrated in figure 2.2. The zeroes of $K(k)$ are on the real axis, and hence K has no singularities or zeroes within the strip of analyticity. We can therefore write

$$\log K(k) = \log K_+(k) - \log K_-(k) \tag{2.38}$$

for all k in the strip. This converts the problem from multiplicative to additive decomposition. However, consideration of $\log K$ introduces branch points at the zeroes of K. Rather than deal with the extra branch cut explicitly, we differentiate (2.38) with respect to k, to obtain

$$\frac{K'(k)}{K(k)} = \frac{K'_+(k)}{K_+(k)} - \frac{K'_-(k)}{K_-(k)}. \tag{2.39}$$

The branch points associated with $\log K(k)$ in (2.38) become simple poles in (2.39), which are easier to deal with. The left hand side of (2.39) is known, and so we now seek $f_+(k)$

analytic in $\tau > 0$ and $f_-(k)$ analytic in $\tau < \delta$, which satisfy

$$f(k) \equiv \frac{K'(k)}{K(k)} = f_+(k) - f_-(k). \tag{2.40}$$

Once $f_\pm(k)$ are known, we can set

$$f_+(k) = \frac{K'_+(k)}{K_+(k)}, \quad f_-(k) = \frac{K'_-(k)}{K_-(k)} \tag{2.41}$$

and integrate to find $K_\pm(k)$.

For $K(k)$ given by (2.37), by differentiating and rearranging we have

$$f(k) = \frac{k}{\sqrt{k^2+\delta^2}(k^2+\delta^2-1)} + \frac{k}{(k^2+\delta^2)(k^2+\delta^2-1)}. \tag{2.42}$$

Both terms in (2.42) have simple poles at $k = \pm(1-\delta^2)^{1/2}$. The first term on the right hand side of (2.42) is unbounded at the branch points at $k = \pm i\delta$, but these branch points have zero residue. The second term on the right hand side of (2.42) has no branch points but does have simple poles at $k = \pm i\delta$. We can decompose the second term by using partial fractions, to obtain

$$f(k) = \frac{k}{\sqrt{k^2+\delta^2}(k^2+\delta^2-1)} - \frac{1}{2(k-i\delta)} - \frac{1}{2(k+i\delta)} + \frac{k}{k^2+\delta^2-1}, \tag{2.43}$$

leaving the term

$$g(k) \equiv \frac{k}{\sqrt{k^2+\delta^2}(k^2+\delta^2-1)} \tag{2.44}$$

to additively decompose.

From Cauchy's integral formula, we know that

$$g(k) = \frac{1}{2\pi i}\oint_\Gamma \frac{g(w)}{w-k}dw \tag{2.45}$$

where $g(w)$ is analytic inside and on the closed curve Γ, which encloses the point $w = k$ in an anticlockwise sense. We initially take Γ to be the long thin rectangle in the strip of analyticity, given by $\Gamma = \Gamma_1 - \Gamma_2$ as shown in figure 2.3(a). Here Γ_1 is the path along the lower side of the rectangle, and Γ_2 is the path along the upper side of the rectangle, both taken in the direction of $\mathrm{Re}(w)$ increasing. Given a particular k within the strip of analyticity, we place the sides of the rectangle so that Γ_1 passes below $w = k$ and Γ_2 passes above $w = k$, and then we have

$$g(k) = \frac{1}{2\pi i}\oint_{\Gamma_1} \frac{g(w)}{w-k}dw - \frac{1}{2\pi i}\oint_{\Gamma_2} \frac{g(w)}{w-k}dw. \tag{2.46}$$

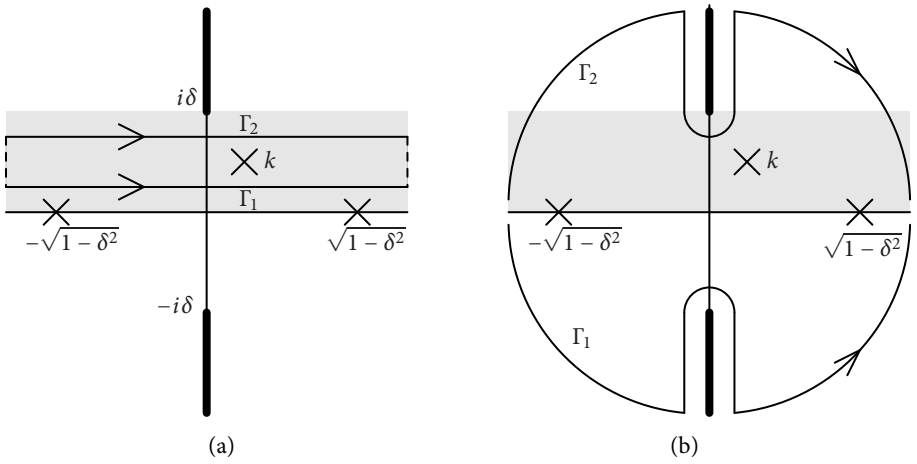

Figure 2.3: Contours in the complex w-plane for decomposition of $g(k)$ using Cauchy's integral formula. The strip of analyticity is shaded, branch cuts are shown in bold, and crosses indicate poles in the integrand of (2.45) . We initially take Γ_1 and Γ_2 to be the top and bottom of a rectangle inside the strip of analyticity, enclosing k, as shown in (a). We then deform Γ_1 and Γ_2 to the paths shown in (b). Now every k, except on the branch cuts, is enclosed by Γ_1 and Γ_2. The deformation for Γ_1 passes the poles at $w = \sqrt{1-\delta^2}$ and $w = -\sqrt{1-\delta^2}$, so the residues from these poles must be included.

We now deform the contours Γ_1 and Γ_2, to take the paths shown in 2.3(b), so that Γ_1 becomes a keyhole contour in the lower half plane, and Γ_2 becomes a keyhole contour in the upper half plane. The deformation for Γ_1 passes the two poles at $w = \pm(1-\delta^2)$, so the residues from these must be included. Now, every k that is not on the branch cuts is enclosed by $\Gamma = \Gamma_1 - \Gamma_2$. The first term in (2.46) is analytic for all k in the upper half plane, and the second term is analytic for all k in the lower half plane. We therefore define a decomposition by

$$g_+(k) = \frac{1}{2\pi i}\oint_{\Gamma_1}\frac{g(w)}{w-k}dw \tag{2.47}$$

and

$$g_-(k) = \frac{1}{2\pi i}\oint_{\Gamma_2}\frac{g(w)}{w-k}dw. \tag{2.48}$$

This decomposition satisfies $g(k) = g_+(k) - g_-(k)$ for all k in the strip of analyticity. This decomposition is not unique as we know that any entire function can be added to both $f_+(k)$ and $f_-(k)$ without changing their analyticity properties. Evaluating (2.47) and (2.48) for $g(k)$ given by (2.44), we find

$$g_+(k) = -\frac{1}{\pi}\int_\delta^\infty \frac{t}{\sqrt{t^2-\delta^2}(t^2-\delta^2+1)(it+k)}dt + \frac{1}{2(k+\sqrt{1-\delta^2})} + \frac{1}{2(k-\sqrt{1-\delta^2})} \tag{2.49}$$

and

$$g_-(k) = -\frac{1}{\pi}\int_\delta^\infty \frac{t}{\sqrt{t^2-\delta^2}(t^2-\delta^2+1)(it-k)}dt. \tag{2.50}$$

The computer algebra package Mathematica can be used to confirm that this decomposition satisfies $g(k) = g_+(k) - g_-(k)$.

Now, up to an undetermined entire function $E_1(k)$, we have

$$f_+(k) = -\frac{1}{\pi}\int_\delta^\infty \frac{t}{\sqrt{t^2-\delta^2}(t^2-\delta^2+1)(it+k)}dt - \frac{1}{2(k+i\delta)} + \frac{2k}{k^2+\delta^2-1} + E_1(k) \tag{2.51}$$

and

$$f_-(k) = -\frac{1}{\pi}\int_\delta^\infty \frac{t}{\sqrt{t^2-\delta^2}(t^2-\delta^2+1)(it-k)}dt + \frac{1}{2(k-i\delta)} + E_1(k). \tag{2.52}$$

We want to choose the function $E_1(k)$ so that $K_\pm(k)$ have known algebraic behaviour as $k \to \infty$. To find $K_\pm(k)$ we use the relationship

$$\log K_\pm(k) = \int_0^k f_\pm(w)dw. \tag{2.53}$$

The terms not involving integrals or E_1 in (2.51) and (2.52) all integrate to give logarithms on the right hand side of (2.53), and hence algebraic behaviour in $K_\pm(k)$. For large k,

$$\begin{aligned} -\frac{1}{\pi}\int_\delta^\infty \frac{t}{\sqrt{t^2-\delta^2}(t^2-\delta^2+1)(it+k)}dt &\approx -\frac{1}{k\pi}\int_\delta^\infty \frac{t}{\sqrt{t^2-\delta^2}(t^2-\delta^2+1)}dt \\ &= -\frac{1}{2k}, \end{aligned} \tag{2.54}$$

so we have from (2.51) and (2.52) that

$$f_+(k) \sim -\frac{1}{2k} - \frac{1}{2(k+i\delta)} + \frac{2k}{k^2+\delta^2-1} + E_1(k) \tag{2.55}$$

and

$$f_-(k) \sim \frac{1}{2k} + \frac{1}{2(k-i\delta)} + E_1(k). \tag{2.56}$$

Substituting (2.55) and (2.56) into (2.53), we find that all the terms in (2.55) and (2.56) except for $E_1(k)$ correspond to algebraic behaviour in $K_\pm(k)$, so we can set $E_1(k) = 0$. Any additive constants arising from the integration or the branches of the logarithms do not affect the qualitative behaviour of $K_\pm(k)$.

We therefore let

$$K_+(k) = \exp\left(\int_0^k f_+(w)dw\right), \quad K_-(k) = \exp\left(\int_0^k f_-(w)dw\right) \tag{2.57}$$

where

$$f_+(k) = -\frac{1}{\pi}\int_\delta^\infty \frac{t}{\sqrt{t^2-\delta^2}(t^2-\delta^2+1)(it+k)}dt - \frac{1}{2(k+i\delta)} + \frac{2k}{k^2+\delta^2-1} \tag{2.58}$$

and

$$f_-(k) = -\frac{1}{\pi}\int_\delta^\infty \frac{t}{\sqrt{t^2-\delta^2}(t^2-\delta^2+1)(it-k)}dt + \frac{1}{2(k-i\delta)}. \tag{2.59}$$

By construction this decomposition satisfies $K(k) = K_+(k)/K_-(k)$ for all k in the strip of analyticity, $K_+(k)$ is analytic for all k in the upper half plane, and $K_-(k)$ is analytic for all k in the lower half plane. $K_+(k)$ and $K_-(k)$ have algebraic behaviour as $k \to \infty$ in their respective half planes.

Returning to the Wiener-Hopf equation (2.36), we can now write

$$\tilde{\phi}_+(k)K_+(k) + \tilde{\phi}_-(k)K_-(k) = 0 \tag{2.60}$$

where the factors $K_\pm(k)$ have been determined. We can now define an entire function from the Wiener-Hopf equation by writing

$$E(k) = \begin{cases} \tilde{\phi}_+(k)K_+(k), & \tau > 0 \\ -\tilde{\phi}_-(k)K_-(k), & \tau < \delta. \end{cases} \tag{2.61}$$

According to our Wiener-Hopf equation, the two piecewise definitions are equal in the common strip of analyticity, and we know that each part of (2.61) is analytic in its half plane of applicability.

To determine the behaviour of $E(k)$ for large k, we now turn to a theorem which relates the behaviour of $\phi(x,0)$ for small x to the behaviour of $\tilde{\phi}_+(k)$ and $\tilde{\phi}_-(k)$ for large k:

Theorem 1 (An Abelian theorem [Crighton et al., 1992]) *Suppose $f(x) = 0$ for $x < 0$, $|f| < Ae^{\alpha x}$ as $x \to \infty$, f is infinitely differentiable for $x > 0$ and $f \sim x^\lambda$ as $x \to 0+$ with $\lambda > -1$. Then*

$$F_+(k) \equiv \int_0^\infty f(x)e^{ikx}dx \sim \int_0^\infty x^\lambda e^{ikx}dx = \frac{\lambda!}{(-ik)^{\lambda+1}} \tag{2.62}$$

as $|k| \to \infty$ in the half-plane of analyticity $\tau > \alpha$. Thus the behaviour of $F_+(k)$ for large $|k|$ in the upper half plane corresponds to the behaviour of $f(x)$ for small positive x.

Similarly if $f(x) = 0$ for $x > 0$, $|f| < Be^{\beta x}$ as $x \to -\infty$ and $f \sim (-x)^\mu$ as $x \to 0-$ with $\mu > -1$ then

$$F_-(k) \equiv \int_{-\infty}^{0} f(x)e^{ikx}dx \sim \int_{-\infty}^{0} (-x)^\mu e^{ikx}dx = \frac{\mu!}{(ik)^{\mu+1}} \tag{2.63}$$

as $|k| \to \infty$ in the half-plane of analyticity $\tau < \beta$. The behaviour of $F_-(k)$ for large $|k|$ in the lower half plane corresponds to the behaviour of $f(x)$ for small negative x.

We want ϕ to be bounded as $x, y \to 0$. By theorem 1, this corresponds to $\phi_+(k) = O(k^{-1})$ as $k \to \infty$ in the upper half plane, and $\phi_-(k) = O(k^{-1})$ as $k \to \infty$ in the lower half plane. As $k \to \infty$ in the respective half planes, the decomposition given by (2.57), (2.58) and (2.59) has

$$K_+(k) \sim \frac{k^2 + \delta^2 - 1}{k^{1/2}(k + i\delta)^{1/2}} = O(k), \quad K_-(k) \sim k^{1/2}(k + i\delta)^{1/2} = O(k). \tag{2.64}$$

According to the definition (2.61), $E(k)$ is an entire function, bounded as $k \to \infty$ in all directions, and hence by Liouville's theorem, $E(k)$ is a constant, say α. Then

$$\tilde{\phi}_+(k) = \frac{\alpha}{K_+(k)}, \quad \tilde{\phi}_-(k) = -\frac{\alpha}{K_-(k)}. \tag{2.65}$$

To invert, we have

$$\phi(x, y) = \frac{\alpha}{2\pi} \int_{-\infty}^{\infty} \exp\left(-ikx - (k^2 + \delta^2)^{1/2} y\right) \left(\frac{1}{K_+(k)} - \frac{1}{K_-(k)}\right) dk \tag{2.66}$$

where the path of integration is taken along the strip of analyticity. The factors $K_+(k)$ and $K_-(k)$ are defined by (2.57), (2.58) and (2.59).

2.4.4 Fourier inversion to find ϕ

We have used the Wiener-Hopf technique to identify, for $\delta > 0$, a suitably bounded solution to the system (2.31). This solution is unique up to a multiplicative constant α, which we expect as the system is linear. This solution is given by (2.57), (2.58), (2.59) and (2.66).

However, we are particularly interested in the solution to the system (2.27), which is the limit of (2.31) as $\delta \to 0$. We therefore want to consider the limit as $\delta \to 0$ of the solution given by (2.57), (2.58), (2.59) and (2.66) This requires us to consider both the contour of integration and the integrand itself as $\delta \to 0$.

Inversion contours for $\delta = 0$

We want to close the inversion contour in the half plane where the real part of $-ikx - (k^2 + \delta^2)^{1/2} y$ is negative. As the branch for $(k^2 + \delta^2)^{1/2}$ is defined so that its real part is always positive, we can always close the integral in the half plane where Re $ikx > 0$. Therefore, for $x < 0$ we close in the upper half plane, and for $x > 0$ we close in the lower half plane. The deformed inversion contours are shown in figure 2.4(b). Closing in the lower half plane encloses the singularities at $\sqrt{1 - \delta^2}$. The residues from these singularities of $1/K_+(k)$ will give us the oscillatory part of $\phi(x, y)$ for $x > 0$.

For $\delta > 0$, the contours for $x > 0$ and $x < 0$ each 'see' only one branch cut. As we let $\delta \to 0$, the two branch points at $\pm i\delta$ converge to 0. For $\delta \to 0$, the contours take the path shown in figure 2.4(c). The singularities at $\pm\sqrt{1 - \delta^2}$ move to ± 1, and are still enclosed by the contour for $x > 0$.

Factorisation for $\delta = 0$

The next step is to calculate $K_\pm(k)$ as $\delta \to 0$. In some ways it is easier to calculate $K_\pm(k)$ for $\delta = 0$ than for $\delta > 0$ because we can do some of the integrals analytically. It will be useful to check that our decomposition satisfies the requirement $K(k) = K_+(k)/K_-(k)$, so we begin by considering the meaning of this factorisation for $\delta = 0$. As $\delta \to 0$ in the definition of K in (2.37), we find

$$K(k) \to \begin{cases} 1 - \dfrac{1}{k}, & \sigma > 0 \\ 1 + \dfrac{1}{k}, & \sigma < 0. \end{cases} \tag{2.67}$$

where $k = \sigma + i\tau$. To proceed with the decomposition, we took logarithms of the relationship

$$\frac{K_+(k)}{K_-(k)} = K(k). \tag{2.68}$$

and then differentiated to obtain

$$f(k) = (\log K(k))' = (\log K_+(k))' - (\log K_-(k))' = f_+(k) - f_-(k). \tag{2.69}$$

Using (2.67) to define $K(k)$ for $\delta = 0$, we expect to find

$$f(k) \to \begin{cases} \dfrac{1}{k(k-1)}, & \sigma > 0 \\ -\dfrac{1}{k(k+1)}, & \sigma < 0 \end{cases} \tag{2.70}$$

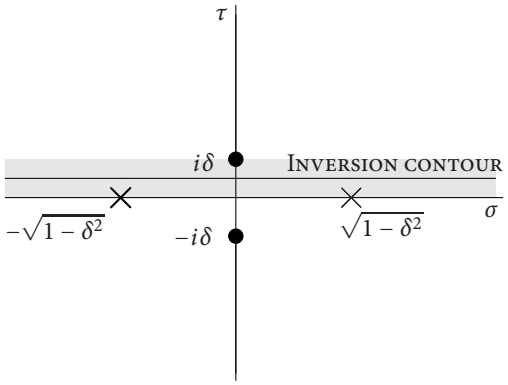

(a) For $\delta > 0$, the Fourier inversion gives ϕ in terms of an integral along the strip of analyticity.

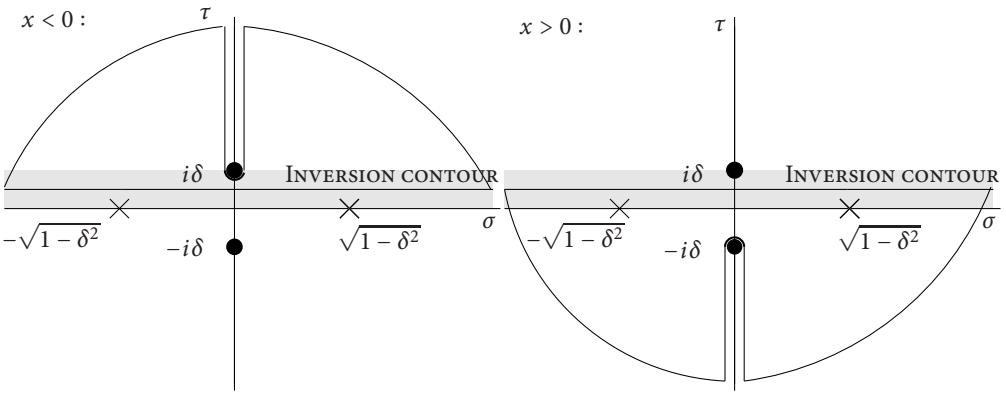

(b) Deformed contours for $\delta > 0$. We use the branch of $(k^2 + \delta^2)^{1/2}$ that has positive real part everywhere except the branch cuts on the imaginary axis, and so can close the inversion contour in the half-plane where $\mathrm{Re}\, ikx > 0$. For $x > 0$ this deformation encloses simple poles at $k = \pm\sqrt{1-\delta^2}$.

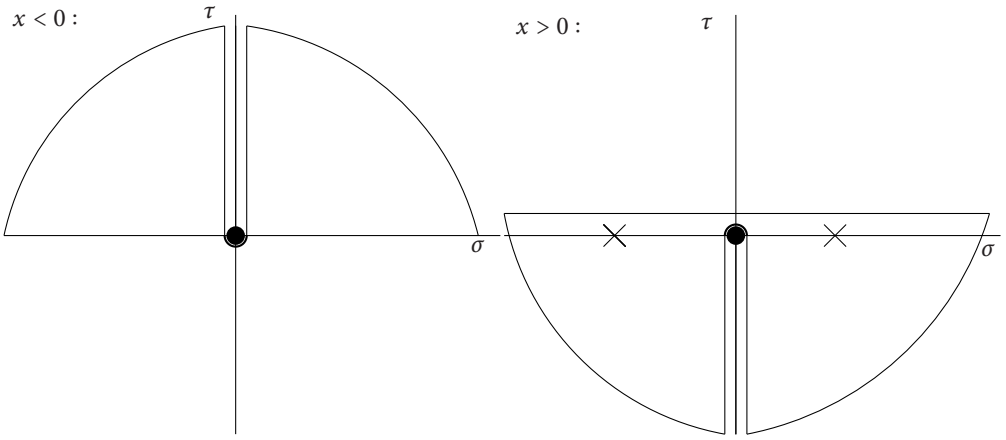

(c) Deformed contours for $\delta = 0$. As $\delta \to 0$, the branch points shown in (b) converge, and we integrate around the positive and negative imaginary axes for $x < 0$ and $x > 0$ respectively.

Figure 2.4: Inversion contours for the Wiener-Hopf dock problem.

as $\delta \to 0$.

With these targets in mind, we shall calculate $f_{\pm}(k)$. Cauchy's integral formula gave a decomposition for $f(k)$ with $\delta > 0$, and the result is given in (2.58) and (2.59). Taking δ to zero in these expressions, we obtain

$$f_{+}(k) = -\frac{1}{\pi}\int_0^{\infty} \frac{1}{(t^2+1)(it+k)}dt - \frac{1}{2k} + \frac{2k}{k^2-1}, \tag{2.71}$$

and

$$f_{-}(k) = -\frac{1}{\pi}\int_0^{\infty} \frac{1}{(t^2+1)(it-k)}dt + \frac{1}{2k}. \tag{2.72}$$

These can also be written as

$$f_{+}(k) = -\frac{1}{\pi}\frac{1}{1-k^2}\int_0^{\infty} (k-it)\left(\frac{1}{t^2+k^2} - \frac{1}{t^2+1}\right)dt - \frac{1}{2k} + \frac{2k}{k^2-1}, \tag{2.73}$$

and

$$f_{-}(k) = -\frac{1}{\pi}\frac{1}{1-k^2}\int_0^{\infty} (-k-it)\left(\frac{1}{t^2+k^2} - \frac{1}{t^2+1}\right)dt + \frac{1}{2k}. \tag{2.74}$$

To evaluate the integrals in (2.73) and (2.74) we use the fact that

$$\int_0^{\infty} \frac{dt}{t^2+w^2} = \frac{\pi}{2w}\operatorname{csgn}(w) \tag{2.75}$$

where $\operatorname{csgn}(w)$ is defined as the sign of the real part of w. Then (2.73) and (2.74) become

$$f_{+}(k) = -\frac{1}{2}\frac{\operatorname{csgn}(k)}{1-k^2} - \frac{3k}{2(1-k^2)} - \frac{i}{2\pi}\frac{\log k^2}{1-k^2} - \frac{1}{2k} \tag{2.76}$$

and

$$f_{-}(k) = \frac{1}{2}\frac{\operatorname{csgn}(k)}{1-k^2} - \frac{k}{2(1-k^2)} - \frac{i}{2\pi}\frac{\log k^2}{1-k^2} + \frac{1}{2k}. \tag{2.77}$$

However, the branch cuts for $\log k^2$ and the definition of $\operatorname{csgn}(k)$ interact in such a way that (2.76) and (2.77) simplify to become

$$f_{+}(k) = -\frac{i}{\pi}\frac{\log_{+}(k)}{1-k^2} - \frac{1}{2(1-k^2)} - \frac{3k}{2(1-k^2)} - \frac{1}{2k} \tag{2.78}$$

and

$$f_{-}(k) = -\frac{i}{\pi}\frac{\log_{-}(k)}{1-k^2} + \frac{1}{2(1-k^2)} - \frac{k}{2(1-k^2)} + \frac{1}{2k}. \tag{2.79}$$

Here we have introduced two new logarithms, $\log_{+}(k)$ and $\log_{-}(k)$. The branch cut for $\log_{+}(k)$ lies along the negative imaginary axis while the branch cut for $\log_{-}(k)$ lies along

the positive imaginary axis. The branches are chosen so that $\log_+(k) = \log_-(k) = \ln(k)$ for real positive k.

At this point we can check that $f_+(k)$ and $f_-(k)$ satisfy $f(k) = f_+(k) - f_-(k)$. For k in the right half plane, the two logarithms are equal, so

$$f(k) = f_+(k) - f_-(k) = \frac{1}{k(k-1)}. \tag{2.80}$$

However, for k in the left half plane, the definitions of $\log_\pm(k)$ are such that $\log_+(k) - \log_-(k) = 2\pi i$, and so

$$f(k) = f_+(k) - f_-(k) = -\frac{1}{k(k+1)}. \tag{2.81}$$

Equations (2.80) and (2.81) both agree with (2.70).

To find $K_\pm(k)$ from $f_\pm(k)$, we use the relationship (2.69) to give

$$K_\pm(k) = \exp \int^k f_\pm(w)dw.$$

We are free to choose the lower limits of these integrals, but they must satisfy the constraint (2.68). The most general way of satisfying this constraint is to have

$$K_+(k) = \exp\left(\int_a^k f_+(w)dw\right)K(a), \qquad K_-(k) = \exp\left(\int_a^k f_-(w)dw\right). \tag{2.82}$$

We now integrate (2.78) and (2.79) to obtain

$$\begin{aligned} K_+(k) = \exp\left(-\frac{i}{\pi}\int_a^k \frac{\log_+(w)}{1-w^2}dw\right)\left(\frac{1+k}{1-k}\right)^{-1/4}\left(\frac{1+a}{1-a}\right)^{1/4} \\ \times\left(\frac{1-k^2}{1-a^2}\right)^{3/4}\left(\frac{k}{a}\right)_+^{-1/2}K(a) \end{aligned} \tag{2.83}$$

and

$$\begin{aligned} K_-(k) = \exp\left(-\frac{i}{\pi}\int_a^k \frac{\log_-(w)}{1-w^2}dw\right)\left(\frac{1+k}{1-k}\right)^{1/4}\left(\frac{1+a}{1-a}\right)^{-1/4} \\ \times\left(\frac{1-k^2}{1-a^2}\right)^{1/4}\left(\frac{k}{a}\right)_-^{1/2}. \end{aligned} \tag{2.84}$$

The subscript '+' again indicates that the function is analytic in the upper half plane, so branch cuts are taken in the lower half plane, along the negative imaginary axis. Correspondingly, functions with subscripts '–' are analytic in the lower half plane and hence have branch cuts along the positive imaginary axis.

It is helpful to collect together the terms involving a by defining

$$A(a) = \exp\left(\frac{i}{\pi}\int_0^a \frac{\log_+(w)}{1-w^2}dw\right) a^{-1/2}(1+a)^{-1/2} \tag{2.85}$$

so that

$$K_+(k) = -\exp\left(-\frac{i}{\pi}\int_0^k \frac{\log_+(w)}{1-w^2}dw\right)\frac{(1+k)^{1/2}(1-k)}{k_+^{1/2}}A(a) \tag{2.86}$$

and

$$K_-(k) = \exp\left(-\frac{i}{\pi}\int_0^k \frac{\log_-(w)}{1-w^2}dw\right)(1+k)^{1/2}k_-^{1/2}A(a). \tag{2.87}$$

We can now regard $A(a)$ as an arbitrary constant.

Calculation of $\phi(x,y)$ for $\delta = 0$

We are now able to begin evaluation of $\phi(x,y)$. In the limit $\delta \to 0$, (2.66) becomes

$$\phi(x,y) = \frac{\alpha}{2\pi}\int_{-\infty}^{\infty} \exp\left(-ikx - k\,\mathrm{csgn}(k)y\right)\left(\frac{1}{K_+(k)} - \frac{1}{K_-(k)}\right)dk. \tag{2.88}$$

For convenience, we split this into two parts. We must calculate

$$\phi_+(x,y) = \int_{-\infty}^{\infty} \exp\left(-ikx - k\,\mathrm{csgn}(k)y\right)\frac{1}{K_+(k)}dk \tag{2.89}$$

and

$$\phi_-(x,y) = \int_{-\infty}^{\infty} \exp\left(-ikx - k\,\mathrm{csgn}(k)y\right)\frac{1}{K_-(k)}dk. \tag{2.90}$$

The closure of the integrals as illustrated in figure 2.4(c) depends on the sign of x. For $x < 0$ we close in the upper half plane, which encloses no poles. However, for $x > 0$ we must close in the lower half plane and this encloses simple poles of $1/K_+(k)$ at $k = \pm 1$.

We will begin by analysing the integral for $x < 0$. We close in the upper half plane. There are no zeroes of $K_\pm(k)$ within the contour, so no residues to concern us. $K_+(k)$ is analytic in the upper half plane, and the integrand for $\phi_+(x,y)$ vanishes along the large semi-circular part of the contour. However, $\mathrm{csgn}(k)y$ changes sign across the positive imaginary axis, and so we get still get a contribution from $\phi_+(x,y)$ when $x < 0$ unless $y = 0$. $K_-(k)$ has a branch cut along the positive imaginary axis, so we expect to get a contribution from $\phi_-(x,y)$ when $x < 0$ regardless of the value of y.

$K_+(it)$	$-\dfrac{A(a)}{i^{1/2}}\dfrac{(1+t^2)^{3/4}}{t^{1/2}}\exp\left(\dfrac{1}{\pi}\displaystyle\int_0^t \dfrac{\log s}{1+s^2}ds\right)$
$K_-(it+)$	$i^{1/2}A(a)(1+it)^{3/4}(1-it)^{-1/4}t^{1/2}\exp\left(\dfrac{1}{\pi}\displaystyle\int_0^t \dfrac{\log s}{1+s^2}ds\right)$
$K_-(it-)$	$-i^{1/2}A(a)(1-it)^{3/4}(1+it)^{-1/4}t^{1/2}\exp\left(\dfrac{1}{\pi}\displaystyle\int_0^t \dfrac{\log s}{1+s^2}ds\right)$
$K_+(-it-)$	$\dfrac{A(a)}{(-i)^{1/2}}\dfrac{(1+it)^{1/4}(1-it)^{5/4}}{t^{1/2}}\exp\left(-\dfrac{1}{\pi}\displaystyle\int_0^t \dfrac{\log s}{1+s^2}ds\right)$
$K_+(-it+)$	$-\dfrac{A(a)}{(-i)^{1/2}}\dfrac{(1-it)^{1/4}(1+it)^{5/4}}{t^{1/2}}\exp\left(-\dfrac{1}{\pi}\displaystyle\int_0^t \dfrac{\log s}{1+s^2}ds\right)$
$K_-(-it)$	$A(a)(-i)^{1/2}t^{1/2}(1+t^2)^{1/4}\exp\left(-\dfrac{1}{\pi}\displaystyle\int_0^t \dfrac{\log s}{1+s^2}ds\right)$

Table 2.1: Explicit values of $K_\pm(k)$ along the branch cuts. Here t is real and positive.

The contribution from $\phi_+(x,y)$ is given, for $x<0$, by

$$\phi_+(x,y) = 2\int_0^\infty \frac{e^{xt}\sin yt}{K_+(it)}dt, \tag{2.91}$$

where $K_+(it)$ is defined in table 2.1, and so we find

$$\phi_+(x,y) = -\frac{2i^{1/2}}{A(a)}\int_0^\infty \frac{t^{1/2}e^{xt}\sin yt}{(1+t^2)^{3/4}}\exp\left(-\frac{1}{\pi}\int_0^t \frac{\log s}{1+s^2}ds\right)dt, \tag{2.92}$$

which vanishes when $y=0$, as expected.

The contribution from $\phi_-(x,y)$ for $x<0$ is slightly more complicated because $K_-(k)$ has a branch cut along the positive imaginary axis. We find

$$\phi_-(x,y) = i\int_0^\infty e^{xt}\left(\frac{e^{-ity}}{K_-(it+)} - \frac{e^{ity}}{K_-(it-)}\right)dt. \tag{2.93}$$

Using table 2.1 to find $K_-(it+)$ and $K_-(it-)$ we obtain

$$\phi_-(x,y) = \frac{2i^{1/2}}{A(a)}\int_0^\infty \frac{e^{xt}(\cos yt - t\sin yt)}{t^{1/2}(1+t^2)^{3/4}}\exp\left(-\frac{1}{\pi}\int_0^t \frac{\log s}{1+s^2}ds\right)dt. \tag{2.94}$$

for $x < 0$.

Adding the contributions from (2.92) and (2.94), for $x < 0$ we have

$$\phi(x,y) = -\frac{i^{1/2}\alpha}{A(a)\pi}\int_0^\infty \frac{e^{xt}\cos yt}{t^{1/2}(1+t^2)^{3/4}}\exp\left(-\frac{1}{\pi}\int_0^t \frac{\log s}{1+s^2}ds\right)dt. \tag{2.95}$$

We can easily check that this satisfies $\nabla^2\phi(x,y) = 0$ and $\phi_y(x,0) = 0$.

The calculation of $\phi(x,y)$ for $x > 0$ is complicated by the presence of singularities at $k = \pm 1$. We again have contributions from both $\phi_+(x,y)$ and $\phi_-(x,y)$. Deforming onto the contours shown in figure 2.4(c), we have

$$\begin{aligned}\phi_+(x,y) = i\int_0^\infty e^{-xt}\left[\frac{e^{-ity}}{K_+(-it-)} - \frac{e^{ity}}{K_+(-it+)}\right]dt \\ -2\pi i\left\{\lim_{k\to 1}\frac{(k-1)e^{-ikx}e^{-ky}}{K_+(k)} + \lim_{k\to -1}\frac{(k+1)e^{-ikx}e^{ky}}{K_+(k)}\right\}\end{aligned} \tag{2.96}$$

and

$$\phi_-(x,y) = 2\int_0^\infty \frac{e^{-xt}\sin yt}{K_-(-it)}dt. \tag{2.97}$$

We are now ready to assemble $\phi_+(x,y)$ and $\phi_-(x,y)$ for $x > 0$, using (2.96) and (2.97). This gives us

$$\begin{aligned}\phi_+(x,y) = \frac{2i^{1/2}}{A(a)}\int_0^\infty \frac{e^{-xt}t^{1/2}}{(1+t^2)^{5/4}}(\cos yt + t\sin yt)\exp\left(\frac{1}{\pi}\int_0^t \frac{\log s}{1+s^2}ds\right)dt \\ -\frac{2\sqrt{2}i^{1/2}\pi}{A(a)}e^{-y}\sin\left(x+\frac{3\pi}{8}\right)\end{aligned} \tag{2.98}$$

and

$$\phi_-(x,y) = \frac{2i^{1/2}}{A(a)}\int_0^\infty \frac{e^{-xt}\sin yt}{t^{1/2}(1+t^2)^{1/4}}\exp\left(\frac{1}{\pi}\int_0^t \frac{\log s}{1+s^2}ds\right)dt. \tag{2.99}$$

To calculate $\phi(x,y)$ for $x > 0$, we again combine $\phi_+(x,y)$ and $\phi_-(x,y)$ using the relationship

$$\phi(x,y) = \frac{\alpha}{2\pi}\phi_+(x,y) - \frac{\alpha}{2\pi}\phi_-(x,y) \tag{2.100}$$

and so we find

$$\begin{aligned}\phi(x,y) = \frac{\alpha i^{1/2}}{\pi A(a)}\int_0^\infty \frac{e^{-xt}(t\cos yt - \sin yt)}{t^{1/2}(1+t^2)^{5/4}}\exp\left(\frac{1}{\pi}\int_0^t \frac{\log s}{1+s^2}ds\right)dt \\ -\frac{\alpha\sqrt{2}i^{1/2}}{A(a)}e^{-y}\sin\left(x+\frac{3\pi}{8}\right).\end{aligned} \tag{2.101}$$

Again, this is harmonic, and we can again verify that $\phi_y = -\phi$ on $y = 0$.

In summary we have, for $x > 0$:

$$\begin{aligned}\phi(x,y) &= -\frac{i^{1/2}\alpha}{A(a)}\sqrt{2}e^{-y}\sin\left(x+\frac{3\pi}{8}\right)\\ &+\frac{i^{1/2}\alpha}{A(a)}\frac{1}{\pi}\int_0^\infty \frac{e^{-xt}(t\cos yt-\sin yt)}{t^{1/2}(1+t^2)^{5/4}}\exp\left(\frac{1}{\pi}\int_0^t\frac{\log s}{1+s^2}ds\right)dt\end{aligned} \tag{2.102}$$

and for $x < 0$:

$$\phi_-(x,y) = -\frac{\alpha i^{1/2}}{\pi A(a)}\int_0^\infty \frac{e^{xt}\cos yt}{t^{1/2}(1+t^2)^{3/4}}\exp\left(-\frac{1}{\pi}\int_0^t\frac{\log s}{1+s^2}ds\right)dt. \tag{2.103}$$

We can check that these have the required properties. Both are harmonic, with the integral parts decaying as $x^2+y^2\to\infty$. The oscillatory part of $\phi_-(x,y)$ is bounded as $x\to\infty$ and decays as $y\to\infty$. The boundary conditions are also met: along $y=0$ we have $\phi_y=-\phi$ on $x>0$ while $\phi_y=0$ on $x<0$. We cannot easily show that ϕ is continuous along the line $x=0$. This should be the case as the piecewise definitions (2.102) and (2.103) were both calculated from the same definition (2.88).

2.4.5 Normalisation

We can also use the Abelian theorem (page 39) to find the value of the normalisation ratio $\alpha/A(a)$. According to the Abelian theorem, if $\phi(x,0)\to 1$ as $x\to 0$, then as $k\to\infty$ in the upper half plane we have

$$\phi^+(k,0)\to\frac{i}{k} \tag{2.104}$$

and as $k\to\infty$ in the lower half plane we have

$$\phi^-(k,0)\to\frac{-i}{k}. \tag{2.105}$$

We also know from (2.65) that

$$\tilde\phi_+(k)=\frac{\alpha}{K_+(k)},\quad \tilde\phi_-(k)=-\frac{\alpha}{K_-(k)}.$$

where the factors $K_\pm(k)$ are defined by (2.86) and (2.87) as

$$K_+(k) = -\exp\left(-\frac{i}{\pi}\int_0^k\frac{\log_+(w)}{1-w^2}dw\right)\frac{(1+k)^{1/2}(1-k)}{k_+^{1/2}}A(a) \tag{2.106}$$

and

$$K_-(k) = \exp\left(-\frac{i}{\pi}\int_0^k\frac{\log_-(w)}{1-w^2}dw\right)(1+k)^{1/2}k_-^{1/2}A(a), \tag{2.107}$$

where α and $A(a)$ may be treated as arbitrary constants.

As we let $k \to \infty$ in the upper half plane we find that

$$K_+(k) \to kA(a) \exp\left(-\frac{i}{\pi}\int_0^k \frac{\log_+(w)}{1-w^2}dw\right). \tag{2.108}$$

If $k = re^{i\theta}$, we have, as $r \to \infty$,

$$K_+(k) \to kA(a) \exp\left(-\frac{ie^{i\theta}}{\pi}\int_0^\infty \frac{\log u + i\theta}{1-u^2e^{2i\theta}}du\right). \tag{2.109}$$

We can evaluate this integral and we find, independently of the value of θ, that

$$e^{i\theta}\int_0^\infty \frac{\log u + i\theta}{1-u^2e^{2i\theta}}due^{i\theta} = -\frac{\pi^2}{4} \tag{2.110}$$

Thus we obtain

$$\tilde{\phi}_+(k,0) = \frac{\alpha}{K_+(k)} \to \frac{\alpha}{A(a)i^{1/2}k} \to \frac{1}{-ik} \tag{2.111}$$

which gives $\alpha/A(a) = -(-i)^{1/2}$.

In a similar manner, we find that as $k \to \infty$ in the lower half plane

$$\int_0^k \frac{\log_- w}{1-w^2}dw \to -\frac{\pi^2}{4},$$

so that $K_-(k) \to kA(a)i^{1/2}$ in the same limit. The Abelian theorem now gives

$$\tilde{\phi}_-(k,0) = -\frac{\alpha}{K_-(k)} \to -\frac{\alpha}{kA(a)i^{1/2}} \to \frac{1}{ik} \tag{2.112}$$

so that we again have $\alpha/A(a) = -(-i)^{1/2}$.

We can verify numerically that this normalisation gives $\phi(0,0) = 1$. However, we have been unable to analytically evaluate the integrals in (2.102) and (2.103) even for this simple case of $x = y = 0$.

2.4.6 Large distance behaviour of ϕ

Normalised so that $\phi(0,0) = 1$, we know that for $x > 0$ we have

$$\begin{aligned}\phi(x,y) =& \sqrt{2}e^{-y}\sin\left(x+\frac{3\pi}{8}\right)\\ &-\frac{1}{\pi}\int_0^\infty \frac{e^{-xt}(t\cos yt - \sin yt)}{t^{1/2}(1+t^2)^{5/4}}\exp\left(\frac{1}{\pi}\int_0^t \frac{\log s}{1+s^2}ds\right)dt,\end{aligned} \tag{2.113}$$

and for $x < 0$ we have

$$\phi(x,y) = \frac{1}{\pi}\int_0^\infty \frac{e^{xt}\cos yt}{t^{1/2}(1+t^2)^{3/4}} \exp\left(-\frac{1}{\pi}\int_0^t \frac{\log s}{1+s^2}ds\right) dt. \tag{2.114}$$

As $x^2 + y^2 \to \infty$, the integrals in (2.113) and (2.114) are dominated by the contribution from near $t = 0$, and so at leading order we find

$$\phi(r,\theta) \sim \begin{cases} \dfrac{r^{-1/2}}{\sqrt{\pi}}\sin\dfrac{\theta}{2} + \sqrt{2}e^{-y}\sin\left(x+\dfrac{3\pi}{8}\right) & \text{for } x > 0. \\ \dfrac{r^{-1/2}}{\sqrt{\pi}}\sin\dfrac{\theta}{2} & \text{for } x < 0. \end{cases} \tag{2.115}$$

Extracting information beyond leading order is difficult because the factor

$$\exp\left(-\frac{1}{\pi}\int_0^t \frac{\log s}{1+s^2}ds\right) \tag{2.116}$$

is not differentiable at $t = 0$, and the logarithm in the integrand gives terms such as t^{-t} and t^t for small t, which cannot be scaled with r in the usual way.

However, we do know that along the half line $x > 0$, $\phi(x,0)$ is given by

$$\begin{aligned} \phi(x,y) &= \sqrt{2}\sin\left(x+\frac{3\pi}{8}\right) \\ -\frac{1}{\pi}\int_0^\infty \frac{e^{-xt}t^{1/2}}{(1+t^2)^{5/4}} &\exp\left(\frac{1}{\pi}\int_0^t \frac{\log s}{1+s^2}ds\right) dt, \end{aligned} \tag{2.117}$$

As $x \to \infty$, the oscillatory term is dominant, but we can also find the leading order behaviour of the algebraic part from a small-t analysis of (2.117). This gives us

$$\phi(x,y) \sim \sqrt{2}\sin\left(x+\frac{3\pi}{8}\right) - \frac{1}{2\sqrt{\pi}}\frac{1}{x^{3/2}}. \tag{2.118}$$

This leading order algebraic part of $\phi(x,0)$ on $x > 0$,

$$-\frac{1}{2\sqrt{\pi}}\frac{1}{x^{3/2}}, \tag{2.119}$$

corresponds exactly to the requirement $\phi_y(x,0) = -\phi(x,0)$ on $x = 0$, where the algebraic part of ϕ is given at leading order by

$$\frac{1}{\sqrt{\pi}}\frac{1}{r^{1/2}}\sin\left(\frac{\theta}{2}\right). \tag{2.120}$$

2.4.7 Numerical evaluation of the Wiener-Hopf solution

The Wiener-Hopf method gives the solution $\phi(x, y)$ as the expressions (2.113) and (2.114). Each of these expressions has a nested integral. We can rewrite the inner integral as

$$\int_0^t \frac{\log s}{1+s^2} ds = \frac{i}{2}\left(\mathrm{Li}_2(is) - \mathrm{Li}_2(-is) + \log s \log\left(\frac{1-is}{1+is}\right)\right) \tag{2.121}$$

where Li_2 is the complex dilogarithm. This special function can be calculated using other algorithms, and so its numerical evaluation can be quicker than using (2.113) and (2.114) directly.

Figure 2.5 show the solution $\phi(x, y)$ evaluated with (2.121) substituted into (2.113) and (2.114). We can observe that $\phi(x, y)$ as calculated numerically is continuous at $x = 0$, is bounded at $x = y = 0$ and tends to zero as $r \to \infty$ except on the positive x-axis, where there is a constant-amplitude wave. The contour plot also demonstrates that $\phi_y = 0$ on the negative x-axis.

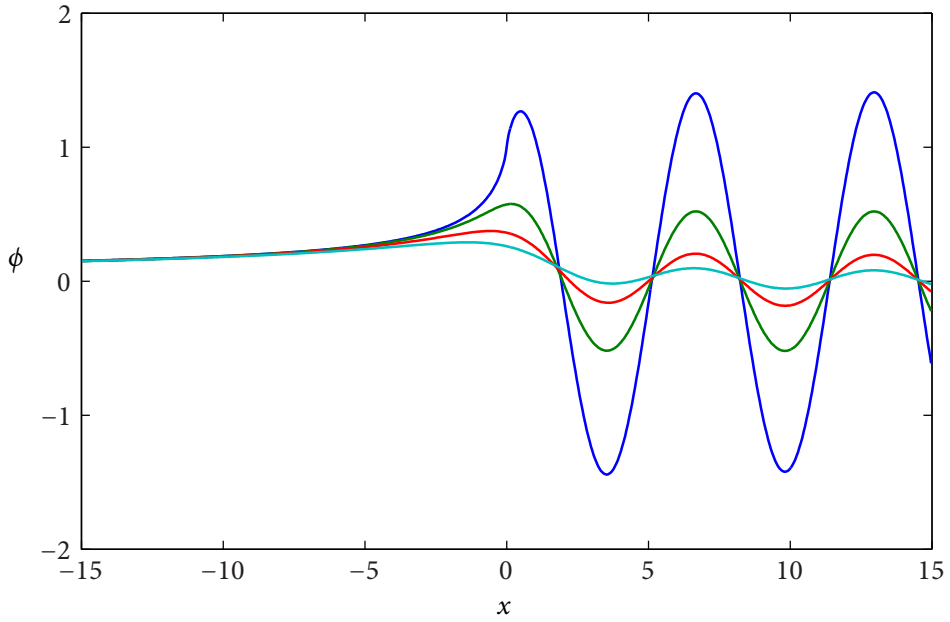

(a) $\phi(x, y)$ for $y = 0$ (blue), $y = 1$ (green), $y = 2$ (red) and $y = 3$ (cyan).

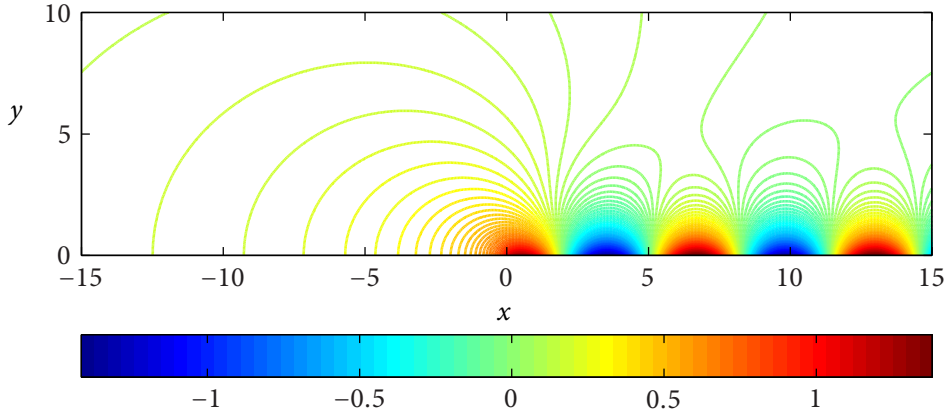

(b) Contour plot of $\phi(x, y)$

Figure 2.5: We can use the expressions (2.113) and (2.114) to calculate $\phi(x, y)$. The plots of ϕ for constant y in (a) show that the solution is continuous at $x = 0$, and that the wave amplitude is constant as $x \to \infty$. Note that although ϕ is continuous at $x = y = 0$, ϕ_y is discontinuous there and ϕ_x has a logarithmic singularity. The contour plot (b) shows that the contour lines are perpendicular to the boundary $y = 0$ for $x < 0$ and so $\phi_y = 0$ there. We see that $\phi(x, y)$ is dominated by surface waves near $y = 0$ for $x > 0$.

2.5 Mellin Transforms

In polar coordinates (r, θ), we wish to find the function Φ that satisfies

$$\frac{1}{r}\frac{\partial}{\partial r}\left(r\frac{\partial \Phi}{\partial r}\right) + \frac{1}{r^2}\frac{\partial^2 \Phi}{\partial \theta^2} = 0 \quad \text{for} \quad 0 \le \theta \le \pi \tag{2.122}$$

$$\frac{1}{r}\frac{\partial \Phi}{\partial \theta} = -\Phi \quad \text{on} \quad \theta = 0 \tag{2.123}$$

$$\frac{1}{r}\frac{\partial \Phi}{\partial \theta} = 0 \quad \theta = \pi. \tag{2.124}$$

Our normalisation condition is that $\Phi(0, \theta) = 1$, and we also require that $\Phi(r, \theta)$ is bounded as $r \to \infty$.

The Mellin transform $\Phi^*(p, \theta)$ of the function $\Phi(r, \theta)$ with respect to r is defined as

$$\Phi^*(p, \theta) = \int_0^\infty r^{p-1}\Phi(r, \theta)dr. \tag{2.125}$$

Here p is a complex variable. The function $\Phi^*(p, \theta)$ is typically analytic for some strip of the complex plane, with the restrictions applying to the real part of p according to the behaviour of $\Phi(r, \theta)$ for both small and large r.

The behaviour of $\Phi(r, \theta)$ for small r is determined by the normalisation condition we have imposed, which implies that the Mellin transform $\Phi^*(p, \theta)$ can exist only for $\mathrm{Re}\, p > 0$. A consequence of this behaviour of Φ for small r is that Φ_y must have a finite discontinuity at $x = 0$ along the line $y = 0$. This necessitates a logarithmic term in the small r expansion of $\Phi(r, \theta)$, the largest of which is $O(r \log r)$.

We expect surface waves along the free-surface $\theta = 0$, of the form $\Phi(x, y) \propto e^{ix-y}$. The Mellin transform of the wave component on the free surface is

$$\Phi_w^*(p, 0) \equiv \int_0^\infty r^{p-1}\cos(r + \varphi)dr = \Gamma(p)\cos\left(\frac{\pi p}{2} + \varphi\right) \tag{2.126}$$

for $0 < \mathrm{Re}\, p < 1$, where $\Gamma(p)$ is the Gamma function.

We also expect an algebraic part of $\Phi(r, \theta)$ for large r, that decays explicitly as $r \to \infty$ on each fixed θ. The largest separable mode in this algebraic part is $O(r^{-1/2}\sin\frac{\theta}{2})$. Hence the Mellin transform of the algebraic part exists and is analytic for $0 < \mathrm{Re}\, p < 1/2$.

In summary, the Mellin transform $\Phi^*(p, \theta)$ should be analytic for $0 < \mathrm{Re}\, p < 1/2$. The function $\Phi^*(p, \theta)$ will be defined by analytic continuation in the remainder of the complex p plane.

2.5.1 Mellin transform of equations

Taking the Mellin transform of the equations (2.122) to (2.124) we find

$$\frac{\partial^2 \Phi^*(p,\theta)}{\partial \theta^2} + p^2 \Phi^*(p,\theta) = 0 \quad \text{for} \quad 0 \le \theta \le \pi \tag{2.127}$$

$$\frac{\partial \Phi^*(p-1,\theta)}{\partial \theta} = -\Phi^*(p,\theta) \quad \text{on} \quad \theta = 0 \tag{2.128}$$

$$\frac{\partial \Phi^*(p-1,\theta)}{\partial \theta} = 0 \quad \text{on} \quad \theta = \pi. \tag{2.129}$$

We see from (2.127) that the Mellin transform of Laplace's equation in polar coordinates takes a simple form. We can therefore write the general solution to (2.127) that also satisfies (2.129) as

$$\Phi^*(p,\theta) = A(p)\cos p(\theta - \pi), \tag{2.130}$$

where $A(p)$ is an arbitrary function of p to be determined. Substituting (2.130) into (2.128) we find that $A(p)$ satisfies the functional difference equation

$$\frac{A(p+1)}{A(p)} = p \tan p\pi. \tag{2.131}$$

2.5.2 Reduction of functional difference equation

A familiar functional difference equation defines the Gamma function:

$$\frac{\Gamma(z+1)}{\Gamma(z)} = z, \tag{2.132}$$

together with the normalisation condition $\Gamma(1) = 1$. The Gamma function and related functions will be critical to solving the dock problem using Mellin transforms. We begin by recalling the identity [NIST, 2011]

$$\sin \pi z = \frac{\pi}{\Gamma(z)\Gamma(1-z)} \tag{2.133}$$

which allows us to rewrite (2.131) as

$$\frac{A(p+1)}{A(p)} = p\frac{\Gamma(\frac{1}{2}+p)\Gamma(\frac{1}{2}-p)}{\Gamma(p)\Gamma(1-p)}. \tag{2.134}$$

We next introduce the Barnes double Gamma function $G(z,\delta)$ [Barnes, 1899] which by definition satisfies the functional difference equation

$$\frac{G(z+1,\delta)}{G(z,\delta)} = \Gamma\left(\frac{z}{\delta}\right) \tag{2.135}$$

together with the normalisation condition $\Gamma(1,\delta) = 1$. Each appearance of p within the Gamma functions on the right hand side of (2.134) has coefficient 1, and so we take $\delta = 1$.

If we now let

$$A(p) = \Gamma(p)\frac{G(\frac{1}{2}+p,1)G(2-p,1)}{G(\frac{3}{2}-p,1)G(p,1)}B(p) \tag{2.136}$$

and substitute (2.136) into (2.134), we find that $B(p)$ satisfies the much simpler functional difference equation

$$B(p+1) = B(p). \tag{2.137}$$

2.5.3 Singularities and large p behaviour of $\Phi^*(p,\theta)$

If $\Phi^*(p,\theta)$ is known, then $\Phi(r,\theta)$ may be found using

$$\Phi(r,\theta) = \frac{1}{2\pi i}\int_{c-i\infty}^{c+i\infty} r^{-p}\Phi^*(p,\theta)dp. \tag{2.138}$$

The positive constant c is chosen to lie in the strip of analyticity so in this case we require $0 < c < 1/2$. This inversion theorem can be derived from the Fourier inversion theorem [Sneddon, 1972].

For the inversion integral to exist, the integrand must be bounded as $t \to \infty$ where $p = c + it$. If we consider the difference equation for $\Phi^*(r,\theta)$, we have

$$\frac{A(p+1)}{A(p)} = p\tan p\pi. \tag{2.139}$$

where

$$\Phi^*(p,\theta) = A(p)\cos p(\theta-\pi). \tag{2.140}$$

If we take $p = c + it$ where t is large and fixed, and let $c \to -\infty$, $\Phi^*(r,\theta)$ decays exponentially so long as $r < 1$. Thus when $r < 1$ we can close the inversion contour in the left half plane $\mathrm{Re}\, p < 1/2$, and replace $\Phi(r,\theta)$ with the sum of residues from any poles in the left half plane. In terms of r-dependence, a simple pole at $p = -n$ gives an $O(r^n)$ residue.

A double pole at $p = -n$ gives an $O(r^n \log r)$ residue. A triple pole at $p = -n$ gives an $O(r^n (\log r)^2)$ residue, and so on. For small r we expect to find that

$$\Phi(r, \theta) \sim 1 + a(\theta) r \log r + b(\theta) r + o(r), \tag{2.141}$$

where $a(\theta)$ and $b(\theta)$ are functions of θ alone. This pole structure corresponds to $\Phi^*(p, \theta)$ having a simple pole at $p = 0$ and a double pole at $p = -1$. No other poles are allowed in $0 \leq \mathrm{Re}\, p < 1$.

The large-p behaviour we require from $\Phi^*(p, \theta)$ is that the integrand

$$r^{-p} \Phi^*(p, \theta) \tag{2.142}$$

is bounded as $\mathrm{Im}\, p \to \infty$.

2.5.4 Singularities and large z behaviour of $\Gamma(z)$ and $G(z, \delta)$

In order to continue, we need to understand the pole structure and large z behaviour of $\Gamma(z)$ and $G(z, \delta)$.

The relevant properties of $\Gamma(z)$ are well known. $\Gamma(z)$ has simple poles at $z = 0, -1, -2, \ldots$ but is analytic everywhere else in the complex z-plane. $\Gamma(z)$ is never zero. The behaviour of $\Gamma(z)$ for large z is given by Stirling's formula [NIST, 2011]:

$$\log \Gamma(z) = z \log z - z - \frac{1}{2} \log z + \frac{1}{2} \log(2\pi) + O\left(\frac{1}{z}\right). \tag{2.143}$$

The large-p behaviour of the Barnes double Gamma function is rather more obscure, but we can make analogous statements (e.g. [Lawrie and King, 1994], [Billingham and King, 1997]). $G(z, \delta)$ has no poles, but does have zeroes at $z = -(m\delta + n)$, where $m, n = 0, 1, 2\ldots$. Thus $1/G(z, \delta)$ has poles at $z = -(m\delta + n)$ where $m, n = 0, 1, 2\ldots$. However, these are not all simple poles. For example, applying the difference relation

$$G(z + 1, \delta) = \Gamma\left(\frac{z}{\delta}\right) G(z, 1), \tag{2.144}$$

we find that $1/G(z, 1)$ has a simple pole at $z = 0$, a double pole at $z = -1$, a triple pole at $z = -2$ and so on. If $\delta = 1/3$, as we will use for a Mellin transform calculation in chapter 3, we find that $1/G(z, 1/3)$ has simple poles at $z = 0, -1/3, -2/3$, double poles at $z = -1, -4/3, -5/3$, triple poles at $z = -2, -7/3, -8/3$ and so on.

The behaviour of $G(z,\delta)$ for large z was investigated by Billingham and King [1997], who showed that for $|z| \gg 1$ and $|\arg(z/\delta)| < \pi$,

$$\begin{aligned}\log G(z,\delta) = {} & \frac{1}{2\delta}z^2\log z - \frac{1}{\delta}\left(\frac{3}{4}+\frac{1}{2}\log\delta\right)z^2 - \frac{1}{2}\left(\frac{1}{\delta}+1\right)z\log z \\ & + \frac{1}{2}\left(\frac{\log\delta}{\delta}+\frac{1}{\delta}+\log\delta+1+\log(2\pi)\right)z + \left(\frac{\delta}{12}+\frac{1}{4}+\frac{1}{12\delta}\right)\log z \\ & + C(\delta) + O\left(\frac{1}{z}\right),\end{aligned} \tag{2.145}$$

where $C(\delta)$ is an $O(1)$ function of δ alone.

Finally we note that if z has positive real part and $\delta > 0$, then $\Gamma(z)$ and $G(z,\delta)$ can be evaluated using the integral definitions

$$\Gamma(z) = \int_0^\infty t^{z-1}e^{-t}dt \tag{2.146}$$

and

$$\begin{aligned}G(z,\delta) = \exp\Bigg(\int_0^\infty \Bigg\{ & \frac{e^{-\delta x}-e^{-zx}}{(1-e^{-x})(1-e^{-\delta x})} - z\frac{e^{-\delta x}}{1-e^{-\delta x}} \\ & + (z-1)\left(\frac{z}{2\delta}-1\right)e^{-\delta x} + \frac{e^{-x}}{1-e^{-x}}\Bigg\}\frac{dx}{x}\Bigg).\end{aligned} \tag{2.147}$$

2.5.5 Matching pole structure

We currently have

$$\Phi^*(p,\theta) = \cos p(\pi-\theta)\Gamma(p)\frac{G(\frac{1}{2}+p,1)}{G(p,1)}\frac{G(2-p,1)}{G(\frac{3}{2}-p,1)}B(p) \tag{2.148}$$

where the $B(p)$ function to be found satisfies $B(p+1) = B(p)$. We require that $\Phi^*(p,\theta)$ has a simple pole at $p = 0$ and a double pole at $p = -1$, with no other singularities in $-1 < \mathrm{Re}\, p < 0$. Using the results of the previous section, we find that $B(p)$ must have simple zeroes at $p = 0$ and $p = -1$. $B(p)$ may have a pole at $p = -1/2$, but must be regular elsewhere in $-1 < \mathrm{Re}\, p < 0$.

We set

$$B(p) = \tan p\pi C(p), \tag{2.149}$$

so that $C(p+1) = C(p)$ and $C(p)$ has no poles in $-1 \le \mathrm{Re}\, p \le 0$. By repeated application of the functional difference equation for $C(p)$, we find that $C(p)$ is an entire function.

2.5.6 Far field behaviour

We have now arrived at the situation where

$$\Phi^*(p,\theta) = C(p)\Gamma(p)\frac{G(\frac{1}{2}+p,1)G(2-p,1)}{G(p,1)G(\frac{3}{2}-p,1)}\tan(\pi p)\cos p(\theta-\pi). \tag{2.150}$$

We know that $C(p)$ is an entire function that satisfies $C(p+1) = C(p)$. We need to determine the behaviour of $C(p)$ as $|\mathrm{Im}(p)| \to \infty$.

If $\Phi^*(p,\theta)$ is known, the inverse function $\Phi(r,\theta)$ is given by

$$\Phi(r,\theta) = \frac{1}{2\pi i}\int_{c-i\infty}^{c+i\infty} r^{-p}\Phi^*(p,\theta)dp \tag{2.151}$$

where the real constant c is chosen to satisfy $0 < c < 1/2$, so that the inversion contour is within the strip of analyticity of $\Phi^*(p,\theta)$, and passes to the right of the singularity at $p = 0$.

For this inversion integral to exist, the integrand must be bounded as $\mathrm{Im}(p) \to \infty$ with $0 < \mathrm{Re}\, p < 1/2$. We are concerned with the asymptotic behaviour of this decay. If we can show $\Phi^*(p,\theta)/C(p)$ decays no faster than algebraically, then $C(p)$ must grow no faster than a polynomial for the integrand to remain bounded. By Liouville's theorem, $C(p)$ would then be a polynomial. However, since the only periodic polynomial is constant, we would have $C(p) = const.$ Although determining the speed of algebraic decay of $\Phi^*(p,\theta)$ is not necessary to fix $C(p)$, it will be useful in considering inversion contours. We therefore consider terms up to $O(\log(p))$ in $\log(\Phi^*(p,\theta)/C(p))$.

We now use the asymptotic expansions from section 2.5.4 and let $p = c + it$ with $0 < c < 1/2$. As $t \to \infty$ we find that

$$\Phi^*(p,\theta) = O\left(C(p)\exp\left[-t\theta + \left(c-\frac{1}{2}\right)\log t\right]\right). \tag{2.152}$$

We require that the integrand

$$r^{-p}\Phi^*(p,\theta) \tag{2.153}$$

is bounded as $t \to \infty$ for $0 \le \theta \le \pi$ and $r > 0$. Thus, regardless of the value of c, $C(p)$ must grow no faster than $O(t^{1/2})$ as $t \to \infty$. Outside the strip of analyticity, $C(p)$ is defined by $C(p+1) = C(p)$, so $C(p)$ must grow no faster than $O(p^{1/2})$ in the whole complex plane. We know that $C(p)$ is entire and is bounded by a polynomial (in this case $p^{1/2}$). Now by

Liouville's theorem, we know that $C(p)$ is identically equal to some polynomial, but as $C(p)$ is also periodic, we must have $C(p)$ constant, $C(p) \equiv \beta$, say. The solution $\Phi^*(p,\theta)$, and equivalently $\Phi(r,\theta)$, is now determined except for the value of the normalisation constant β.

2.5.7 Expansion for small r

The inversion integral is

$$\Phi(r,\theta) = \frac{1}{2\pi i}\int_{c-i\infty}^{c+i\infty} r^{-p}\Phi^*(p,\theta)dp, \tag{2.154}$$

while the Mellin transform $\Phi^*(p,\theta)$ decays as

$$\Phi^*(p,\theta) = O\left(\exp\left[-t\theta + \left(c-\frac{1}{2}\right)\log t\right]\right). \tag{2.155}$$

For small r, we have $\log r < 0$, and so r^{-c} decays as $c \to -\infty$. Thus the inversion integrand decays exponentially as $c \to -\infty$, and the integral can be closed in the left half plane. For small r, $\Phi(r,\theta)$ can be written as a sum of residues from the poles in the left half plane.

Along the negative real axis, the only poles are at $p = 0, -1, -2, \ldots$, of order $1, 2, 3\ldots$ respectively. We can write the sum of these contributions as

$$\Phi(r,\theta) = \sum_{n=0}^{\infty}\frac{1}{n!}\frac{d^n}{dp^n}\left[(p+n)^{n+1}r^{-p}\Phi^*(p,\theta)\right]_{p=-n}, \tag{2.156}$$

or more explicitly

$$\Phi(r,\theta) = \beta\sum_{n=0}^{\infty}\frac{1}{n!}\frac{d^n}{dp^n}\left[(p+n)^{n+1}r^{-p}\Gamma(p)\frac{G(\frac{1}{2}+p,1)G(2-p,1)}{G(p,1)G(\frac{3}{2}-p,1)}\tan(\pi p)\cos p(\theta-\pi)\right]_{p=-n}. \tag{2.157}$$

The task of evaluating the general term of this sum is unappealing. However, we can calculate the first few terms.

The normalisation constant β can be determined from the first term in (2.157)

$$\Phi(0,\theta) = 1 = \beta\frac{G(\frac{1}{2},1)G(2,1)}{G(\frac{3}{2},1)}\lim_{p\to 0}\left(\frac{p\Gamma(p)\tan\pi p}{G(p,1)}\right) = \frac{\beta\pi}{\Gamma(\frac{1}{2})}. \tag{2.158}$$

As $\Gamma(1/2) = \sqrt{\pi}$, we choose $\beta = 1/\sqrt{\pi}$ to obtain $\Phi(0,\theta) = 1$.

The $n = 1$ contribution from the sum (2.157) can be split into two parts, according to r dependence. We have

$$\begin{aligned}\Phi(r,\theta) \sim 1 - r\log r \frac{1}{\sqrt{\pi}} \frac{G(-\frac{1}{2},1)G(3,1)}{G(\frac{5}{2},1)} \cos(\pi-\theta) \lim_{p\to -1}\left[\frac{(p+1)^2\Gamma(p)\tan\pi p}{G(p,1)}\right] \\ + r\frac{1}{\sqrt{\pi}} \lim_{p\to -1}\frac{d}{dp}\left[\frac{(p+1)^2\Gamma(p)\tan\pi p}{G(p,1)}\frac{G(\frac{1}{2}+p,1)G(2-p,1)}{G(\frac{3}{2}-p,1)}\cos p(\theta-\pi)\right] \\ + O(r^2(\log r)^2)\end{aligned} \tag{2.159}$$

which simplifies to become

$$\begin{aligned}\Phi(r,\theta) \sim 1 - \frac{r\log r\cos\theta}{\pi} \\ + r\frac{1}{\sqrt{\pi}} \lim_{p\to -1}\frac{d}{dp}\left[\frac{(p+1)^2\Gamma(p)\tan\pi p}{G(p,1)}\frac{G(\frac{1}{2}+p,1)G(2-p,1)}{G(\frac{3}{2}-p,1)}\cos p(\theta-\pi)\right] \\ + O(r^2(\log r)^2).\end{aligned} \tag{2.160}$$

We can also split off the θ dependence from the last term. This gives

$$\begin{aligned}\Phi(r,\theta) \sim 1 - \frac{r\log r\cos\theta}{\pi} + \frac{r(\theta-\pi)\sin\theta}{\pi} \\ - r\frac{1}{\sqrt{\pi}}\cos\theta \lim_{p\to -1}\frac{d}{dp}\left[\frac{(p+1)^2\Gamma(p)\tan\pi p}{G(p,1)}\frac{G(\frac{1}{2}+p,1)G(2-p,1)}{G(\frac{3}{2}-p,1)}\right] \\ + O(r^2(\log r)^2).\end{aligned} \tag{2.161}$$

Thus we have an expansion for small r,

$$\Phi(r,\theta) \sim 1 - \frac{r\log r\cos\theta}{\pi} + \frac{r(\theta-\pi)\sin\theta}{\pi} + Ar\cos\theta + O(r^2(\log r)^2), \tag{2.162}$$

where the constant A is defined by

$$A = -\frac{1}{\sqrt{\pi}} \lim_{p\to -1}\frac{d}{dp}\left[\frac{(p+1)^2\Gamma(p)\tan\pi p}{G(p,1)}\frac{G(\frac{1}{2}+p,1)G(2-p,1)}{G(\frac{3}{2}-p,1)}\right]. \tag{2.163}$$

Regardless of the value of A, we find that this expansion satisfies our requirements so far. It is harmonic. It meets the normalisation condition $\Phi(0,\theta) = 1$. Each term satisfies $\Phi_\theta = 0$ on $\theta = \pi$. The condition $\Phi_\theta = -r\Phi$ on $\theta = 0$ is met up to $O(r)$.

2.5.8 Expansion for large r

Ignoring whether the contour can validly be deformed in this way, let us consider, for large r, the contribution from the poles in the right half plane. There are poles at $p = 1/2, 3/2, 5/2, ...$, of order $1, 2, 3, ...$ respectively. If there is no contribution from the contour at $p = \infty$, then

$$\Phi(r,\theta) = -\sum_{n=0}^{\infty} \frac{1}{n!}\frac{d^n}{dp^n}\left[\left(p-n-\frac{1}{2}\right)^{n+1} r^{-p}\Phi^*(p,\theta)\right]_{p=n+\frac{1}{2}}, \tag{2.164}$$

where

$$\Phi^*(p,\theta) = -\frac{1}{\sqrt{\pi}}\Gamma(p)\frac{G(\frac{1}{2}+p,1)G(2-p,1)}{G(p,1)G(\frac{3}{2}-p,1)}\tan(\pi p)\cos p(\theta-\pi). \tag{2.165}$$

The $n = 0$ term refers to a simple pole at $p = 1/2$, which contributes

$$\frac{1}{\sqrt{\pi}} r^{-1/2}\sin\left(\frac{\theta}{2}\right), \tag{2.166}$$

which is the leading order part of the 'algebraic' far field, as predicted by the Wiener-Hopf method in equation (2.115).

The $n = 1$ term again refers to a double pole, this time at $p = 3/2$. This again leads to three types of behaviour with r and θ. We have

$$\begin{aligned}\Phi(r,\theta) \sim\ & \frac{1}{\sqrt{\pi}} r^{-1/2}\sin\left(\frac{\theta}{2}\right) - \frac{r^{-3/2}\log r}{\sqrt{\pi}}\sin\left(\frac{3\theta}{2}\right)\frac{1}{2\pi} \\ & - \frac{\pi-\theta}{\sqrt{\pi}} r^{-3/2}\cos\left(\frac{3\theta}{2}\right)\frac{1}{2\pi} \\ & + \frac{1}{\sqrt{\pi}} r^{-3/2}\sin\left(\frac{3\theta}{2}\right)\frac{d}{dp}\left[\left(p-\tfrac{3}{2}\right)^2\Gamma(p)\frac{G(\frac{1}{2}+p,1)G(2-p,1)}{G(p,1)G(\frac{3}{2}-p,1)}\tan(\pi p)\right]_{p=3/2} \\ & + O(r^{-5/2}(\log(r))^2).\end{aligned} \tag{2.167}$$

This function is analytic and satisfies $\Phi_\theta = 0$ on $\theta = \pi$. We expect constant-amplitude waves to arise on the free surface at $\theta = 0$, which will not arise from this sum-of-residues expansion. The waves on $\theta = 0$ must arise from a contribution from the contour at infinity preventing deformation onto this contour. We will not investigate this further here.

2.5.9 Numerical evaluation of the Mellin transform solution

With the normalisation constant β known we have

$$\Phi(r,\theta) = \frac{1}{2\pi i}\int_{c-i\infty}^{c+i\infty} r^{-p}\Phi^*(p,\theta)dp, \tag{2.168}$$

where

$$\Phi^*(p,\theta) = \frac{1}{\sqrt{\pi}}\Gamma(p)\frac{G(\frac{1}{2}+p,1)G(2-p,1)}{G(p,1)G(\frac{3}{2}-p,1)}\tan(\pi p)\cos p(\theta-\pi). \tag{2.169}$$

We can use symmetry to write the inversion integral as

$$\Phi(r,\theta) = \frac{1}{\pi}\int_0^\infty \mathrm{Re}\{r^{-(c+it)}\Phi^*(c+it,\theta)\}dt \tag{2.170}$$

The integrand decays exponentially as $t\to\infty$ if $0<\theta\le\pi$, but on $\theta=0$ we have as $t\to\infty$

$$r^{-(c+it)}\Phi^*(c+it,\theta) = O\left(t^{c-1/2}\right),$$

where we take c fixed and $0<c<1/2$. The integrand is oscillatory, so $\Phi(r,\theta)$ as defined by (2.170) exists even for $\theta=0$, but the convergence is very slow. Figure 2.6 shows plots of $\Phi(r,\theta)$ calculated from (2.170) with $c=1/4$ for various values of $\theta>0$.

For $\theta=0$ it is helpful to deform the contour so that the amplitude of the integrand decays faster with t. Taking $c=1/4$ we have

$$\Phi(r,\theta) = \frac{1}{2\pi i}\int_{1/4-i\infty}^{1/4+i\infty} r^{-p}\Phi^*(p,\theta)dp. \tag{2.171}$$

We can move the path of integration to $c=-3/4$, but must take into account the pole at $p=0$. This gives

$$\begin{aligned}\Phi(r,\theta) &= 1 + \frac{1}{2\pi i}\int_{-3/4-i\infty}^{-3/4+i\infty} r^{-p}\Phi^*(p,\theta)dp\\ &= 1 + \frac{r^{3/4}}{\pi}\int_0^\infty \mathrm{Re}\{r^{-it}\Phi^*(-\tfrac{3}{4}+it,\theta)\}dt.\end{aligned} \tag{2.172}$$

We have

$$\Phi^*(-\tfrac{3}{4}+it,\theta) = A(-\tfrac{3}{4}+it)\cos\left[(-\tfrac{3}{4}+it)(\theta-\pi)\right] \tag{2.173}$$

and

$$A(-\tfrac{3}{4}+it) = \frac{A(\frac{1}{4}+it)}{(-\frac{3}{4}+it)\tan\pi(\frac{1}{4}+it)}. \tag{2.174}$$

This gives us

$$\Phi(r,\theta) = 1 - \frac{r^{3/4}}{\pi}\int_0^\infty \mathrm{Re}\left\{\frac{r^{-it}A(\frac{1}{4}+it)\cos\pi(\frac{1}{4}+it)}{(-\frac{3}{4}+it)\tan\pi(\frac{1}{4}+it)}\right\}dt \tag{2.175}$$

This expression is useful as the integrand now decays as $O(t^{-5/4})$ rather than $O(t^{-1/4})$. Figure 2.7 shows $\Phi(r,0)$ calculated using (2.175).

2.6 Conclusion

We have found an exact solution to the dock problem described in section 2.1 using two different methods, the first based on the Wiener-Hopf technique with Fourier transforms, and the second using Mellin transforms. The methods that we used have a number of essential similarities. We take a transform of the problem, to obtain an equation that is valid in some strip of the complex transform space. We use analytic continuation to extend the equation beyond this strip to the entire complex plane. We use information about the behaviour of $\Phi(r,\theta)$ for small and large r to determine certain boundedness properties of the transformed functions. Eventually, we use Liouville's theorem to replace an unknown entire function with a constant. We write down the transformed functions in terms of these constants, and invert the transforms to obtain Φ.

The Wiener-Hopf method required us to modify our problem to obtain a strip of analyticity of finite width, by introducing δ. We had to solve the problem for $\delta > 0$ before considering what happened when $\delta \to 0$. However, we did eventually obtain a solution in compact form. We found for $x > 0$ that

$$\begin{aligned}\phi(x,y) =& \sqrt{2}e^{-y}\sin\left(x+\frac{3\pi}{8}\right)\\ &-\frac{1}{\pi}\int_0^\infty \frac{e^{-xt}(t\cos yt - \sin yt)}{t^{1/2}(1+t^2)^{5/4}}\exp\left(\frac{1}{\pi}\int_0^t \frac{\log s}{1+s^2}ds\right)dt,\end{aligned} \tag{2.176}$$

and for $x < 0$ that

$$\phi(x,y) = \frac{1}{\pi}\int_0^\infty \frac{e^{xt}\cos yt}{t^{1/2}(1+t^2)^{3/4}}\exp\left(-\frac{1}{\pi}\int_0^t \frac{\log s}{1+s^2}ds\right)dt. \tag{2.177}$$

The calculation using the Mellin transform method was in some ways more straightforward – we simply followed the standard routine for such problems. However, the form of solution we were able to obtain is more difficult to understand. We found that

$$\Phi(r,\theta) = \frac{1}{\pi}\int_0^\infty \mathrm{Re}\{r^{-(c+it)}\Phi^*(c+it,\theta)\}dt \tag{2.178}$$

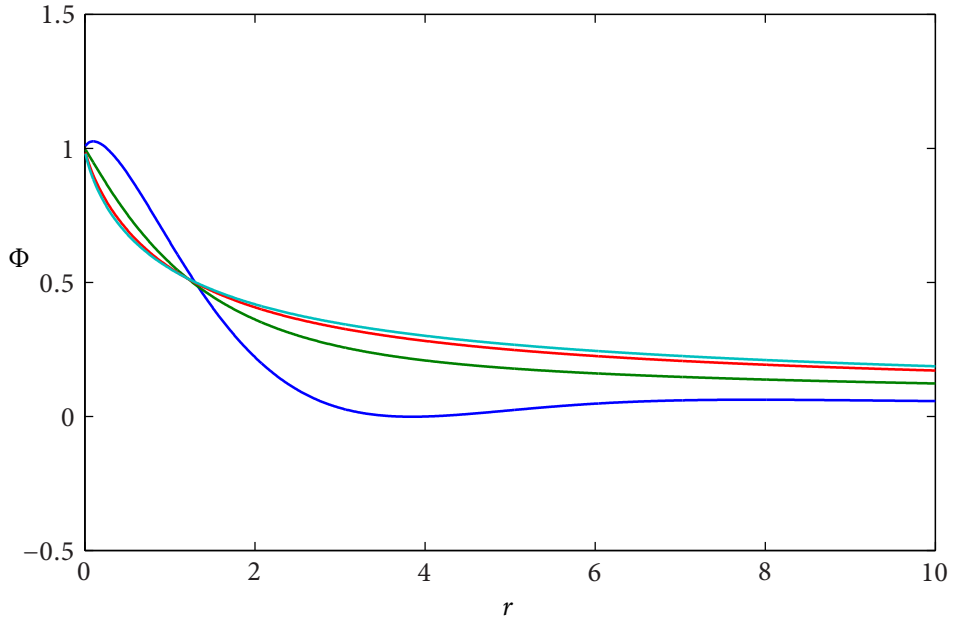

Figure 2.6: The dock problem solution $\Phi(r,\theta)$ for $\theta = \pi/4$ (blue), $\theta = \pi/2$ (green), $\theta = 3\pi/4$ (red), $\theta = \pi$ (cyan) calculated by evaluating (2.170) numerically. The integrand decays exponentially for $\theta > 0$, and so we obtain smooth results for these integrals. We see that $\Phi(r,\theta) \to 1$ as $r \to 0$ for $\theta > 0$. We cannot calculate $\Phi(0,\theta)$ directly from (2.170).

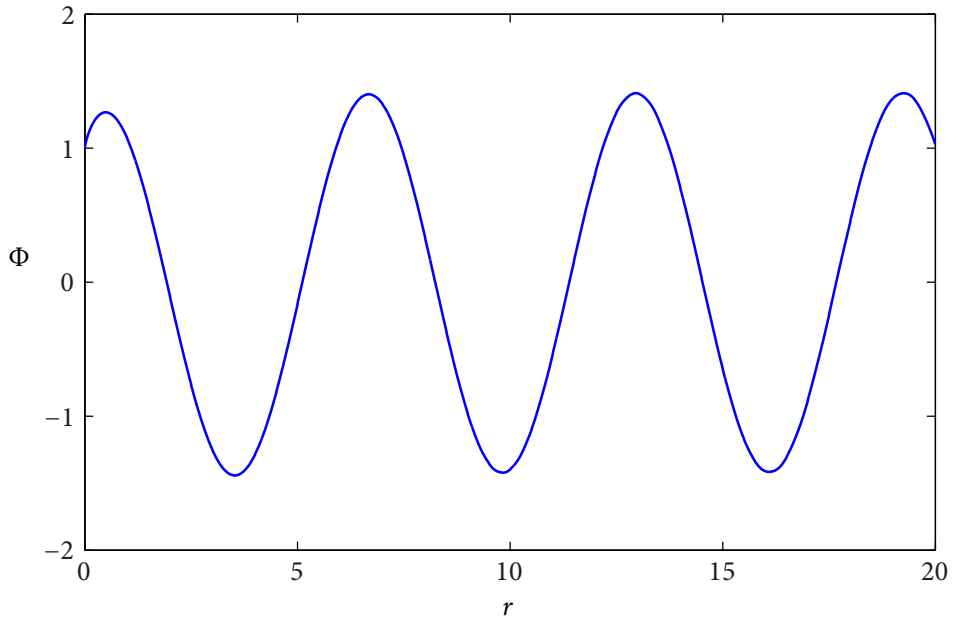

Figure 2.7: The dock problem solution Φ on the free-surface $\theta = 0$. $\Phi(r,0)$ is calculated by evaluating (2.175) numerically, with $c = -3/4$ so that the integrand decays as $t^{-5/4}$.

where $0 < c < 1/2$ and

$$\Phi^*(p,\theta) = \frac{1}{\sqrt{\pi}}\Gamma(p)\frac{G(\frac{1}{2}+p,1)G(2-p,1)}{G(p,1)G(\frac{3}{2}-p,1)}\tan(\pi p)\cos p(\theta-\pi), \tag{2.179}$$

and so our solution is given in terms of integrals of Gamma functions and double Gamma functions. The Mellin transform method does allow us to determine an asymptotic expansion for $\Phi(r,\theta)$ for small and large r, though obtaining subsequent terms in the expansion requires differentiation of double Gamma functions. However, it is difficult to distinguish the oscillatory part of $\Phi(r,\theta)$ in the Mellin transform solution, which would be required, for example, to obtain the amplitude and phase of the free-surface wave.

Chapter 3

Surface-tension-driven flow in a half-plane

We study the motion of a fat wedge of inviscid fluid, of angle $\pi - \epsilon$ with $\epsilon \ll 1$, in contact with a rigid wall along one edge. Initially the fluid is at rest. When $t = 0$, the contact angle at the tip of the wedge is changed to $\pi - \lambda\epsilon$. The resulting flow and motion of the contact point are determined by a balance of surface tension and inertia. As there are no geometric lengthscales imposed, we obtain a similarity solution, with lengths scalings as $t^{2/3}$. When $\lambda = O(1)$, we can linearise the domain to a half plane, with the free surface displacement coupled to the velocity potential via linear boundary conditions. We solve the leading order BVP numerically, with the aid of the boundary integral method, and also present asymptotic solutions for $\lambda \gg 1$ and $|\lambda - 1| \ll 1$. For $\lambda \gg 1$, the asymptotic solution can be constructed in terms of an inner and an outer region, with the phase and amplitude of the capillary wave on the free surface set in the inner region via the solution to the dock problem. The decay of the mean free surface displacement matches into the outer region to determine the relationship between λ and the contact point position x_c. For $|\lambda - 1| \ll 1$, the leading order problem can be solved exactly using Mellin transforms.

3.1 Introduction

Keller and Miksis [1983] first drew attention to inviscid, surface-tension driven flow in wedges. In their model problem, a fluid wedge of angle 2α is at rest until time $t = 0$, when the angle at the tip is suddenly changed to 2β and then remains constant. This disruption drives a recoiling flow in the fluid, with the free surface and contact point

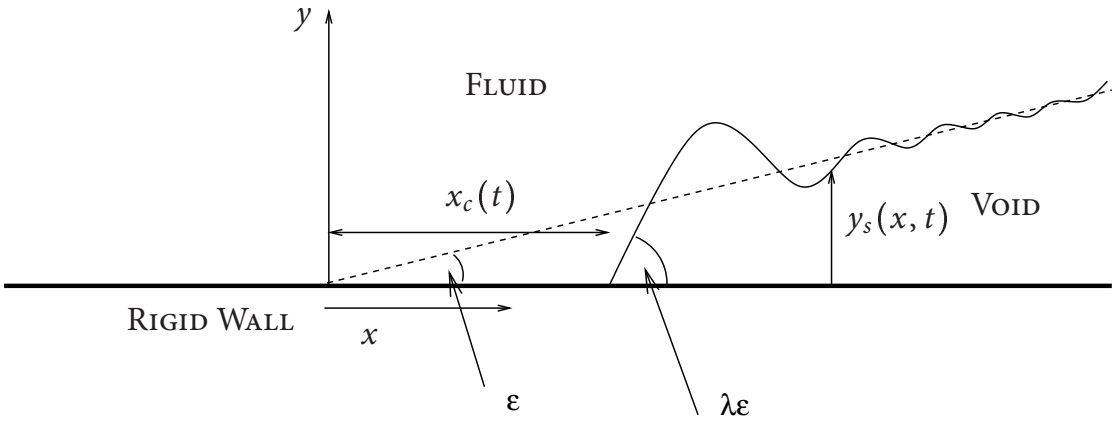

Figure 3.1: Initially the free surface is given by the dashed line, and the fluid occupies a fat wedge. When $t = 0$, the contact angle at the tip of the wedge is suddenly changed from $\pi - \epsilon$ to $\pi - \lambda\epsilon$, and the fluid recoils. The position of the free surface is given by $y = y_s(x,t)$ and position of the contact point is $x = x_c(t)$.

also displaced. With the flow determined by a balance of surface tension and inertia, and problem geometry specified by angles, a self-similar solution is obtained with lengths scaling as $t^{2/3}$.

For arbitrary α and β, the equations derived by Keller & Miksis yield nonlinear PDEs with the flow domain to be determined as part of the solution. Lawrie [1990] considered a linear system for $|\alpha - \beta| \ll 1$ on a wedge shaped domain, and showed that an analytic solution based on Mellin transforms exists when $\alpha = p\pi/2q$ with p odd. However, the linearisation fails near the contact point, and so the displacement of the contact point cannot be incorporated into the leading order equations. King [1991] subsequently showed that the leading order flow for the slender wedge case, $\alpha = \epsilon$, $\beta = \lambda\epsilon$, is nonlinear, and can be described by a pair of coupled ODEs for the potential in the wedge and the free surface position. Billingham [2006] used Kuzmak's method to solve this sytem when $1 \ll \lambda \ll \epsilon^{-1}$ and found that the displacement of the contact point scales as $x_c = O(\epsilon^{1/3}\lambda^{2/3})$.

Billingham and King [2005] considered the inverted problem with $\alpha = \pi - \epsilon$ and $\beta = \pi/2$, so that fluid surrounds a slender void. This corresponds to a large change in contact angle. They found that no solution exists for $\alpha < 2.87°$ because large amplitude capillary waves on the free surface cause it to touch the rigid wall. If the void is replaced by a low density inviscid fluid, the flow pinches off for a slightly larger range of α, as the fast flow in the slender wedge sucks the interface down.

In this chapter, we consider the case $\alpha = \pi - \epsilon$, $\beta = \pi - \lambda\epsilon$, as shown in figure 3.1. This is equivalent to a fat wedge of fluid coalescing with a rigid wall, with the new contact angle given by $\pi - \lambda\epsilon$. In the limit $\epsilon \to 0$ with $\lambda = O(1)$, we obtain a linear half plane problem, which we solve numerically using a boundary integral method in section 3.3 The simplified flow domain also allows us to find asymptotic solutions for $|\lambda - 1| \ll 1$ and for $1 \ll \lambda \ll \epsilon^{-1}$.

For $|\lambda - 1| \ll 1$ we obtain a linear parameter-free system similar to those obtained by Lawrie [1990], which we solve exactly using Mellin transforms. For $1 \ll \lambda \ll \epsilon^{-1}$, the displacement of the contact point x_c becomes important at leading order, and leads to a matched asymptotic structure, with a dock problem in the inner region. For large λ, the contact point displacement is related to λ by $x_c = O(\lambda^{2/9})$.

The amplitude of the capillary waves in our problem grows with λ. We find that the free surface touches the wall when $\lambda = \lambda_c \approx 31.9$, and no solution exists for $\lambda > \lambda_c$.

3.2 Problem formulation

3.2.1 Governing equations

The flow is at rest when $t = 0$ and so is initially irrotational. As the fluid is inviscid, the flow remains irrotational for all time. We may therefore make use of a velocity potential ϕ to write the fluid velocity as $\mathbf{u} = \nabla\phi$. The mass conservation condition can then be expressed as

$$\nabla^2\phi = 0 \tag{3.1a}$$

within the fluid.

For $t > 0$ the conditions at the contact point are

$$y_s = 0 \quad \text{and} \quad \frac{dy_s}{dx} = \tan\lambda\epsilon \quad \text{at} \quad x = x_c(t), \tag{3.1b}$$

where $y_s(x,t)$ is the position of the free surface. Away from the contact point the flow must match onto its initial state of rest, so

$$y_s \sim x\tan\epsilon \quad \text{as} \quad x \to \infty \tag{3.1c}$$

and

$$\phi \to 0 \quad \text{as} \quad r \to \infty. \tag{3.1d}$$

Along the interface we have dynamic and kinematic boundary conditions. The interface itself is a streamline so the Bernoulli condition gives

$$\frac{\partial \phi}{\partial t} + \frac{1}{2}|\nabla \phi|^2 + \frac{\sigma}{\rho}\kappa = 0 \quad \text{on} \quad y = y_s(x,t) \quad \text{for} \quad x > x_c(t). \tag{3.1e}$$

Here κ is the curvature of the interface, given by

$$\kappa = \frac{y_s''}{(1+y_s'^2)^{3/2}},$$

where $y_s' = \partial y_s/\partial x$. The kinematic condition is

$$\frac{\partial \phi}{\partial y} = \frac{\partial y_s}{\partial t} + \frac{\partial \phi}{\partial x}\frac{\partial y_s}{\partial x} \quad \text{on} \quad y = y_s(x,t) \quad \text{for} \quad x > x_c(t). \tag{3.1f}$$

Finally, at all times there must be no normal flow through the rigid wall so that

$$\frac{\partial \phi}{\partial y} = 0 \quad \text{on} \quad y = 0 \quad \text{for} \quad x < x_c(t). \tag{3.1g}$$

3.2.2 Similarity solution

There is no lengthscale imposed by the geometry of this problem. The only dimensional physical parameters on which our solution may depend are the density ρ and the coefficient of surface tension σ. To form a lengthscale, we must introduce the time t since the change in contact angle, and so we obtain a typical lengthscale

$$L \equiv \left(\frac{\sigma}{\rho}\right)^{1/3} t^{2/3}.$$

We are now able to remove the time dependence from the problem by using the similarity variables defined by

$$y_s = L\bar{y}_s, \quad x_c = L\bar{x}_c, \quad x = L\bar{x}, \quad y = L\bar{y}, \quad \phi = \frac{L^2}{t}\bar{\phi}.$$

Equations (3.1a) to (3.1d) and (3.1g) are unchanged under the transformation to the new variables, except that $\bar{x}_c = x_c(t)/L$ is now a constant to be determined. However, the interface conditions (3.1e) and (3.1f) become

$$\frac{1}{3}\bar{\phi} - \frac{2}{3}\left(\bar{x}\frac{\partial \bar{\phi}}{\partial \bar{x}} + \bar{y}\frac{\partial \bar{\phi}}{\partial \bar{y}}\right) + \frac{1}{2}|\nabla \bar{\phi}|^2 + \frac{\bar{y}_s''}{(1+\bar{y}_s'^2)^{3/2}} = 0 \quad \text{on} \quad \bar{y} = \bar{y}_s(x) \quad \text{for} \quad \bar{x} > \bar{x}_c \tag{3.2}$$

and

$$\frac{\partial \bar{\phi}}{\partial \bar{y}} + \frac{2}{3}\bar{x}\bar{y}_s' - \frac{2}{3}\bar{y}_s - \frac{\partial \bar{\phi}}{\partial \bar{x}}\bar{y}_s' = 0 \quad \text{on} \quad \bar{y} = \bar{y}_s(x) \quad \text{for} \quad \bar{x} > \bar{x}_c. \tag{3.3}$$

3.2.3 Linearisation for $\epsilon \ll 1$ with $\lambda = O(1)$

We now consider the behaviour of our system as $\epsilon \to 0$, where the initial wedge angle is given by $\pi - \epsilon$. A corresponding problem for the slender wedge of angle ϵ was considered by King [1991]. While King was able to take advantage of the restriction of scale in the y direction and thus reduce the leading order problem to a pair of coupled nonlinear ordinary differential equations, we have no geometrically imposed lengthscale in the x or y direction. Instead we have from (3.1a) that the scales for variation in the x and y directions must balance, and with the only other scale for variation given by $\bar{x}_c$, we put $\partial_{\bar{x}}, \partial_{\bar{y}} = O(\epsilon^{-a})$ and $\bar{x}_c = O(\epsilon^a)$. From (3.1b) we have $(\bar{y}_s)_{\bar{x}} = O(\epsilon^{a+1})$, while evaluating (3.3) at the contact point gives $\bar{\phi} = O(\epsilon^{2a+1})$. Finally, considering the balance in (3.2) at the contact point gives $a = 0$, and so we obtain $\bar{y}_s = O(\epsilon)$, $\bar{\phi} = O(\epsilon)$ and $\bar{x}, \bar{y}, \bar{x}_c = O(1)$ as $\epsilon \to 0$.

We define rescaled variables for $\bar{y}_s$ and $\bar{\phi}$ and also find it convenient to shift the origin to $\bar{x} = \bar{x_c}$, thus we shall put

$$\bar{y}_s = \epsilon H, \quad \bar{\phi} = \epsilon \Phi, \quad (x, y, x_c) = (\bar{x} - \bar{x}_c, \bar{y}, \bar{x}_c).$$

As we let $\epsilon \to 0$ with $\lambda = O(1)$, at leading order we obtain a linear system for H, Φ and x_c, given by

$$\nabla^2 \Phi = 0 \quad \text{for} \quad y > 0, \tag{3.4a}$$

$$\frac{1}{3}\Phi - \frac{2}{3}(x + x_c)\frac{\partial \Phi}{\partial x} + H_{xx} = 0 \quad \text{on} \quad y = 0 \quad \text{for} \quad x > 0, \tag{3.4b}$$

$$\frac{\partial \Phi}{\partial y} + \frac{2}{3}(x + x_c)H_x - \frac{2}{3}H = 0 \quad \text{on} \quad y = 0 \quad \text{for} \quad x > 0, \tag{3.4c}$$

$$\frac{\partial \Phi}{\partial y} = 0 \quad \text{on} \quad y = 0 \quad \text{for} \quad x < 0, \tag{3.4d}$$

$$H = 0 \quad \text{and} \quad H_x = \lambda \quad \text{at} \quad x = 0, \tag{3.4e}$$

$$H \sim x + x_c \quad \text{as} \quad x \to \infty, \tag{3.4f}$$

$$\Phi \to 0 \quad \text{as} \quad x^2 + y^2 \to \infty. \tag{3.4g}$$

These equations are linear, with the only inhomogeneity coming from the boundary condition (3.4f). We are now solving for Φ on a known domain, the half plane $y > 0$, although we still need to determine the linearised free surface displacement H as part of the solution.

3.3 Numerical solution

The equations derived in the previous section give a partial differential equation for $\Phi(x, y)$ in $y \geq 0$, with conditions on Φ or its normal derivatives on the boundary of the half plane. We could solve this system numerically by truncating the half plane $y \geq 0$ at some distance R from the origin, discretising this two dimensional domain and explicitly solving for H and Φ. However, we are most interested in the solution near $y = 0$ for $x \geq 0$. We can use a Green's function method to reduce the system to an ordinary differential equation and an integral equation along the half-line $y = 0$, $x \geq 0$.

3.3.1 Derivation of integral equation

In two dimensions the Green's function $G(\mathbf{x}, \mathbf{x}') = \ln|\mathbf{x} - \mathbf{x}'|/2\pi$ has the property

$$\nabla^2 G(\mathbf{x}, \mathbf{x}') = \delta(\mathbf{x} - \mathbf{x}'),$$

where δ is the Dirac delta function. We can use the Green's function to write the solution to (3.4a) and (3.4g) as a boundary integral equation, given by

$$\Phi(x, 0) = \frac{1}{\pi} \int_{-\infty}^{\infty} \ln|x - x'| \frac{\partial \Phi}{\partial y}(x', 0) dx'.$$

Upon substituting the form of Φ_y from (3.4c) and (3.4d) we obtain

$$\Phi(x, 0) = \frac{2}{3\pi} \int_{0}^{\infty} \ln|x - x'| (H(x') - (x' + x_c) H_x(x')) dx'. \tag{3.5a}$$

This integral equation, together with the ODE

$$\frac{1}{3}\Phi - \frac{2}{3}(x + x_c)\Phi_x + H_{xx} = 0, \tag{3.5b}$$

the boundary conditions at $x = 0$

$$H(0) = 0, \quad H_x(0) = \lambda, \tag{3.5c}$$

and the condition that

$$\Phi \to 0 \quad \text{and} \quad H = x + x_c + o(1) \quad \text{as} \quad x \to \infty, \tag{3.5d}$$

gives us a set of equations for $\Phi(x, 0)$ and $H(x)$ in $x \geq 0$.

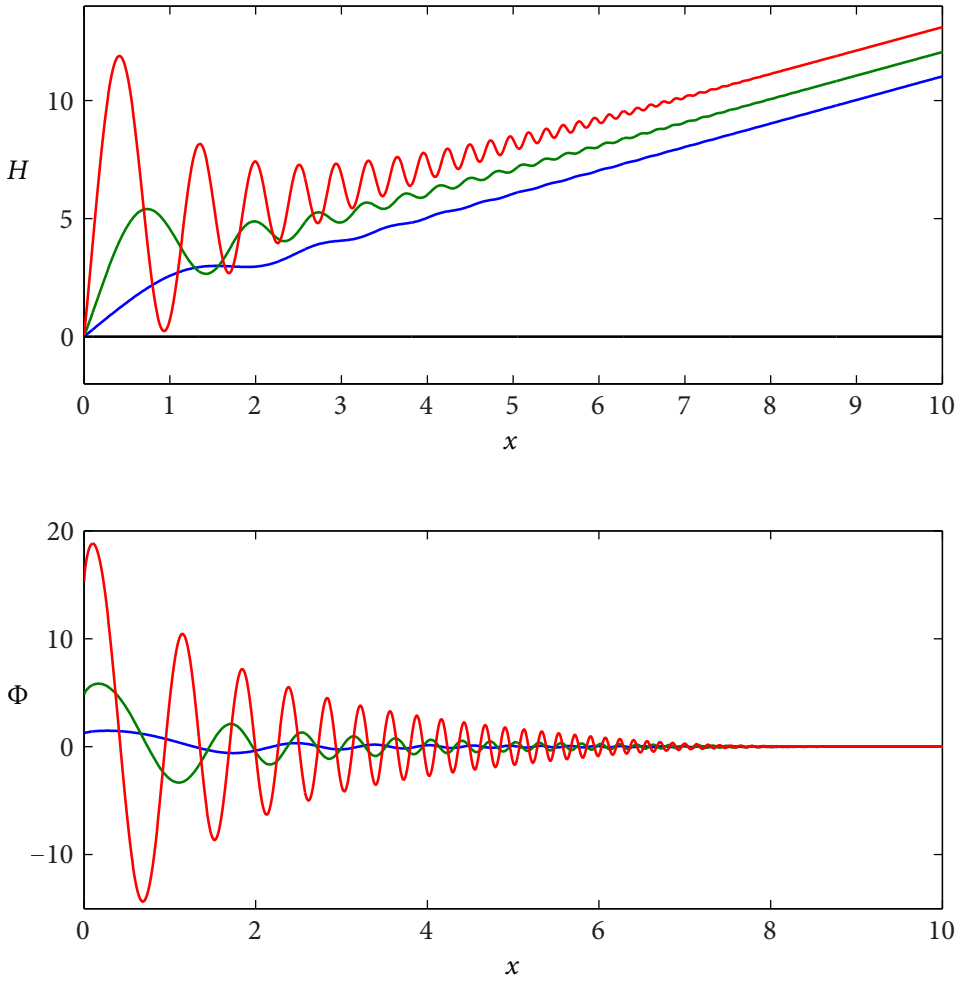

Figure 3.2: Numerically calculated boundary integral solutions for H and Φ for $x_c = 1, 2, 3$ (blue, green, red). The corresponding values of λ are 2.89, 9.35 and 34.1.

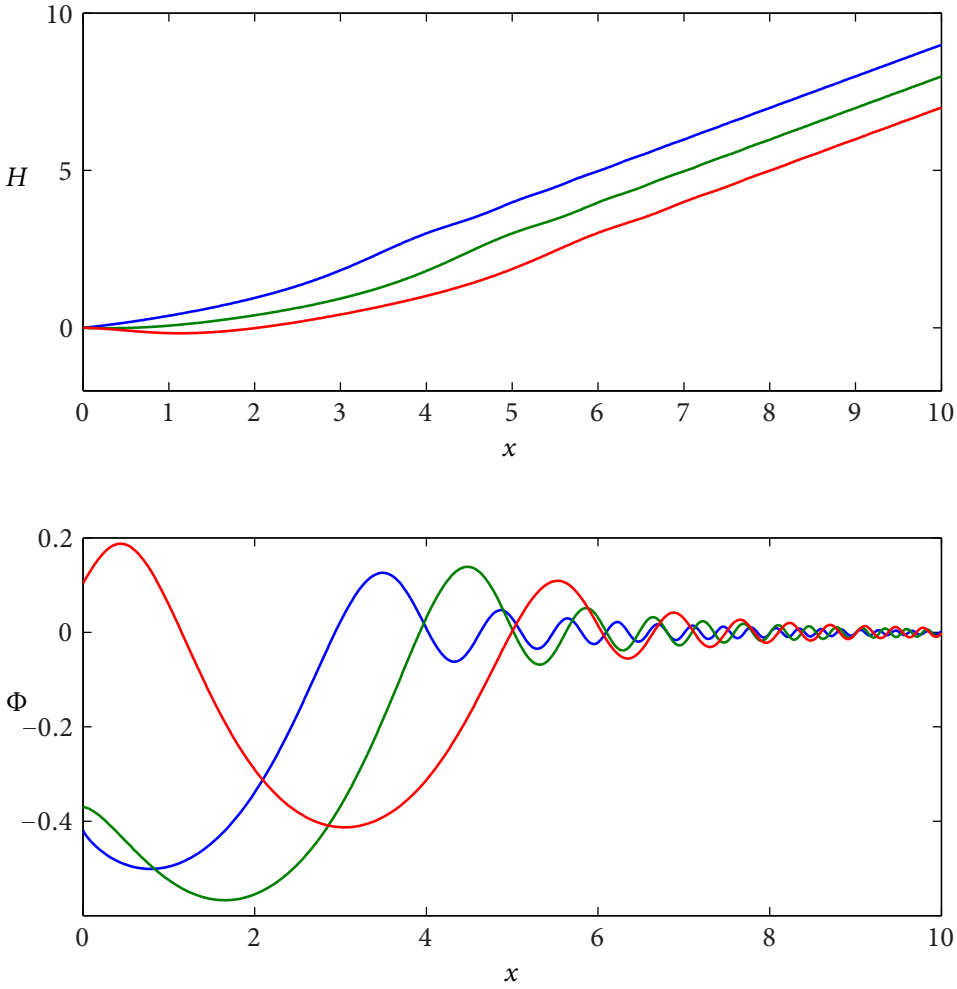

Figure 3.3: Boundary integral solutions for H and Φ at $x_c = -1, -2, -3$ (blue, green, red). The corresponding values of λ are 0.27, −0.079, −0.047.

3.3.2 Discretisation of the boundary integral system

We can discretise equations (3.5a) to (3.5d) to give a numerical solution for H and Φ. Treating λ as an unknown function of x_c allows the equations (3.5a) to (3.5d) to be considered as a linear system in H, Φ and λ, with coefficients depending nonlinearly on x_c. We discretise the derivatives in (3.5a) and (3.5b) using four point finite difference schemes to avoid grid sized oscillations that emerge using central differencing. To evaluate the integral in (3.5a), we assume that $H(x) - (x + x_c)H_x(x)$ varies linearly between grid points. This linear system gives a dense matrix equation of size $2N + 1$ that we invert to find H, Φ and λ.

3.3.3 Numerical results

The boundary integral solutions shown in figures 3.2 and 3.3 display quite different behaviour for positive and negative x_c. In figure 3.2, as x_c is increased, the solution is dominated by capillary waves whose amplitude and frequency grows with x_c. We find numerically that the free surface touches the rigid wall when $\lambda = \lambda_{max} = 37.8$, which corresponds to $x_c = 3.09$. We can find a solution to the system (3.4) for $\lambda > \lambda_{max}$, but the free surface intersects the rigid wall and so the solution is unphysical. Similarly, there is no physical solution for $\lambda < 0$, which corresponds to $x_c \approx -1.7$.

Figure 3.4 is a logarithmic plot of λ against x_c, which suggests a scaling relationship between λ and x_c for large positive x_c. In section 3.4 we construct an asymptotic solution to the system (3.4) for large x_c, and hence $\lambda \gg 1$.

For $x_c = 0$, we know that an exact solution is given by $H = x$, $\lambda = 1$ and $\Phi = 0$. In section 3.5 we find an asymptotic solution to (3.4) for small x_c by linearising about this exact solution. Figure 3.4 also shows λ as calculated by the boundary integral method for $-2 < x_c < 2$.

3.4 Solution for large x_c

3.4.1 Scaling

As λ increases, we observe from the numerical results that the wavelength of the capillary waves decreases. We look for a scaling where H and Φ vary on a lengthscale that is much shorter than x_c. From (3.4a), the lengthscales in the x and y directions must balance,

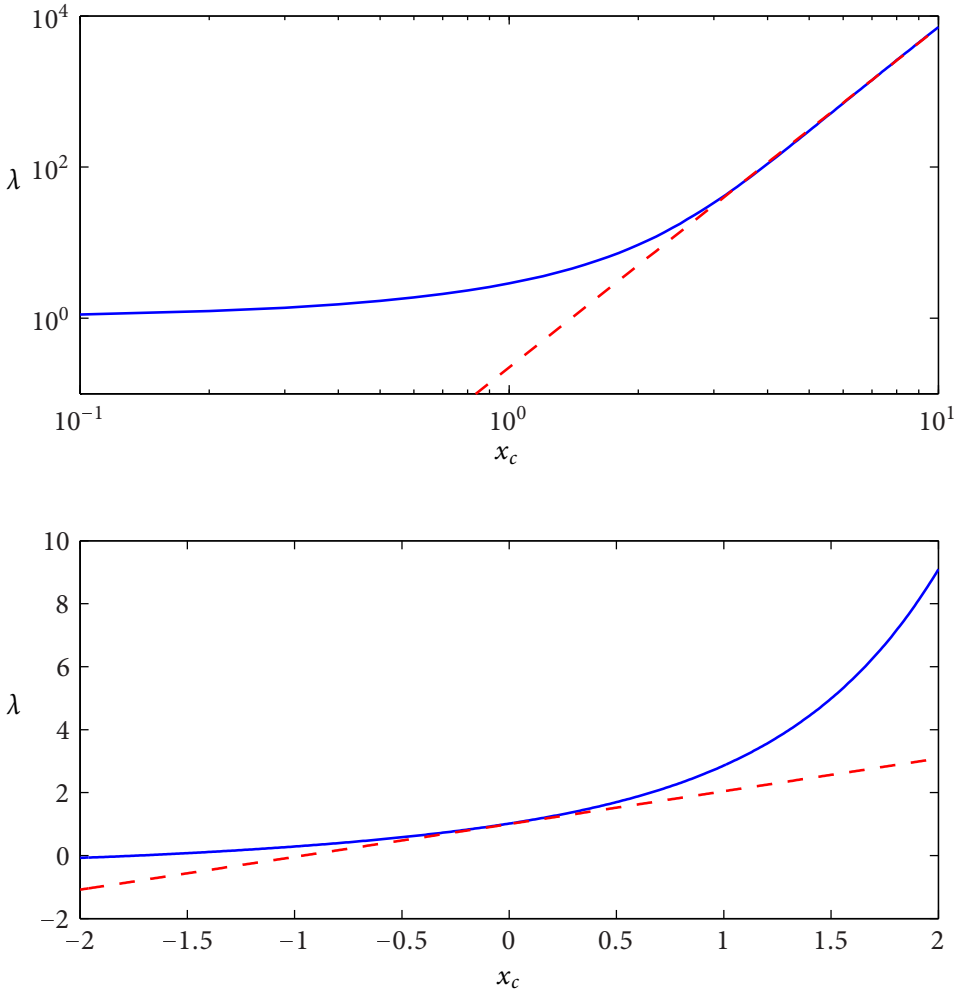

Figure 3.4: Comparison of numerical results from boundary integral calculations (solid line) with asymptotic results (dashed) for λ as a function of x_c for small and large x_c given by (3.34) and (3.69) respectively.

and so we obtain from (3.4b), (3.4c) and (3.4e) that $\partial_x, \partial_y = O(x_c^2)$, $H = O(\lambda x_c^{-2})$ and $\Phi = O(\lambda x_c^{-1})$.

We rescale by letting

$$H = \frac{\lambda}{x_c^2}\hat{H}, \quad \Phi = \frac{\lambda}{x_c}\hat{\Phi}, \quad (x, y) = \left(\frac{\hat{x}}{x_c^2}, \frac{\hat{y}}{x_c^2}\right).$$

For convenience we define $\tilde{\epsilon} = x_c^{-3}$ and $\lambda = \lambda^* x_c^3$. We require $\hat{H}, \hat{\Phi}$ to be $O(1)$ as $\tilde{\epsilon} \to 0$. Note that we have not yet determined how λ^* scales with x_c.

In terms of these rescaled variables we now wish to solve

$$\hat{\nabla}^2\hat{\Phi} = 0 \quad \text{for} \quad \hat{y} > 0, \tag{3.6a}$$

$$\frac{1}{3}\tilde{\epsilon}\hat{\Phi} - \frac{2}{3}(1 + \tilde{\epsilon}\hat{x})\frac{\partial\hat{\Phi}}{\partial\hat{x}} + \frac{d^2\hat{H}}{d\hat{x}^2} = 0 \quad \text{on} \quad \hat{y} = 0 \quad \text{when} \quad \hat{x} > 0, \tag{3.6b}$$

$$\frac{\partial\hat{\Phi}}{\partial\hat{y}} + \frac{2}{3}(1 + \tilde{\epsilon}\hat{x})\frac{d\hat{H}}{d\hat{x}} - \frac{2}{3}\tilde{\epsilon}\hat{H} = 0 \quad \text{on} \quad \hat{y} = 0 \quad \text{when} \quad \hat{x} > 0, \tag{3.6c}$$

$$\frac{\partial\hat{\Phi}}{\partial\hat{y}} = 0 \quad \text{on} \quad \hat{y} = 0 \quad \text{when} \quad \hat{x} < 0, \tag{3.6d}$$

$$\hat{H} = 0 \quad \text{and} \quad \frac{d\hat{H}}{d\hat{x}} = 1 \quad \text{at} \quad \hat{x} = 0, \tag{3.6e}$$

$$\hat{H} \sim \frac{1 + \tilde{\epsilon}\hat{x}}{\lambda^*} \quad \text{as} \quad \hat{x} \to \infty, \tag{3.6f}$$

$$\hat{\Phi} \to 0 \quad \text{as} \quad \hat{x}^2 + \hat{y}^2 \to \infty. \tag{3.6g}$$

3.4.2 Inner problem

We consider a matched asymptotic expansion to the system (3.6) in the limit $\tilde{\epsilon} \equiv x_c^{-3} \to 0$. There is clearly a non-uniformity in the equations (3.6b), (3.6c) and (3.6f) when $\hat{x} = O(\tilde{\epsilon}^{-1})$ and this outer region will be discussed in section 3.4.3. However, in the inner region, we take $\hat{x} = O(1)$ and expand $\hat{H}$ and $\hat{\Phi}$ as

$$\hat{H} = \hat{H}_0 + \tilde{\epsilon}\hat{H}_1 + O(\tilde{\epsilon}^2), \quad \hat{\Phi} = \hat{\Phi}_0 + \tilde{\epsilon}\hat{\Phi}_1 + O(\tilde{\epsilon}^2).$$

At leading order when $\hat{x} = O(1)$, we find that $\hat{H}_0$ and $\hat{\Phi}_0$ satisfy

$$\hat{\nabla}^2\hat{\Phi}_0 = 0 \quad \text{for} \quad \hat{y} > 0, \tag{3.7a}$$

$$-\frac{2}{3}\frac{\partial\hat{\Phi}_0}{\partial\hat{x}}+\frac{d^2\hat{H}_0}{d\hat{x}^2}=0 \quad \text{on} \quad \hat{y}=0 \quad \text{when} \quad \hat{x}>0, \tag{3.7b}$$

$$\frac{\partial\hat{\Phi}_0}{\partial\hat{y}}+\frac{2}{3}\frac{d\hat{H}_0}{d\hat{x}}=0 \quad \text{on} \quad \hat{y}=0 \quad \text{when} \quad \hat{x}>0, \tag{3.7c}$$

$$\frac{\partial\hat{\Phi}_0}{\partial\hat{y}}=0 \quad \text{on} \quad \hat{y}=0 \quad \text{when} \quad \hat{x}<0, \tag{3.7d}$$

$$\hat{H}_0=0 \quad \text{and} \quad \frac{d\hat{H}_0}{d\hat{x}}=1 \quad \text{at} \quad \hat{x}=0, \tag{3.7e}$$

We integrate (3.7b) to give

$$\frac{2}{3}\hat{\Phi}_0=\frac{d\hat{H}_0}{d\hat{x}}+M_0 \quad \text{on} \quad \hat{y}=0 \quad \text{when} \quad \hat{x}>0, \tag{3.8}$$

where M_0 is an $O(1)$ constant of integration. This can then be substituted into (3.7c) to give

$$\frac{\partial\hat{\Phi}_0}{\partial\hat{y}}+\frac{4}{9}\hat{\Phi}_0=\frac{2}{3}M_0 \quad \text{on} \quad \hat{y}=0 \quad \text{when} \quad \hat{x}>0. \tag{3.9}$$

We now write the general solution to (3.7a), (3.9) and (3.7d) as

$$\hat{\Phi}_0(\hat{x},\hat{y})=\frac{3}{2}\phi\left(\frac{4}{9}\hat{x},\frac{4}{9}\hat{y}\right)+\frac{3}{2}M_0 \tag{3.10}$$

where $\phi(x,y)$ satisfies the following:

$$\begin{cases} \nabla^2\phi = 0 & \text{for} \quad y>0, \\ \dfrac{\partial\phi}{\partial y} = -\phi \quad \text{on} \quad y=0 & \text{for} \quad x>0, \\ \dfrac{\partial\phi}{\partial y} = 0 \quad \text{on} \quad y=0 & \text{for} \quad x<0, \\ \phi(0,0) = 1. & \end{cases} \tag{3.11}$$

Comparing (3.10) to (3.8), (3.7e) and the normalisation condition $\phi(0,0)=1$, we see that $\hat{H}$ is given in terms of ϕ by

$$\hat{H}_0(\hat{x})=\int_0^{\hat{x}}\phi\left(\frac{4}{9}\hat{x}',0\right)d\hat{x}'. \tag{3.12}$$

The system of equations (3.11) are exactly those for the dock problem with normal incidence, which was first solved by Friedrichs and Lewy [1948]. Solution of the system (3.11) by use of the Wiener-Hopf method, and by Mellin transforms, is discussed in chapter

2. The solution is plotted in figures 2.5(a) and 2.5(b). For $x > 0$, $\phi(x, y)$ is given by

$$\begin{aligned}\phi(x, y) =& \sqrt{2}e^{-y}\sin\left(x + \frac{3\pi}{8}\right) \\ &- \frac{1}{\pi}\int_0^\infty \frac{e^{-xu}(u\cos yu - \sin yu)}{u^{1/2}(1+u^2)^{5/4}} \exp\left(\frac{1}{\pi}\int_0^u \frac{\log s}{1+s^2}ds\right) du,\end{aligned} \tag{3.13}$$

while $\phi(x, y)$ is given for $x < 0$ by

$$\phi(x, y) = \frac{1}{\pi}\int_0^\infty \frac{e^{xu}\cos yu}{u^{1/2}(1+u^2)^{3/4}} \exp\left(-\frac{1}{\pi}\int_0^u \frac{\log s}{1+s^2}ds\right) du. \tag{3.14}$$

The function $\phi(x, y)$ is continuous along the line $x = 0$. The surface wave is exponentially small as $y \to \infty$, and contributes to $\phi(x, y)$ only for $x > 0$, and so the line $x = 0$ is a Stokes line for the surface wave.

The solution to the inner problem is given in terms of ϕ by (3.10) and (3.12). Thus we integrate the expression for $\phi(x, y)$ to find $\hat{H}_0$. This gives us

$$\hat{H}_0 = \frac{9}{4}\left(-\sqrt{2}\cos\left(\frac{4\hat{x}}{9} + \frac{3\pi}{8}\right) + \frac{1}{\pi}\int_0^\infty \frac{e^{-4\hat{x}u/9}}{u^{1/2}(1+u^2)^{5/4}} \exp\left(\frac{1}{\pi}\int_0^u \frac{\log s}{1+s^2}ds\right) du\right). \tag{3.15}$$

There is no constant term in this expression because the constant of integration exactly cancels, using

$$\frac{1}{\pi}\int_0^\infty \frac{1}{u^{1/2}(1+u^2)^{5/4}} \exp\left(\frac{1}{\pi}\int_0^u \frac{\log s}{1+s^2}ds\right) du = \sqrt{2}\cos\left(\frac{3\pi}{8}\right). \tag{3.16}$$

This is a direct consequence of the no-net-flux condition on $\phi(x, y)$, and can be verified numerically.

Now that $\phi(x, y)$ is known explicitly, we can find the leading order behaviour of $\hat{\Phi}_0$ and $\hat{H}_0$ as $\hat{r} \to \infty$. As $x^2 + y^2 \to \infty$, the integrals in both (3.13) and (3.14) are dominated by the contribution from near $u = 0$, and at leading order we obtain

$$\hat{\Phi}_0(\hat{r}, \theta) \sim \frac{3}{2}M_0 + \frac{9}{4}\frac{\hat{r}^{-1/2}}{\sqrt{\pi}}\sin\frac{\theta}{2} + \begin{cases} \frac{3}{2}\sqrt{2}e^{-4\hat{y}/9}\sin\left(\frac{4\hat{x}}{9} + \frac{3\pi}{8}\right) & \text{for } \hat{x} > 0, \\ 0 & \text{for } \hat{x} < 0. \end{cases} \tag{3.17}$$

At leading order for large $\hat{x}$, the corresponding expression for $\hat{H}_0$ is

$$\hat{H}_0(\hat{x}) \sim \frac{9}{4}\left(-\sqrt{2}\cos\left(\frac{4\hat{x}}{9} + \frac{3\pi}{8}\right) + \frac{3}{2\sqrt{\pi}}\frac{1}{\hat{x}^{1/2}}\right). \tag{3.18}$$

This outer limit of the inner problem gives the leading order matching condition.

3.4.3 Outer problem

A non-uniformity occurs in the sytem (3.6a) to (3.6f) when $\hat{x} = O(\tilde{\epsilon}^{-1})$. We therefore rescale to an outer region with new $O(1)$ variables X and Y where $X = \tilde{\epsilon}\hat{x}$ and $Y = \tilde{\epsilon}\hat{y}$. Retaining only the outer boundary conditions this time, we find

$$\nabla^2\hat{\Phi} = 0 \quad \text{for} \quad Y > 0, \tag{3.19a}$$

$$\frac{1}{3}\hat{\Phi} - \frac{2}{3}(1+X)\frac{\partial\hat{\Phi}}{\partial X} + \tilde{\epsilon}\frac{d^2\hat{H}}{dX^2} = 0 \quad \text{on} \quad Y = 0 \quad \text{when} \quad X > 0, \tag{3.19b}$$

$$\frac{\partial\hat{\Phi}}{\partial Y} + \frac{2}{3}(1+X)\frac{d\hat{H}}{dX} - \frac{2}{3}\hat{H} = 0 \quad \text{on} \quad Y = 0 \quad \text{when} \quad X > 0, \tag{3.19c}$$

$$\frac{\partial\hat{\Phi}}{\partial Y} = 0 \quad \text{on} \quad Y = 0 \quad \text{when} \quad X < 0, \tag{3.19d}$$

$$\hat{H} \sim \frac{1+X}{\lambda^*} \quad \text{as} \quad X \to \infty, \tag{3.19e}$$

$$\hat{\Phi} \to 0 \quad \text{as} \quad R \to \infty. \tag{3.19f}$$

As $X \to 0$ we must match the outer solution with the outer limit of the inner solution, which is given by

$$\hat{\Phi}_0(R,\theta) \sim \frac{3}{2}M_0 + \frac{9}{4}\frac{\tilde{\epsilon}^{1/2}}{R^{1/2}\sqrt{\pi}}\sin\frac{\theta}{2} + \begin{cases} \frac{3}{2}\sqrt{2}e^{-4Y/9\tilde{\epsilon}}\sin\left(\frac{4X}{9\tilde{\epsilon}} + \frac{3\pi}{8}\right), & X > 0, \\ 0, & X < 0, \end{cases} \tag{3.20}$$

and

$$\hat{H}_0(X) \sim \frac{9}{4}\left(-\sqrt{2}\cos\left(\frac{4X}{9\tilde{\epsilon}} + \frac{3\pi}{8}\right) + \frac{3}{2\sqrt{\pi}}\frac{\tilde{\epsilon}^{1/2}}{X^{1/2}}\right). \tag{3.21}$$

These include the $O(1)$ constant term M_0 in $\hat{\Phi}$, $O(1)$ oscillatory terms in both $\hat{H}$ and $\hat{\Phi}$ and also $O(\tilde{\epsilon}^{1/2})$ algebraic terms. Based on our understanding of the outer limit of the inner problem, we expand $\hat{\Phi}$ and $\hat{H}$ in the outer field as

$$\hat{\Phi} = \bar{\Phi}_{osc} + \bar{\Phi}_0 + \tilde{\epsilon}^{1/2}\bar{\Phi}_1 + o(\tilde{\epsilon}^{1/2}), \quad \hat{H} = \bar{H}_{osc} + \bar{H}_0 + \tilde{\epsilon}^{1/2}\bar{H}_1 + o(\tilde{\epsilon}^{1/2}). \tag{3.22}$$

The first term in each expansion is oscillatory in X, while $\bar{\Phi}_0$, $\bar{H}_0$, $\bar{\Phi}_1$ and $\bar{H}_1$ are all $O(1)$ algebraic functions of X and Y. As the equations are linear, we can consider algebraic and oscillatory terms separately. We begin with the algebraic terms.

At $O(1)$, (3.19b) gives

$$\frac{1}{3}\bar{\Phi}_0 - \frac{2}{3}(1+X)\frac{\partial \bar{\Phi}_0}{\partial X} = 0 \quad \text{on} \quad Y = 0 \quad \text{when} \quad X > 0. \tag{3.23}$$

If $\bar{\Phi}_0$ is non-zero along the half line $X > 0$, $Y = 0$, then to satisfy this boundary condition we must have

$$\bar{\Phi}_0 \propto (1+X)^{1/2}.$$

However, this grows as $X \to \infty$, thus violating (3.19f), and so $\bar{\Phi}_0$ must vanish along the line $X > 0$, $Y = 0$. $\bar{\Phi}_0$ must also decay as $R \to \infty$ but be bounded as $R \to 0$ to meet the matching condition (3.20) at $O(1)$, and so we conclude that $\bar{\Phi}_0 = 0$ and hence $M_0 = 0$.

With $\bar{\Phi}_0 = 0$, taking (3.19c) at $O(1)$ now yields

$$\frac{2}{3}(1+X)\frac{d\bar{H}_0}{dX} - \frac{2}{3}\bar{H}_0 = 0, \tag{3.24}$$

which has general solution

$$\bar{H}_0 = N_0(1+X).$$

Then as $X \to 0$, we have $\bar{H}_0 \to N_0$, but there are no $O(1)$ constant terms in the outer limit of the inner expansion for $\hat{H}$, and so we must have $N_0 = 0$ and $\bar{H}_0 = 0$.

With both $\bar{\Phi}_0$ and $\bar{H}_0$ now zero, the remaining terms in our outer expansions are

$$\hat{\Phi} = \bar{\Phi}_{osc} + \tilde{\epsilon}^{1/2}\bar{\Phi}_1 + o(\tilde{\epsilon}^{1/2}), \quad \hat{H} = \bar{H}_{osc} + \tilde{\epsilon}^{1/2}\bar{H}_1 + o(\tilde{\epsilon}^{1/2}). \tag{3.25}$$

These should match the oscillatory and algebraic components of the inner field.

We now consider the algebraic part of (3.19b) at $O(\tilde{\epsilon}^{1/2})$. This yields

$$\frac{1}{3}\bar{\Phi}_1 - \frac{2}{3}(1+X)\frac{\partial \bar{\Phi}_1}{\partial X} = 0 \quad \text{on} \quad Y = 0 \quad \text{when} \quad X > 0. \tag{3.26}$$

and following the same argument as before, to avoid growth as $X \to \infty$ we must have $\bar{\Phi}_1(X, 0) = 0$ for $X > 0$. Then $\bar{\Phi}_1$ satisfies, in terms of polar coordinates (R, θ),

$$\nabla^2 \bar{\Phi}_1 = 0 \quad \text{in} \quad 0 \le \theta \le \pi,$$

$$\bar{\Phi}_1 = 0 \quad \text{on} \quad \theta = 0$$

and

$$\frac{\partial \bar{\Phi}_1}{\partial \theta} = 0 \quad \text{on} \quad \theta = \pi,$$

while the matching condition is

$$\bar{\Phi}_1 \sim \frac{9}{4}\frac{1}{R^{1/2}\sqrt{\pi}}\sin\frac{\theta}{2} \quad \text{as} \quad R \to 0.$$

We can solve this system exactly by putting

$$\bar{\Phi}_1 = \frac{9}{4}\frac{1}{R^{1/2}\sqrt{\pi}}\sin\frac{\theta}{2}. \tag{3.27}$$

We next consider (3.19c) at $O(\tilde{\epsilon}^{1/2})$, which gives

$$\frac{\partial\bar{\Phi}_1}{\partial Y} + \frac{2}{3}(1+X)\frac{d\bar{H}_1}{dX} - \frac{2}{3}\bar{H}_1 = 0, \quad X > 0, \quad Y = 0. \tag{3.28}$$

With $\bar{\Phi}_1$ given by (3.27), we now have an ordinary differential equation for $\bar{H}_1$. That is,

$$\frac{9}{8\sqrt{\pi}}\frac{1}{X^{3/2}} + \frac{2}{3}(1+X)\frac{d\bar{H}_1}{dX} - \frac{2}{3}\bar{H}_1 = 0 \quad \text{on} \quad Y = 0 \quad \text{when} \quad X > 0. \tag{3.29}$$

The solution of this equation is

$$\bar{H}_1 = A_1(1+X) + \frac{81}{16\sqrt{\pi}}\left(\sqrt{X} + (1+X)\arctan\sqrt{X}\right) + \frac{27}{8\sqrt{\pi}}\frac{1}{\sqrt{X}}, \tag{3.30}$$

where A_1 is an arbitrary constant. The matching condition on $\bar{H}_1$ is given from (3.21) by

$$\bar{H}_1(X) \sim \frac{27}{8\sqrt{\pi}}\frac{1}{X^{1/2}} \quad \text{as} \quad X \to 0.$$

and so we must have $A_1 = 0$.

We can determine λ^* at leading order by considering the large X behaviour of (3.30) with $A_1 = 0$. As $X \to \infty$ we have

$$\bar{H}_1 = \frac{81\sqrt{\pi}}{32}(1+X) + O(X^{-3/2}). \tag{3.31}$$

and so at leading order as $\tilde{\epsilon} \to 0$ and $X \to \infty$, we have

$$\hat{H} \sim \tilde{\epsilon}^{1/2}\frac{81\sqrt{\pi}}{32}(1+X). \tag{3.32}$$

Comparing with (3.19e) we find

$$\lambda^* \sim \tilde{\epsilon}^{-1/2}\frac{32}{81\sqrt{\pi}} \quad \text{as} \quad \tilde{\epsilon} \to 0 \tag{3.33}$$

and so at leading order for large x_c we find

$$\lambda \sim x_c^{9/2}\frac{32}{81\sqrt{\pi}} \quad \text{as} \quad x_c \to \infty. \tag{3.34}$$

This asymptotic result is compared to the boundary integral solution for λ in figure 3.4.

3.4.4 Capillary waves

Although λ^* is determined at leading order by the behaviour of the algebraic part of $\hat{H}$ and $\hat{\Phi}$, the capillary waves make a distinctive contribution to $\hat{H}$ and $\hat{\Phi}$ along the half line $Y = 0$, $X > 0$. We therefore wish to determine the amplitude and phase of these waves.

Self-similar capillary waves on the surface of inviscid fluid wedges were initially studied by Keller and Miksis [1983]. They used a WKB method to find solutions to the linearised system, and found that at large distance from the contact point, the phase of the interface displacement grows as $4x^3/27$ and the amplitude decays as $x^{-7/2}$. For our large-λ analysis, we will find that the capillary waves in the outer region display exactly this behaviour of amplitude and phase. For general wedge angles, the movement of the contact line cannot be described by a linear perturbation of the geometry. However, our half-plane problem allows the contact point to move freely without disturbing the leading order flow domain, and so we are able to determine the initial amplitude and phase of the wave by matching to the inner region solution.

We are looking for oscillatory terms in $\tilde{\Phi}$ and $\tilde{H}$, which we will denote by

$$\bar{\Phi}_{osc} = e^{f(X,Y)/\tilde{\epsilon}}, \quad \bar{H}_{osc} = e^{g(X)/\tilde{\epsilon}}.$$

The boundary conditions are that $\bar{\Phi}_{osc}$ and $\bar{H}_{osc}$ both vanish as $R \to \infty$, and that to leading order in $\tilde{\epsilon}$ each also matches the oscillatory part of the inner expansion as $X \to 0$. In terms of $f(X, Y)$, the Laplace equation (3.19a) becomes

$$\frac{f_X^2}{\tilde{\epsilon}^2} + \frac{f_Y^2}{\tilde{\epsilon}^2} + \frac{1}{\tilde{\epsilon}}\nabla^2 f = 0. \tag{3.35}$$

For small $\tilde{\epsilon}$ we expand f as

$$f = f_0 + \tilde{\epsilon} f_1 + \tilde{\epsilon}^2 f_2 + O(\tilde{\epsilon}^3) \tag{3.36}$$

and so we have from (3.35) at leading order

$$f_{0X}^2 + f_{0Y}^2 = 0,$$

which has solution $f_{0X} = \pm i f_{0Y}$. If f_0 satisfies this equation, then f_0 also identically satisfies $\nabla^2 f_0 = 0$, and so at next order from (3.35) we have

$$f_{0X} f_{1X} + f_{0Y} f_{1Y} = 0,$$

and so f_1 satisfies $f_{1X} = \pm i f_{1Y}$ with the same choice of sign as for f_0. We find that at every order $\nabla^2 f = 0$, and so (3.35) is replaced by

$$f_X^2 + f_Y^2 = 0,$$

which has exact solution

$$f_Y = \pm i f_X.$$

This holds at every order, and the same choice of sign must be taken at each order. We conclude that in this WKB analysis we must have

$$(\bar{\Phi}_{osc})_Y = \pm i (\bar{\Phi}_{osc})_X.$$

As a consequence of this relationship, the boundary conditions (3.19b) and (3.19c) become two coupled ordinary differential equations for $\bar{\Phi}_{osc}(X, 0)$ and $\bar{H}_{osc}$ along the half line $X > 0$. We have:

$$\tilde{\epsilon}(\bar{H}_{osc})_{XX} - \frac{2}{3}(1+X)(\bar{\Phi}_{osc})X + \frac{1}{3}\bar{\Phi}_{osc} = 0 \tag{3.37}$$

and

$$\pm i(\bar{\Phi}_{osc})_X + \frac{2}{3}(1+X)(\bar{H}_{osc})_X - \frac{2}{3}\bar{H}_{osc} = 0. \tag{3.38}$$

We can eliminate $\bar{H}_{osc}$ between these (3.37) and (3.38) to obtain

$$\pm i\tilde{\epsilon}(\bar{\Phi}_{osc})_{XX} + \frac{4}{9}(1+X)^2(\bar{\Phi}_{osc})_X - \frac{2}{9}(1+X)\bar{\Phi}_{osc} = 0.$$

Now letting $\bar{\Phi}_{osc} = e^{f/\tilde{\epsilon}}$, we have

$$\pm i\tilde{\epsilon}\left(\frac{f_X^2}{\tilde{\epsilon}^2} + \frac{f_{XX}}{\tilde{\epsilon}}\right) + \frac{4}{9}(1+X)^2\frac{f_X}{\tilde{\epsilon}} - \frac{2}{9}(1+X) = 0. \tag{3.39}$$

Using the expansion (3.36), we find at leading order in (3.39) that

$$\pm i f_{0X}^2 + \frac{4}{9}(1+X)^2 f_{0X} = 0,$$

which has solution

$$f_0 = \pm i\frac{4}{27}(1+X)^3.$$

We neglect additive constants in f as these correspond to multiplying Φ_{osc} by a constant amplitude.

At next order in (3.39), we have that

$$\pm i(2f_{0X}f_{1X} + f_{0XX}) + \frac{4}{9}(1+X)^2 f_{1X} - \frac{2}{9}(1+X) = 0,$$

from which we find

$$f_1 = -\frac{5}{2}\log(1+X).$$

These two terms in the expansion of f are enough to determine the behaviour of this oscillatory term in $\hat{\Phi}$. Subsequent terms in f give small corrections to the phase and amplitude of the oscillatory term. Each choice of sign gives a valid solution to the equations for $\bar{\Phi}_{osc}$. We can write the general solution for $\bar{\Phi}_{osc}$ as

$$\bar{\Phi}_{osc} = A\frac{\exp\left(i\frac{4}{27}\frac{(1+X+iY)^3}{\tilde{\epsilon}}\right)}{(1+X+iY)^{5/2}} + B\frac{\exp\left(-i\frac{4}{27}\frac{(1+X-iY)^3}{\tilde{\epsilon}}\right)}{(1+X-iY)^{5/2}}$$

where A and B are arbitrary complex constants.

To match the outer limit of the inner solution, we require that

$$\bar{\Phi}_{osc} \to \frac{3}{2}\sqrt{2}\sin\left(\frac{4X}{9\tilde{\epsilon}} + \frac{3\pi}{8}\right) \quad \text{as} \quad X \to 0.$$

Thus we can now write the solution for $\bar{\Phi}_{osc}$ as

$$\bar{\Phi}_{osc} = \mathrm{Re}\left\{\frac{3}{i\sqrt{2}}\frac{\exp\left(\frac{4i}{27}\frac{(1+X+iY)^3-1}{\tilde{\epsilon}} + \frac{3\pi i}{8}\right)}{(1+X+iY)^{5/2}}\right\}. \tag{3.40}$$

The oscillation vanishes along the Stokes line where the imaginary part of the argument of the exponential vanishes. At leading order in $\tilde{\epsilon}$, the Stokes line is given by

$$Y_{Stokes} = \left(\frac{(1+X)^3 - 1}{3(1+X)}\right)^{1/2}. \tag{3.41}$$

For large X this line is given approximately by $Y = (1+X)/\sqrt{3}$, and so in the far field the wave vanishes along the line $\theta = \pi/6$. As $X \to 0$, the outer Stokes line given by (3.41) matches the inner Stokes line on $\theta = \pi/2$ as given by (3.17).

To find the oscillatory part of $\hat{H}$ we integrate along the line $Y = 0$ using the boundary condition (3.19c). After integration by parts we find

$$\bar{H}_{osc} = -\frac{9\sqrt{2}}{4}\frac{\cos\left(\frac{4}{27}\frac{(1+X)^3-1}{\tilde{\epsilon}} + \frac{3\pi}{8}\right)}{(1+X)^{7/2}} + O(\tilde{\epsilon}). \tag{3.42}$$

As $X \to 0$ this matches the oscillatory part of outer limit of the inner solution, which is

$$\hat{H}_0(X) \sim -\frac{9}{4}\sqrt{2}\cos\left(\frac{4X}{9\tilde{\epsilon}} + \frac{3\pi}{8}\right).$$

3.4.5 Composite solution

We can now assemble a composite solution for $\hat{H}$ and $\hat{\Phi}$ from the inner, outer and oscillatory components (3.15), (3.10), (3.25), (3.30), (3.27), (3.42) and (3.40). Note that the oscillatory term in Φ is only included when $X > 0$ and $Y < Y_{Stokes}$, where Y_{Stokes} is the Stokes line given by (3.41).

Figure 3.5 compares the composite solution to the boundary integral solution for $x_c = 3.0124$. This is the critical value of x_c at which the composite solution first touches the rigid wall, and corresponds to an asymptotic value of $\lambda = 31.9$.

3.5 Solution for small x_c

For small x_c we linearise about the state of rest given by $\lambda = 1$, $x_c = 0$, $H = x$ and $\Phi = 0$. We write

$$H = x + x_c(1 + \bar{H}_0) + O(x_c^2), \quad \Phi = x_c\bar{\Phi}_0 + O(x_c^2), \quad \lambda = 1 + x_c\bar{\lambda}_0 + O(x_c^2).$$

We find that $\bar{H}_0$, $\bar{\Phi}_0$ and $\bar{\lambda}_0$ satisfy

$$\nabla^2\bar{\Phi}_0 = 0 \quad \text{for} \quad y > 0, \tag{3.43a}$$

$$\frac{1}{3}\bar{\Phi}_0 - \frac{2}{3}x\frac{\partial\bar{\Phi}_0}{\partial x} + \bar{H}_{0xx} = 0 \quad \text{on} \quad y = 0 \quad \text{when} \quad x > 0, \tag{3.43b}$$

$$\frac{\partial\bar{\Phi}_0}{\partial y} + \frac{2}{3}x\bar{H}_{0x} - \frac{2}{3}\bar{H}_0 = 0 \quad \text{on} \quad y = 0 \quad \text{when} \quad x > 0, \tag{3.43c}$$

$$\frac{\partial\bar{\Phi}_0}{\partial y} = 0 \quad \text{on} \quad y = 0 \quad \text{when} \quad x < 0, \tag{3.43d}$$

$$\bar{H}_0 = -1 \quad \text{and} \quad \bar{H}_{0x} = \bar{\lambda}_0 \quad \text{at} \quad x = 0, \tag{3.43e}$$

$$\bar{H}_0 \to 0 \quad \text{as} \quad x \to \infty, \tag{3.43f}$$

$$\bar{\Phi}_0 \to 0 \quad \text{as} \quad x^2 + y^2 \to \infty, \tag{3.43g}$$

which is a parameter free system. This problem for $\bar{H}_0$, $\bar{\Phi}_0$ and $\bar{\lambda}_0$ can be solved numerically using a version of the boundary integral method discussed in section 3.3, or analytically, using Mellin transforms.

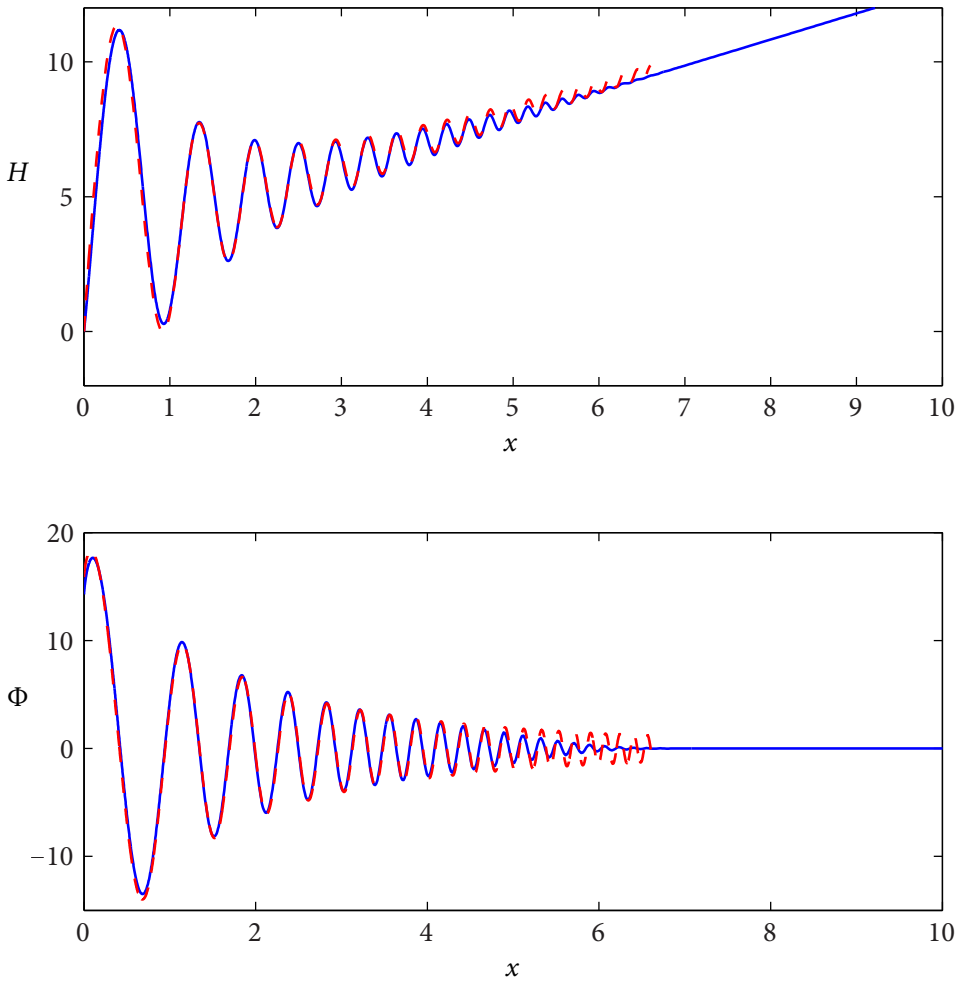

Figure 3.5: Comparison of composite (solid lines) and numerical solutions (dashed lines) for $x_c = 3.0124$, which is the value of x_c for which the composite solution for H first touches the rigid wall at $Y = 0$. The leading order asymptotic solution gives $\lambda = 31.9$ for $x_c = 3.0124$, while the boundary integral method gives $\lambda = 32.4$ for this value of x_c.

In chapter 2, we solved the dock problem firstly by using the Wiener-Hopf technique with Fourier transforms, and secondly by using Mellin transforms. The Fourier transform version of (3.43) has derivatives with respect to both k and y due to the appearance of the x-factors in (3.43b) and (3.43c), which makes solution by the Wiener-Hopf technique unfeasible. However, we find that the Mellin transform solution of (3.43) is no more complicated than that for the dock problem.

Mellin transforms are often useful in wedge geometries (see Sneddon [1972]), and have been used to solve linearised surface tension problems very similar to the one here, see Lawrie [1990] in particular. Lawrie considers our linearised surface equations on a wedge of angle α, and finds solutions for $\alpha = p\pi/2q$ where p and q have no common factors and p is odd. For our problem we have wedge angle $\alpha = \pi$, and so must construct the solution ourselves.

We use polar coordinates to take advantage of the symmetries of Mellin transforms. We define Mellin transforms of $\bar{\Phi}_0$ and $\bar{H}_0$ by

$$\bar{\Phi}_0^*(p,\theta) = \int_0^\infty r^{p-1}\bar{\Phi}_0(r,\theta)dr, \qquad \bar{H}_0^*(p) = \int_0^\infty r^{p-1}\bar{H}_0(r)dr. \tag{3.44}$$

Here p is a complex transform variable. With $\bar{H}_0^*(p)$ and $\bar{\Phi}_0^*(p,\theta)$ defined as in (3.44), the Mellin inversion theorem (see Sneddon [1972]) gives

$$\bar{H}_0(r) = \frac{1}{2\pi i}\int_{c-i\infty}^{c+i\infty} \bar{H}_0^*(p)r^{-p}dp, \tag{3.45}$$

and

$$\bar{\Phi}_0(r,\theta) = \frac{1}{2\pi i}\int_{d-i\infty}^{d+i\infty} \bar{\Phi}_0^*(p,\theta)r^{-p}dp. \tag{3.46}$$

Here the constants c and d are chosen so that the integration contours lie within the strip of analyticity for $\bar{H}_0^*(p)$ and $\bar{\Phi}_0^*(p)$ respectively. The strips of analyticity are defined as the complex p for which the Mellin transforms (3.44) are analytic and depend on the small and large r behaviour of $\bar{H}_0(r)$ and $\bar{\Phi}_0(r,\theta)$.

To determine for which p the transforms $\bar{\Phi}_0^*(p,\theta)$ and $\bar{H}_0^*(p)$ exist and are analytic, we must consider the behaviour for small and large r of $\bar{\Phi}_0(r,\theta)$ and $\bar{H}_0(r)$.

3.5.1 Expected solution behaviour

For small r we have from the boundary conditions that $\bar{H}_0(0) = -1$ and $\bar{H}_{0r}(0) = \bar{\lambda}_0$ where $\bar{\lambda}_0$ is finite. To avoid a source in the flow, we also require $\bar{\Phi}_0(r,\theta) = O(1)$ as

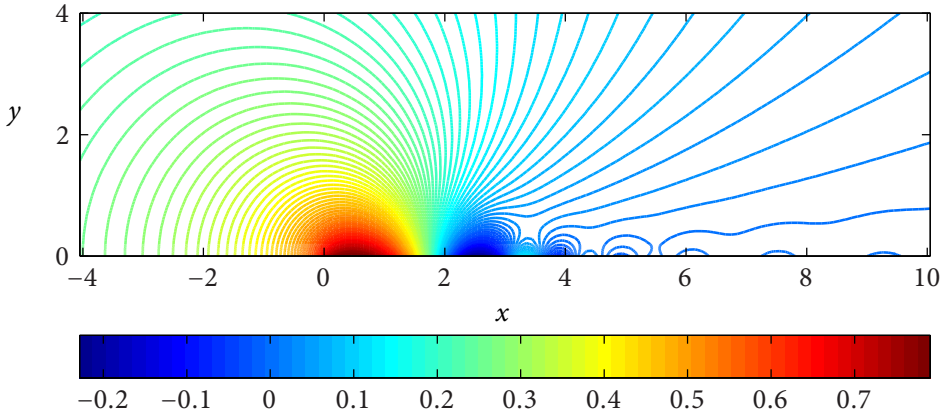

Figure 3.6: Contour plot of small-x_c asymptotic solution for $\bar{\Phi}_0$, which satisfies the system (3.43), calculated using Mellin transforms.

$r \to 0$. It is useful to note that if there is no source in the flow, the no-net-flux condition gives, via (3.43c), that $\bar{H}_0^*(1) = 0$. For large r, we find that $\bar{H}_0(r) = O(r^{-3/2})$, $\Phi(r,\theta) = O(r^{-1/2}\sin\frac{\theta}{2})$ for $0 < \theta \le \pi$ and $\bar{\Phi}_0(r,0) = O(r^{-7/2})$. Combining these descriptions, we find $\bar{H}_0^*(p)$ is analytic for $0 < \operatorname{Re} p < 3/2$, $\bar{\Phi}_0^*(p,\theta)$ is analytic for $0 < \operatorname{Re} p < 1/2$ and that $\bar{\Phi}_0^*(p,0)$ is analytic for $0 < \operatorname{Re} p < 7/2$.

We once again expect capillary waves near the surface $\theta = 0$. These grow in phase as $O(r^3)$ for large r but have decaying amplitudes, of $O(r^{-7/2})$ in $H(r)$ and of $O(r^{-5/2})$ in $\Phi(r,\theta)$. The capillary wave contributions to $H(r)$ and $\Phi(r,\theta)$ do not alter the strips of analyticity for $H^*(p)$ and $\Phi^*(p,\theta)$.

3.5.2 Mellin transform of equations

To solve this system using Mellin transforms, we first rewrite the problem using polar coordinates. We obtain

$$\frac{1}{r}\frac{\partial}{\partial r}\left(r\frac{\partial\bar{\Phi}_0}{\partial r}\right) + \frac{1}{r^2}\frac{\partial^2\bar{\Phi}_0}{\partial\theta^2} = 0 \quad \text{in} \quad 0 \le \theta \le \pi, \tag{3.47a}$$

$$\frac{1}{3}\bar{\Phi}_0 - \frac{2}{3}r\frac{\partial\bar{\Phi}_0}{\partial r} + \bar{H}_{0rr} = 0 \quad \text{on} \quad \theta = 0, \tag{3.47b}$$

$$\frac{1}{r}\frac{\partial\bar{\Phi}_0}{\partial\theta} + \frac{2}{3}r\bar{H}_{0r} - \frac{2}{3}\bar{H}_0 = 0 \quad \text{on} \quad \theta = 0, \tag{3.47c}$$

$$\frac{1}{r}\frac{\partial \bar{\Phi}_0}{\partial \theta} = 0 \quad \text{on} \quad \theta = \pi, \tag{3.47d}$$

$$\bar{H}_0 = -1 \quad \text{and} \quad \bar{H}_{0r} = \bar{\lambda}_0 \quad \text{at} \quad r = 0, \tag{3.47e}$$

$$\bar{H}_0(r) \to 0 \quad \text{as} \quad r \to \infty, \tag{3.47f}$$

$$\bar{\Phi}_0 \to 0 \quad \text{as} \quad r \to \infty \quad \text{for} \quad 0 < \theta \leq \pi. \tag{3.47g}$$

Taking Mellin transforms of the equations (3.47a) to (3.47d) gives

$$\frac{\partial^2}{\partial \theta^2}\left(\bar{\Phi}_0^*(p,\theta)\right) + p^2\bar{\Phi}_0^*(p,\theta) + \left[r^{p+1}\frac{\partial \bar{\Phi}_0}{\partial r} - pr^p\bar{\Phi}_0\right]_0^\infty = 0 \tag{3.48a}$$

for $0 \leq \theta \leq \pi$,

$$\begin{aligned}\frac{1}{3}(1+2p)\bar{\Phi}_0^*(p,0) + (p-1)(p-2)\bar{H}_0^*(p-2) \\ + \left[-\frac{2}{3}r^p\bar{\Phi} + r^{p-1}\bar{H}_{0r} - (p-1)r^{p-2}\bar{H}_0\right]_0^\infty = 0\end{aligned} \tag{3.48b}$$

and

$$\frac{\partial}{\partial \theta}\bar{\Phi}_0^*(p-1,\theta) - \frac{2}{3}(1+p)\bar{H}_0^*(p) + \left[\frac{2}{3}r^p\bar{H}_0\right]_0^\infty = 0 \tag{3.48c}$$

on $\theta = 0$, and

$$\frac{\partial}{\partial \theta}\bar{\Phi}_0^*(p-1,\theta) = 0 \tag{3.48d}$$

on $\theta = \pi$.

The end point contributions in the first three equations vanish for $0 < \operatorname{Re} p < 1/2$, for $2 < \operatorname{Re} p < 7/2$ and for $0 < \operatorname{Re} p < 3/2$ respectively, and it is for these p only that the Mellin transforms $\bar{H}_0^*(p)$ and $\bar{\Phi}_0^*(p,\theta)$ are defined by the integrals in (3.44). However, we may extend the equations outside of these strips by analytic continuation. Thus we have, for all p, that

$$\frac{\partial^2}{\partial \theta^2}\left(\bar{\Phi}_0^*(p,\theta)\right) + p^2\bar{\Phi}_0^*(p,\theta) = 0 \quad \text{for} \quad 0 \leq \theta \leq \pi, \tag{3.49a}$$

$$\frac{1}{3}(1+2p)\bar{\Phi}_0^*(p,0) + (p-1)(p-2)\bar{H}_0^*(p-2) = 0 \quad \text{on} \quad \theta = 0, \tag{3.49b}$$

$$\frac{\partial}{\partial \theta}\bar{\Phi}_0^*(p-1,\theta) - \frac{2}{3}(1+p)\bar{H}_0^*(p) = 0 \quad \text{on} \quad \theta = 0, \tag{3.49c}$$

and

$$\frac{\partial}{\partial\theta}\bar{\Phi}_0^*(p-1,\theta)=0 \quad \text{on} \quad \theta=\pi. \tag{3.49d}$$

The general solution to (3.49a) that also satisfies (3.49d) is

$$\bar{\Phi}_0^*(p,\theta)=Q_0(p)\cos(p(\theta-\pi)). \tag{3.50}$$

We may write (3.49b) and (3.49c) in terms of $Q_0(p)$ and $\bar{H}_0^*(p)$ to give

$$\frac{1}{3}(1+2p)Q_0(p)\cos p\pi+(p-1)(p-2)\bar{H}_0^*(p-2)=0 \tag{3.51}$$

and

$$-(p-1)Q_0(p-1)\sin p\pi-\frac{2}{3}(1+p)\bar{H}_0^*(p)=0. \tag{3.52}$$

We eliminate $Q_0(p)$ between these two equations to give a single functional difference equation for $\bar{H}_0^*(p)$. Thus we find that

$$\bar{H}_0^*(p+3)+\frac{9}{2}\frac{p(p+1)(p+2)}{(p+4)(2p+5)}\tan p\pi\bar{H}_0^*(p)=0, \tag{3.53}$$

where Q_0 is given in terms of $\bar{H}_0^*$ by

$$Q_0(p)=-3\frac{(p-1)(p-2)}{1+2p}\frac{H^*(p-2)}{\cos p\pi}. \tag{3.54}$$

3.5.3 Simplification of functional difference equations

We begin by recalling the identity

$$\tan\pi z=\frac{\Gamma(\frac{1}{2}-z)\Gamma(\frac{1}{2}+z)}{\Gamma(z)\Gamma(1-z)}, \tag{3.55}$$

so that we may write (3.53) as

$$\bar{H}_0^*(p+3)+\frac{9}{2}\frac{p(p+1)(p+2)}{(p+4)(2p+5)}\frac{\Gamma(\frac{1}{2}-p)\Gamma(\frac{1}{2}+p)}{\Gamma(p)\Gamma(1-p)}\bar{H}_0^*(p)=0. \tag{3.56}$$

To make progress with these functional difference equations we will make use of Gamma functions, which satisfy

$$\Gamma(z+1)=z\Gamma(z),$$

and Barnes double Gamma functions, $G(z,\delta)$, which are defined so that

$$G(z+1,\delta) = \Gamma\left(\frac{z}{\delta}\right) G(z,\delta),$$

along with the normalisation condition $G(1,\delta) = 1$. This allows us to solve the equation for $\bar{H}_0^*(p)$ by putting

$$\bar{H}_0^*(p) = \left(\frac{27}{4}\right)^{p/3} \frac{\Gamma(\frac{p}{3})\Gamma(\frac{p+1}{3})\Gamma(\frac{p+2}{3})}{\Gamma(\frac{p+4}{3})\Gamma(\frac{p}{3}+\frac{5}{6})} \frac{G(\frac{p}{3}+\frac{1}{6},\frac{1}{3})G(\frac{4}{3}-\frac{p}{3},\frac{1}{3})}{G(\frac{p}{3},\frac{1}{3})G(\frac{7}{6}-\frac{p}{3},\frac{1}{3})} W(p) \tag{3.57}$$

whereupon we find $W(p)$ satisfies the far simpler difference equation $W(p+3)+W(p) = 0$.

3.5.4 Mellin inversion and pole structure

The Mellin inversion theorem states that

$$\bar{H}_0(r) = \frac{1}{2\pi i} \int_{c-i\infty}^{c+i\infty} \bar{H}_0^*(p) r^{-p} dp, \tag{3.58}$$

where the constant c satisfies $0 < c < 3/2$; the path of integration passes to the right of the singularity at $p = 0$ and lies entirely within the strip of analyticity $0 < \mathrm{Re}\, p < 3/2$. For this inversion integral to be valid, the integrand must be bounded as $p \to \infty$ within the strip of analyticity.

We currently have $\bar{H}_0^*(p)$ given by (3.57), with $W(p+3)+W(p) = 0$. Using asymptotic results from Billingham and King [1997] we find that $\bar{H}_0^*(c+i\tau)$ decays exponentially as $c \to -\infty$ with τ large and fixed. Thus for small r, the integrand

$$\bar{H}_0^*(p) r^{-p}$$

decays exponentially in the left half plane, and so we can replace the integral in (3.58) with a suitable sum of residues from poles in the left half plane.

A pole of order m at $p = -n$ gives a residue with r-dependence $O(r^n(\log r)^{m-1})$, and so the behaviour of $\bar{H}_0(r)$ for small r given in section 3.5.1 is equivalent to requiring that $\bar{H}_0^*(p)$ has simple poles at $-2, -1, 0$, but no other singularities in the strip $-2 < \mathrm{Re}\, p < 0$. We also know that $\bar{H}_0^*(p)$ is analytic in the strip $0 < \mathrm{Re}\, p < 3/2$. Thus we need $\bar{H}_0^*(p)$ to be finite at every p in the strip $-2 < \mathrm{Re}\, p < 3/2$, except for simple poles at $p = 0, -1, -2$.

The double Gamma function $G(z,\delta)$ has no singularities but does have zeros at $z = -(m\delta + n)$, where $m, n = 0, 1, 2\ldots$ (see Lawrie and King [1994]). In particular, by

applying the functional difference equation for $G(z,1/3)$, we find that $1/G(z,1/3)$ has simple poles at $z = 0,-1/3,-2/3$, double poles at $z = -1,-4/3,-5/3$, triple poles at $z = -2,-7/3,-8/3$ and so on.

Using this information about the zeros of $G(z,1/3)$ together with standard properties of $\Gamma(z)$, we find that the expression

$$\frac{\bar{H}_0^*(p)}{W(p)} = \left(\frac{27}{4}\right)^{p/3} \frac{\Gamma(\frac{p}{3})\Gamma(\frac{p+1}{3})\Gamma(\frac{p+2}{3})}{\Gamma(\frac{p+4}{3})\Gamma(\frac{p}{3}+\frac{5}{6})} \frac{G(\frac{p}{3}+\frac{1}{6},\frac{1}{3})G(\frac{4}{3}-\frac{p}{3},\frac{1}{3})}{G(\frac{p}{3},\frac{1}{3})G(\frac{7}{6}-\frac{p}{3},\frac{1}{3})} \tag{3.59}$$

has double poles at $p = 0$, $p = -1$ and $p = -2$, has simple zeros at $p = -1/2$ and $p = -3/2$, and is finite and non-zero at every other p in the strip $-3/2 < \mathrm{Re}\, p < 3/2$.

To meet our requirements for $\bar{H}_0^*(p)$, we set

$$W(p) = \tan p\pi \sin(\tfrac{\pi}{3}(p-\tfrac{1}{2}))V(p), \tag{3.60}$$

where $V(p)$ must have no singularities in $-2 < \mathrm{Re}\, p < 3/2$, and satisfies $V(p+3) = V(p)$. Thus $V(p)$ is an entire function. We now use Liouville's theorem to determine $V(p)$.

For the inversion integral (3.58) to exist, the integrand must be bounded as $t \to \infty$ where $p = c + it$, for each c such that $0 < c < 3/2$ and for each $r > 0$. Now, as $t \to \infty$, we find

$$\bar{H}_0^*(c+it)r^{-(c+it)} = O\left(V(p)t^{c/3-5/3}\right) \tag{3.61}$$

and this must be bounded as for $0 < c < 3/2$. Setting $c = 3/2$, we find $V(p)$ grows no faster that $O(t^{7/6})$ as $t \to \infty$, and so by Liouville's theorem we can write

$$V(p) \equiv \alpha p + \beta.$$

However, we know that $V(p)$ is periodic, and so $\alpha = 0$ and $V(p) \equiv \beta$. We have

$$\bar{H}_0^*(p) = \beta\left(\frac{27}{4}\right)^{p/3} \frac{\Gamma(\frac{p}{3})\Gamma(\frac{p+1}{3})\Gamma(\frac{p+2}{3})}{\Gamma(\frac{p+4}{3})\Gamma(\frac{p}{3}+\frac{5}{6})} \frac{G(\frac{p}{3}+\frac{1}{6},\frac{1}{3})G(\frac{4}{3}-\frac{p}{3},\frac{1}{3})}{G(\frac{p}{3},\frac{1}{3})G(\frac{7}{6}-\frac{p}{3},\frac{1}{3})} \times \tan p\pi \sin(\tfrac{\pi}{3}(p-\tfrac{1}{2})) \tag{3.62}$$

This gives us a unique solution for $\bar{H}_0$, up to the multiplicative constant β to be determined by the normalisation condition $\bar{H}_0(0) = -1$. We can check that $\bar{H}_0^*(p)$ as defined by (3.62) has simple poles at $p = 0,-1,-2$ and at $p = 3/2$, has a simple zero at $p = 1$ and is finite and non-zero elsewhere in $-3/2 \le \mathrm{Re}\, p \le 3/2$.

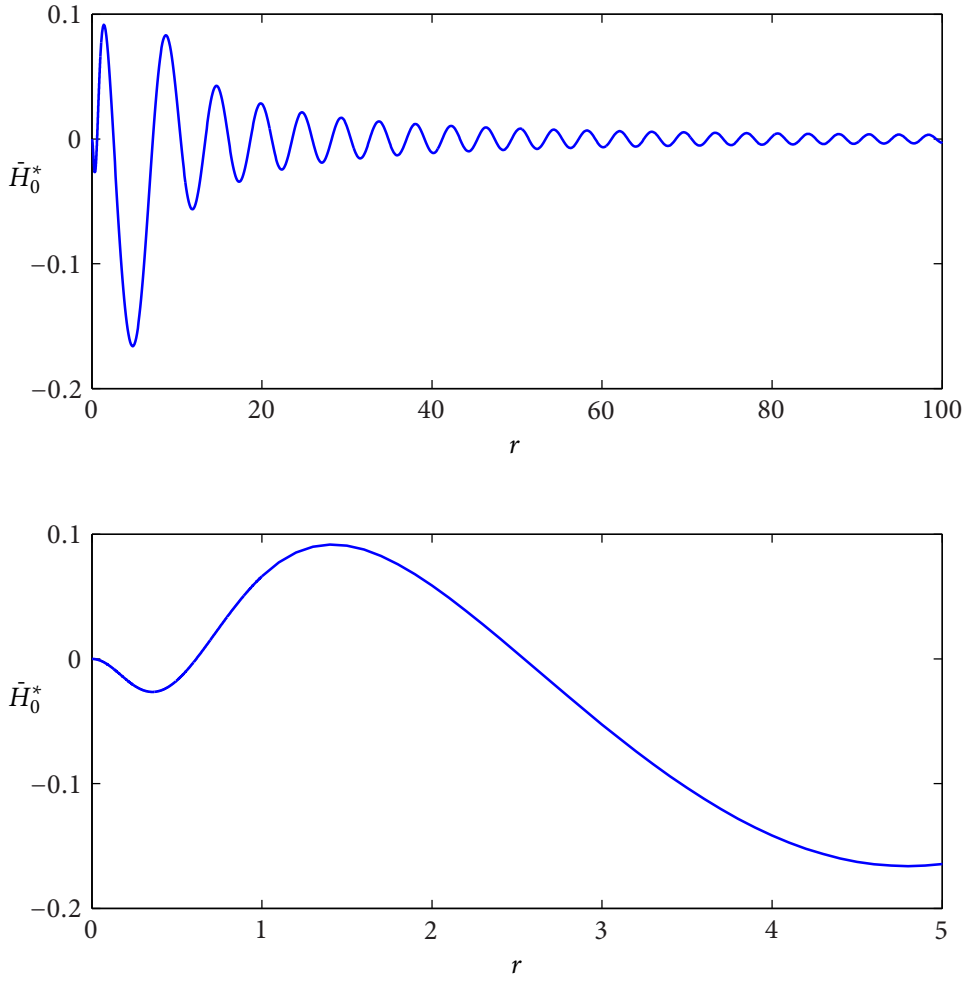

Figure 3.7: The real part of $\bar{H}_0^*(1+it)$ from (3.62) with normalisation constant β given by (3.67). The first plot shows t from 0 to 100, and we can see that $\bar{H}_0^*(1+it)$ is oscillatory, with slowly decaying amplitude. The second graph shows t from 0 to 5, and demonstrates that the condition $\bar{H}_0^*(1) = 0$ is met.

3.5.5 Expansion for small r and normalisation

For $r < 1$ we can close the inversion contour in the left half plane, and thus obtain a sum of residues from $p = 0, -1, -2, \ldots$. We find

$$\bar{H}_0(r) = \sum_{n=0}^{\infty} \mathrm{Res}\{\bar{H}_0^*(p) r^{-p}, p = -n\}. \tag{3.63}$$

Evaluating the residues from the first three poles, we find

$$\begin{aligned} \bar{H}_0(r) \sim & -\frac{9\beta\sqrt{\pi}}{2}\frac{\Gamma(\frac{2}{3})}{\Gamma(\frac{5}{6})} G(\tfrac{1}{3},\tfrac{1}{3}) + 6\beta\sqrt{3\pi}\left(\frac{27}{4}\right)^{-1/3} \frac{G(\frac{5}{6},\frac{1}{3})}{G(\frac{1}{2},\frac{1}{3})} r \\ & - \frac{9\beta\sqrt{3}}{4}\left(\frac{27}{4}\right)^{-2/3} \frac{\Gamma(\frac{5}{6})}{\Gamma(\frac{2}{3})} \frac{G(\frac{1}{2},\frac{1}{3})}{G(\frac{1}{3},\frac{1}{3}) G(\frac{5}{6},\frac{1}{3})} r^2 + O(r^3 \log(r)), \end{aligned} \tag{3.64}$$

as $r \to 0$. The resulting expressions can be simplified greatly by the use of two formulae given by Barnes [1899]:

$$G(\delta, \delta) = (2\pi)^{(\delta-1)/2} \delta^{-1/2}, \tag{3.65}$$

and

$$G(z + \delta, \delta) = (2\pi)^{(\delta-1)/2} \delta^{-z+1/2} \Gamma(z) G(z, \delta). \tag{3.66}$$

To satisfy the normalisation condition $H(0) = -1$, we set

$$\beta = \frac{2^{4/3}}{3^{3/2}\pi^{1/6}} \frac{\Gamma(\frac{5}{6})}{\Gamma(\frac{2}{3})}. \tag{3.67}$$

Comparing (3.64) with (3.47e) we then find

$$\bar{\lambda}_0 = \frac{8\pi}{9\Gamma(\frac{1}{3})} \approx 1.0424, \tag{3.68}$$

so that

$$\lambda \sim 1 + \frac{8\pi}{9\Gamma(\frac{1}{3})} x_c \tag{3.69}$$

as $x_c \to 0$. This is compared to the boundary integral calculations for $\lambda(x_c)$ in figure 3.4.

3.5.6 Inversion for general r

For general r we calculate $\bar{H}_0(r)$ and $\bar{\Phi}_0(r, \theta)$ by evaluating the inversion integral numerically. As $\mathrm{Re}\{\bar{H}_0^*(c + it)\} = \mathrm{Re}\{\bar{H}_0^*(c - it)\}$, we can rewrite (3.45) as

$$\bar{H}_0(r) = \frac{1}{\pi} \int_0^{\infty} \mathrm{Re}\{\bar{H}_0^*(c + it) r^{-c-it}\} dt, \tag{3.70}$$

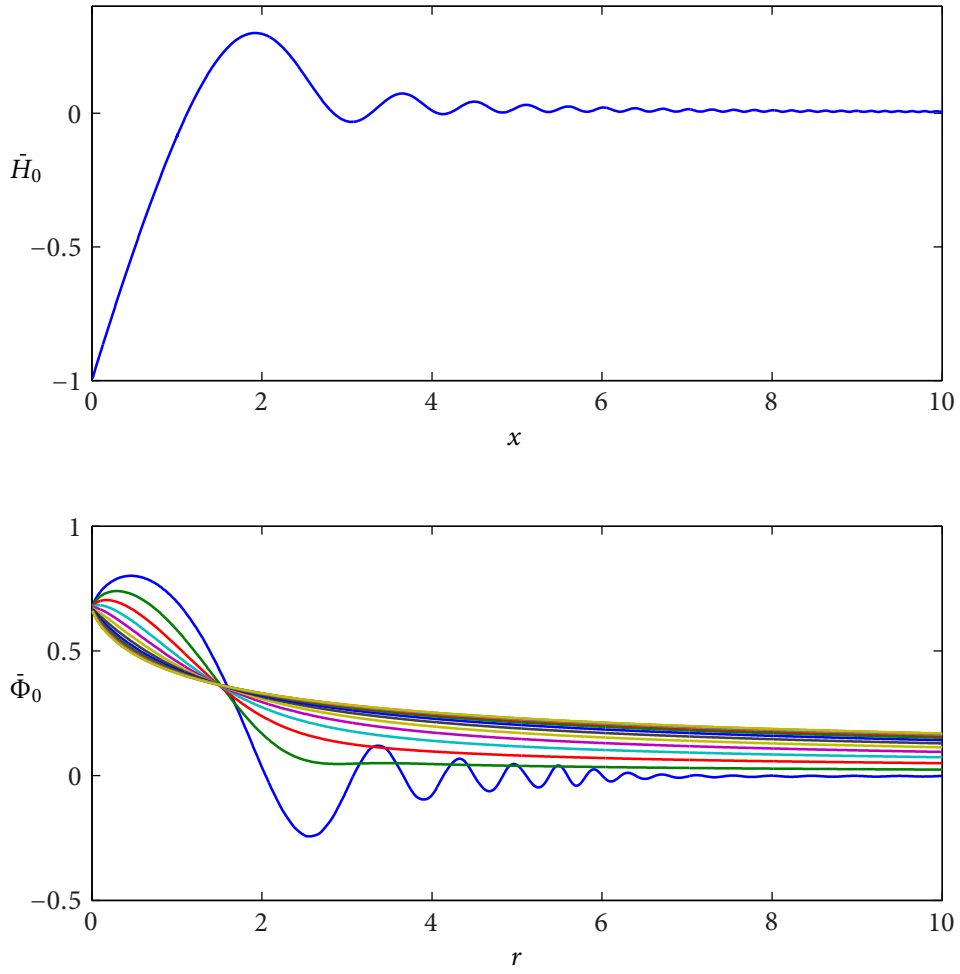

Figure 3.8: The analytical solution for $\bar{H}_0(r)$ and $\bar{\Phi}_0(r,0)$ (blue line in second plot). The analytical result is calculated by numerical evaluation of (3.70) with $c = 1$, with the upper limit of integration taken to be 500. The analytical solution has $\bar{\lambda}_0 = 1.04241$. The plot for $\bar{\Phi}_0$ also shows $\bar{\Phi}_0$ at $\theta = \pi/12, \pi/6, \ldots, \pi$, which correspond to $\bar{\Phi}_0(10,\theta)$ increasing.

which should be independent of c so long as $0 < c < 3/2$. The equivalent expression for $\bar{\Phi}_0(r,\theta)$ is

$$\bar{\Phi}_0(r,\theta) = \frac{1}{\pi}\int_0^\infty \mathrm{Re}\{\bar{\Phi}_0^*(d+it,\theta)r^{-d-it}\}dt. \tag{3.71}$$

We know that

$$\bar{\Phi}_0^*(p,\theta) = Q_0(p)\cos p(\theta-\pi) = \frac{2}{3}\frac{p+2}{p}\frac{\bar{H}_0^*(p+1)}{\sin p\pi}\cos p(\theta-\pi). \tag{3.72}$$

From the definition of $\bar{H}_0^*(p)$ given by (3.62), we know that $\bar{H}_0^*(p)$ has a simple pole at $p = 3/2$ and a simple zero at $p = 1$, but is finite and non-zero for all other p in the strip $1 \le \mathrm{Re}\, p \le 3/2$. Then by (3.72), $\bar{\Phi}_0^*(p,\theta)$ has simple poles at $p = 0$ and $p = 1/2$, so we must take $0 < d < 1/2$ in (3.71).

To evaluate the double Gamma functions in (3.62) we use the integral expression from Billingham and King [1997], which converges for $\delta > 0$ and $\mathrm{Re}\, z > 0$.

$$\begin{aligned} G(z,\delta) = \exp\Bigg(\int_0^\infty \Bigg\{ &\frac{e^{-\delta u} - e^{-zu}}{(1-e^{-u})(1-e^{-\delta u})} - z\frac{e^{-\delta u}}{1-e^{-\delta u}} \\ &+(z-1)\left(\frac{z}{2\delta}-1\right)e^{-\delta u} + \frac{e^{-u}}{1-e^{-u}}\Bigg\}\frac{du}{u}\Bigg). \end{aligned} \tag{3.73}$$

The range of integration in both (3.70) and (3.73) must be truncated in order to calculate the integrals numerically. The integrand in (3.73) decays exponentially as $x \to \infty$ if $\delta > 0$ and $\mathrm{Re}\, z > 0$. However, the integrand in (3.70) decays only algebraically as $t \to \infty$, as given by (3.61) and shown in figure 3.7. To improve the numerical convergence of this integral, it is helpful to deform the inversion contour in (3.45) to reduce the real part of p. Such a deformation must take into account the poles in $\bar{H}_0^*(p)$.

Figure 3.8 compares $\bar{H}_0$ and $\bar{\Phi}_0$ calculated via a boundary integral discretisation of (3.43a) to the exact solution given by (3.45). Figure 3.8 also shows $\bar{\Phi}_0(r,\theta)$ for various θ. This shows that the capillary waves are only noticeable very near the surface $\theta = 0$.

3.6 Conclusion

This chapter has been concerned with finding asymptotic solutions to the linear system (3.4) for large λ and for $|\lambda - 1| \ll 1$, and numerical solutions when $\lambda = O(1)$. In both cases we obtained good agreement between numerical and asymptotic results. For large λ we obtained a solution using matched asymptotic expansions, with the main detail of the

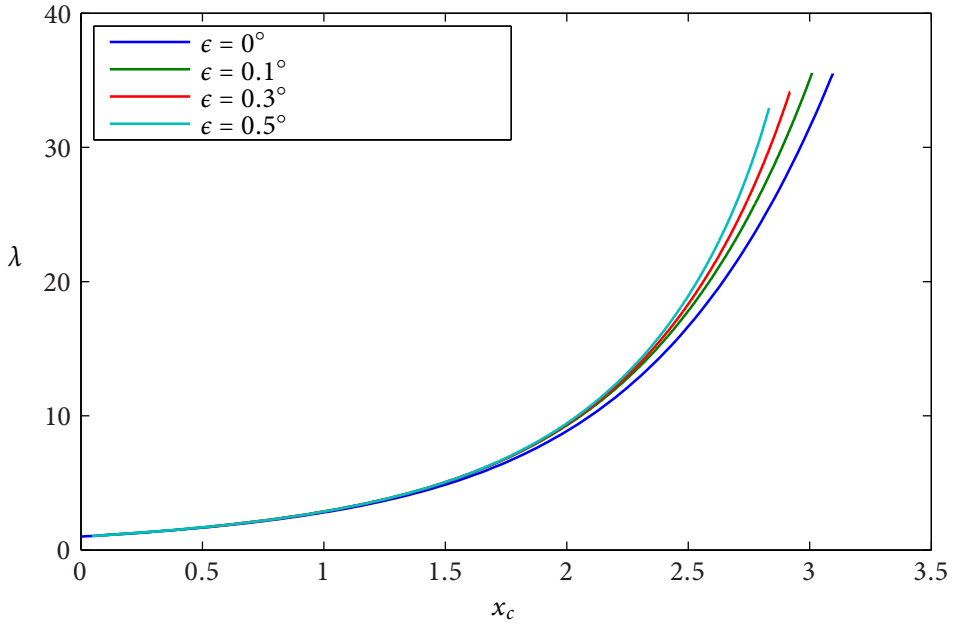

Figure 3.9: Comparison of numerical solutions to the linear problem (3.4) to solutions to the full nonlinear problem given by (3.1a) to (3.1d), (3.1g), (3.2) and (3.3) for $\epsilon = 0.1°$, $\epsilon = 0.3°$ and $\epsilon = 0.5°$. Each line stops when the free surface touches the rigid wall.

flow determined by the dock problem in the inner region, and the relationship between λ and x_c found by matching to the outer region. For small $|\lambda - 1|$, the solution of the leading order problem was found using Mellin transforms.

The linear equations (3.4c) and (3.4d) imply that Φ_y is discontinuous at the origin if $\lambda x_c \neq 0$, and so the first derivative of Φ has a logarithmic singularity at the origin. As a result, the linearisation given in section 3.2.3 fails when $\epsilon \log r = O(1)$. The same singularity is seen in the leading order approximation of flow past a thin sharp aerofoil (see Van Dyke [1975], pp 68-70). The size of the nonuniform region is exponentially small, and so unlikely to have any serious effect on the solution.

We can use the numerical method given by Billingham and King [2005] to compare the solution to the linear system (3.4) to the full problem given by (3.1a) to (3.1d), (3.1g), (3.2) and (3.3). Figure 3.9 shows good agreement with $\lambda(x_c)$ resulting from such a comparison.

As λ increases, the amplitude of the capillary waves in our solution grows. For sufficiently large λ, as shown in figure 3.5, the amplitude becomes so large that the capillary waves intersect with the position of the rigid wall, thus invalidating the solution. If the

'void' in figure 3.1 was replaced by a low density inviscid fluid, then mass conservation would be violated if the free surface touched the wall. Furthermore, if the free surface was close to the rigid wall, there would be a very fast flow in the slender low density region, which would influence the flow in the fat wedge.

King [1991] and Billingham [2006] considered the complementary problem to figure 3.1, with fluid occupying only the slender wedge. As $\epsilon \to 0$, they obtained a system that could be described by coupled nonlinear ODEs. For large λ, Billingham [2006] solved this system using Kuzmak's method for a nonlinear oscillator.

For the two fluid problem, with fluid of density ρ_1 inside the slender wedge and density ρ_2 in the fat wedge, a balance is obtained between the nonlinear system studied by King [1991], and the linear 2D problem in this chapter, when $\rho_1/\rho_2 = O(\epsilon)$. At leading order, this gives another half plane problem, but with the free surface equations (3.4b) and (3.4c) replaced by three coupled nonlinear ODEs for the free surface position H and the velocity potentials in the two fluids, which we will study in the next chapter.

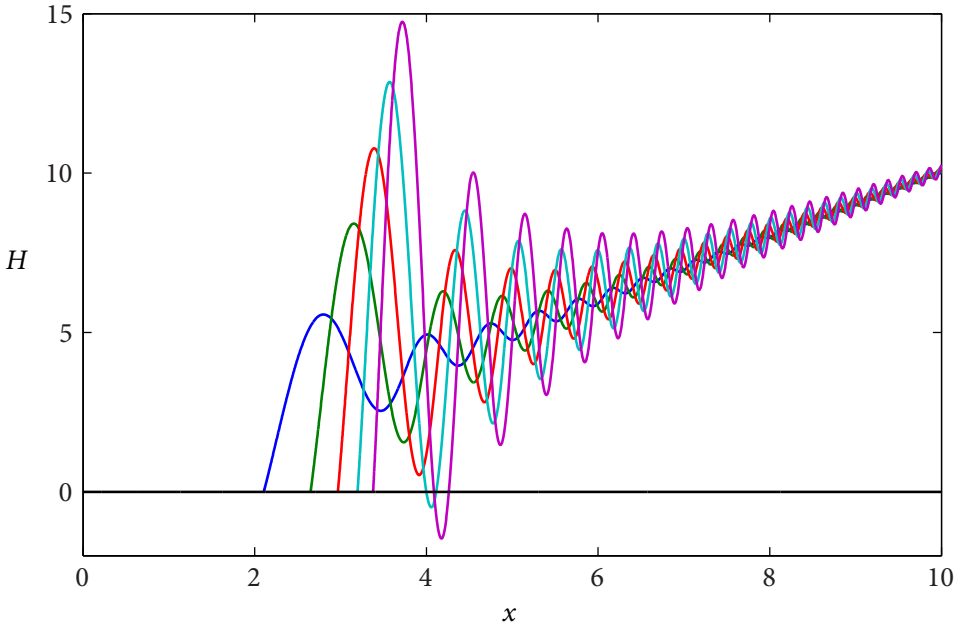

Figure 3.10: For $x_c > 3.01$, or $\lambda > 30$, the large-λ asymptotic solution for H for $\rho_1 = 0$ becomes non-physical, with the linearised interface height intersecting the rigid wall. The solutions shown here are for $\lambda = 10, 20, 30, 40, 50$, which correspond to $x_c = 2.1050, 2.6508, 2.9686, 3.1878, 3.3791$ respectively. In chapter 4 we consider the effect of allowing fluid 1 to have finite but low density. We find that this prevents pinch-off for finite λ.

Chapter 4

Two-fluid half-plane problem

For a fat wedge of inviscid fluid recoiling around a slender void, self-similar solutions are only available for a limited range of contact angle and wedge angle, due to large-amplitude capillary waves which causes the free surface to touch itself, pinching off immediately in the self-similar case. If the slender void is filled with a low density inviscid fluid, a rapid flow is driven in 'neck' regions as the free surface approaches pinch-off. In this chapter, we consider the same contact and wedge angle limits as in chapter 3, so that the flow domain for the fluid in the fat wedge can again be approximated by a half-plane, but seek solutions for a distinguished density ratio which maximises the interaction between flows in the slender and fat wedge. We find a rapidly-varying solution to this two-fluid problem by use of the method of multiple scales. On a fast scale, free surface deformations are determined by solutions to a nonlinear, nonlocal set of periodic oscillator equations. We also calculate secularity equations to determine how the oscillator equation parameters vary on the slow scale. These secularity equations are coupled to a non-homogenisable region near the contact point, where the non-periodic effects of the rigid wall must be taken fully into account.

4.1 Introduction

In chapter 3, we considered the case of a single inviscid fluid recoiling around a slender void. The initial contact angle $\pi - \epsilon$ was suddenly changed to $\pi - \lambda\epsilon$, and the fluid recoils accordingly. We found an asymptotic solution to this problem for the double limit $1 \ll \lambda \ll \epsilon^{-1}$. However, we found that these asymptotic solutions for the interface position would intersect with the position of the rigid wall for λ larger than about 30.

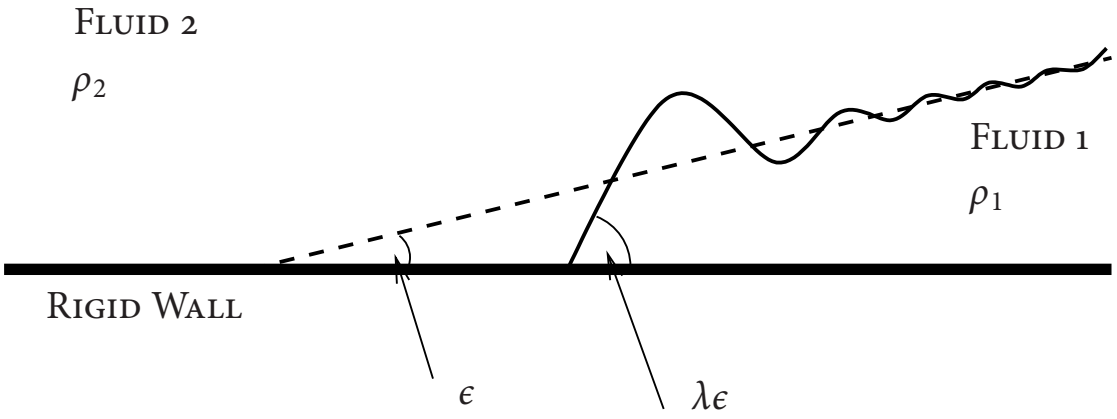

Figure 4.1: We consider the case $\epsilon \ll 1$, so that fluid 1 occupies a slender wedge, and fluid 2 occupies a fat wedge. We choose a distinguished density ratio, so that the flow in both fluids features in the leading order problem for $\epsilon \to 0$. We find that this corresponds to fluid 1 having a much smaller density than fluid 2, with $\rho_1/\rho_2 = O(\epsilon)$. We limit our analysis to moderate λ, so that $\lambda\epsilon \ll 1$.

We now consider filling the slender void with a low density inviscid fluid. As the interface starts to form necks near the rigid wall, then a flow occurs between the interface and the wall to satisfy mass conservation and self-similarity. The flow through these narrow necks is much faster than the two-dimensional flow in the fat wedge, and so the fluid in the slender wedge can have a significant effect on the interface with a much lower density than the fluid in the fat wedge.

For the case where the fluid in the fat wedge has zero density, Billingham [2006] has shown that solutions exist for all λ in $1 \ll \lambda \ll \epsilon^{-1}$. In the previous chapter, we showed that if the fluid in the slender wedge has zero density, pinchoff occurs at finite λ. In this chapter, we identify a distinguished density ratio, where $\rho_1/\rho_2 = O(\lambda\epsilon)$, in which the velocity potential in each fluid has a leading order effect on the interface position, and find that the highly oscillatory large-λ asymptotic solutions are valid for $\lambda \to \infty$ for this distinguished density ratio.

The two-fluid recoiling inviscid wedge problem can be uniquely described by the contact angle $\beta \equiv \lambda\epsilon$, the wedge angle ϵ and the density ratio ρ_1/ρ_2. Here we are interested in the case with $\epsilon \ll 1$, $\rho_1/\rho_2 = O(\epsilon)$ and $\lambda = O(1)$. Fluid 1 occupies an initially slender wedge of angle ϵ and has density ρ_1 (see figure 4.1). Fluid 2 occupies an initially fat wedge of angle $\pi - \epsilon$ and has density ρ_2. As $\epsilon \to 0$, we find on kinematic grounds that $\mathbf{u}_1 = O(1)$ and $\mathbf{u}_2 = O(\epsilon)$, so that a distinguished limit is obtained in the Bernoulli equation when

$\rho_1/\rho_2 = O(\epsilon)$.

In section 4.2, we derive self-similar equations for the nonlinear two-fluid problem. In section 4.3, we examine this system of equations in the limit $\epsilon \to 0$ with $\lambda = O(1)$ and derive a leading order system for the distinguished density ratio $\rho_1/\rho_2 = O(\epsilon)$. The leading order system consists of two nonlinear ODEs coupled to a linear PDE for the flow in the fat wedge, rather than a fully nonlinear free boundary problem. This system can be solved numerically, with the PDE reduced to an integral equation which can be solved numerically using a similar method to the previous chapter. We discuss the numerical solutions in section 4.4. The nonlinear ODEs are solved using a relaxation method, with parameter continuation used to obtain solutions to the more nonlinear parameter regimes. For large λ, necks appear in the solutions, which correspond to large gradients in the potential in the slender wedge.

We next consider the double limit $\epsilon \to 0$, $\lambda \to \infty$ with $\lambda\epsilon \ll 1$, in section 4.5. A scaling analysis of the leading order system for small ϵ, looking for a balance for large λ, suggested that the distinguished density ratio is $\rho_1/\rho_2 = O(\lambda\epsilon)$ in this double limit, *i.e.* when the density ratio is of the same order as the contact angle.

We use Kuzmak's method to find a solution to the leading order system arising from this double-distinguished density ratio. In section 4.5 we derive equations for the leading-order nonlinear nonlocal oscillator and secularity equations that describe the slow variation of the oscillator parameters. In section 4.6 we explore various properties of the oscillator equation solutions. In section 4.7 we find solutions to the secularity equations for different values of the distinguished density ratio η. We find that Kuzmak's method fails in an inner region near the contact point, where the free surface takes several wavelengths to adjust to the discontinuous imposition of the rigid wall boundary conditions. As the contact angle condition is given at the contact point, we find that we must solve a PDE to interpret the contact angle conditions as boundary conditions for the secularity equations. The numerical solution of this PDE is discussed in appendix A.

4.2 Full governing equations

4.2.1 Nonlinear interface equations

Surface tension provides a pressure difference across the interface proportional to curvature. By integrating the Euler equations, we obtain the Bernoulli equation, which holds along the interface $y = Y(x,t)$:

$$\rho_1\left(\frac{\partial\phi_1}{\partial t}+\frac{1}{2}\left|\nabla\phi_1\right|^2\right)-\rho_2\left(\frac{\partial\phi_2}{\partial t}+\frac{1}{2}\left|\nabla\phi_2\right|^2\right)=\sigma\kappa=\sigma\frac{Y_{xx}}{(1+Y_x^2)^{3/2}}. \tag{4.1}$$

Here ϕ_1 and ϕ_2 are the velocity potentials in the two fluids. Fluid 1 occupies the slender wedge and fluid 2 occupies the fat wedge, as shown in figure 4.1. In the bulk of the fluid, mass conservation gives $\nabla^2\phi_{1,2}=0$ in fluids 1 and 2 respectively.

The kinematic condition is that the normal velocity of a point $\mathbf{R}=(x,Y(x,t))$ on the boundary is equal to the normal velocity of the fluid on either side of the boundary. The unit normal directed into fluid 2 is

$$\mathbf{n}=\frac{(-Y_x,1)}{(1+Y_x^2)^{1/2}} \tag{4.2}$$

so the kinematic condition can be written as

$$\mathbf{n}\cdot\mathbf{R}_t=\frac{Y_t}{(1+Y_x^2)^{1/2}}=\mathbf{n}\cdot\nabla\phi_1=\mathbf{n}\cdot\nabla\phi_2, \tag{4.3}$$

or

$$\frac{\partial Y}{\partial t}=\frac{\partial\phi}{\partial y}-\frac{\partial\phi}{\partial x}\frac{\partial Y}{\partial x}. \tag{4.4}$$

At the contact point, we have

$$Y=0,\quad Y_x=\tan(\lambda\epsilon), \tag{4.5}$$

while

$$Y\sim x\tan\epsilon\quad\text{as}\quad x\to\infty. \tag{4.6}$$

There is no normal flow through the rigid wall, so

$$\frac{\partial\phi_1}{\partial y}(x,0)=0,\quad\text{for}\quad x>x_c, \tag{4.7}$$

and

$$\frac{\partial\phi_2}{\partial y}(x,0)=0,\quad\text{for}\quad x<x_c. \tag{4.8}$$

The far field conditions on $\phi_{1,2}$ are that $\phi_1\to 0$ as $|\mathbf{x}|\to\infty$ for $\mathbf{x}$ in fluid 1, and $\phi_2\to 0$ as $|\mathbf{x}|\to\infty$ for $\mathbf{x}$ in fluid 2.

4.2.2 Similarity solution

The only dimensional parameters in the problem are the surface tension coefficient σ and the fluid densities ρ_1 and ρ_2. We cannot construct a lengthscale from these two parameters alone. Instead, we must invoke time t since coalescence in order to obtain a lengthscale, hence the only solutions are similarity solutions.

We define

$$L = \left(\frac{\sigma}{\rho}\right)^{1/3} t^{2/3},$$

where ρ is some reference density to be chosen later. We nondimensionalise all lengths according to L, and so define the barred variables:

$$\bar{x} = x/L, \quad \bar{y} = y/L, \quad \bar{Y} = Y/L, \quad \bar{x}_c = x_c/L. \tag{4.9}$$

The velocity potential ϕ has dimensions L^2/t, so we define

$$\bar{\phi}_{1,2} = \frac{\rho^{2/3}}{t^{1/3}\sigma^{2/3}}\phi_{1,2}. \tag{4.10}$$

We choose axes so that the contact point is at $x = 0$, $y = 0$, so that the contact point equations (4.5) become

$$\bar{Y}(0) = 0, \quad \bar{Y}_{\bar{x}}(0) = \tan(\lambda\epsilon), \tag{4.11}$$

while the far-field equation (4.6) becomes

$$\bar{Y} \sim (\bar{x} + \bar{x}_c)\tan\epsilon \quad \text{as} \quad \bar{x} \to \infty \tag{4.12}$$

and the rigid wall conditions (4.7) and (4.8) become

$$\frac{\partial\bar{\phi}_1}{\partial\bar{y}}(\bar{x}, 0) = 0, \quad \text{for} \quad \bar{x} > 0 \tag{4.13}$$

and

$$\frac{\partial\bar{\phi}_2}{\partial\bar{y}}(\bar{x}, 0) = 0, \quad \text{for} \quad \bar{x} < 0 \tag{4.14}$$

respectively.

In similarity variables, the Bernoulli equation becomes

$$\begin{aligned}\frac{\rho_1}{\rho}\left[\frac{1}{3}\bar{\phi}_1 - \frac{2}{3}\left((\bar{x}+\bar{x}_c)\frac{\partial\bar{\phi}_1}{\partial\bar{x}} + \bar{y}\frac{\partial\bar{\phi}_1}{\partial\bar{y}}\right) + \frac{1}{2}\left(\frac{\partial\bar{\phi}_1}{\partial\bar{x}}\right)^2 + \frac{1}{2}\left(\frac{\partial\bar{\phi}_1}{\partial\bar{y}}\right)^2\right] \\ -\frac{\rho_2}{\rho}\left[\frac{1}{3}\bar{\phi}_2 - \frac{2}{3}\left((\bar{x}+\bar{x}_c)\frac{\partial\bar{\phi}_2}{\partial\bar{x}} + \bar{y}\frac{\partial\bar{\phi}_2}{\partial\bar{y}}\right) + \frac{1}{2}\left(\frac{\partial\bar{\phi}_2}{\partial\bar{x}}\right)^2 + \frac{1}{2}\left(\frac{\partial\bar{\phi}_2}{\partial\bar{y}}\right)^2\right] \\ = \frac{Y_{\bar{x}\bar{x}}}{(1+Y_{\bar{x}}^2)^{3/2}}\end{aligned} \tag{4.15}$$

and the kinematic boundary conditions become

$$\frac{2}{3}(\bar{x}+\bar{x}_c)\bar{Y}_{\bar{x}} - \frac{2}{3}\bar{Y} = \bar{Y}_{\bar{x}}\frac{\partial\bar{\phi}_1}{\partial\bar{x}} - \frac{\partial\bar{\phi}_1}{\partial\bar{y}} = \bar{Y}_{\bar{x}}\frac{\partial\bar{\phi}_2}{\partial\bar{x}} - \frac{\partial\bar{\phi}_2}{\partial\bar{y}}, \tag{4.16}$$

which both hold on the free surface, so $(\bar{x},\bar{y}) = (\bar{x},\bar{Y}(\bar{x}))$.

4.3 Leading order half-plane problem for $\epsilon \ll 1$

4.3.1 Distinguished density ratio

The flows in the two fluids behave differently as $\epsilon \to 0$. This can be observed in the interpretation of the kinematic condition in the two fluids at the contact point itself. In the slender wedge, the angle between the wall and the free surface is very small, so the flow is predominantly in the $\bar{x}$-direction, and we require

$$\frac{\partial\bar{\phi}_1}{\partial\bar{y}}(0,0) = 0, \qquad \frac{\partial\bar{\phi}_1}{\partial\bar{x}}(0,0) = \frac{2}{3}\bar{x}_c. \tag{4.17}$$

In the fat wedge, $\bar{\phi}_{2\bar{x}}$ and $\bar{\phi}_{2\bar{y}}$ are of strictly comparable size, while $\bar{Y}_{\bar{x}} = O(\epsilon)$ at the contact point, thus

$$\frac{\partial\bar{\phi}_2}{\partial\bar{y}}(0,0) = -\frac{2}{3}\bar{x}_c\tan\lambda\epsilon = O(\bar{x}_c\epsilon), \qquad \frac{\partial\bar{\phi}_2}{\partial\bar{x}}(0,0) = O(\bar{x}_c\epsilon). \tag{4.18}$$

Regardless of the scalings for x_c and the lengthscale for variations in x, we find the horizontal velocities in the slender wedge are $O(\epsilon^{-1})$ times larger than in the fat wedge as $\epsilon \to 0$ with λ fixed.

The relative contributions to the Bernoulli equation (4.15) at the contact point $\bar{x} = 0$ from $\bar{\phi}_1$ and $\bar{\phi}_2$ respectively have magnitude

$$\rho_1\bar{\phi}_1 = O(\rho_1\bar{x}_c^2), \quad \rho_2\bar{\phi}_2 = O(\rho_2\epsilon\bar{x}_c^2). \tag{4.19}$$

and so the distinguished density ratio as $\epsilon \to 0$ with $\lambda = O(1)$ is $\rho_1/\rho_2 = O(\epsilon)$.

4.3.2 Derivation of leading order problem

We now define

$$\rho_1 = \epsilon k \rho, \quad \rho_2 = \rho, \tag{4.20}$$

where ρ is the reference density used in nondimensionalisation. Then the Bernoulli and kinematic conditions become

$$\begin{aligned} \epsilon k \left[\frac{1}{3}\bar{\phi}_1 - \frac{2}{3}\left((\bar{x} + \bar{x}_c)\frac{\partial \bar{\phi}_1}{\partial \bar{x}} + \bar{y}\frac{\partial \bar{\phi}_1}{\partial \bar{y}} \right) + \frac{1}{2}\left(\frac{\partial \bar{\phi}_1}{\partial \bar{x}} \right)^2 + \frac{1}{2}\left(\frac{\partial \bar{\phi}_1}{\partial \bar{y}} \right)^2 \right] \\ - \left[\frac{1}{3}\bar{\phi}_2 - \frac{2}{3}\left((\bar{x} + \bar{x}_c)\frac{\partial \bar{\phi}_2}{\partial \bar{x}} + \bar{y}\frac{\partial \bar{\phi}_2}{\partial \bar{y}} \right) + \frac{1}{2}\left(\frac{\partial \bar{\phi}_2}{\partial \bar{x}} \right)^2 + \frac{1}{2}\left(\frac{\partial \bar{\phi}_2}{\partial \bar{y}} \right)^2 \right] \\ = \frac{Y_{\bar{x}\bar{x}}}{(1 + Y_{\bar{x}}^2)^{3/2}} \end{aligned} \tag{4.21}$$

and

$$\frac{2}{3}(\bar{x} + \bar{x}_c)\bar{Y}_{\bar{x}} - \frac{2}{3}\bar{Y} = \bar{Y}_{\bar{x}}\frac{\partial \bar{\phi}_1}{\partial \bar{x}} - \frac{\partial \bar{\phi}_1}{\partial \bar{y}} = \bar{Y}_{\bar{x}}\frac{\partial \bar{\phi}_2}{\partial \bar{x}} - \frac{\partial \bar{\phi}_2}{\partial \bar{y}}, \tag{4.22}$$

both of which apply on $\bar{y} = \bar{Y}(\bar{x})$.

The condition $\bar{Y}_{\bar{x}}(0) = \tan \lambda\epsilon$ gives $\bar{Y} = O(\epsilon \bar{x}_c)$. Then (4.22), evaluated at the contact point, gives $\bar{\phi}_1 = O(\bar{x}_c^2)$ and $\bar{\phi}_2 = O(\epsilon \bar{x}_c^2)$. Finally, (4.21) evaluated at the contact point gives $\bar{x}_c = O(1)$ as $\epsilon \to 0$.

We therefore rescale $\bar{Y}$ and $\bar{\phi}_1$ and $\bar{\phi}_2$ according to

$$\bar{Y} = \epsilon H, \quad \bar{\phi}_1 = \phi_1, \quad \bar{\phi}_2 = \epsilon \Phi. \tag{4.23}$$

The scales for $\bar{x}$ and $\bar{y}$ variation are unchanged as $\epsilon \to 0$, so we let $\bar{x} = x$, $\bar{y} = y$ and $\bar{x}_c = x_c$.

At leading order we can reduce the equations on $\phi_1(x, y)$ to ODEs. We currently have

$$\begin{aligned} \nabla^2 \phi_1 = 0 \quad &\text{in} \quad 0 < y < \epsilon H(x) \quad \text{for} \quad x > 0, \\ \frac{\partial \phi_1}{\partial y} = 0 \quad &\text{on} \quad y = 0 \quad \text{for} \quad x > 0. \end{aligned} \tag{4.24}$$

We now rescale to the height of the wedge by writing $y = \epsilon \hat{y}$. Then ϕ_1 satisfies

$$\begin{aligned} \frac{\partial^2 \phi_1}{\partial x^2} + \frac{1}{\epsilon^2}\frac{\partial^2 \phi_1}{\partial \hat{y}^2} = 0 \quad &\text{in} \quad 0 < \hat{y} < H(x) \quad \text{for} \quad x > 0, \\ \frac{\partial \phi_1}{\partial \hat{y}} = 0 \quad &\text{on} \quad \hat{y} = 0 \quad \text{for} \quad x > 0. \end{aligned} \tag{4.25}$$

Expanding ϕ_1 in powers of ϵ, we find that

$$\phi_1 = P(x) + \epsilon B(x) + \epsilon^2 \left[C(x) - \frac{\hat{y}^2}{2} P''(x) \right] + O(\epsilon^3), \tag{4.26}$$

so that at leading order,

$$\phi_1(x, \epsilon H(x)) = P(x), \qquad \frac{\partial \phi_1}{\partial y}(x, \epsilon H(x)) = -\epsilon H(x) P''(x). \tag{4.27}$$

Substituting (4.27) and (4.23) into (4.21) and (4.22), we obtain the leading order equations

$$k \left[\frac{1}{3} P - \frac{2}{3}(x + x_c) P_x + \frac{1}{2} P_x^2 \right] - \left[\frac{1}{3} \Phi - \frac{2}{3}(x + x_c) \Phi_x \right] = H_{xx} \tag{4.28}$$

and

$$\frac{2}{3}(x + x_c) H_x - \frac{2}{3} H = (H P_x)_x = -\Phi_y, \tag{4.29}$$

to be applied on the half line $x > 0$, $y = 0$.

4.3.3 Summary of two-fluid half-plane problem

At leading order in ϵ we have a half plane problem, with the equations (4.28) and (4.29) to be applied on the half line $x > 0$, $y = 0$. We want to find solutions for given values of the contact angle parameter λ and the density ratio k. The functions to be determined are the velocity potential in the fat wedge, $\Phi(x, y)$, for $-\infty \le x \le \infty$, $y > 0$, the interface height $H(x)$ for $x > 0$, and the leading-order velocity potential in the slender wedge $P(x)$ for $x > 0$. We must also solve for the eigenvalue x_c, which is the contact point displacement.

This problem can be summarised as follows:

$$\nabla^2 \Phi = 0 \quad \text{for} \quad y > 0, \tag{4.30}$$

$$\Phi_y(x, 0) = \begin{cases} \frac{2}{3} H - \frac{2}{3}(x + x_c) H_x & \text{on } x > 0, \\ 0 & \text{on } x < 0, \end{cases} \tag{4.31}$$

with

$$k \left[\frac{1}{3} P - \frac{2}{3}(x + x_c) P_x + \frac{1}{2} P_x^2 \right] - \left[\frac{1}{3} \Phi(x, 0) - \frac{2}{3}(x + x_c) \Phi_x(x, 0) \right] = H_{xx} \tag{4.32}$$

and

$$\frac{2}{3}(x + x_c) H_x - \frac{2}{3} H = (H P_x)_x. \tag{4.33}$$

Equations (4.32) and (4.33) each hold on $x > 0$, $y = 0$.

The boundary conditions at the contact point are that

$$H(0) = 0, \quad \text{and} \quad H_x(0) = \lambda \tag{4.34}$$

while in the far field,

$$H \to x + x_c, \quad P \to 0, \quad \Phi \to 0 \quad \text{as} \quad x \to \infty. \tag{4.35}$$

As shown in section 3.3.1, equations (4.30) and (4.31) are equivalent to

$$\Phi(x,0) = \frac{2}{3\pi} \int_0^\infty \log|x - x'| \{H(x') - (x' + x_c) H_x(x')\} dx'. \tag{4.36}$$

We can also derive the kinematic equation for $P(x)$ (4.33) and the integral equation (4.36) from the integral equations for the nonlinear free-boundary problem. This derivation is discussed in appendix B.

4.4 Numerical solution to half-plane problem

We need to solve for $H(x)$, $P(x)$ and $\Phi(x)$ for $x > 0$, and for the eigenvalue x_c. These are related by two ODEs:

$$k\left[\frac{1}{3}P - \frac{2}{3}(x + x_c)P_x + \frac{1}{2}P_x^2\right] - \left[\frac{1}{3}\Phi - \frac{2}{3}(x + x_c)\Phi_x\right] = H_{xx} \tag{4.37}$$

and

$$\frac{2}{3}(x + x_c)H_x - \frac{2}{3}H = (HP_x)_x, \tag{4.38}$$

and the integral equation

$$\Phi(x) = \frac{2}{3\pi} \int_0^\infty \log|x - x'| \{H(x') - (x' + x_c) H_x(x')\} dx'. \tag{4.39}$$

These are subject to the boundary conditions (4.34) and (4.35).

This is a nonlinear system with two independent parameters: the density parameter k and the contact angle parameter λ. In chapter 3, we had $k = 0$, and found that by fixing x_c and allowing λ to vary, we obtained a linear system that could be solved using one Newton iteration. However, if $k \neq 0$, the system is always nonlinear, and so there is no advantage in fixing x_c rather than λ. In the next section, we find that a distinguished density ratio occurs if $k = O(\lambda)$ as $\lambda \to \infty$, and so we obtain solutions comparable to

the asymptotic solutions by continuation in the independent parameters μ and λ, where $k = \mu\lambda$. Equation (4.39), which describes Φ, is nonlocal. Since (4.37) depends on Φ, this nonlocal coupling means we cannot solve the ODE boundary value problem in (4.37) and (4.38) by shooting forward from $x = 0$. Instead we use finite difference formulae to rewrite the ODEs and integral equation as nonlinear algebraic equations involving H, P and Φ at fixed grid points. We then solve this using Newton iteration.

To obtain a numerically tractable BVP, we truncate the upper limit of the integral in (4.39) to $x' = x_T$, and also apply the boundary conditions (4.35) at $x = x_T$. Use of non-uniform grid spacing allows us to obtain good resolution in regions of high curvature, while also reaching a reasonable truncation point given constraints on the total number of grid points.

We use three-point centered finite difference formulae to discretise (4.37) and (4.38), and so the discretisation error for these ODEs is $O(h^2)$. The integral equation (4.39) is discretised by assuming that the term $H-(x+x_c)H_x$ in (4.39) varies linearly between grid points and then calculating the logarithmic integrals analytically, thus avoiding numerical errors due to the logarithmic singularity in kernel of the integral. We note that (4.39) gives Φ as a linear function of H and x_c, and so we can reduce the size of the matrix equation by replacing Φ in (4.37) by $M \cdot H$, where M is a dense matrix that depends on the grid for x and varies linearly on x_c, but is independent of H. We must recalculate M whenever a new grid is chosen.

Once we have formulated the discretised boundary value problem, we obtain solutions by continuation in λ, starting from the configuration with $\lambda = 1$ and $x_c = 0$, where $H = x$ and $P = \Phi = 0$ is a solution. We note (e.g. in figure 4.2(a)) that as λ increases, the solutions for H start to form neck regions in which the curvature H_{xx} is large. We therefore concentrate grid points in these neck regions, but the need to recalculate the dense matrix M represents a significant penalty for grid redistribution.

There are two main sources of error for this numerical solution; the use of finite grid spacing h in formulating the discretised version of the ODEs and integral equation, and the use of a finite truncation point x_T. We can check the rate of solution convergence with respect to these discretisation parameters. For both uniform and non-uniform grids, we find that the eigenvalue x_c and the scalar solution measures $P(0)$ and $\Phi(0)$ converge

as $O(N^{-\alpha})$ as the total number of points N is varied, where $\alpha \approx 1.9$, which is consistent with the prediction of $O(h^2)$ accuracy for a fixed value of x_T.

In order to test the solution sensitivity to the truncation value x_T, we can add extra points to the end of an existing grid. Solutions to the two versions of the single fluid problem feature capillary waves which grow in frequency and decay in amplitude as x increases. We expect similar behaviour here, and so cannot resolve waves out to infinity. If waves are resolved to our truncation point, the position of the truncation point within a wavelength will have a significant effect on our results. Instead we suppress the effect of the capillary waves for large x by taking increasing grid spacing as x increases. This forces the numerical calculated waves to decay more rapidly in amplitude for large x, as shown in figure 3.5 for the single-fluid problem studied in chapter 3. For the two-fluid problem, we find numerically that when $k = 5$ and $\lambda = 5$, the solution eigenvalue x_c converges as $O(x_T^{-2.2})$. The velocity potential values $P(0)$ and $\Phi(0)$ are found to converge as $O(x_T^{-0.96})$. The Bernoulli equation is unaffected by adding a constant to P and Φ if the linear combination $kP - \Phi$ is preserved. As the values of P and Φ otherwise only occur in the boundary conditions (4.35), the convergence rate of $P(0)$ and $\Phi(0)$ may be slower than other solution measures. The solutions shown in the following figures are for $x_T = 50$.

Figures 4.2(a) and 4.2(b) show solutions for the interface position $H(x)$ for $k = 1$ and $k = \lambda$ respectively. Both these solutions and the solutions for $k = 0$, shown in figure 3.10, feature large amplitude capillary waves. As λ increases, the amplitude of these capillary waves increases. However, the solutions for $k = 0$ become negative and intersect with the rigid wall for large λ, while the solutions for $k = 1$ and $k = \mu\lambda$ never make contact with the wall, but instead approach the wall in a number of neck regions, where the interface is highly curved. Figure 4.3(a) shows the height of the first neck region as a function of λ for a selection of density ratios. We see that $k = 0$ is the only density ratio for which the interface intersects the rigid wall. Figure 4.3(b) shows the magnitude of H as a function of λ.

Figure 4.4 shows the velocity potential functions $P(x)$ and $\Phi(x, 0)$ corresponding to the solution for $\lambda = 50$ shown in figure 4.2(b). We observe that $\Phi(x, 0)$ shows large amplitude capillary waves, as do the solutions for $k = 0$ shown in figure 3.3. There is an

upward shift in the mean of Φ near $x = 0$, which will also emerge in the composite solution for Φ for large λ. The numerical solution for $P(x)$ shows small amplitude oscillations about a slowly varying mean. We find that P_x becomes large and negative as the interface height $H(x)$ approaches zero.

Figure 4.5 shows the contact point position x_c as a function of λ for various density ratios. We find that solutions for $k = O(1)$ and $k = O(\lambda)$ exhibit a different scaling for $\lambda \to \infty$ than the solution for $k = 0$ does. We found in chapter 3 that $x_c = O(\lambda^{2/9})$ for large λ when $k = 0$. In section 4.5 we analyse the two-fluid problem for large-λ and find $x_c = O(\lambda^{1/3})$ for finite density ratio.

Finally, figure 4.6 shows λ/x_c^3 and $P(0)/x_c^2$ for various λ as a function of the parameter η, defined by $\lambda/\eta = \rho_1/\rho_2$. The values λ/x_c^3 and $P(0)/x_c^2$ are eigenvalues for the large λ asymptotic analysis, and should tend to a constant, which depends on η, as $\lambda \to \infty$. Figure 4.6 also shows these eigenvalues as predicted by the large λ solution.

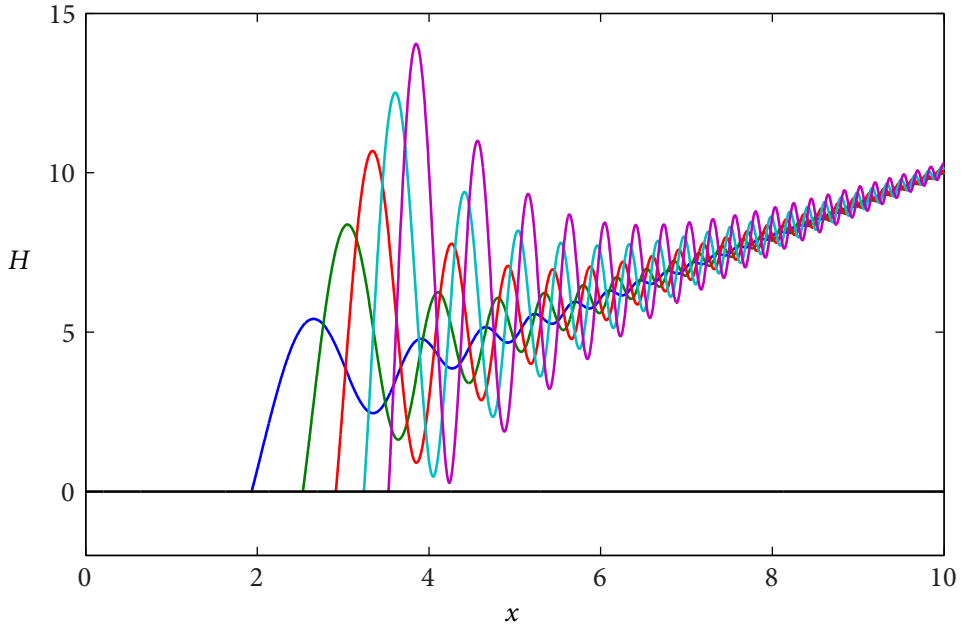

(a) Interface positions $H(x)$ for $\lambda = 10, 20, 30, 40, 50$, with $k = 1$.

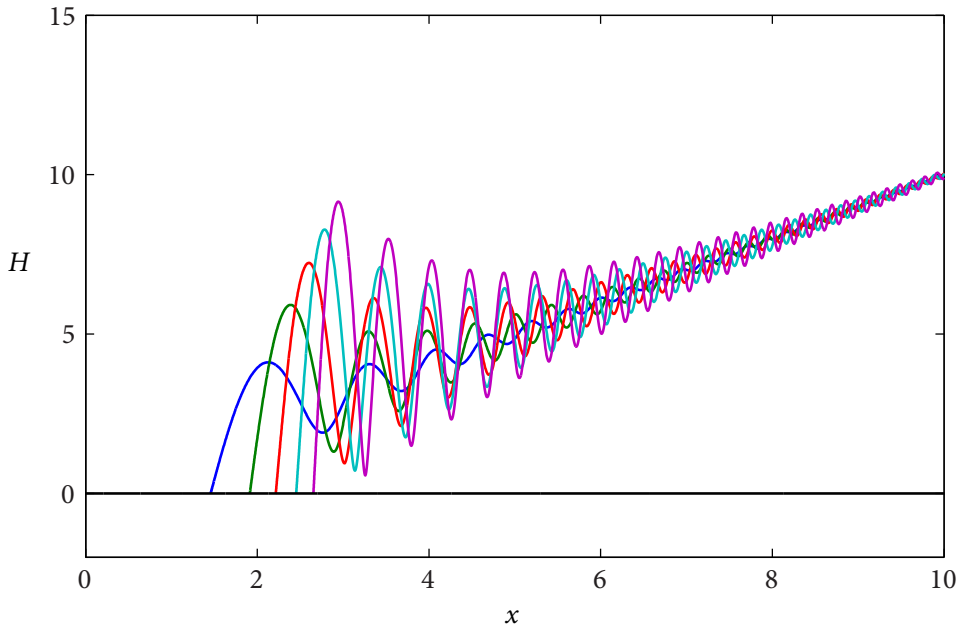

(b) Interface positions $H(x)$ for $\lambda = 10, 20, 30, 40, 50$, with $k = \mu\lambda$, $\mu = 1$.

Figure 4.2: Solutions to the two-fluid half-plane-problem. In both cases, x_c is a strictly increasing function of λ. Comparing these plots to figure 3.10, we see that for both cases the low density fluid in the slender wedge prevents the free surface position pinching-off for finite λ. The contact-point position and the height of the first maximum of H in (a) is similar to figure 3.10 for $k = 0$, but the solution for $k = \lambda$ shown in (b) appears to have a different scaling.

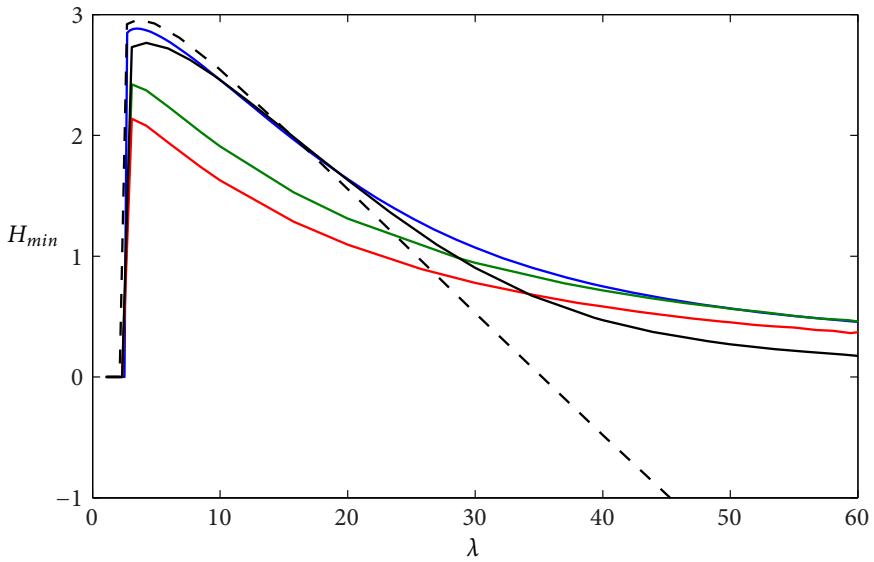

(a) Height of first minimum of H

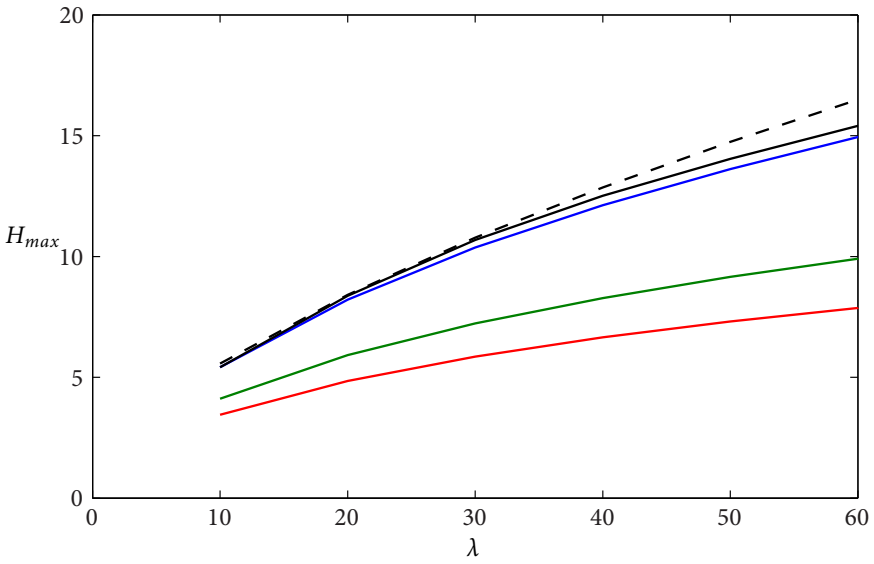

(b) Height of first maximum of H

Figure 4.3: The heights of the first local maxima and minima for H as a function of λ. The density ratios shown are: $k = 0$ (black dashed line), $k = 1$ (black solid line), and $k = \mu\lambda$ with $\mu = 0.1$ (blue), $\mu = 1$ (green) and $\mu = 2$ (red). Specific interface shapes can be seen for $k = 0$ in figure 3.10, for $k = 1$ in figure 4.2(a) and for $\mu = 1$ in figure 4.2(b).

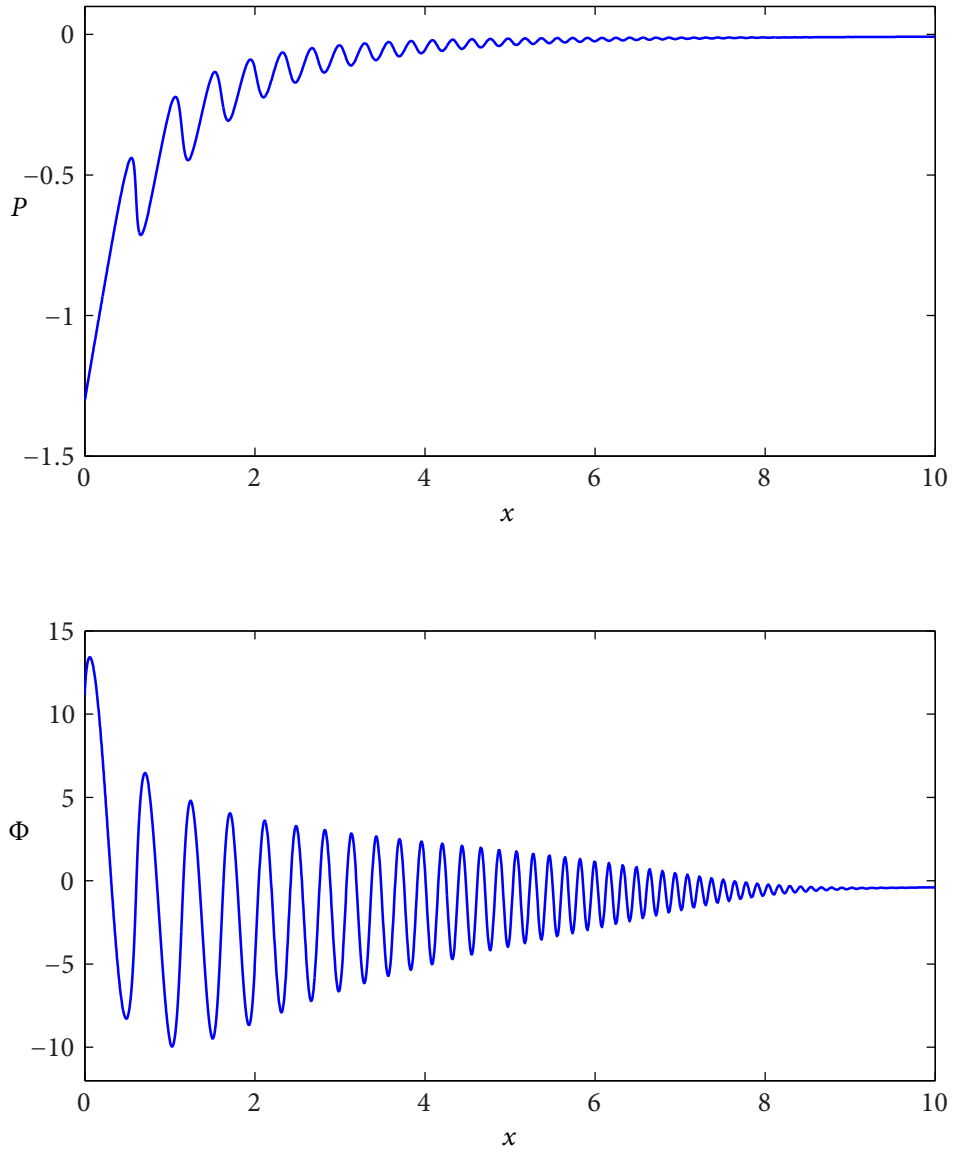

Figure 4.4: The velocity potential in fluid 1 is $P(x)$ and in fluid 2 is $\epsilon\Phi(x,0)$, where P and Φ are found by solving the system (4.37) to (4.39). The solutions shown are for $k = \lambda$, $\lambda = 50$, which corresponds to the magenta plot of H in figure 4.2(b).

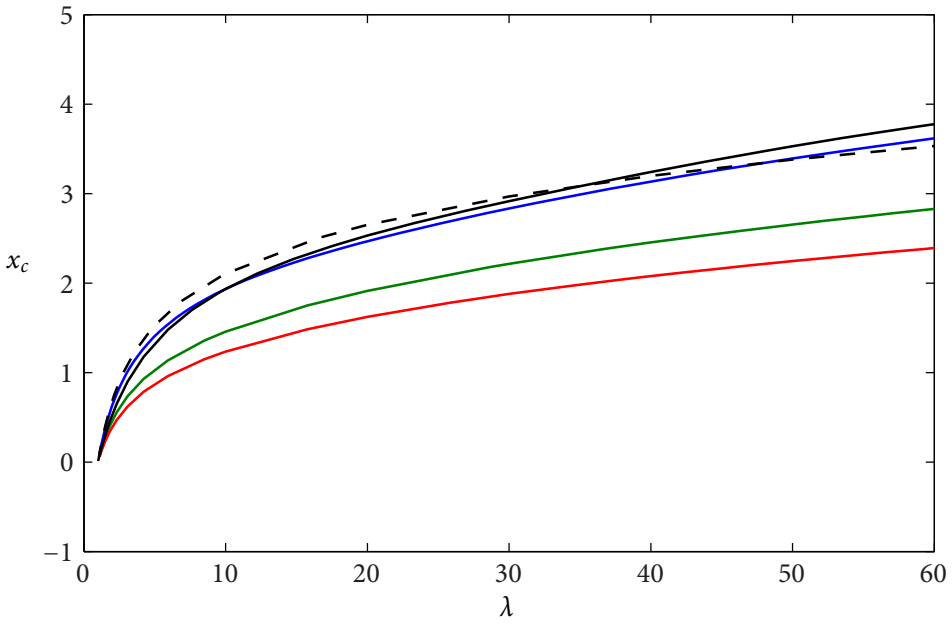

Figure 4.5: The contact point position x_c as a function of λ for various density ratios in the two-fluid problem. The density ratios shown are: $k = 0$ (black dashed line), $k = 1$ (black solid line), and $k = \mu\lambda$ with $\mu = 0.1$ (blue), $\mu = 1$ (green) and $\mu = 2$ (red).

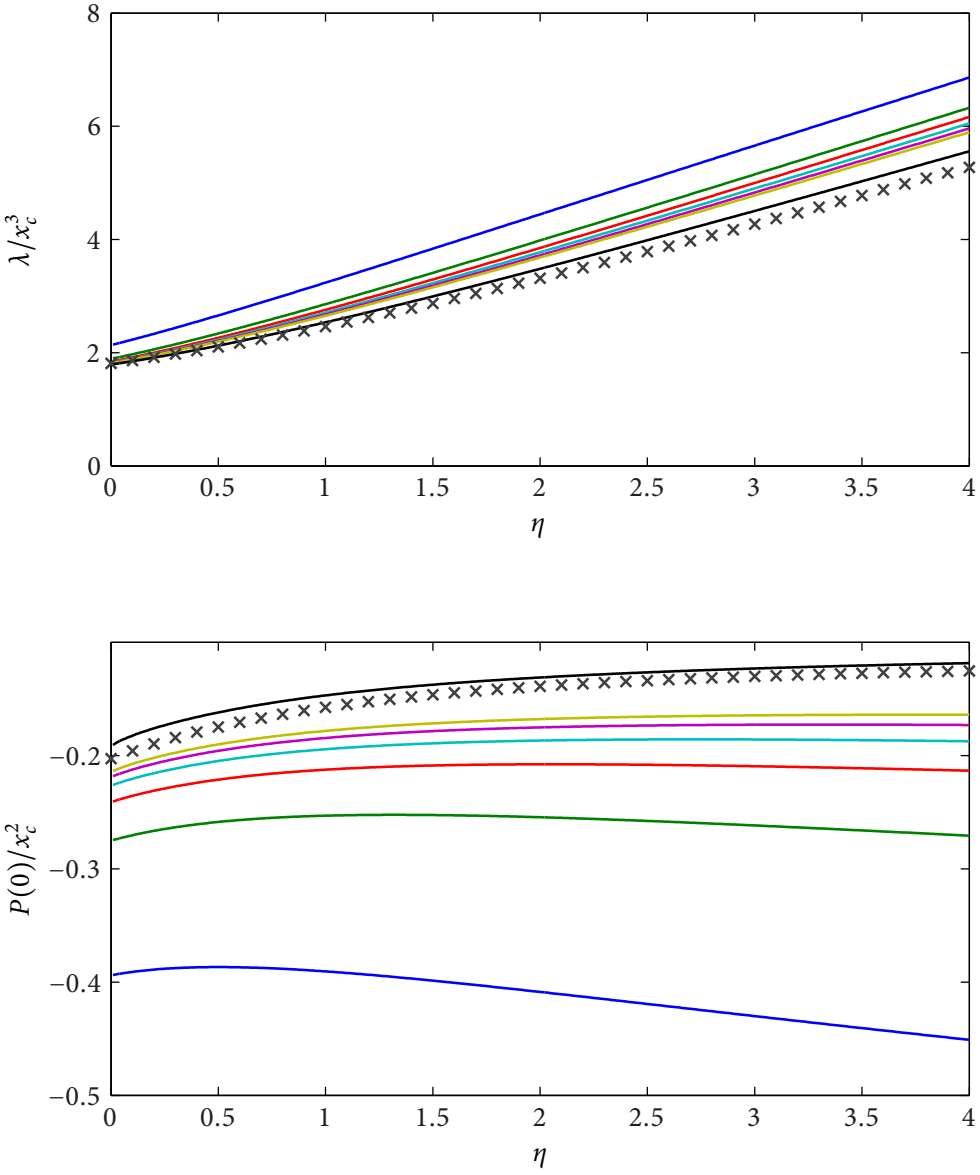

Figure 4.6: The eigenvalues λ^* and $\bar{P}(0)$ are shown with black crosses for secularity solutions, using the 'gold' function from figure 4.13 for $\tilde{\omega}(\sigma)$ The sequence blue to gold shows solutions to the two-fluid half-plane problem for $\lambda = 10, 20, 30, 40, 50, 60$. The asymptotic solution for large λ in section 4.5 predicts that $\lambda = O(x_c^3)$ and $P(0) = O(x_c^2)$ as $\lambda \to \infty$. The expansion is in whole powers of the small parameter $\epsilon \equiv x_c^{-3}$, so we expect $\lambda/x_c^3 \to \lambda^*(\eta) + O(\lambda^{-1})$, and $P(0)/x_c^3 \to \bar{P}(0,\eta) + O(\lambda^{-1})$, both as $\lambda \to \infty$. Richardson extrapolation confirms the error of these quantities as $O(\lambda^{-1})$. The black line shows the extrapolation for $\lambda = \infty$ based on the half-plane-problem calculations for $\lambda = 50$ and $\lambda = 60$.

4.5 Asymptotic solution for large x_c using Kuzmak's method

4.5.1 Scaling and trial expansions

We would like to find an asymptotic solution to the system described in section 4.3.3, for large λ and for general density ratio k. We already have asymptotic solutions for $k = 0$ (chapter 3) and for $k = \infty$ [Billingham, 2006]. In this chapter, we seek an asymptotic solution for a distinguished ratio k which maximises the interaction between the two fluids in the limit $1 \ll \lambda \ll \epsilon^{-1}$.

The numerical solutions to the half-plane-problem indicate that as λ increases, H, P and Φ exhibit large-amplitude, high-frequency oscillations on the free surface, with a slowly varying mean and amplitude of these waves. We therefore look for a multiple-scales solution, with variation over a slow and fast lengthscale. This is consistent with the analysis of Billingham [2006] and also of chapter 3, where we found wavelength $x = O(x_c^{-2})$ and slow variation on the lengthscale $x = O(x_c)$.

From the kinematic condition (4.33) evaluated at $x = 0$, we know $P_x = O(x_c)$ and $\Phi_x = O(x_c\lambda)$. In order for P_x and Φ_x to balance in (4.32) at the contact point, we need $k = O(\lambda)$. We therefore redefine the density ratio:

$$k = \mu\lambda, \tag{4.40}$$

and consider solutions with $\mu = O(1)$ as $\lambda \to \infty$.

As in the analysis for $k = 0$, we choose $\hat{\epsilon} = x_c^{-3}$ as our small parameter. We rescale the system given in section 4.3.3 by writing

$$H = \frac{\lambda}{x_c^2}\hat{H}, \quad \Phi = \frac{\lambda}{x_c}\hat{\Phi}, \quad P = x_c^2\hat{P}. \tag{4.41}$$

This scaling corresponds to oscillations in H, P and Φ having wavelength $O(x_c^{-2})$ near $x = 0$. This gives the short lengthscale for the solution. The leading order equations are nonlinear, so the wavelength of each capillary wave may depend on its amplitude. We therefore use an analysis based on Kuzmak's method, which is a variation of the method of multiple scales for nonlinear oscillators, where the wavelength is scaled to 1 by use of a free parameter. We also expect variation on a slower lengthscale, where $x = O(x_c)$. To use Kuzmak's method, we define two lengthscales in the x direction,

$$X = x/x_c, \qquad \hat{x} = \hat{\epsilon}^{-1}\theta_1(X, Y) + p(X, Y), \tag{4.42}$$

and corresponding lengthscales in the y direction,

$$Y = y/x_c, \qquad \hat{y} = \hat{\epsilon}^{-1}\theta_2(X, Y) + q(X, Y). \tag{4.43}$$

The functions θ_1 and θ_2 should be chosen so that the wavelength of the oscillations in $\hat{x}$ and $\hat{y}$ is exactly 1.

We now consider how the functions θ_1 and θ_2 are related. In chapter 3, the equations were linear, so we could consider capillary waves in Φ as the real part of a function of $X + iY$, with analytic continuation used to determine Φ away from the positive X-axis where it was initially calculated. The equations here are nonlinear, so we cannot simply take real parts, but would like to take advantage of the algebraic simplifications offered by considering Φ as a function of a single variable $X + iY$.

For this large-λ analysis, we will assume that the map $(X, Y) \to (\hat{x}, \hat{y})$ is conformal. Then there are no cross derivative terms between x and y in the expansion of Laplace's equation in $\hat{x}$, $\hat{y}$, X and Y. Under the assumption of conformal mapping, the functions $\theta_1 + i\theta_2$ and $p + iq$ are both analytic functions of $X + iY$, and hence obey the Cauchy-Riemann equations:

$$\theta_{1X} = \theta_{2Y} = \omega(X, Y), \qquad \theta_{2X} = -\theta_{1Y} = \Omega(X, Y), \tag{4.44}$$

$$p_X = q_Y, \qquad p_Y = -q_X. \tag{4.45}$$

We gain a further constraint by requiring that $Y = 0$ coincides with $\hat{y} = 0$, so that the free surface occupies the positive $\hat{x}$-axis and positive X-axis. We therefore have $\theta_2(X, 0) = 0$ and $q(X, 0) = 0$, and so on the free surface, where $\hat{x} > 0$ and $\hat{y} = 0$, we find that $\Omega = 0$ and $p_Y = -q_X = 0$.

We treat $\hat{\Phi}$ as a function of the four independent variables X, Y, $\hat{x}$, $\hat{y}$, and $\hat{H}$ and $\hat{P}$ as functions of $\hat{x}$ and X, though we will shortly find that $\hat{P}$ is independent of $\hat{x}$ at leading order. The term $x + x_c$ which appears in (4.31), (4.32), (4.33) and (4.35) is written in terms of the slow variable X, so $x + x_c = (1 + X)x_c$. We expand in integer powers of $\hat{\epsilon}$, writing

$$\hat{H} = \hat{H}_0(\hat{x}, X) + \hat{\epsilon}\hat{H}_1(\hat{x}, X) + O(\hat{\epsilon}^2), \tag{4.46}$$

$$\hat{P} = \bar{P}(X, \hat{x}) + \hat{\epsilon}\hat{P}_0(\hat{x}, X) + \hat{\epsilon}^2\hat{P}_1(\hat{x}, X) + O(\hat{\epsilon}^3), \tag{4.47}$$

$$\hat{\Phi} = \hat{\bar{\Phi}}_0(\hat{x}, \hat{y}, X, Y) + \hat{\epsilon}\hat{\Phi}_1(\hat{x}, \hat{y}, X, Y) + O(\hat{\epsilon}^2). \tag{4.48}$$

Derivatives with respect to x and y become

$$\frac{\partial}{\partial x} = \frac{1}{x_c}\left[\frac{\partial}{\partial X} + (\hat{\epsilon}^{-1}\omega + p_X)\frac{\partial}{\partial \hat{x}} + (\hat{\epsilon}^{-1}\Omega + q_X)\frac{\partial}{\partial \hat{y}}\right] \tag{4.49}$$

and

$$\frac{\partial}{\partial y} = \frac{1}{x_c}\left[\frac{\partial}{\partial Y} + (-\hat{\epsilon}^{-1}\Omega + p_Y)\frac{\partial}{\partial \hat{x}} + (\hat{\epsilon}^{-1}\omega + q_Y)\frac{\partial}{\partial \hat{y}}\right] \tag{4.50}$$

respectively. On the free surface, we have $\Omega = 0$ and $p_Y = q_X = 0$, so the derivatives (4.49) and (4.50) become:

$$\frac{\partial}{\partial x} = \frac{1}{x_c}\left[\frac{\partial}{\partial X} + (\hat{\epsilon}^{-1}\omega + p_X)\frac{\partial}{\partial \hat{x}}\right] \tag{4.51}$$

and

$$\frac{\partial}{\partial y} = \frac{1}{x_c}\left[\frac{\partial}{\partial Y} + (\hat{\epsilon}^{-1}\omega + q_Y)\frac{\partial}{\partial \hat{y}}\right]. \tag{4.52}$$

4.5.2 Kinematic conditions

Slender wedge

We begin with the rescaled kinematic equation for P:

$$\begin{aligned}\frac{2}{3}(1+X)(\hat{H}_{\hat{x}}+(\hat{\epsilon}^{-1}\omega + p_X)\hat{H}_{\hat{x}}) - \frac{2}{3}\hat{H} \\ = \left(\partial_X + (\hat{\epsilon}^{-1}\omega + p_X)\partial_{\hat{x}}\right)\left(\hat{P}_{\hat{x}} + (\hat{\epsilon}^{-1}\omega + p_X)\hat{P}_{\hat{x}}\right)\end{aligned} \tag{4.53}$$

We expand $\hat{H}$ and $\hat{P}$ using (4.46) and (4.47). At $O(\hat{\epsilon}^{-2})$, (4.53) gives

$$\omega^2 \bar{P}_{\hat{x}\hat{x}} = 0. \tag{4.54}$$

However, each term in the expansions (4.46), (4.47) and (4.48) is required to be periodic in $\hat{x}$ with period 1, and so $\bar{P}$ must be independent of $\hat{x}$. We henceforth consider $\bar{P}$ to be a function of the slow variable X only.

At $O(\hat{\epsilon}^{-1})$, we find from (4.53) that

$$\frac{2}{3}\omega(1+X)\hat{H}_{0\hat{x}} = \omega^2 \hat{H}_0 \hat{P}_{0\hat{x}\hat{x}} + \omega \hat{H}_{0\hat{x}}\left[\bar{P}_X + \omega \hat{P}_{0\hat{x}}\right]. \tag{4.55}$$

This can be integrated once in $\hat{x}$ to give:

$$\bar{P}_X + \omega \hat{P}_{0\hat{x}} = \frac{2}{3}(1+X) - \frac{A(X)}{\hat{H}_0}. \tag{4.56}$$

Here $A(X)$ is a constant of integration. We require that $\hat{P}_0$ is strictly periodic, so integrating (4.56) over one period gives our first secularity condition:

$$\bar{P}_X = \frac{2}{3}(1+X) - A(X)\int_0^1 \frac{1}{\hat{H}_0}d\hat{x}. \tag{4.57}$$

Equation (4.53) at $O(1)$ gives:

$$\begin{aligned}
&\frac{2}{3}(1+X)\left[\omega\hat{H}_{1\hat{x}} + p_X\hat{H}_{0\hat{x}} + \hat{H}_{0X}\right] - \frac{2}{3}\hat{H}_0 \\
&= \hat{H}_0\left[\omega^2\hat{P}_{1\hat{x}\hat{x}} + 2p_X\omega\hat{P}_{0\hat{x}\hat{x}} + 2\omega\hat{P}_{0\hat{x}X} + \omega_X\hat{P}_{0\hat{x}} + \bar{P}_{XX}\right] + \omega^2\hat{H}_1\hat{P}_{0\hat{x}\hat{x}} \\
&+ \omega\hat{H}_{0\hat{x}}\left[\omega\hat{P}_{1\hat{x}} + p_X\hat{P}_{0\hat{x}} + \hat{P}_{0X}\right] + \left[\omega\hat{H}_{1\hat{x}} + p_X\hat{H}_{0\hat{x}} + \hat{H}_{0X}\right]\left[\bar{P}_X + \omega\hat{P}_{0\hat{x}}\right].
\end{aligned} \tag{4.58}$$

Rearranging and integrating, with the aid of (4.56), gives

$$\omega\hat{P}_{1\hat{x}} + p_X\hat{P}_{0\hat{x}} + \hat{P}_{0X} = \frac{A(X)\hat{H}_1}{\hat{H}_0^2} + \frac{1}{\omega\hat{H}_0}\left(\hat{x}A_X(X) - \frac{4}{3}\int_0^{\hat{x}}\hat{H}_0 d\hat{x}\right) + \frac{B(X)}{\hat{H}_0}, \tag{4.59}$$

where $B(X)$ is another constant of integration. We know that $\hat{P}_0$, $\hat{H}_0$, $\hat{P}_{1\hat{x}}$ and $\hat{H}_1$ are periodic, so by comparing (4.59) evaluated at $\hat{x} = 0$ and $\hat{x} = 1$ we obtain a second secularity condition:

$$A_X = \frac{4}{3}\int_0^1 \hat{H}_0 d\hat{x}. \tag{4.60}$$

Fat wedge

Along the free surface, the kinematic equation on the fat wedge can be written as

$$\hat{\Phi}_Y + (\hat{\epsilon}^{-1}\omega + q_Y)\hat{\Phi}_{\hat{y}} = \frac{2}{3}\hat{H} - \frac{2}{3}(1+X)(\hat{H}_{\hat{x}} + (\hat{\epsilon}^{-1}\omega + p_X)\hat{H}_{\hat{x}}). \tag{4.61}$$

We expand $\hat{H}$ and $\hat{\Phi}$ using (4.46) and (4.48). At $O(\hat{\epsilon}^{-1})$, (4.61) gives

$$\hat{\Phi}_{0\hat{y}} = -\frac{2}{3}(1+X)\hat{H}_{0\hat{x}} \tag{4.62}$$

and at $O(1)$, after applying (4.62), we obtain

$$\hat{\Phi}_{1\hat{y}} = -\frac{2}{3}(1+X)\hat{H}_{1\hat{x}} + \frac{1}{\omega}\left(\frac{2}{3}\hat{H}_0 - \frac{2}{3}(1+X)\hat{H}_{0X} - \hat{\Phi}_{0Y}\right), \tag{4.63}$$

as $p_X = q_Y$ on the free surface $X > 0$, $Y = 0$.

4.5.3 Laplace's equation

In the bulk of the fluid, we have Laplace's equation:

$$\begin{aligned} 0 = &\left[\partial_X + (\hat{\epsilon}^{-1}\omega + p_X)\partial_{\hat{x}} + (\hat{\epsilon}^{-1}\Omega + q_X)\partial_{\hat{y}}\right]^2 \hat{\Phi} \\ &+ \left[\partial_Y + (-\hat{\epsilon}^{-1}\Omega + p_Y)\partial_{\hat{x}} + (\hat{\epsilon}^{-1}\omega + q_Y)\partial_{\hat{y}}\right]^2 \hat{\Phi}. \end{aligned} \tag{4.64}$$

After expansion using (4.48) and some algebra, making use of the relations $p_X = q_Y$ and $p_Y = -q_X$, we find

$$\begin{aligned} 0 =&(\omega^2 + \Omega^2)(\hat{\Phi}_{0\hat{x}\hat{x}} + \hat{\Phi}_{0\hat{y}\hat{y}}) \\ &+ \hat{\epsilon}(\omega^2 + \Omega^2)(\hat{\Phi}_{1\hat{x}\hat{x}} + \hat{\Phi}_{1\hat{y}\hat{y}}) \\ &+ 2\hat{\epsilon}(\omega\hat{\Phi}_{0\hat{x}X} + \Omega\hat{\Phi}_{0\hat{y}X} - \Omega\hat{\Phi}_{0\hat{x}Y} + \omega\hat{\Phi}_{0\hat{y}Y}) \\ &+ \hat{\epsilon}(\omega p_X - \Omega p_Y)(\hat{\Phi}_{0\hat{x}\hat{x}} + \hat{\Phi}_{0\hat{y}\hat{y}}) \\ &+ O(\hat{\epsilon}^2). \end{aligned} \tag{4.65}$$

At leading order, (4.65) gives

$$(\omega^2 + \Omega^2)(\hat{\Phi}_{0\hat{x}\hat{x}} + \hat{\Phi}_{0\hat{y}\hat{y}}) = 0, \tag{4.66}$$

and so at next order we have

$$(\omega^2 + \Omega^2)(\hat{\Phi}_{1\hat{x}\hat{x}} + \hat{\Phi}_{1\hat{y}\hat{y}}) = -2\omega(\hat{\Phi}_{0\hat{x}X} + \hat{\Phi}_{0\hat{y}Y}) + 2\Omega(\hat{\Phi}_{0\hat{x}Y} - \hat{\Phi}_{0\hat{y}X}). \tag{4.67}$$

We want to use (4.67) as the basis for a secularity condition on $\hat{\Phi}_0$ and its derivatives. To do so we use the divergence theorem and a form of Green's theorem on the semi-infinite rectangle R in $(\hat{x}, \hat{y})$ space given by $0 < \hat{x} < 1$, $0 < \hat{y} < \infty$. We know that $\hat{\Phi}_1$ and $\hat{\Phi}_0$ are periodic in $\hat{x}$ with period 1.

We use a Fourier series expansion to determine the $\hat{y}$ dependence of $\hat{\Phi}_0$, and write

$$\hat{\Phi}_0(\hat{x}, \hat{y}, X, Y) = W_0(X, Y) + \sum_{n=1}^{\infty} b_n(X, Y)\sin(2\pi n\hat{x})e^{-2\pi n\hat{y}}. \tag{4.68}$$

The corresponding Fourier series for $\hat{H}_0$ is

$$\hat{H}_0 = \bar{H}_0 - \frac{3}{2(1+X)}\sum_{n=1}^{\infty} b_n \cos(2\pi n\hat{x}). \tag{4.69}$$

The Fourier series expansions for $\hat{H}_0$ and $\hat{\Phi}_0$ satisfy the leading order kinematic and mass conservation equations on Φ.

From the divergence theorem and the periodicity conditions, we can write

$$\int_0^\infty \int_0^1 (\hat{\Phi}_{1\hat{x}\hat{x}} + \hat{\Phi}_{1\hat{y}\hat{y}}) d\hat{x} d\hat{y} = -\int_0^1 \hat{\Phi}_{1\hat{y}}(\hat{x}, 0) d\hat{x}. \tag{4.70}$$

Substituting (4.68) into (4.70), we find that the right-hand-side of (4.70) is zero and so

$$0 = \int_0^1 \hat{\Phi}_{1\hat{y}} d\hat{x}. \tag{4.71}$$

We have a kinematic equation involving $\hat{\Phi}_{1\hat{y}}$ from (4.63), so as $\hat{H}_1$ is periodic in $\hat{x}$, we obtain

$$W_{0Y}(X, 0) = \frac{2}{3} \int_0^1 \hat{H}_0 d\hat{x} - \frac{2}{3}(1 + X) \int_0^1 \hat{H}_{0X} d\hat{x}, \tag{4.72}$$

which gives a third secularity condition. We know that

$$A_X = \frac{4}{3} \int_0^1 \hat{H}_0 d\hat{x}, \tag{4.73}$$

so we can rewrite (4.72) as

$$W_{0Y}(X, 0) = \frac{1}{2} A_X - \frac{1}{2}(1 + X) A_{XX}. \tag{4.74}$$

This gives us a condition on W_0, but does not provide any information about the leading order oscillator as W_0 does not appear in the oscillator equations. However, $W_0(X, Y)$ will turn out to be important in assembling the composite solution for $\hat{\Phi}$.

We still need another secularity condition. We observe that, according to the divergence theorem and periodicity,

$$\int_0^\infty \int_0^1 \hat{\Phi}_{0\hat{x}} (\hat{\Phi}_{1\hat{x}\hat{x}} + \hat{\Phi}_{1\hat{y}\hat{y}}) d\hat{x} d\hat{y} = \int_0^1 \hat{\Phi}_1 \hat{\Phi}_{0\hat{x}\hat{y}} - \hat{\Phi}_{0\hat{x}} \hat{\Phi}_{1\hat{y}} d\hat{x}. \tag{4.75}$$

We can use (4.67) to write

$$\begin{aligned}(\omega^2 + \Omega^2) \int_0^\infty \int_0^1 \hat{\Phi}_{0\hat{x}} (\hat{\Phi}_{1\hat{x}\hat{x}} + \hat{\Phi}_{1\hat{y}\hat{y}}) d\hat{x} d\hat{y} = &-2\omega \int_0^\infty \int_0^1 \hat{\Phi}_{0\hat{x}} (\hat{\Phi}_{0\hat{x}X} + \hat{\Phi}_{0\hat{y}Y}) d\hat{x} d\hat{y} \\ &+ 2\Omega \int_0^\infty \int_0^1 \hat{\Phi}_{0\hat{x}} (\hat{\Phi}_{0\hat{x}Y} - \hat{\Phi}_{0\hat{y}X}) d\hat{x} d\hat{y}.\end{aligned} \tag{4.76}$$

From the Fourier series expansion (4.68), it follows that

$$\int_0^\infty \hat{\Phi}_{0\hat{x}} \hat{\Phi}_{0\hat{y}Y} d\hat{x} d\hat{y} = 0. \tag{4.77}$$

On $Y = 0$, we have $\Omega = 0$, and (4.76) becomes

$$\omega^2 \int_0^\infty \int_0^1 \hat{\Phi}_{0\hat{x}}(\hat{\Phi}_{1\hat{x}\hat{x}} + \hat{\Phi}_{1\hat{y}\hat{y}})d\hat{x}d\hat{y} = -\omega \frac{d}{dX} \int_0^\infty \int_0^1 \hat{\Phi}_{0\hat{x}}^2 d\hat{x}d\hat{y}, \tag{4.78}$$

which we substitute into (4.75) to yield

$$\frac{1}{\omega(X,0)} \frac{d}{dX} \left(\int_0^\infty \int_0^1 \hat{\Phi}_{0\hat{x}}^2 d\hat{x}d\hat{y} \right) = \int_0^1 \hat{\Phi}_{1\hat{x}}\hat{\Phi}_{0\hat{y}} + \hat{\Phi}_{0\hat{x}}\hat{\Phi}_{1\hat{y}} d\hat{x}. \tag{4.79}$$

We can eliminate the $\hat{y}$ derivatives in (4.79) using the kinematic boundary conditions on the fat wedge, given by (4.62) and (4.63), so that (4.79) can be rewritten as

$$\begin{aligned} \frac{1}{\omega} \frac{d}{dX} \left(\int_0^\infty \int_0^1 \hat{\Phi}_{0\hat{x}}^2 d\hat{x}d\hat{y} \right) = &-\frac{2}{3}(1+X) \int_0^1 \hat{\Phi}_{1\hat{x}}\hat{H}_{0\hat{x}} + \hat{\Phi}_{0\hat{x}}\hat{H}_{1\hat{x}} d\hat{x} \\ &+ \frac{1}{\omega} \int_0^1 \hat{\Phi}_{0\hat{x}} \left(\frac{2}{3}\hat{H}_0 - \frac{2}{3}(1+X)\hat{H}_{0X} - \hat{\Phi}_{0Y} \right) d\hat{x}. \end{aligned} \tag{4.80}$$

On parity grounds we find that from the Fourier series (4.68) that

$$\int_0^1 \hat{\Phi}_{0\hat{x}}\hat{H}_{0\hat{x}} d\hat{x} = 0 \quad \text{and} \quad \int_0^1 \hat{\Phi}_{0\hat{x}}\hat{\Phi}_{0Y} d\hat{x} = 0, \tag{4.81}$$

so we can simplify (4.80) to

$$\begin{aligned} \frac{d}{dX} \left(\int_0^\infty \int_0^1 \hat{\Phi}_{0\hat{x}}^2 d\hat{x}d\hat{y} \right) = &-\frac{2}{3}\omega(1+X) \int_0^1 \hat{\Phi}_{1\hat{x}}\hat{H}_{0\hat{x}} + \hat{\Phi}_{0\hat{x}}\hat{H}_{1\hat{x}} d\hat{x} \\ &+ \int_0^1 \hat{\Phi}_{0\hat{x}} \left(\frac{2}{3}\hat{H}_0 - \frac{2}{3}(1+X)\hat{H}_{0X} \right) d\hat{x}. \end{aligned} \tag{4.82}$$

Equation (4.82) is the main result from the analysis of Laplace's equation, and will lead to an important secularity condition. We will need to use the Bernoulli equation to evaluate the term

$$\int_0^1 (\hat{\Phi}_{1\hat{x}}\hat{H}_{0\hat{x}} + \hat{\Phi}_{0\hat{x}}\hat{H}_{1\hat{x}}) d\hat{x},$$

and to provide another equation to complete the set of oscillator equations.

4.5.4 Bernoulli's equation

The rescaled Bernoulli equation is

$$\begin{aligned} &\hat{\epsilon}^2 \left[\partial_X + (\hat{\epsilon}^{-1}\omega + p_X)\partial_{\hat{x}} \right]^2 \hat{H} \\ &\quad = \mu \left[\frac{1}{3}\hat{P} - \frac{2}{3}(1+X)(\hat{P}_X + (\hat{\epsilon}^{-1}\omega + p_X)\hat{P}_{\hat{x}}) + \frac{1}{2}(\hat{P}_X + (\hat{\epsilon}^{-1}\omega + p_X)\hat{P}_{\hat{x}})^2 \right] \\ &\quad - \eta\hat{\epsilon} \left[\frac{1}{3}\hat{\Phi} - \frac{2}{3}(1+X)(\hat{\Phi}_X + (\hat{\epsilon}^{-1}\omega + p_X)\hat{\Phi}_{\hat{x}}) \right]. \end{aligned} \tag{4.83}$$

We have added a second density parameter η, which is the density of the fluid in the fat wedge relative to the density used for nondimensionalisation. If we put $\eta = 0$ we recover a scaled version of the problem of recoil of a slender wedge of fluid considered by Billingham [2006].

We expand $\hat{H}$, $\hat{P}$ and $\hat{\Phi}$ using (4.46), (4.47) and (4.48). We recall that as a result of (4.54), $\bar{P}$ in (4.47) is now a function of the slow variable X only, so $\hat{P}_{\hat{x}} = O(\hat{\epsilon})$. At leading order, (4.83) gives

$$\begin{aligned}\omega^2\hat{H}_{0\hat{x}\hat{x}} =&\mu\left[\frac{1}{3}\bar{P} - \frac{2}{3}(1+X)(\bar{P}_X + \omega\hat{P}_{0\hat{x}}) + \frac{1}{2}(\bar{P}_X + \omega\hat{P}_{0\hat{x}})^2\right]\\ &+ \frac{2}{3}\eta(1+X)\omega\hat{\Phi}_{0\hat{x}}\end{aligned} \tag{4.84}$$

However, we know from the kinematic equation on the slender wedge (4.56) that

$$\bar{P}_X + \omega\hat{P}_{0\hat{x}} = \frac{2}{3}(1+X) - \frac{A(X)}{\hat{H}_0}. \tag{4.85}$$

Substituting (4.85) into (4.84) gives

$$\omega^2\hat{H}_{0\hat{x}\hat{x}} = \mu\left[\frac{1}{3}\bar{P}(X) - \frac{2}{9}(1+X)^2 + \frac{1}{2}\frac{A(X)^2}{\hat{H}_0^2}\right] + \frac{2}{3}\eta(1+X)\omega\hat{\Phi}_{0\hat{x}}, \tag{4.86}$$

which is a further equation involving the leading order nonlinear oscillator. We also have (4.56) and (4.62). However, we need a further condition in order to specify the amplitude of oscillations in $\hat{H}_0$.

Examining (4.83) at $O(\hat{\epsilon})$, we obtain

$$\begin{aligned}&\omega^2\hat{H}_{1\hat{x}\hat{x}} + 2p_X\omega\hat{H}_{0\hat{x}\hat{x}} + 2\omega\hat{H}_{0\hat{x}X} + \omega_X\hat{H}_{0\hat{x}}\\ &\qquad=\mu\left[\frac{1}{3}\hat{P}_0 - \frac{A}{\hat{H}_0}\left(\omega\hat{P}_{1\hat{x}} + p_X\hat{P}_{0\hat{x}} + \hat{P}_{0X}\right)\right]\\ &\qquad\quad-\eta\left[\frac{1}{3}\hat{\Phi}_0 - \frac{2}{3}(1+X)\left(\omega\hat{\Phi}_{1\hat{x}} + p_X\hat{\Phi}_{0\hat{x}} + \hat{\Phi}_{0X}\right)\right].\end{aligned} \tag{4.87}$$

We substitute for $\hat{P}_1$ from (4.59), so that we may rewrite (4.87) as

$$-\mu\frac{A^2(X)H_1}{H_0^3} + \frac{2}{3}\eta(1+X)\omega\hat{\Phi}_{1\hat{x}} - \omega^2\hat{H}_{1\hat{x}\hat{x}} = F_0(\hat{x}, X) \tag{4.88}$$

where

$$\begin{aligned}F_0(\hat{x}, X) \equiv&2p_X\omega\hat{H}_{0\hat{x}\hat{x}} + 2\omega\hat{H}_{0\hat{x}X} + \omega_X\hat{H}_{0\hat{x}}\\ &- \mu\left[\frac{1}{3}\hat{P}_0 - \frac{A(X)}{\omega\hat{H}_0^2}\left(\hat{x}A_X - \frac{4}{3}\int_0^{\hat{x}}\hat{H}_0 d\hat{x}\right) - \frac{A(X)B(X)}{\hat{H}_0^2}\right]\\ &+ \eta\left[\frac{1}{3}\hat{\Phi}_0 - \frac{2}{3}(1+X)\left(p_X\hat{\Phi}_{0\hat{x}} + \hat{\Phi}_{0X}\right)\right].\end{aligned} \tag{4.89}$$

Now, using (4.86) and (4.88), we find

$$\frac{2}{3}\eta\omega(1+X)\int_0^1(\hat{\Phi}_{1\hat{x}}\hat{H}_{0\hat{x}}+\hat{\Phi}_{0\hat{x}}\hat{H}_{1\hat{x}})d\hat{x}=\int_0^1\hat{H}_{0\hat{x}}F_0(\hat{x},X)d\hat{x}. \tag{4.90}$$

The secularity condition (4.82) from the analysis of Laplace's equation now becomes

$$\begin{aligned}\frac{d}{dX}\left(\int_0^\infty\int_0^1\hat{\Phi}_{0\hat{x}}^2d\hat{x}d\hat{y}\right)=&-\frac{1}{\eta}\int_0^1\hat{H}_{0\hat{x}}F_0(\hat{x},X)d\hat{x}\\&+\int_0^1\hat{\Phi}_{0\hat{x}}\left(\frac{2}{3}\hat{H}_0-\frac{2}{3}(1+X)\hat{H}_{0X}\right)d\hat{x},\end{aligned} \tag{4.91}$$

which involves only properties of the leading order oscillator. Using the definition of F_0 from (4.89), we have

$$\begin{aligned}\int_0^1\hat{H}_{0\hat{x}}F_0(\hat{x},X)d\hat{x}=&\frac{d}{dX}\left(\omega\int_0^1\hat{H}_{0\hat{x}}^2d\hat{x}\right)\\&+\eta\left[\frac{1}{3}\int_0^1\hat{\Phi}_0\hat{H}_{0\hat{x}}d\hat{x}-\frac{2}{3}(1+X)\int_0^1\hat{\Phi}_{0X}\hat{H}_{0\hat{x}}d\hat{x}\right]\\&-\frac{5}{3}\frac{A\mu}{\omega}\left(1-\int_0^1\hat{H}_0d\hat{x}\int_0^1\hat{H}_0^{-1}d\hat{x}\right).\end{aligned} \tag{4.92}$$

We can use the Fourier series expansion of $\hat{\Phi}_0$ and $\hat{H}_0$ from (4.68) and (4.69) to write

$$\frac{2}{3}(1+X)\int_0^1\hat{H}_0\hat{\Phi}_{0\hat{x}}d\hat{x}=-\sum_{n=1}^\infty b_n^2\pi n=-2\int_0^\infty\int_0^1\hat{\Phi}_{0\hat{x}}^2d\hat{x}d\hat{y} \tag{4.93}$$

and so (4.91) becomes

$$\begin{aligned}&\frac{d}{dX}\left(\omega\int_0^1\hat{H}_{0\hat{x}}^2d\hat{x}+\frac{1}{3}(1+X)\eta\int_0^1\hat{H}_0\hat{\Phi}_{0\hat{x}}d\hat{x}\right)\\&=\frac{5}{3}\frac{A\mu}{\omega}\left(1-\int_0^1\hat{H}_0d\hat{x}\int_0^1\hat{H}_0^{-1}d\hat{x}\right)+\frac{5}{3}\eta\int_0^1\hat{H}_0\hat{\Phi}_{0\hat{x}}d\hat{x}.\end{aligned} \tag{4.94}$$

For ease of notation, we define an 'energy' by

$$E(X):=\omega\int_0^1\hat{H}_{0\hat{x}}^2d\hat{x}+\frac{1}{3}(1+X)\eta\int_0^1\hat{H}_0\hat{\Phi}_{0\hat{x}}d\hat{x} \tag{4.95}$$

so that the secularity condition (4.94) becomes

$$\frac{dE}{dX}=\frac{5}{3}\frac{A\mu}{\omega}\left(1-\int_0^1\hat{H}_0d\hat{x}\int_0^1\hat{H}_0^{-1}d\hat{x}\right)+\frac{5}{3}\eta\int_0^1\hat{H}_0\hat{\Phi}_{0\hat{x}}d\hat{x}. \tag{4.96}$$

Finally, we can show that E is always positive. Integrating the oscillator Bernoulli equation (4.86) over one period gives

$$\left[\frac{1}{3}\bar{P}(X)-\frac{2}{9}(1+X)^2\right]+\frac{A^2}{2}\int_0^1\frac{1}{\hat{H}_0^2}d\hat{x}=0 \tag{4.97}$$

and multiplying (4.86) by $\hat{H}_0$ and integrating gives

$$\begin{aligned}\mu\left[\frac{1}{3}\bar{P}(X)-\frac{2}{9}(1+X)^2\right]\int_0^1 \hat{H}_0 d\hat{x}+\frac{\mu A^2}{2}\int_0^1 \frac{1}{\hat{H}_0}d\hat{x}\\ +\frac{2}{3}\eta(1+X)\omega\int_0^1 \hat{H}_0\hat{\Phi}_{0\hat{x}}d\hat{x}=-\omega^2\int_0^1 \hat{H}_{0\hat{x}}^2 d\hat{x}.\end{aligned} \tag{4.98}$$

We can therefore rewrite E as

$$E(X)=\frac{\omega}{2}\int_0^1 \hat{H}_{0\hat{x}}^2 d\hat{x}+\frac{\mu A^2}{4\omega}\left[\int_0^1 \hat{H}_0 d\hat{x}\int_0^1 \frac{1}{\hat{H}_0^2}d\hat{x}-\int_0^1 \frac{1}{\hat{H}_0}d\hat{x}\right]. \tag{4.99}$$

As $\hat{H}_0$ is positive, the term in square brackets is greater than or equal to zero by the Cauchy-Schwarz inequality, and we want $\omega > 0$, so $E(X) \geq 0$ for all X. $E(X)$ is zero if and only if $\hat{H}_0$ is constant.

4.5.5 Summary: Oscillator equation and secularity conditions

Oscillator equations

The nonlinear oscillator can be described by the leading order equations:

$$\mu\left[\frac{1}{3}\bar{P}-\frac{2}{9}(1+X)^2+\frac{1}{2}\frac{A^2}{\hat{H}_0^2}\right]+\frac{2}{3}\eta(1+X)\omega\hat{\Phi}_{0\hat{x}}=\omega^2\hat{H}_{0\hat{x}\hat{x}}, \tag{4.100}$$

$$\hat{\Phi}_{0\hat{y}}=-\frac{2}{3}(1+X)\hat{H}_{0\hat{x}}, \tag{4.101}$$

$$\hat{\Phi}_{0\hat{x}\hat{x}}+\hat{\Phi}_{0\hat{y}\hat{y}}=0 \quad \text{for} \quad \hat{y}>0 \tag{4.102}$$

and

$$E(X)=\omega\int_0^1 \hat{H}_{0\hat{x}}^2 d\hat{x}+\frac{1}{3}(1+X)\eta\int_0^1 \hat{H}_0\hat{\Phi}_{0\hat{x}}d\hat{x}. \tag{4.103}$$

with $\hat{\Phi}_0$ bounded as $\hat{y}\to\infty$. The slowly varying parameters $A(X)$, $\bar{P}(X)$ and $E(X)$ are fixed for each oscillation. $\omega(X)$ is a free parameter to ensure periodicity with period 1. A selection of numerical solutions to these oscillator equations are shown in figure 4.7.

Secularity conditions

We need three secularity conditions to determine how A, $\bar{P}$ and E vary with X. Two come from the kinematic condition on the thin wedge:

$$\frac{d\bar{P}}{dX}=\frac{2}{3}(1+X)-A(X)\int_0^1 \frac{1}{\hat{H}_0}d\hat{x} \tag{4.104}$$

and

$$\frac{dA}{dX} = \frac{4}{3}\int_0^1 \hat{H}_0 d\hat{x}. \tag{4.105}$$

The third secularity condition incorporates terms from all the equations:

$$\frac{dE}{dX} = \frac{5}{3}\frac{A\mu}{\omega}\left(1 - \int_0^1 \hat{H}_0 d\hat{x}\int_0^1 \hat{H}_0^{-1} d\hat{x}\right) + \frac{5}{3}\eta\int_0^1 \hat{H}_0\hat{\Phi}_{0\hat{x}} d\hat{x}. \tag{4.106}$$

This analysis has also uncovered the further secularity condition (4.72), which gives us W_{0Y} on the free surface. The function W_0 describes the two-dimensional variation of the mean of $\hat{\Phi}$. This is uncoupled from the oscillator equations and the other secularity conditions. Although we do not need to know W_0 to solve the secularity equations, we find that W_0 is important in determining the correct composite solution for $\hat{\Phi}$. The equations for W_0 are discussed further in section 4.7.5.

4.6 Oscillator solution properties

For a given set of parameters A, P, E and X, and the density parameters μ and η, we want to find a solution $\hat{H}_0(\hat{x})$, $\hat{\Phi}_0(\hat{x},\hat{y})$ to the system of oscillator equations (4.100) to (4.103). We must also determine ω, which is a free parameter to ensure periodicity with period 1.

For notational convenience, we define two new parameters:

$$Q(X) := \frac{4}{9}(1+X)^2 - \frac{2}{3}\bar{P}(X), \qquad B(X) := \frac{4}{9}\eta(1+X)^2, \tag{4.107}$$

and rescale $\hat{\Phi}_0$:

$$\hat{\Phi}_0 = \frac{2}{3}(1+X)\Psi, \tag{4.108}$$

and drop all hats and subscripts for this section.

Given positive values for the parameters A, Q, B and E, we seek a solution ω, $H(x)$, $\Psi(x,y)$ to

$$\frac{\mu}{2}\left[\frac{A(X)^2}{H^2} - Q(X)\right] + \omega B(X)\Psi_x = \omega^2 H_{xx} \quad \text{on } y = 0, \tag{4.109}$$

$$\Psi_y = -H_x \quad \text{on } y = 0, \tag{4.110}$$

$$\Psi_{xx} + \Psi_{yy} = 0 \quad \text{for } y > 0 \tag{4.111}$$

and

$$E(X) = \omega \int_0^1 H_x^2 dx + \frac{B}{2} \int_0^1 H\Psi_x dx. \tag{4.112}$$

To make use of the secularity conditions, we need to calculate three integrals of $H(x)$:

$$\int_0^1 H(x)dx, \quad \int_0^1 \frac{1}{H(x)}dx, \quad \int_0^1 H(x)\Psi_x(x,0)dx, \tag{4.113}$$

as well as the eigenvalue ω.

The system (4.109) to (4.112) is translationally invariant in x. If $E > 0$, we know that $H(x)$ is non-constant, and so we can specify that $H(x)$ has a local maximum at $x = 0$. We have been unable to find any solutions to the oscillator equations that have a local maximum at $x = 0$ but that do not have H even in x and Ψ odd in x. Suitable solutions with these symmetries appear to be available for all positive values of A, Q, B and E. In the rest of this chapter, we will assume that all oscillator solutions have $H(x)$ symmetric and $\Psi(x, y)$ antisymmetric in x, which simplifies the analysis of these equations.

4.6.1 Numerical solution with spectral derivatives

Given an even periodic trial solution $H(x)$, we can find Fourier coefficients a_n so that $H(x)$ can be written as

$$H(x) = a_0 + \sum_{n=1}^{\infty} a_n \cos(2\pi n x). \tag{4.114}$$

Then by solving (4.110) and (4.111), we find

$$\Psi(x, y) = -\sum_{n=1}^{\infty} a_n \sin(2\pi n x) e^{-2\pi n y} \tag{4.115}$$

with

$$\Psi_x(x, 0) = -\sum_{n=1}^{\infty} (2\pi n) a_n \cos(2\pi n x) \tag{4.116}$$

and

$$H_{xx} = -\sum_{n=1}^{\infty} (2\pi n)^2 a_n \cos(2\pi n x). \tag{4.117}$$

We truncate these sums at $n = N/2$. We can find matrices M_1 and M_2, such that

$$M_1 \cdot H = \Psi_x, \qquad M_2 \cdot H = H_{xx}. \tag{4.118}$$

The matrices M_1 and M_2 depend only on the discretisation of x, and are dense if calculated using spectral derivatives. Both M_1 and M_2 will be symmetric if we assume $H(x)$ is even and periodic. As Ψ_x has been expressed as a Fourier series above, it seems natural to also use spectral derivatives for H_{xx} for this problem. Alternatively, we could use a finite difference scheme to determine H_{xx}, in which case M_2 would be sparse. We use N evenly-spaced points in discretising this system, with $x_n = (n - 1/2)/N$. We seek a solution that is even in x, so there are $N/2$ independent values of H to be found.

The residual vector is composed of the following function evaluated at x_i, $i = 1, .., N/2$:

$$F_i = \omega^2 (M_2)_{ij} H_j - \omega B (M_1)_{ij} H_j + \frac{\mu}{2}\left[Q - \frac{A^2}{H_i^2}\right]. \tag{4.119}$$

The final equation comes from E, which fixes the free parameter ω:

$$\begin{aligned} F_{N/2+1} &= E + \omega \int_0^1 H H_{xx} dx - \frac{B}{2}\int_0^1 H \Psi_x dx \\ &= E - \frac{1}{N} H_i H_j \left(-\omega (M_2)_{ij} + \frac{B}{2}(M_1) ij\right). \end{aligned} \tag{4.120}$$

The $N/2$ independent values of H and the eigenvalue ω are to be determined in order to ensure $F = 0$. We use Newton iteration to find numerical solutions to the nonlinear system, coupled to continuation in A, Q, B and E to provide the initial guesses. The code uses an exact Jacobian, which can be expressed concisely in terms of the matrices M_1 and M_2. As the points x_n are uniformly spaced, we calculate the integrals in (4.113) simply by taking the mean of the relevant quantities across the independent values of H.

The oscillator solutions shown in figure 4.7 were calculated numerically, with $N = 200$, using finite difference derivatives for H_{xx} and spectral derivatives for Ψ_x. Convergence testing shows that for moderate values of A, Q, B and E and H_{xx} calculated using second order centred finite difference formulae, the eigenvalue ω and the integral solution measures given in (4.113) converge as $O(N^{-2})$ as $N \to \infty$. If H_{xx} is calculated using a spectral scheme, the convergence of these solution measures is much faster. However, as $A \to 0$, we find that the minimum of H approaches zero, with rapid variation in H_x in a region of width $O(A^2)$ near this minimum. As a result, the solution becomes increasingly less smooth as $A \to 0$, and $O(A^{-2})$ uniformly-spaced grid points are needed in order that the neck region is sufficiently resolved. For general η, we find that $A = O(X)$ as $X \to 0$, and so direct numerical solution of the oscillator equations becomes infeasible for small X.

When $\eta = 0$, the oscillator equations reduce to ODEs that can be solved exactly in terms of elliptic integrals. We discuss this exact oscillator solution and the solution to the resulting secularity equations, in section 4.6.2. For finite values of η, there is no analytical solution to the oscillator equations. In section 4.6.3, we derive asymptotic solutions to the oscillator equations for small A that are valid for finite η. We expect to find that $E \to 0$ as $X \to \infty$, and so derive asymptotic solutions for small E in section 4.6.4.

4.6.2 Solution in terms of elliptic integrals for $\eta = 0$

For $\eta = 0$, $\mu = 1$, we need to solve the ODE:

$$\frac{1}{2}\left[\frac{A^2}{H^2} - Q\right] = \omega^2 H_{xx}, \tag{4.121}$$

with the eigenvalue ω chosen so that the solution has period 1. The value of E is fixed, giving the integral constraint

$$E(X) = \omega \int_0^1 H_x^2 dx. \tag{4.122}$$

Following Billingham [2006], we find that we can solve these equations exactly for general values of the parameters A, Q and E in terms of elliptic integrals (B is zero here). We then rewrite the secularity equations in terms of complete elliptic integrals; we find that one of the secularity equations decouples from the other two. By redefining our independent variable, we can write the two coupled secularity equations as an autonomous system, and so we reduce the system to a single first-order ODE. We choose suitable boundary conditions, and integrate in X to find $\bar{P}(0)$ and λ^*, and find the resulting envelope of oscillations. However, for finite non-zero η and μ, the three equations do not decouple and there is no autonomous system. We must instead find $\bar{P}(0)$, and hence λ^* by explicit shooting in X.

For $\eta = 0$, we begin by integrating (4.121) after multiplying by H_x to obtain

$$-\frac{1}{2}\left[\frac{A^2}{H} + QH\right] = \frac{\omega^2 H_x^2}{2} + const. \tag{4.123}$$

H_x is zero at the maximum and minimum values of H, which we denote H_M and H_0 respectively, so we can write (4.123) as

$$\omega^2 H_x^2 = \left[A^2\left(\frac{1}{H_M} - \frac{1}{H}\right) + Q(H_M - H)\right]. \tag{4.124}$$

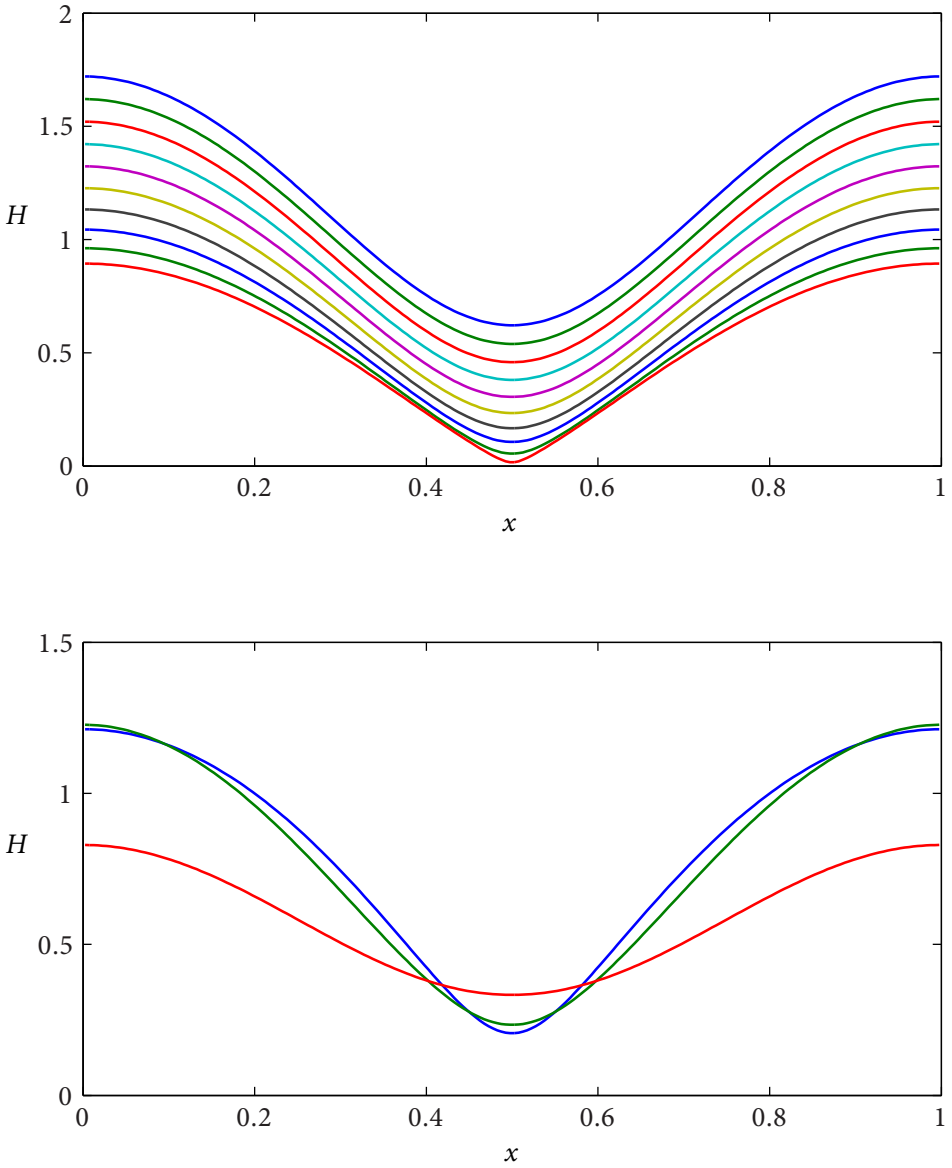

Figure 4.7: Solutions to the oscillator equations can be found using a spectral method to calculate $\hat{\Phi}_{0\hat{x}}$ from $\hat{H}_0$ coupled to a Newton solver to deal with the nonlinearities. The upper plot shows solutions for $B = 1$, $Q = 1$, $E = 1$ and $A = 0.1, 0.2, .., 1$, with the height of H increasing with A. The lower plot shows solutions for $A = 0.5$, $Q = 1$, $E = 1$ and $B = 0$ (blue), $B = 1$ (green) and $B = 10$ (red).

We define an aspect ratio $\alpha = H_0/H_M$ which by (4.124) also satisfies

$$\alpha = \frac{A^2}{QH_M^2}. \tag{4.125}$$

We can now write (4.124) as

$$\omega^2 H_x^2 = QH_M\left[1 - \frac{H}{H_M} + \alpha\left(1 - \frac{H_M}{H}\right)\right]. \tag{4.126}$$

We can integrate (4.126) to find the energy E as a function of α, A and Q:

$$E = 2\frac{A^{3/2}}{\alpha^{3/4}Q^{1/4}}\int_\alpha^1 \sqrt{1 - y + \alpha\left(1 - \frac{1}{y}\right)}dy. \tag{4.127}$$

Here the integration variable $y = H/H_M$. Equation (4.127) allows us to determine α as a function of E. Having chosen α, we can calculate the other solution properties by direct integration:

$$\omega = \frac{1}{2}\sqrt{\frac{Q}{H_M}}\left(\int_\alpha^1 \left(1 - y + \alpha\left(1 - \frac{1}{y}\right)\right)^{-1/2} dy\right)^{-1}, \tag{4.128}$$

$$\int_0^1 H dx = \frac{2H_M^{3/2}\omega}{\sqrt{Q}}\int_\alpha^1 y\left(1 - y + \alpha\left(1 - \frac{1}{y}\right)\right)^{-1/2} dy \tag{4.129}$$

and

$$\int_0^1 H^{-1} dx = \frac{2\omega}{\sqrt{H_M Q}}\int_\alpha^1 y^{-1}\left(1 - y + \alpha\left(1 - \frac{1}{y}\right)\right)^{-1/2} dy. \tag{4.130}$$

The integrals in (4.127) to (4.130) can be rewritten in terms of complete elliptic integrals of the first and second kind, denoted **K** and **E** respectively. We use the definition from MATLAB, for which

$$\mathbf{K}(m) = \int_0^1 (1 - t^2)^{-1/2}(1 - mt^2)^{-1/2} dt \tag{4.131}$$

and

$$\mathbf{E}(m) = \int_0^1 (1 - t^2)^{-1/2}(1 - mt^2)^{1/2} dt. \tag{4.132}$$

These functions can be evaluated in MATLAB using the command $[K, E] = \text{ellipke}(m)$.

Using Maple to perform the algebraic manipulation, we find

$$\int_\alpha^1 \sqrt{1 - y + \alpha\left(1 - \frac{1}{y}\right)}dy = \frac{2}{3}(1 + \alpha)\mathbf{E}(1 - \alpha) - \frac{4}{3}\alpha\mathbf{K}(1 - \alpha), \tag{4.133}$$

$$\int_\alpha^1 \left(1 - y + \alpha\left(1 - \frac{1}{y}\right)\right)^{-1/2} dy = 2\mathbf{E}(1-\alpha), \tag{4.134}$$

$$\int_\alpha^1 y\left(1 - y + \alpha\left(1 - \frac{1}{y}\right)\right)^{-1/2} dy = \frac{4}{3}(1+\alpha)\mathbf{E}(1-\alpha) - \frac{2}{3}\alpha\mathbf{K}(1-\alpha) \tag{4.135}$$

and

$$\int_\alpha^1 y^{-1}\left(1 - y + \alpha\left(1 - \frac{1}{y}\right)\right)^{-1/2} dy = 2\mathbf{K}(1-\alpha). \tag{4.136}$$

In terms of these elliptic integrals, the secularity equations become

$$\frac{dA}{dX} = \frac{4}{9}\frac{A}{\sqrt{\alpha Q}}[2(1+\alpha) - \alpha\kappa], \tag{4.137}$$

$$\frac{d\bar{P}}{dX} = \frac{2}{3}(1+X) - \alpha^{1/2}Q^{1/2}\kappa \tag{4.138}$$

and

$$\frac{dE}{dX} = \frac{20}{3}\frac{A^{3/2}\mathbf{E}(1-\alpha)}{\alpha^{1/2}Q^{3/4}}\left[1 - \frac{\kappa}{3}(2(1+\alpha) - \alpha\kappa)\right] \tag{4.139}$$

where $\kappa \equiv \kappa(\alpha) = \mathbf{K}(1-\alpha)/\mathbf{E}(1-\alpha)$.

We can now make the system autonomous by letting $S = \log(1+X)$ and writing

$$Q = \frac{4}{9}(1+X)^2 - \frac{2}{3}\bar{P} \equiv (1+X)^2\tilde{Q}, \qquad \tilde{P} = \frac{\bar{P}}{(1+X)^2} \tag{4.140}$$

so $\tilde{Q}$ is defined as

$$\tilde{Q} = \frac{4}{9} - \frac{2}{3}\tilde{P}. \tag{4.141}$$

The first two secularity equations, (4.137) and (4.138), become

$$\frac{dA}{dS} = \frac{4}{9}\frac{A}{\alpha^{1/2}\tilde{Q}^{1/2}}[2(1+\alpha) - \alpha\kappa] \tag{4.142}$$

and

$$\frac{d\tilde{P}}{dS} = -2\tilde{P} + \frac{2}{3} - \alpha^{1/2}\tilde{Q}^{1/2}\kappa. \tag{4.143}$$

The final secularity condition, (4.139) can be used together with the definition of E:

$$E = \frac{2A^{3/2}}{\alpha^{1/4}Q^{1/4}}\left[\frac{2}{3}(1+\alpha)\mathbf{E}(1-\alpha) - \frac{4}{3}\alpha\mathbf{K}(1-\alpha)\right] \tag{4.144}$$

and the observation that

$$\frac{d}{d\alpha}\left[\frac{2}{3}(1+\alpha)\mathbf{E}(1-\alpha) - \frac{4}{3}\alpha\mathbf{K}(1-\alpha)\right] = \mathbf{E}(1-\alpha) - \mathbf{K}(1-\alpha), \tag{4.145}$$

to derive an ODE for α:

$$\begin{aligned}\frac{d\alpha}{dX} = &-\frac{20}{3}\frac{\alpha^{3/2}}{(1-\alpha)Q^{1/2}}\left(1-\frac{\kappa}{3}(2(1+\alpha)-\alpha\kappa)\right)\\ &+\frac{8}{9}\frac{1}{1-\alpha}\sqrt{\frac{\alpha}{Q}}(1+\alpha-2\alpha\kappa)(2(1+\alpha)-\alpha\kappa)\\ &-\frac{2}{9}\frac{\alpha}{Q(1-\alpha)}(1+\alpha-2\alpha\kappa)\left(\frac{2}{3}(1+X)+\sqrt{\alpha Q}\kappa\right),\end{aligned} \tag{4.146}$$

and its autonomous counterpart:

$$\begin{aligned}\frac{d\alpha}{dS} = &-\frac{4}{27}\frac{\alpha}{(1-\alpha)\tilde{Q}}\left\{1+\alpha-2\alpha\kappa\right\}\\ &-\frac{2}{9}\frac{\alpha^{1/2}}{(1-\alpha)\tilde{Q}^{1/2}}\left\{\alpha(1+\alpha)\kappa-2(4\alpha^2-7\alpha+4)\right\},\end{aligned} \tag{4.147}$$

which is consistent with Billingham [2006].

The two equations (4.143) and (4.147) decouple from (4.142) to give an autonomous system with two variables (recall that κ is a function of α only and $\tilde{Q}$ is a function of $\tilde{P}$ only). Rather than integrate these equations with respect to S, we can consider $\tilde{P}$ as a function of α by using (4.143) and (4.147) to write

$$\frac{d\tilde{P}}{d\alpha} = \frac{d\tilde{P}}{ds}\left(\frac{d\alpha}{ds}\right)^{-1} = f(\alpha,\tilde{P}). \tag{4.148}$$

We now consider boundary conditions on α and $\tilde{P}$. At $X=0$, we want to apply the boundary condition $\hat{H}_0(0,X)=0$, while $\hat{H}_0$ remains bounded, so the aspect ratio $\alpha\to 0$. The amplitude of oscillations in $\hat{H}_0$ tends to zero as $X\to\infty$, so $\alpha\to 1$ as $X\to\infty$. The leading order velocity potential $\tilde{P}$ is bounded as $X\to 0$ and tends to zero as $X\to\infty$. We integrate from $\alpha=0$ to $\alpha=1$, seeking a solution $\tilde{P}(\alpha)$ that is bounded as $\alpha\to 0$ and that has $\tilde{P}=(1+X)^2\tilde{P}\to 0$ as $\alpha\to 1$.

The limit $\alpha\to 0$ is an integrable singularity for $\tilde{P}(\alpha)$. We can expand κ for small α to find

$$\kappa(\alpha)\equiv\frac{\mathbf{K}(1-\alpha)}{\mathbf{E}(1-\alpha)}\sim\log(4)-\frac{\log\alpha}{2}+O(\alpha\log^2\alpha). \tag{4.149}$$

If $\tilde{P}(0)<0$, as suggested by our numerical solutions, then $\tilde{Q}$ tends to a non-zero constant as $S\to 0$, and we find from (4.143) that

$$\frac{d\tilde{P}}{dS}=O(1)\quad\text{as}\quad S\to 0 \tag{4.150}$$

At leading order for small α, (4.147) gives

$$\frac{d\alpha}{dS} \sim \frac{16}{9}\frac{\alpha^{1/2}}{\tilde{Q}^{1/2}} + O(\alpha) \tag{4.151}$$

which has solution

$$\alpha^{1/2} \sim \frac{8}{9}\frac{S}{\tilde{Q}^{1/2}}, \tag{4.152}$$

so $\alpha = O(S^2)$ for small S. Combining (4.150) and (4.151) we see that

$$\frac{d\tilde{P}}{d\alpha} \propto \alpha^{-1/2} \quad \text{for} \quad \alpha \ll 1, \tag{4.153}$$

which is consistent with $\tilde{P}$ tending to a finite value as $\alpha \to 0$.

To find the initial value $\tilde{P}(0)$, we must link to the far-field behaviour of $\bar{P}$. As $X \to \infty$, we seek a solution with $\alpha \to 1$ and $\bar{P} \to 0$. The equivalent condition on $\tilde{P}$ is $\tilde{P} = o((1+X)^{-2})$ as $X \to \infty$, or $\tilde{P} = o(e^{-2S})$ as $S \to \infty$. As discussed by Billingham [2006], this means we have to approach the stable node at $\tilde{P} = 0$, $\alpha = 1$ in the direction parallel to the α axis in the $(\alpha, \tilde{P})$ plane. This is because, for $1 - \alpha \ll 1$ and $\tilde{P} \ll 1$, the linearised version of (4.143) is

$$\frac{d\tilde{P}}{dS} \approx -\frac{3}{2}\tilde{P}, \tag{4.154}$$

which has solution $\tilde{P} = O(e^{-3S/2})$, which decays too slowly for $\bar{P} \to 0$. The linearisation holds for $(1-\alpha)$ and $\tilde{P}$ being of the same order. To achieve faster decay, $\tilde{P}$ must approach 0 much faster than α approaches 1, which means the correct trajectory should reach the node while travelling parallel to the α-axis.

The derivative $d\tilde{P}/dS$ is not finite at $\alpha = 0$, and the functions (4.143) and (4.147) are not defined at $\alpha = 0$, so we integrate from $(\alpha, \tilde{P}) = (1-b, 0)$ to $\alpha = b$, where $b \ll 1$. We integrate the ODE (4.148) using the 'ode45' routine in Matlab, with small tolerances and evaluate the elliptic integrals using the 'ellipke' function in Matlab. We can also perform this numerical calculation in Maple. Both Maple and Matlab show convincing convergence towards the value $\bar{P}(0) = -0.2031$ as $b \to 0$. This is in disagreement with the value $\bar{P}(0) = -0.1939$ obtained by Billingham [2006]; Billingham does not have details of his calculation.

We should also solve the equation for A. If α and $\tilde{Q}$ are known functions of S, then (4.142) gives a separable equation for $A(s)$, which we solve to find

$$\log\left(\frac{A(S_1)}{A(S_2)}\right) = \frac{4}{9}\int_{S_1}^{S_2} \frac{1}{\alpha^{1/2}\tilde{Q}^{1/2}}[2(1+\alpha) - \alpha\kappa]dS. \tag{4.155}$$

For large X, we expect to find

$$A \sim \frac{1}{\lambda^*}\frac{2}{3}(1+X)^2, \tag{4.156}$$

so it is helpful to rescale by defining $\tilde{A} = A/(1+X)^2$, which satisfies

$$\frac{d\tilde{A}}{dS} = \tilde{A}\left\{\frac{4}{9}\frac{1}{\alpha^{1/2}\tilde{Q}^{1/2}}[2(1+\alpha)-\alpha\kappa]-2\right\}. \tag{4.157}$$

The term in braces in this equation is finite for all α, and tends to zero as $\alpha \to 1$.

In order to apply the boundary condition $\hat{H}_0 = 0$ at $\hat{x} = 0$, $X = 0$, we must have $A(0) = 0$ for consistency with the leading order Bernoulli equation (4.100). For small X, we want $A \to A_X(0)\cdot X$. For $\alpha \ll 1$:

$$\frac{d\tilde{A}}{dS} \approx \tilde{A}\left\{\frac{8}{9}\frac{1}{\alpha^{1/2}\tilde{Q}^{1/2}}-2\right\}, \tag{4.158}$$

so now we have

$$\frac{d\tilde{A}}{dS} = \tilde{A}\left\{\frac{1}{S}-2\right\} \tag{4.159}$$

which is consistent with $\tilde{A} = O(S)$ as $S \to 0$.

We find

$$\lambda^* = \lim_{\alpha_1\to 0}\frac{2}{3}\left(\frac{\tilde{Q}(0)}{\alpha_1}\right)^{1/2}\exp\left(-\int_{\alpha_1}^{1}\frac{\left\{\frac{4}{9}\frac{1}{\alpha^{1/2}\tilde{Q}^{1/2}}[2(1+\alpha)-\alpha\kappa]-2\right\}}{\frac{d\alpha}{dS}(\alpha,\tilde{Q})}d\alpha\right). \tag{4.160}$$

As this calculation requires the path $\tilde{Q}(\alpha)$, it can be combined with the integration of $d\tilde{P}/d\alpha$ to find $\tilde{P}(0)$. We find $\lambda^* = 1.8071$ for $b = 1e-7$ in comparison to the value $0.8231^{-3} = 1.7993$ obtained by Billingham [2006]. Figure 4.8 shows the solution $\tilde{P}(\alpha)$, $\tilde{A}(\alpha)$ for the correctly bounded solution, and also the solution envelope for $\hat{H}_0$ in terms of X.

4.6.3 Asymptotic solution for $A \ll 1$

An important limit of the oscillator solutions is the case $A \to 0$, which we will find is applicable to the limit $X \to 0$, where $A = O(X)$. Figure 4.7 shows a sequence of numerical oscillator solutions for various A with Q, B and E fixed. As $A \to 0$ we find that the solution H approaches 0 in a highly curved neck region near $x = 1/2$, which requires a large number of uniformly-spaced points in the spectral solution to resolve accurately.

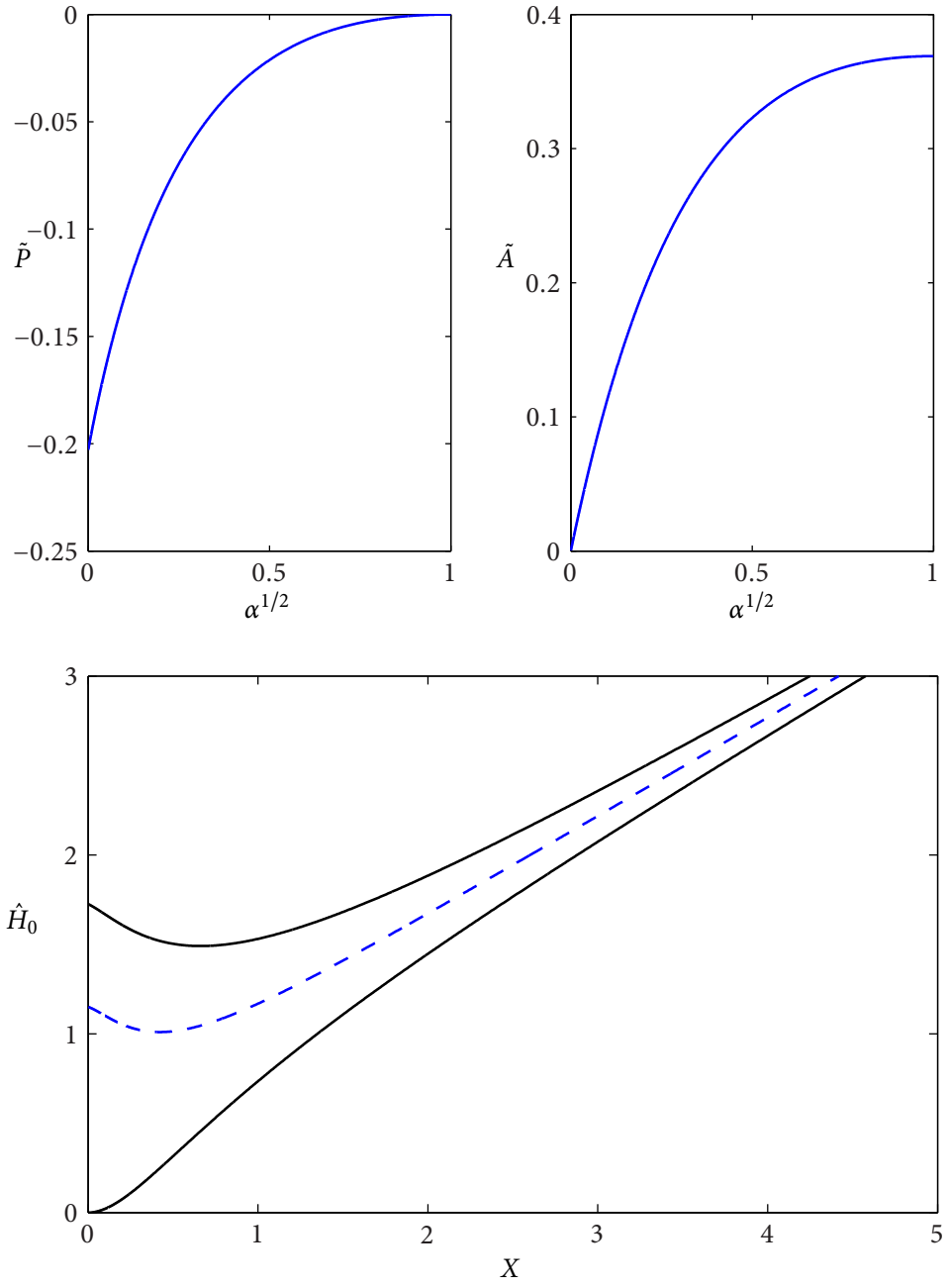

Figure 4.8: The solution to the secularity equations for $\eta = 0$ that has $\tilde{P} \to 0$ as $X \to \infty$. For this density ratio, the oscillator equations can be solved exactly in terms of elliptic integrals. The top two plots show the solution $\tilde{P}(\alpha)$ and $\tilde{A}(\alpha)$ that satisfy $\tilde{P}(X) \to 0$ as $X \to \infty$. The lower plot shows the envelope for $\hat{H}_0$ (solid black lines) and the mean value of $\hat{H}_0$ (dashed blue line). This solution is calculated by integrating from $\alpha = 10^{-7}$ to $1 - 10^{-7}$.

We therefore want to find an asymptotic solution to the system (4.109) to (4.112) in the limit $A \to 0$. We choose a coordinate system so that the minimum of H occurs at $x = 0$. The solution is symmetric about $x = 1/2$, so we can focus our attention on the interval $0 < x < 1/2$. We find an outer region where $x \gg A^2$, in which H tends towards a constant, parabola-like shape as $A \to 0$. This outer solution satisfies a linear PDE, and is dependent on the density in both fluids. We then rescale to an inner region of size A^2, where the linearisation fails. Here the leading order equation is a nonlinear ODE, which we solve exactly and match to the outer solution.

We then calculate the integrals necessary for the secularity conditions. In particular, the integral of H^{-1} requires both the inner and outer solutions, and is shown to depend logarithmically on A at leading order.

Outer solution

In the outer region, we can write $H \sim H_0 + o(1)$ and $\Psi \sim \Psi_0 + o(1)$, where H_0 and Ψ_0 satisfy the Bernoulli equation

$$\omega^2 H_{0xx} = \omega B \Psi_{0x} - \frac{\mu Q}{2}. \tag{4.161}$$

We integrate this once to reach

$$\omega^2 H_{0x} = \omega B \Psi_0 - \frac{\mu Q}{2}\left(x - \frac{1}{2}\right) \tag{4.162}$$

for $0 < x < 1$, and by periodicity elsewhere. The constant of integration in (4.162) has been chosen so that $H_0(0) = H_0(1)$ if Ψ_0 is antisymmetric about the line $x = 1/2$.

If $B = 0$, we can integrate (4.162) again to reach

$$H_0 = kx(1 - x) \tag{4.163}$$

for $0 < x < 1$ and by periodicity elsewhere, where

$$k = \frac{\mu Q}{4\omega^2}. \tag{4.164}$$

Thus H_0 has a discontinuous first derivative at $x = 0$. Assuming that H is symmetric and Ψ antisymmetric, we find from (4.162) that for any value of B, H_{0x} is discontinuous at $x = 0$, with $H_{0x}(0\pm) = \pm k$, with k given by (4.164). We must use Fourier series to calculate

Ψ_0 from H_0 to satisfy the condition $\Psi_{0y} = -H_{0x}$. We write

$$H_0(x) = kx(1-x) + \sum_{n=1}^{\infty} c_n(\cos(2\pi nx) - 1) \tag{4.165}$$

and

$$\Psi_0 = -\sum_{n=1}^{\infty} a_n \sin(2\pi nx). \tag{4.166}$$

Given that $\Psi_{0y} = -H_{0x}$, we find from (4.162) that

$$a_n = -\frac{\mu Q}{(2\pi n\omega)^2} + \frac{B\mu Q}{(2\pi n\omega)^2(B - 2\pi n\omega)} \qquad \text{for } n \geq 1 \tag{4.167}$$

and

$$c_n = \frac{B\mu Q}{(2\pi n\omega)^2(B - 2\pi n\omega)} \qquad \text{for } n \geq 1. \tag{4.168}$$

We find from (4.168) that the Fourier series component of (4.165) converges sufficiently rapidly to have a continuous first derivative everywhere, and so the discontinuities are contained in the term $kx(1-x)$.

Figure 4.9 shows two outer solutions $\hat{H}_0$ calculated using (4.165) for different values of B. The leading order expansion for small x is $H \sim kx$, which we will use as a matching condition for the neck region analysis.

Solution in neck region

The repeated outer solution shown in figure 4.9 is 'V' shaped near $x = 0$ and touches $H = 0$. The neglected term A^2/H^2 in the nonlinear Bernoulli equation (4.109) can be balanced by curvature at leading order in a region of width $x = O(A^2)$ in which $H = O(A^2)$.

We rescale into this region by letting $x = A^2\tilde{x}$, $y = A^2\tilde{y}$, $H = A^2\tilde{H}$, $\Psi = A^2\tilde{\Psi}$. Then the Bernoulli equation becomes

$$\omega^2 \tilde{H}_{\tilde{x}\tilde{x}} = A^2\omega B\tilde{\Psi}_{\tilde{x}} + \frac{\mu}{2}\left[\frac{1}{\tilde{H}^2} - A^2Q\right]. \tag{4.169}$$

Now let $\tilde{H} = \tilde{H}_0 + O(A^2)$. At leading order in A^2 we have:

$$\omega^2 \tilde{H}_{0\tilde{x}\tilde{x}} = \frac{\mu}{2}\frac{1}{\tilde{H}_0^2}. \tag{4.170}$$

We can integrate this once to get

$$\tilde{H}_{0\tilde{x}}^2 = k^2 - \frac{\mu}{\tilde{H}_0\omega^2}, \tag{4.171}$$

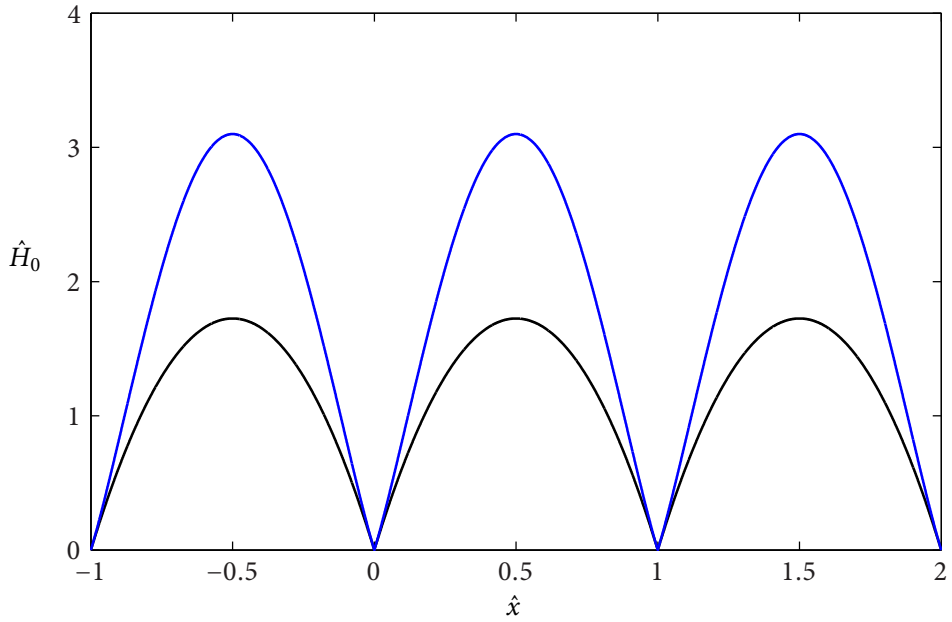

Figure 4.9: The interface position $\hat{H}_0$ for the outer solution for $A \ll 1$, defined by (4.165). Here $\tilde{P} = -0.2029$, which is the value of $\tilde{P}(0)$ that satisfies $\tilde{P}(X) \to 0$ as $X \to 0$ for the elliptic integral solution for $\eta = 0$ in section 4.6.2. The value of ω is chosen for this calculation so that $\omega k = 1$ at $\hat{x} = 0$, which is the correct boundary condition at $X = 0$ for $\eta = 0$. The black line shows $\hat{H}_0$ for $\mu = 1$, $\eta = 0$. The blue line shows $\hat{H}_0$ defined by (4.165) for $\mu = 1$, $\eta = 1$, so $B = 4/9$.

where the constant of integration has been chosen so that $\tilde{H}_{0\tilde{x}} \to k$ as $\tilde{H}_0 \to \infty$, to match the inner limit of the outer solution. At $\tilde{x} = 0$, we have $\tilde{H}_{0\tilde{x}} = 0$, so

$$\tilde{H}_0(0) = \frac{\mu}{\omega^2 k^2}. \tag{4.172}$$

We define a rescaled variable $Y = \tilde{H}_0/\tilde{H}_0(0)$. We can rewrite (4.171) in terms of Y to give

$$Y_{\tilde{x}} = \frac{k}{\tilde{H}_0(0)}\sqrt{1 - \frac{1}{Y}}. \tag{4.173}$$

This separable equation can be integrated to give $\tilde{x}$ as a function of Y, yielding

$$\frac{k}{\tilde{H}_0(0)}\tilde{x} = \sqrt{Y(Y-1)} + \frac{1}{2}\log\left(2Y - 1 + 2\sqrt{Y(Y-1)}\right). \tag{4.174}$$

We expand (4.174) for large Y to reach

$$\frac{k}{\tilde{H}_0(0)}\tilde{x} = Y + \frac{1}{2}\log Y - \frac{1}{2} + \log 2 + O(Y^{-1}), \tag{4.175}$$

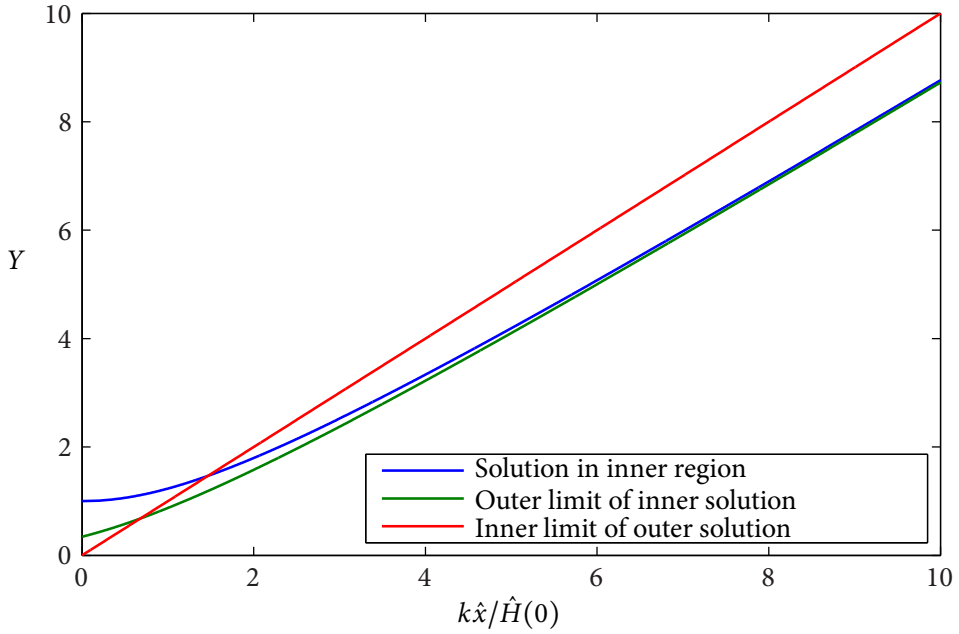

Figure 4.10: The leading order solution for H in the inner (neck) region, given by (4.174), and the matching conditions with the outer region.

and so the outer limit of the inner solution is

$$\tilde{H}_0 \sim k\tilde{x} + \tilde{H}_0(0)\left[-\frac{1}{2}\log\left(\frac{\tilde{H}_0}{\tilde{H}_0(0)}\right) + \frac{1}{2} - \log 2\right] + O(\tilde{H}_0(0)^2/\tilde{H}_0). \tag{4.176}$$

Matching

We match the inner and outer solutions by the value of H_x. We know $H_{0x} \to k$ as $x \to 0$, where

$$k = \frac{\mu Q}{4\omega^2}. \tag{4.177}$$

By choosing the same k in the inner solution, we can match the solution in the inner and outer regions, with the matching term given by $H \sim kx$.

The current matching condition only involves the first term: we choose k to be the same as derived from the inner limit of the outer solution. For fixed A, the unmatched term in square brackets in (4.176) grows as $\tilde{x} \to \infty$. However, the error caused by this unmatched term goes to zero as $A \to 0$. The inner solution and its outer limit are plotted in figure 4.10.

The leading order composite solution is given by

$$H(x) \sim H_0(x) + A^2 \tilde{H}_0\left(\frac{x}{A^2}\right) - kx, \tag{4.178}$$

in the interval $0 < x < 1/2$, by reflection in $1/2 < x < 1$, and periodicity elsewhere.

Calculation of integrals

To implement the secularity conditions, we need to calculate a number of integral functions of the composite solution. The analysis so far has assumed that ω is fixed. In fact, ω is determined by the value of E, and so must satisfy the equation

$$E = \omega \int_0^1 H_x^2 dx + \frac{B}{2} \int_0^1 H \Psi_x dx. \tag{4.179}$$

As $A \to 0$ with ω fixed, we find

$$\begin{aligned} E &\sim \omega \int_0^1 H_{0x}^2 dx + \frac{B}{2} \int_0^1 H_0 \Psi_{0x} dx \\ &= \sum_{n=1}^{\infty} \frac{\pi n a_n^2}{2} (4n\pi\omega - B) \\ &= \frac{(\mu Q)^2}{48\omega^3} - \frac{B(\mu Q)^2}{8\pi^2\omega^3} \sum_{n=1}^{\infty} \frac{B - 3\pi n\omega}{n^2(B - 2\pi n\omega)^2}. \end{aligned} \tag{4.180}$$

This leading order expression for $E(\omega)$ is independent of A, so at leading order in A we take $\omega = \omega_0(E)$ by solving (4.180) for ω.

To find A_X and E_X, we also need to evaluate

$$\begin{aligned} \int_0^1 H(x) dx &\sim \int_0^1 H_0(x) dx + O(A^2) \\ &= \frac{\mu Q}{24\omega^2} - \sum_{n=1}^{\infty} \frac{B\mu Q}{(2\pi n\omega)^2 (B - 2\pi n\omega)} \end{aligned} \tag{4.181}$$

and

$$\begin{aligned} \int_0^1 H(x) \Psi_x(x) dx &\sim \int_0^1 H_0(x) \Psi_{0x}(x) dx + O(A^2) \\ &= -\pi \sum_{n=1}^{\infty} n a_n^2. \end{aligned} \tag{4.182}$$

The remaining integral that we require for the secularity equations is

$$\int_0^1 \frac{1}{H(x)} dx. \tag{4.183}$$

The calculation of this integral is more interesting, because it has $O(1)$ contributions from the inner and outer regions. Neither the inner nor outer integral converges separately, as $H \to kx$ in the matching region and the integral of x^{-1} does not converge as $x \to 0$ or $x \to \infty$. However, for a given value of A, the composite solution is smooth, bounded below by a non-zero constant and is only integrated over a finite x interval, so the composite integral should converge. We can write

$$\begin{aligned}\int_0^1 H^{-1}dx &= 2\int_0^{1/2} H^{-1}dx \\ &\sim 2\int_\delta^{1/2} \frac{1}{H_0(x)}dx + 2\int_0^\delta \frac{1}{A^2\tilde{H}_0(x/A^2)}dx \\ &= 2\int_\delta^{1/2} \frac{1}{H_0(x)}dx + 2\int_0^{\delta/A^2} \frac{1}{\tilde{H}_0(\tilde{x})}d\tilde{x}.\end{aligned} \tag{4.184}$$

We choose the intermediate lengthscale δ to satisfy $A^2 \ll \delta \ll 1$. We can explicitly subtract the singularity from the outer integral by writing

$$\begin{aligned}\int_\delta^{1/2} \frac{1}{H_0(x)}dx &= \int_\delta^{1/2}\left(\frac{1}{H_0(x)} - \frac{1}{kx}\right)dx + \int_\delta^{1/2}\frac{1}{kx}dx \\ &= \int_0^{1/2}\left(\frac{1}{H_0(x)} - \frac{1}{kx}\right)dx + \frac{1}{k}\left(\log\frac{1}{2} - \log\delta\right) + O(\delta),\end{aligned} \tag{4.185}$$

where we have replaced the limit of integration as $\delta \to 0$ by 0. We can do the integral involving $\tilde{H}_0$ in (4.185) exactly, and then expand for $A^2 \ll \delta \ll 1$:

$$\begin{aligned}\int_0^{\delta/A^2} \frac{1}{\tilde{H}_0(\tilde{x})}d\tilde{x} &= \frac{1}{k}\int_1^{\tilde{H}_0(\delta/A^2)/\tilde{H}_0(0)} \frac{dY}{Y\sqrt{1-1/Y}} \\ &= \frac{2}{k}\left[\log\left(\sqrt{Y-1}+\sqrt{Y}\right)\right]_1^{\tilde{H}_0(\delta/A^2)/\tilde{H}_0(0)} \\ &\sim \frac{2\log 2}{k} + \frac{1}{k}\log\left(\frac{k\delta}{A^2\tilde{H}_0(0)}\right).\end{aligned} \tag{4.186}$$

Combining the expression for the outer integral from (4.185) and the expression for the inner integral from (4.186), we obtain

$$\int_0^1 H^{-1}dx \sim 2\int_0^{1/2}\left(\frac{1}{H_0(x)} - \frac{1}{kx}\right)dx + \frac{2}{k}\log\left(\frac{2k}{A^2\tilde{H}_0(0)}\right), \tag{4.187}$$

which is independent of δ, as it should be, but does have a logarithmic dependence on A.

We can calculate these integrals exactly for $B = 0$. We know that $H_0 = kx(1-x)$, so

$$2\int_0^{1/2}\left(\frac{1}{H_0(x)} - \frac{1}{kx}\right)dx = \frac{1}{k}\log 2, \tag{4.188}$$

For any density ratio, the constants k and $\tilde{H}_0(0)$ which appear in (4.187) are given by

$$k = \frac{\mu Q}{4\omega^2}, \qquad \tilde{H}_0(0) = \frac{\mu}{\omega^2 k^2}, \tag{4.189}$$

and so when $B = 0$ we find

$$\int_0^1 H^{-1} dx \sim \frac{8\omega^2}{\mu Q} \log\left(\frac{\mu^2 Q^3}{2^4 \omega^4 A^2}\right). \tag{4.190}$$

For $\eta > 0$, we have $B > 0$ and must resort to the Fourier series expression for $H_0(x)$ in (4.165) to evaluate the outer integral in (4.187). The integral

$$\int_0^{1/2} \left(\frac{1}{H_0(x)} - \frac{1}{kx}\right) dx \tag{4.191}$$

should converge for any truncation of the sum in (4.165).

Figures 4.11 compares various properties, including these integrals, for oscillator solutions with $A < 1$, for the numerical solutions, the small-A asymptotic solution, and the exact solution for $B = 0$. We find that there is good agreement between the exact solution and the small-A asymptotic solution when $A < 0.1$, and between the exact solution and numerical solution for $N = 200$ when $A > 0.1$. Figure 4.12 shows solution properties for $B = 1$, where there is no exact solution, but the asymptotic and numerical solutions again agree when $A \approx 0.1$.

4.6.4 Asymptotic solution for $E \ll 1$

For large X, we expect the amplitude of oscillation in $\hat{H}_0$ and $\hat{\Phi}_0$ to tend to zero, with the mean of $\hat{H}_0$ given by $\hat{H}_0 = O(1 + X)$. The parameter E is always positive and strictly decreasing, so for large X we expect solutions with small E.

If $E \ll 1$, we can obtain an approximate solution by linearising about constant H. We let

$$H(x) = \bar{H}_0 + K\cos(2\pi x), \qquad \Psi = -K\sin(2\pi x)e^{-2\pi y}, \tag{4.192}$$

where $\bar{H}_0$ and K are constants. Then by linearising the Bernoulli equation, we find that

$$\bar{H}_0 = \frac{A}{\sqrt{Q}}, \qquad 4\pi\omega = B + \sqrt{B^2 + \frac{4\mu A^2}{\bar{H}_0^3}}. \tag{4.193}$$

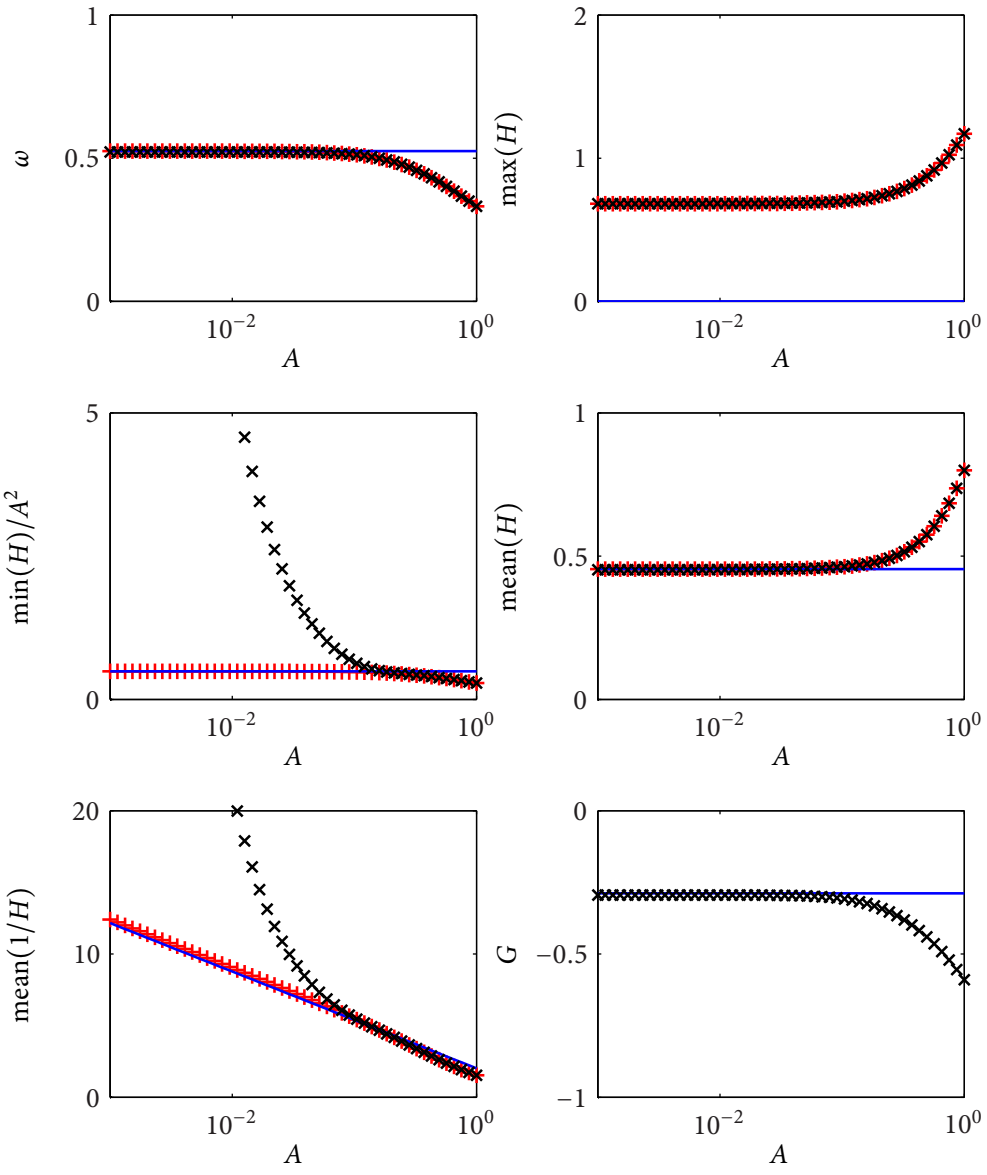

Figure 4.11: Solution outputs for $Q = 3$, $E = 1.3$ and $B = 0$ for $A < 1$. Here the equations are ODEs that can be solved exactly. Exact solutions are plotted with red plusses, numerical solutions with black crosses, and the small A asymptotic results with solid blue lines. The numerical solutions have $N = 200$, and H_{xx} calculated using two-point centred finite difference formulae. The exact solution tracks the numerical solution for $A > 0.1$. For $A < 0.1$, the small-A asymptotic solution is much closer to the exact solution than the numerical solution is. The quantity G is defined as $\int_0^1 H\Psi_x dx$.

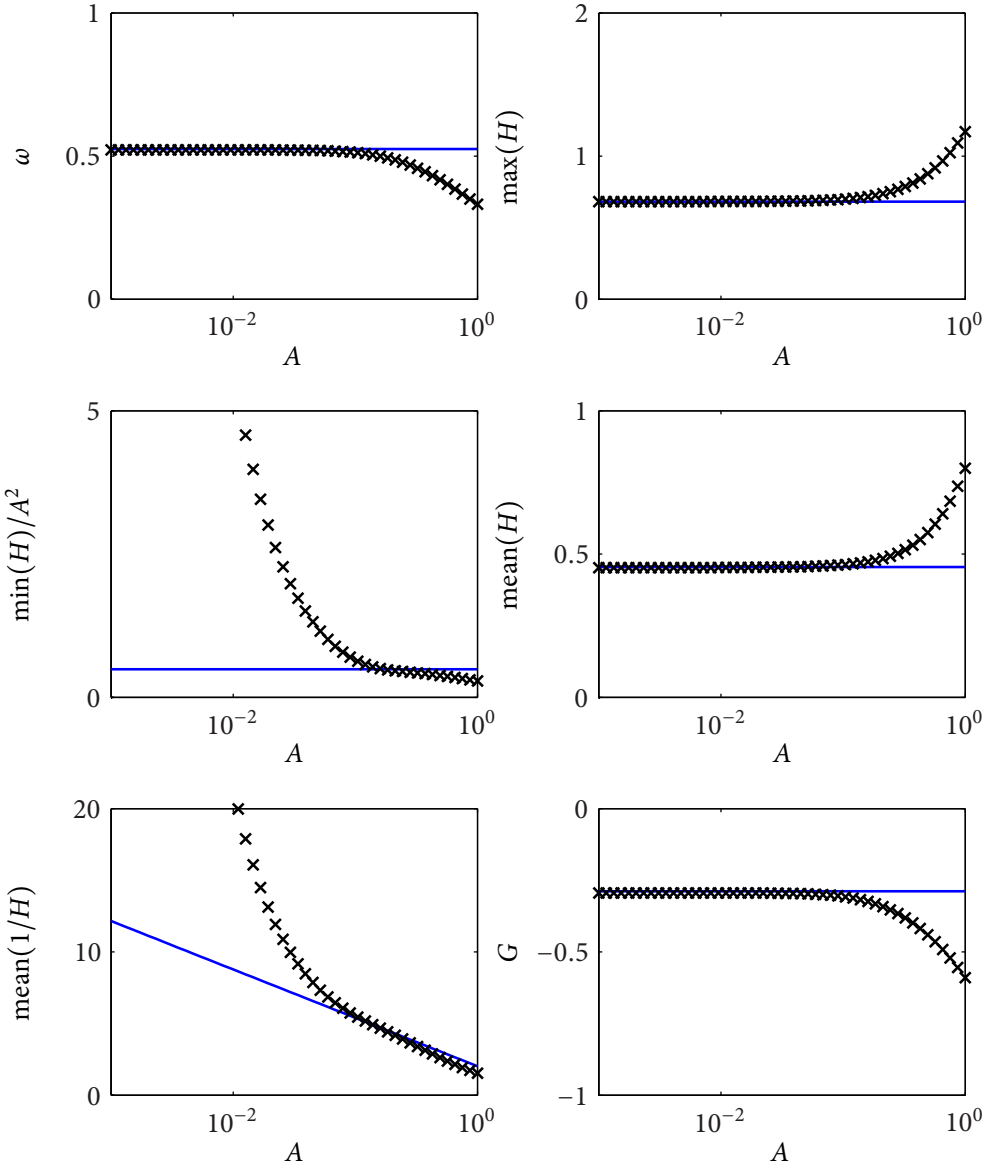

Figure 4.12: Solution outputs for $Q = 3$, $E = 1.3$ and $B = 1$ for $A < 1$. Numerical solutions are plotted with black crosses, and asymptotic results with solid blue lines. The numerical solutions have $N = 200$, and H_{xx} calculated using two-point centred finite difference formulae. We no longer have an exact solution for comparison. The asymptotic and numerical solutions are in rough agreement at $A = 0.1$. Above this, we expect the numerical solution to be more accurate, while the asymptotic solution should be more accurate for $A < 0.1$. The deviation at $A = 0.1$ is consistent with the comparison to the exact result in figure 4.11

The amplitude of the oscillation, K, is determined by the value of E. We can evaluate E using (4.112) to reach

$$E = 2\pi K^2\left(\pi\omega - B/4\right) = \frac{\pi K^2}{2}\sqrt{B^2 + \frac{4\mu A^2}{\bar{H}_0^3}}. \tag{4.194}$$

Recall $B = 4\eta(1+X)^2/9$, while

$$\bar{H}_0 \to \frac{1+X}{\lambda^*}, \quad A \to \frac{2(1+X)^2}{3\lambda^*} \quad \text{as } X \to \infty. \tag{4.195}$$

According to (4.193), the flow in the slender wedge has negligible influence on the determination of ω once

$$(1+X)^3 \gg \frac{9\mu}{\eta^2}\lambda^*. \tag{4.196}$$

With $\hat{H}_0$ given by (4.192), the derivative E_X from (4.106) becomes

$$\frac{dE}{dX} = \frac{5}{3}\frac{A\mu}{\omega}\left(1 - \int_0^1 \frac{1}{1+\alpha\cos(2\pi x)}dx\right) - \frac{10}{9}\pi\eta(1+X)K^2, \tag{4.197}$$

where the small parameter $\alpha = K/\bar{H}_0$. We therefore require the expansion for small α of the function

$$f(\alpha) := \int_0^1 \frac{1}{1+\alpha\cos(2\pi x)}d\hat{x} = (1-\alpha^2)^{1/2}. \tag{4.198}$$

Expanding this for small α, we find

$$f(\alpha) \sim 1 + \alpha^2/2 + O(\alpha^4) \quad \text{as} \quad \alpha \to 0. \tag{4.199}$$

So now we have

$$\frac{dE}{dX} = -K^2\left[\frac{5}{6}\frac{A\mu}{\omega\bar{H}_0^2} + \frac{10}{9}\eta(1+X)\pi\right], \tag{4.200}$$

which is always negative. For large X, or for all X if $\mu = 0$, we find that $\omega \propto (1+X)^2$, $K \propto (1+X)^{-7/2}$ and $E \propto (1+X)^{-5}$. If $\eta = 0$, we find $\omega \propto (1+X)^{1/2}$, $E \propto (1+X)^{-5/2}$ and $K \propto (1+X)^{-3/2}$.

For large X, we expect to find $A = O((1+X)^2)$, $P \to 0$ and $E \to 0$. In this limit, the secularity equations are not particularly sensitive to small changes in A or $\bar{P}$, but for small E, an integration error might mean a negative value of E is requested by a numerical BVP or ODE solver. We can reduce the sensitivity of the numerical integration of the secularity equations to small errors by solving for $R(X)$ rather than $E(X)$, where $R(X) = -\log(E(X))$. By considering R instead, we can ensure solution parameters are only requested for positive values of E. Under this change of variables, we have $R_X = -E_X/E$.

4.7 Solution of secularity equations

4.7.1 Boundary conditions as $X \to 0$: An inner problem

In section 4.5 we derived an asymptotically homogenised description for capillary waves along the free surface on the positive X-axis. Here 'asymptotically homogenised' or 'method of multiple scales' means that for any given value of X, the free surface displacement tends to a strictly periodic function as the small parameter $\hat{\epsilon} \to 0$, which is the limit in which the short wavelength of individual oscillations separate from slow variation of the oscillator parameters.

In our system, the point $(\hat{x}, \hat{y}) = (0, 0)$ corresponds to a discontinuous change in boundary condition along the line $\hat{y} = 0$. We have a free surface along $\hat{y} = 0$, $\hat{x} > 0$, in which the oscillator equations can support oscillations indefinitely, but a rigid wall on $\hat{y} = 0$, $\hat{x} < 0$ where $\hat{\Phi}$ must decay monotonically as $\hat{x} \to -\infty$. The free surface displacement and velocity potential take an $O(1)$ number of oscillations to adjust to the imposition of the rigid wall conditions. On the $\hat{x}$-scale, the adjustment length L depends on the density ratio between the two fluids, but is independent of the small parameter $\hat{\epsilon}$, so does not vanish even in the limit $\hat{\epsilon} \to 0$.

The result is that the inner region, a region of size a few wavelengths centred around the contact point, is non-homogenisable, and we must explicitly solve a non-periodic half-plane-problem in order to interpret the contact angle condition

$$\omega \hat{H}_{0\hat{x}}(\hat{x} = 0, X = 0) = 1 \tag{4.201}$$

as a boundary condition for the multiple scales analysis. We now consider the form this inner problem should take.

The original, non-multiple scale, kinematic equation (4.33) for $P(x)$ is

$$\frac{2}{3}(x + x_c)H_x - \frac{2}{3}H = (HP_x)_x \tag{4.202}$$

which can be integrated once to give

$$P_x = \frac{2}{3}(x + x_c) - \frac{4}{3}\frac{\int_0^x H(x')dx'}{H(x)}, \tag{4.203}$$

where we have used the boundary condition $H(0) = 0$. Now compare this to the secularity

equations for $\bar{P}$ and A:

$$\frac{d\bar{P}}{dX} = \frac{2}{3}(1+X) - A(X)\int_0^1 \frac{1}{\hat{H}_0}d\hat{x} \tag{4.204}$$

and

$$\frac{dA}{dX} = \frac{4}{3}\int_0^1 \hat{H}_0 d\hat{x}, \tag{4.205}$$

and we can see that $A(X)$ measures the area slowly accumulated between the contact point and X. In particular, we must have $A(0) = 0$ for consistency with the boundary condition $\hat{H}_0(0,0) = 0$.

With $A(0) = 0$, at $X = 0$, the leading order kinematic condition for the thin wedge (4.56) gives

$$\bar{P}_X(0) + \omega\hat{P}_{0\hat{x}}(\hat{x},0) = \frac{2}{3}. \tag{4.206}$$

At $X = 0$ the leading order Bernoulli equation (4.100) is

$$\mu\left[\frac{1}{3}\bar{P} - \frac{2}{3}(\bar{P}_X + \omega\hat{P}_{0\hat{x}}) + \frac{1}{2}(\bar{P}_X + \omega\hat{P}_{0\hat{x}})^2\right] + \frac{2}{3}\eta\omega\hat{\Phi}_{0\hat{x}} = \omega^2\hat{H}_{0\hat{x}\hat{x}}. \tag{4.207}$$

Substituting for $\hat{P}_0$ from (4.206), this becomes

$$\mu\left[\frac{1}{3}\bar{P}(0) - \frac{2}{9}\right] + \frac{2}{3}\eta\omega\hat{\Phi}_{0\hat{x}} = \omega^2\hat{H}_{0\hat{x}\hat{x}}. \tag{4.208}$$

The kinematic condition on the fat wedge gives

$$\hat{\Phi}_{0\hat{y}} = -\frac{2}{3}\hat{H}_{0\hat{x}}, \tag{4.209}$$

on $\hat{y} = 0$ for $\hat{x} > 0$. This must be considered along with the rigid wall condition

$$\hat{\Phi}_{0\hat{y}} = 0, \tag{4.210}$$

on $\hat{y} = 0$ for $\hat{x} < 0$, and that requirement that $\hat{\Phi}_0$ must be harmonic in $\hat{y} > 0$.

There are three unknown parameters in the oscillator equations: $A(X)$, $\bar{P}(X)$ and $E(X)$, with $\omega(X)$ determined as an eigenvalue from the leading order oscillator equations. If $A(0) = 0$ and $\hat{H}_0$ is finite as $X \to 0$, we have $A = O(X)$. The initial value $\bar{P}(0)$ is unknown, but $\bar{P}_X = O(1)$ as $A \to 0$, so $\bar{P} = O(1)$ as $X \to 0$. The initial value of $E(X)$ is also unknown, with $E(X)$ strictly decreasing and $E_X(0) = O(A\log A + \eta)$. We therefore expect $E(0) = O(1)$. This indicates that the inner limit of the secularity equations is $A = O(X)$, $\bar{P} = O(1)$ and $E = O(1)$ as $X \to 0$.

We discussed solutions to the oscillator equations for $A \ll 1$, $\bar{P} = O(1)$ and $E = O(1)$ in section 4.6.3. We found that for small A, the solution $\hat{H}_0(\hat{x})$ tends towards a constant parabola-like shape in an outer region, shown in figure 4.9. For $A > 0$, these parabola-like shapes are connected by thin neck regions, of width and height $O(A^2)$. $\hat{H}_{0\hat{x}}$ changes sign but not magnitude as it passes through a neck region. We therefore expect that the limit of the oscillator solutions as $X \to 0$ should consist of a sequence of these parabola-like regions, with $\hat{H}_{0\hat{x}}$ discontinuous, changing sign but not magnitude, at points where $\hat{H}_0 = 0$.

When $\eta = 0$, Billingham [2006] showed that the solution at $X = 0$ is $\hat{H}_0 \propto \hat{x}(1 - \hat{x})$ in $0 < \hat{x} < 1$, repeated periodically for $\hat{x} > 1$, so that $\hat{H}_{0\hat{x}}$ is discontinuous whenever $\hat{H}_0 = 0$. However if $\eta > 0$, a strictly periodic solution of this form, where $\hat{H}_0$ is periodic with period 1 for all $\hat{x} > 0$, cannot satisfy the equations derived above for $X = 0$. This is because any non-constant periodic function $\hat{H}_0(\hat{x})$ fed into the half-plane-problem for $\hat{\Phi}_0(\hat{x}, \hat{y})$ gives a solution that is non-periodic along $\hat{x} > 0$, $\hat{y} = 0$, providing an unbalanced non-periodic term in (4.208).

For $\eta \neq 0$, we must instead look for a solution in which $\hat{H}_0(\hat{x})$ and $\hat{\Phi}_0(\hat{x}, 0)$ are not periodic but tend towards a periodic solution as $\hat{x} \to \infty$. Inspired by Billingham [2006] and the small A (hence small X) two-fluid oscillator results from section 4.6.3, we seek a solution that has $\hat{H}_0(\hat{x})$ continuous and always non-negative, with $\hat{H}_{0\hat{x}}(\hat{x})$ changing sign discontinuously whenever $\hat{H}_0 = 0$.

For integration of the secularity conditions, we are interested in the limit as $X \to 0$ of A_X, $\bar{P}$ and E. This limit as $X \to 0$ should be equivalent to the limit as $\hat{x} \to \infty$ of the new inner problem solution. The outer limit of the inner solution is periodic with period 1, and can be expressed in terms of Fourier coefficients:

$$\begin{aligned} \hat{H}_{0\hat{x}} &= \sum_{n=1}^{\infty} a_n(\cos(2\pi n(\hat{x} + \varphi)) - 1), \\ \hat{\Phi}_0(\hat{x}, \hat{y}) &= -\frac{2}{3}\sum_{n=1}^{\infty} a_n \sin(2\pi n(\hat{x} + \varphi)) \exp(-2\pi n \hat{y}) \end{aligned} \tag{4.211}$$

where

$$a_n = -\frac{\mu Q_0}{(2\pi n\omega)^2} + \frac{B_0 \mu Q_0}{(2\pi n\omega)^2(B_0 - 2\pi n\omega)}. \tag{4.212}$$

Here $Q_0 = 4/9 - 2\bar{P}(0)/3$, $B_0 = 4\eta/9$ and φ is a constant phase shift that must be determined as part of the inner problem solution.

The Fourier coefficients given by (4.212) still contain two unknown parameters: the eigenvalue ω and the secularity variable Q_0 which is a function of $\bar{P}(0)$. We expect that $\bar{P}(0)$ will eventually be determined by the condition $\bar{P} \to 0$ as $X \to \infty$. However, the calculation of ω as a function of $\bar{P}(0)$, η and μ requires the solution of the full inner half-plane problem in order to make use of the boundary condition $\omega \hat{H}_{0\hat{x}}(0,0) = 1$.

We can rescale the inner problem so that the resulting half-plane problem has only one independent variable. We do so by letting

$$\omega = \omega_0 \tilde{\omega}, \quad \omega_0 = \frac{\mu Q_0}{2}, \quad \sigma = \frac{8\eta}{9\mu Q_0}, \tag{4.213}$$

and then we find that $\tilde{\omega}$ depends only on σ, and is independent of Q_0. We discuss the resulting single-parameter inner problem in more detail in appendix A.

In terms of these variables, the Fourier coefficients (4.212) become

$$a_n = \frac{1}{\mu Q_0} \frac{1}{\pi^2 n^2 \tilde{\omega}^2} \left(\frac{\sigma}{\sigma - 2\pi n \tilde{\omega}} - 1 \right). \tag{4.214}$$

We can use this Fourier series to write the initial conditions for the other two secularity variables given by

$$A_X(0) = -\frac{4}{3} \sum_{n=1}^{\infty} a_n, \qquad E(0) = \sum_{n=1}^{\infty} \frac{\pi n a_n^2}{2} (4\pi n \omega - B_0), \tag{4.215}$$

as

$$A_X(0) = \frac{1}{\mu Q_0} \tilde{A}(\sigma), \qquad E(0) = \frac{1}{\mu Q_0} \tilde{E}(\sigma) \tag{4.216}$$

where

$$\tilde{A}(\sigma) = \frac{1}{\tilde{\omega}^2} \left(\frac{2}{9} - \frac{4\sigma}{3\pi^2} \sum_{n=1}^{\infty} \frac{1}{n^2(\sigma - 2\pi n \tilde{\omega})} \right) \tag{4.217}$$

and

$$\tilde{E}(\sigma) = \frac{1}{\pi \tilde{\omega}^2} \sum_{n=1}^{\infty} \frac{4\pi n \tilde{\omega} - \sigma}{n(\sigma - 2\pi n \tilde{\omega})^2}. \tag{4.218}$$

If $\tilde{\omega}(\sigma)$ is known, it is straightforward to evaluate $\tilde{A}(\sigma)$ and $\tilde{E}(\sigma)$ using (4.217) and (4.218).

In appendix A, we discuss the numerical calculation of $\tilde{\omega}(\sigma)$. There is some uncertainty as to whether the resulting function $\tilde{\omega}(\sigma)$ is correct, especially as there is a discretisation-related branch structure for this function. However, we do have two constraints on $\tilde{\omega}(\sigma)$. Firstly, we know that $\tilde{\omega}(0) = 1/2$. Secondly, we expect that $\tilde{\omega}(\sigma)$ should

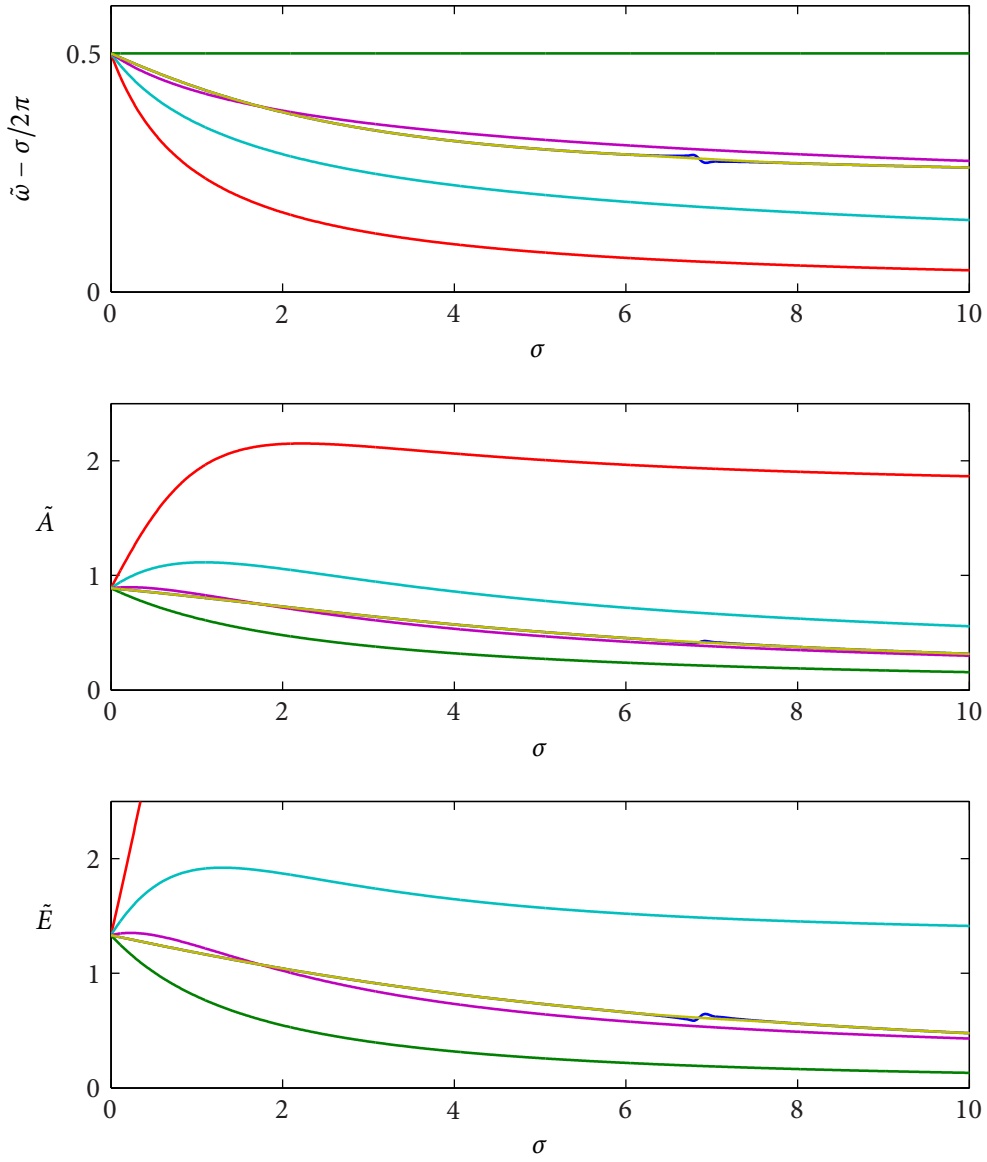

Figure 4.13: The boundary conditions at $X = 0$ can be written in terms of the functions $\tilde{A}(\sigma)$ and $\tilde{E}(\sigma)$ defined by (4.217) and (4.218). However, these function definitions also involve the eigenvalue $\tilde{\omega}(\sigma)$, which is calculated by solving the inner problem discussed in appendix A. This figure shows $\tilde{A}(\sigma)$ and $\tilde{E}(\sigma)$ for some candidates for the function $\tilde{\omega}(\sigma)$. The blue line shows a numerical solution to the inner half-plane-problem, and corresponds to the red line (complete with kink) in figure A.4. The gold line here is identical to the blue line for $\sigma < 6$ and $\sigma > 8$, but uses a cubic spline for $6 < \sigma < 8$, thus smoothing over the kink. The other functions shown are $\tilde{\omega} - \sigma/2\pi = 1/2$ (green), $\tilde{\omega} - \sigma/2\pi = (1+\sigma)^{-1/4}/2$ (magenta), $\tilde{\omega} - \sigma/2\pi = (1+\sigma)^{-1/2}/2$ (cyan) and $\tilde{\omega} - \sigma/2\pi = (1+\sigma)^{-1}/2$ (red).

be continuous, and $\tilde{\omega}(\sigma) > \sigma/2\pi$ for all σ to avoid the singularity in the denominator of (4.217) and (4.218). Figure 4.13 shows $\tilde{A}(\sigma)$ and $\tilde{E}(\sigma)$ calculated for various candidate functions $\tilde{\omega}(\sigma)$ that meet these conditions.

4.7.2 Boundary conditions as $X \to \infty$

The boundary conditions for $X \to \infty$ are much simpler than those at $X = 0$. As $X \to \infty$ we require:

$$\hat{H}_0(\hat{x}, X) \to \frac{1+X}{\lambda^*}, \quad \bar{P} \to 0, \quad \hat{\Phi} \to 0, \tag{4.219}$$

where $\lambda^* = \hat{\epsilon}\lambda_0$. In terms of A, $\bar{P}$ and E, these are equivalent to

$$A(X) \sim \frac{1}{\lambda^*}\frac{2}{3}(1+X)^2, \quad \bar{P}(X) \to 0, \quad E(X) \to 0 \tag{4.220}$$

as $X \to \infty$. We find that solutions to the secularity equations starting from reasonable values of A, $\bar{P}$ and E at $X = 0$ nearly always satisfy $E \to 0$ as $X \to \infty$. If $E = 0$, $\hat{H}_0$ is a constant with respect to X, and we also obtain $A = O(1+X)^2$. However, the boundary condition $\bar{P} \to 0$ is non-trivial, and closes the system by providing a third boundary condition, in addition to knowing A/X and E at $X = 0$ in terms of σ. We must use shooting or a relaxation scheme to relate σ at $X = 0$ to $\bar{P}$ as $X \to \infty$.

4.7.3 Secularity solutions for finite density ratio

We integrate the secularity equations given in section 4.5.5 with boundary conditions from sections 4.7.1 and 4.7.2, using values for $\tilde{\omega}(\sigma)$ calculated by the numerical method discussed in appendix A, and shown by the gold line in figure 4.13. For very small X, we use the asymptotic oscillator solutions for small A discussed in section 4.6.3, and then use the spectral method discussed in section 4.6.1 to find numerical oscillator solutions for larger X. We use the solution for $E \ll 1$ derived in section 4.6.4 as an initial guess for the nonlinear oscillator solver when X is large. We use a shooting scheme to choose $\bar{P}(0)$ so that $\bar{P}(X_{END}) = 0$, where X_{END} is the truncation point of our integration.

For $\eta = 0$, $\mu = 1$, we found an exact solution to the oscillator equations using elliptic integrals, and used this to obtain a numerical solution to the secularity equations. This solution is discussed in section 4.6.2 and plotted in figure 4.8. The unique solution to the secularity equations and boundary conditions has $\bar{P}(0) = -0.2031$. We use a continuation

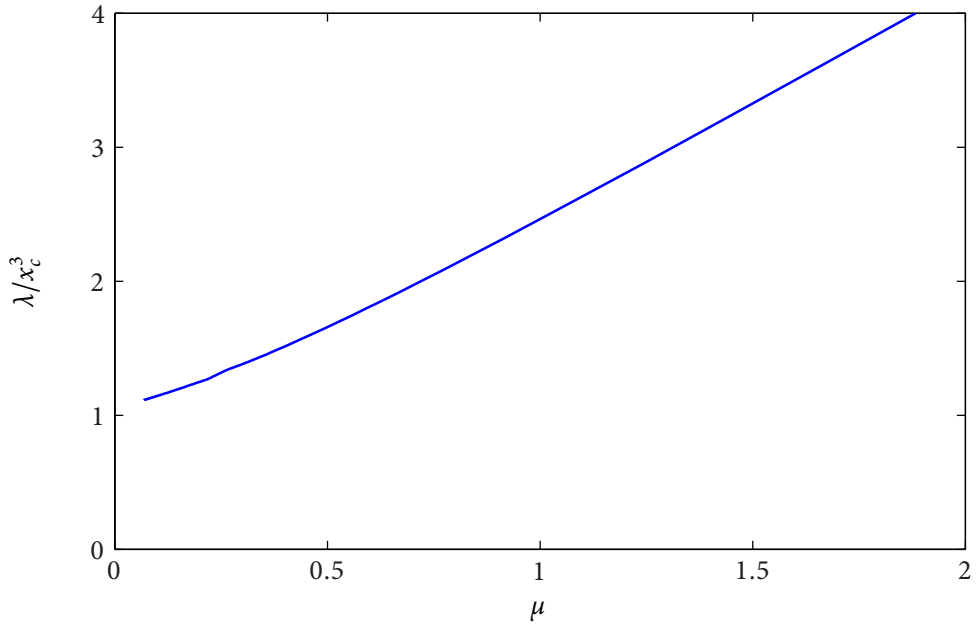

Figure 4.14: The eigenvalue $\lambda^* = \lambda/x_c^3$ resulting from the large-λ asymptotic analysis with $\eta = 1$ and μ varying. This is a rescaling of the result for η varying and $\mu = 1$ shown by the black crosses in figure 4.6.

scheme starting from this solution for $\eta = 0$ to obtain solutions to the secularity BVP for $\eta > 0$. The values of λ^* and $\bar{P}(0)$ obtained from the numerical integration of this BVP, with shooting for $\bar{P}(0)$, are shown in figure 4.6 for $\mu = 1$ and η varying.

We can rescale these results to give solutions for $\eta = 1$ and μ varying, so that the density of the fluid in the fat wedge is fixed. We denote the eigenvalue λ^* corresponding to density parameters η and μ by $\lambda^*(\eta, \mu)$. By rescaling the half-plane problem given in section 4.3.3, we find

$$\lambda^*(1, \eta^{-1}) = \frac{\lambda^*(\eta, 1)}{\eta}. \tag{4.221}$$

The function $\lambda^*(1, \mu)$ obtained by rescaling the solution shown in figure 4.6 is plotted in figure 4.14. These numerical solutions suggest that $\lambda^*(1, \mu) \to \lambda_0^*$ as $\mu \to 0$, where λ_0^* is a constant. If this is true, then we should also find that $x_c^3 \sim \lambda_0^* \lambda$ for solutions with $k = O(1)$, where $\rho_1/\rho_2 = k\epsilon$. Our analysis in chapter 3 showed that $x_c = O(\lambda^{2/9})$ as $\lambda \to \infty$ when $k = 0$. The numerical solutions to the two-fluid half-plane problem discussed in section 4.4 showed qualitatively different behaviour for $k = 0$ and $k = O(1)$, with H pinching off for large λ when $k = 0$, but forming narrow necks which do not pinch off when $k = O(1)$.

We now investigate the behaviour of the secularity equations for large η, which is applicable to the limit $\mu \to 0$. In this limit, we find a simpler relationship between the eigenvalue λ^* and the inner problem solution $\tilde{\omega}(\sigma)$, which does not require the explicit solution of the secularity equations for individual values of η.

4.7.4 Large η solution behaviour

In section 4.6.4, we discussed oscillator solution behaviour as $E \to 0$. We found that the solution was primarily determined by the linear terms corresponding to the fluid in the fat wedge, once $(1+X)^3 \gg 9\mu\lambda^*/\eta^2$. As η increases, the range of X for which flow in the slender wedge has a significant effect on the oscillator solution diminishes. However, a significant effect due to the nonlinear terms remains, which is the requirement that by averaging the oscillator Bernoulli equation (4.109) over one period, the solution $H(x)$ must satisfy

$$\int_0^1 \frac{1}{\hat{H}_0^2} dx = \frac{Q}{A^2}, \tag{4.222}$$

independently of the value of μ, provided that $\mu > 0$.

We can write an approximate solution to the oscillator equations defined in section 4.6 as

$$\hat{H}_0 \sim \bar{H} + K\cos(2\pi x), \quad \omega = \frac{B}{2\pi}, \quad E = \frac{\pi K^2 B}{2}, \tag{4.223}$$

where $\bar{H}$ is a constant to be determined. This is similar to the analysis for small E discussed in section 4.6.4. However, here we allow the amplitude K to be of the same order as $\bar{H}$. The value of $\bar{H}$ is determined by the constraint (4.222). If H is given by (4.223), we can calculate the left-hand-side of (4.222) as

$$\int_0^1 \frac{1}{\hat{H}_0^2} dx = \frac{1}{\bar{H}^2}\int_0^1 \left(1 + (K/\bar{H})\cos(2\pi x)\right)^{-2} dx = \frac{1}{\bar{H}^2}\left(1 - \left(\frac{K}{\bar{H}}\right)^2\right)^{-3/2}, \tag{4.224}$$

so $\bar{H}$ can be found by solution of

$$\left(\frac{\bar{H}^2}{K^2} - 1\right)^{3/2} \frac{K^2}{\bar{H}^2} = \frac{A^2}{QK^2}. \tag{4.225}$$

This cubic equation has a unique solution with $\bar{H}/K > 1$ if $A^2/QK^2 > 0$.

As found in section 4.6.4, if $\mu = 0$, the equation for E_X gives

$$\frac{dE}{dX} = -\frac{5E}{(1+X)}, \tag{4.226}$$

so we can replace E and K by

$$E = E_0(1+X)^{-5}, \qquad K = K_0(1+X)^{-7/2}. \tag{4.227}$$

The secularity equations for A and $\bar{P}$ can be written as

$$A_X = \frac{4}{3}\bar{H} \tag{4.228}$$

and

$$\begin{aligned}\bar{P}_X =& \frac{2}{3}(1+X) - A\int_0^1 \frac{1}{\hat{H}_0}dx \\ =& \frac{2}{3}(1+X) - \frac{A}{\bar{H}}\left(1-\frac{K^2}{\bar{H}^2}\right)^{-1/2} \\ =& \frac{2}{3}(1+X) - \left(\frac{AQ}{\bar{H}}\right)^{1/3}.\end{aligned} \tag{4.229}$$

In order to be able to meet the boundary condition $\hat{H}_0$ at $\hat{x} = X = 0$, we must have $\min(\hat{H}_0) \to 0$ as $X \to 0$, then $\bar{H}(0) = K_0$, so the initial condition for A is

$$A_X = \frac{4}{3}\bar{H} \sim \frac{4}{3}K_0 \quad \text{as} \quad X \to 0. \tag{4.230}$$

For large X, we expect

$$\bar{H} \to \frac{1+X}{\lambda^*(\eta,1)}, \qquad A = O(1+X)^2. \tag{4.231}$$

We can rescale to remove most of the dependence on K_0 by defining $A = K_0 a$ and $\bar{H} = K_0\bar{h}$, so that the equations become

$$a_X = \frac{4}{3}\bar{h} \tag{4.232}$$

and

$$\bar{P}_X = \frac{2}{3}(1+X) - \left(\frac{aQ}{\bar{h}}\right)^{1/3}, \qquad Q = \frac{4}{9}(1+X)^2 - \frac{2}{3}\bar{P}, \tag{4.233}$$

where $\bar{h}$ is the unique solution with $\bar{h} > (1+X)^{-7/2}$ of

$$\left(\frac{\bar{h}^2}{(1+X)^7} - 1\right)^{3/2} \frac{(1+X)^{7/2}}{\bar{h}} = \frac{a^2}{Q(1+X)^7}. \tag{4.234}$$

The boundary conditions become

$$a = \frac{4}{3}X \quad \text{as} \quad X \to 0 \tag{4.235}$$

and

$$\bar{h} \to \frac{1+X}{K_0\lambda^*(\eta,1)}. \tag{4.236}$$

Once again, $\bar{P}(0)$ is found by shooting so that $\bar{P} \to 0$ as $X \to \infty$. We find that $\bar{P}(0) = -0.1090$ and $K_0\lambda^*(\eta,1) = 3.3535$. Figure 4.15 shows the solution envelope for the a, $\bar{h}$, $\bar{P}$ system.

The value of the constant K_0 varies with σ and η, and is related to $A_X(0)$ by

$$A_X(0) = \frac{4}{3}K_0. \tag{4.237}$$

We know that $A_X(0) = \tilde{A}(\sigma)/\mu Q_0$, where $\tilde{A}$ is defined by the infinite sum (4.217). We can estimate the leading order behaviour of K_0 as $\eta \to \infty$ by assuming that we can approximate $\tilde{A}(\sigma)$ by the first term in the sum in (4.217), so that

$$\tilde{A}(\sigma) \sim \frac{16}{3}\frac{1}{\sigma}\frac{1}{2\pi\tilde{\omega}-\sigma} \qquad \text{as } \sigma \to \infty. \tag{4.238}$$

Then recalling the definition of σ from (4.213), we find

$$K_0 \sim \frac{9}{2\eta}\frac{1}{2\pi\tilde{\omega}-\sigma} \qquad \text{as } \eta \to \infty \tag{4.239}$$

so we predict that

$$\lambda^*(\eta,1) \sim 3.3535 \times \frac{2\eta}{9}(2\pi\tilde{\omega}-\sigma) \quad \text{as} \quad \eta \to \infty. \tag{4.240}$$

We can rescale this result to give $\lambda^*(\mu,1)$ as $\mu \to 0$. We find that $\lambda^*(\mu,1)$ tends to a non-zero constant as $\mu \to 0$ if $2\pi\tilde{\omega}-\sigma$ tends to a constant as $\sigma \to \infty$. Figure 4.16 shows the behaviour of λ^* and $\bar{P}(0)$ as $\mu \to 0$ with $\eta = 1$. Figure 4.17 shows the behaviour of $\tilde{\omega}$ as $\sigma \to \infty$.

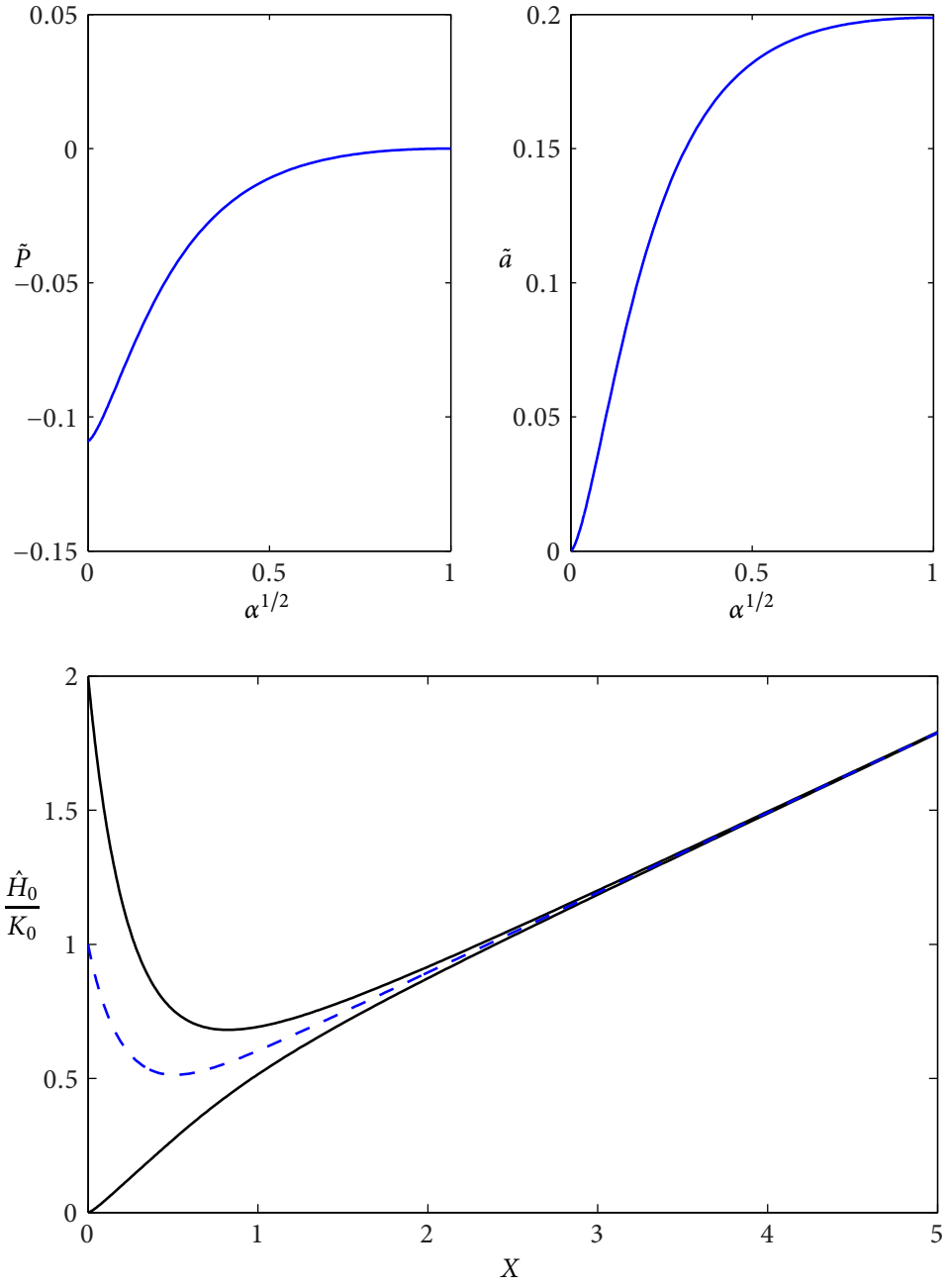

Figure 4.15: The large-η asymptotic solution envelope. This figure should be compared to figure 4.8 on page 137, which shows a similar plot for the $\eta = 0$ secularity solution. For comparison with figure 4.8, we plot $\tilde{P} = \bar{P}/(1+X)^2$ and $\tilde{a} = a/(1+X)^2 = A/K_0(1+X)^2$ against the aspect ratio $\alpha = (\bar{H} - K)/(\bar{H} + K)$. The lower plot shows the maximum, minimum and mean of $\bar{H}/K_0 \equiv H$ against X. Note that the solution envelope here decays much more quickly with respect to X than the solution shown in figure 4.8.

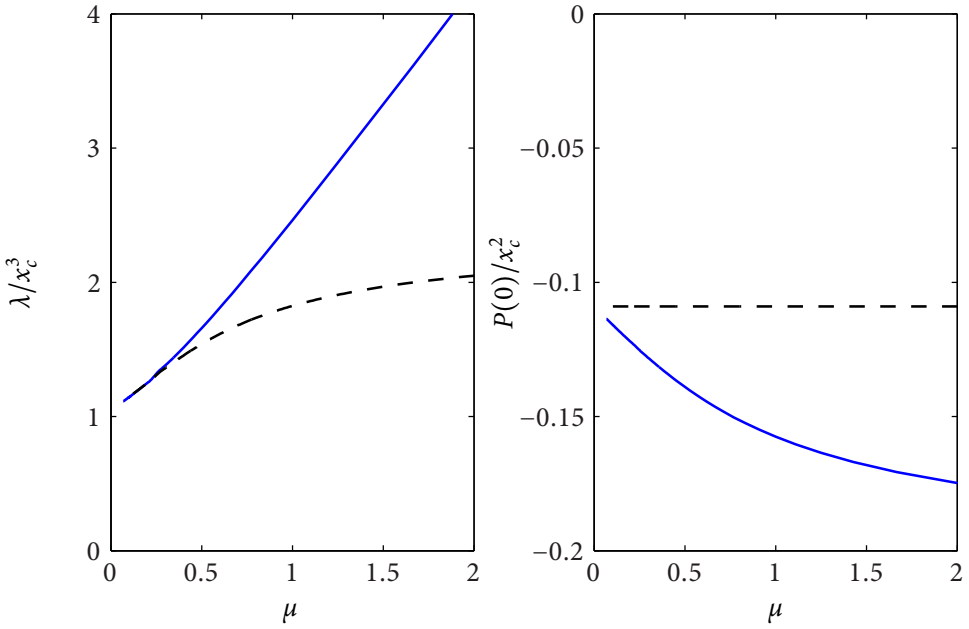

Figure 4.16: Comparison of secularity solution eigenvalues for $\eta = 1$ as a function of μ (solid blue line) and large η asymptotic solution (dashed black line) from section 4.7.4. Both are calculated using $\tilde{\omega}(\sigma)$ from the 'gold' curve in figure 4.13.

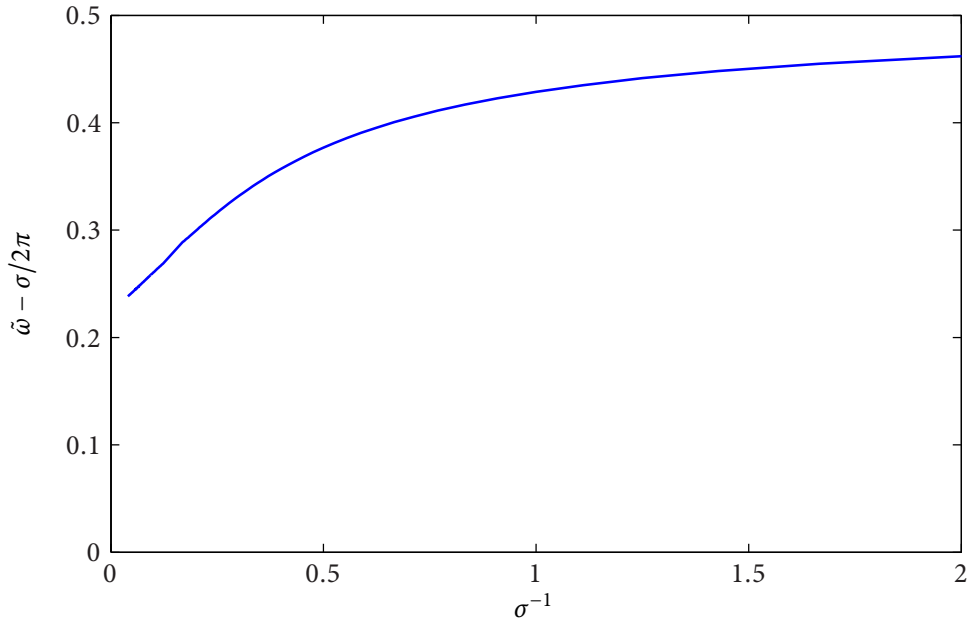

Figure 4.17: The behaviour of the eigenvalue $\lambda^*(1,\mu)$ for small μ is related to the value of $\tilde{\omega} - \sigma/2\pi$ as $\sigma \to \infty$ by (4.240). We find that $\lambda^*(1,\mu)$ tends to a non-zero constant as $\mu \to 0$ if $\tilde{\omega} - \sigma/2\pi$ tends to a non-zero constant as $\sigma \to \infty$.

4.7.5 Composite solutions

Once appropriate boundary conditions have been determined, integration of the secularity equations readily gives the secularity variables A, $\bar{P}$ and E as functions of the slow variable X. To find a composite solution for a particular value of $\hat{\epsilon} = x_c^{-3}$, we must refer to particular values of the oscillator solution $\hat{H}_0(\hat{x}, X)$. We know that $\hat{x}$ and X are related by

$$\frac{d\hat{x}}{dX} = \hat{\epsilon}^{-1}\omega(X). \tag{4.241}$$

We therefore need to integrate $\omega(X)$ to find $\hat{x}$ as a function of X and $\hat{\epsilon}$. This can be calculated as a further secularity equation, where we integrate ω to find $\theta_1(X, 0)$, where $\hat{x} = \hat{\epsilon}^{-1}\theta_1(X, 0) + O(1)$.

The oscillator solutions plotted so far in this chapter all have minima for H at $\hat{x} = 1/2$. This is an arbitrary choice of phase, as the periodic oscillator equations are invariant under translation in $\hat{x}$. The inner problem solutions calculated in appendix A for $\eta > 0$ have a phase shift $\bar{z}$ between the application of the contact point at $\hat{x} = 0$ and the contact points for the periodic far-field solution for H. There is therefore a constant phase shift at $X = 0$ to be determined. In addition, we also have an undetermined $O(1)$ phase shift $p(X, Y)$ which allows a slow drift in phase for $X > 0$.

Once we have chosen a phase for $X = 0$, we can calculate $\hat{x}$ at leading order in $\hat{\epsilon}$ and obtain $\hat{H}_0(\hat{x}, X)$ by interpolating against the periodic solution. The leading order composite solution for $\hat{H}$ becomes

$$\hat{H} \sim \hat{H}_0\left(\frac{\theta_1(X,0)}{\hat{\epsilon}} + \bar{z} - \frac{1}{2}, X\right) - \hat{H}_0\left(\frac{\theta_1(X,0)}{\hat{\epsilon}} + \bar{z} - \frac{1}{2}, 0\right) + \frac{2}{\mu Q_0} h\left(\frac{\theta_1(X,0)}{\hat{\epsilon}}\right), \tag{4.242}$$

where the calculation of $\hat{H}_0$ is discussed in section 4.6 and the inner solution function h is discussed in appendix A. Figure 4.18 shows an outer composite solution for $\hat{H}$, which uses only the first term in (4.242). This inherits a phase shift from the inner problem, and should be correct for $X \gg \epsilon$. However, this outer composite solution does not satisfy the condition $\hat{H} = 0$ at $\hat{x} = X = 0$, as the adjustment of phase necessary for this condition occurs in the inner region.

Figure 4.19 shows the interface shape $\hat{H}$ for a numerical solution to the half-plane problem (4.3.3) for $\mu = 1$ and $\eta = 1$ with $\lambda = 50$ and $\hat{\epsilon} = 0.535$. We find that the shape of this finite-λ solution agrees reasonably well with the large-λ envelope, but the two

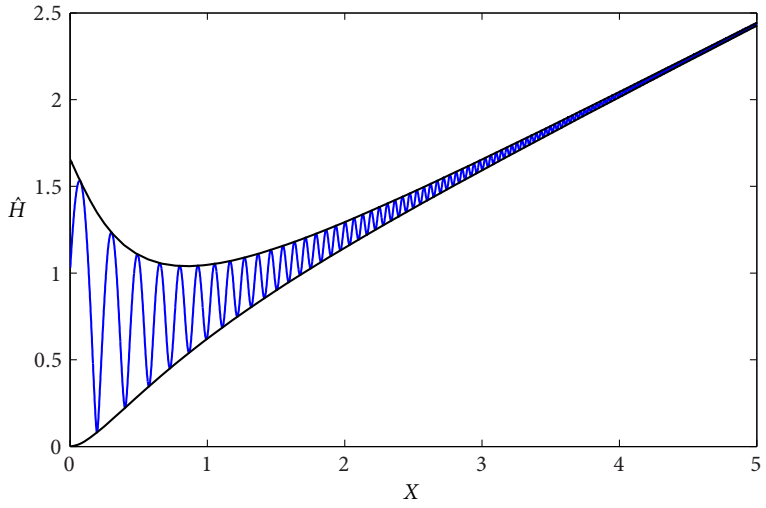

Figure 4.18: A composite outer solution and solution envelope for $\hat{H}$ with $\eta = 1$, $\mu = 1$. Here $\hat{\epsilon} = x_c^{-3} = 0.05$. The 'outer' composite solution has a phase such that $\hat{H}$ does not reach 0 at $X = 0$. The inner problem should cause an adjustment on the lengthscale $X = O(\epsilon)$ such that $\hat{H}$ does touch down at $\hat{x} = X = 0$. However, it is difficult to match these components together numerically to calculate composite solutions, as the phase of inner and outer solutions are not entirely in synch, and subtracting slightly out-of-phase oscillatory solutions gives a resulting solution with erroneous discontinuities.

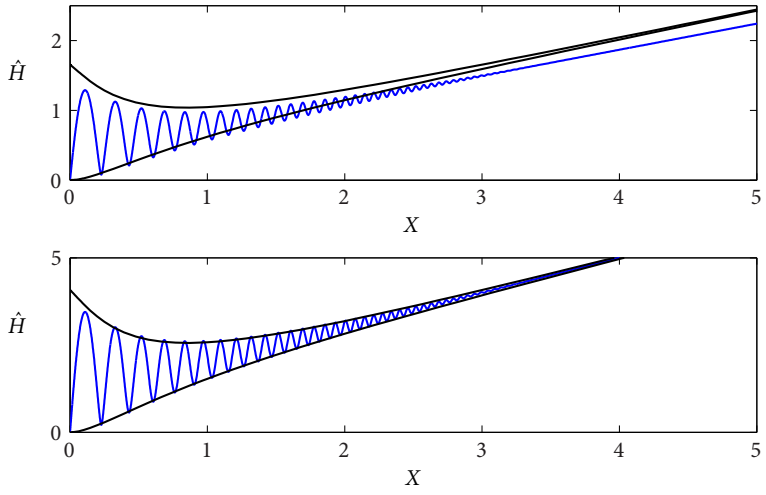

Figure 4.19: Rescaled interface position $\hat{H}$ for the same numerical solution as shown in figures 4.2(b) and 4.24, with $\lambda = 50$, $\mu = 1$, $\eta = 1$. There is a discrepancy between values of λ^* for the numerical and asymptotic solutions which causes the deviation shown in the upper figure. The lower figure scales both solutions by plotting $\lambda^* \hat{H}$ so that they must coincide for large X.

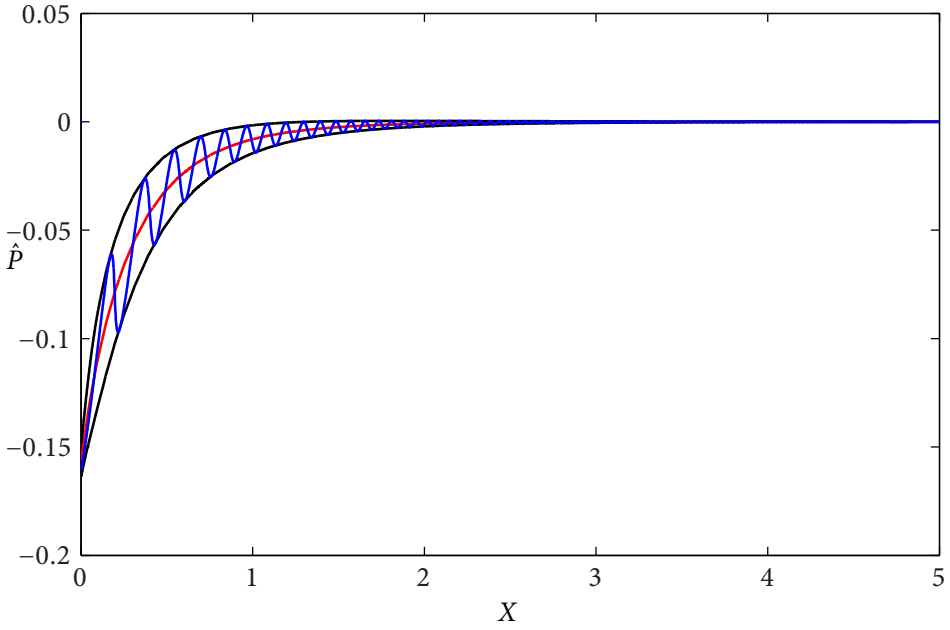

Figure 4.20: A composite solution for $\hat{P}$ (blue), with $\eta = 1$, $\mu = 1$, $\hat{\epsilon} = x_c^{-3} = 0.05$. As $\hat{\epsilon} \to 0$, we find $\hat{P}(\hat{x}, X) \to \bar{P}(X)$, with oscillations about the slow mean (red) $\bar{P}$ of amplitude $O(\epsilon)$. The solution envelope (black) here is for $\hat{\epsilon} = 0.05$. Note that the wave amplitude for $\hat{P}_0$ tends to zero as $X \to 0$.

solutions have different values of $\lambda^* = \lambda/x_c^3$, and so we obtain much better agreement by rescaling the two solutions so that they coincide for $X \to \infty$.

The velocity potential in the slender wedge is given by $\hat{P} = \bar{P}(X) + \hat{\epsilon}\hat{P}_0(\hat{x}, X)$, where $\hat{P}_0$ satisfies

$$\hat{P}_{0\hat{x}} = \frac{A(X)}{\omega(X)}\left(\int_0^1 \frac{1}{\hat{H}_0}\,d\hat{x} - \frac{1}{\hat{H}_0}\right) \tag{4.243}$$

and

$$\hat{P} \sim \bar{P}(X) + \hat{\epsilon}\hat{P}_0\left(\frac{\theta_1(X,0)}{\hat{\epsilon}} + \bar{z} - \frac{1}{2}, X\right). \tag{4.244}$$

Figure 4.20 shows a composite solution for $\hat{P}(X)$ and the solution envelope, which depends on $\hat{\epsilon}$.

Along the free surface $X > 0$, $Y = 0$, the velocity potential in the fat wedge, $\hat{\Phi}$, is given at leading order by

$$\begin{aligned}\hat{\Phi} \sim\ & \hat{\Phi}_{osc}\left(\frac{\theta_1(X,0)}{\hat{\epsilon}} + \bar{z} - \frac{1}{2}, X\right) - \hat{\Phi}_{osc}\left(\frac{\theta_1(X,0)}{\hat{\epsilon}} + \bar{z} - \frac{1}{2}, 0\right) \\ & + W_0(X,0) + \frac{4}{3\mu Q_0}\phi\left(\frac{\theta_1(X,0)}{\hat{\epsilon}}, 0\right) + C_1,\end{aligned} \tag{4.245}$$

where C_1 is a constant. Here $\hat{\Phi}_{osc}$ is $\hat{\Phi}_0$ from section 4.6 and ϕ is the velocity potential for the rescaled inner problem discussed in appendix A. The first two components of this composite expression are $W_0(X, Y = 0)$, which contains the slow variation of the mean of $\hat{\Phi}$ that is independent of $\hat{x}$ and the purely oscillatory term $\hat{\Phi}_{osc}(\hat{x}, X)$ which is obtained by solving the oscillator equations. We subtract the term $\hat{\Phi}_{osc}(\hat{x}, 0)$, as this is the outer limit of the inner solution and also the inner limit of $\hat{\Phi}_{osc}(\hat{x}, X)$. The inner solution itself is given by $4\phi(\hat{x}, \hat{y})/3\mu Q_0$. All the secularity and oscillator equations derived so far are independent of an additive constant in $\hat{\Phi}$ or W_0, and so we can choose C_1 so that $\hat{\Phi} \to 0$ as $|X| \to \infty$. For $X > 0$, we can calculate $\hat{\Phi}_{osc}$ by interpolating against known solutions to the oscillator equations. The calculation of the inner solution $\phi(\hat{x}, \hat{y})$ is discussed in appendix A.

Along the rigid wall given by $X < 0$, $Y = 0$, we can write

$$\hat{\Phi} \sim W_0(X, 0) + \frac{4}{3\mu Q_0}\phi(\hat{x}, 0) + C_1. \tag{4.246}$$

Here the relationship between X and $\hat{x}$ is less clear, as there are no periodic oscillations to use to determine ω. If $X \ll 1$, we can say $\hat{x} = \theta_1(X, Y)/\hat{\epsilon} \sim \omega(0)X/\hat{\epsilon}$, which will suffice for matching purposes, so we reach

$$\hat{\Phi} \sim W_0(X, 0) + \frac{4}{3\mu Q_0}\phi\left(\frac{\omega(0)X}{\hat{\epsilon}}, 0\right) + C_1. \tag{4.247}$$

In order to construct the composite solution for $\hat{\Phi}$, we must define the function $W_0(X, Y)$. On the free surface, we know from equation (4.74) that

$$\frac{\partial W_0}{\partial Y} = \frac{d}{dX}\left(A - \frac{1}{2}(1 + X)A_X\right) \equiv V_X \quad \text{on } X > 0,\ Y = 0. \tag{4.248}$$

Although we have not analysed Laplace's equation to sufficient order, it seems likely that as the lowest order non-oscillatory component of $\hat{\Phi}$, the slow function $W_0(X, Y)$ will also obey

$$W_{0XX} + W_{0YY} = 0 \quad \text{for } Y > 0 \tag{4.249}$$

and

$$\frac{\partial W_0}{\partial Y} = 0 \quad \text{on } X < 0,\ Y = 0. \tag{4.250}$$

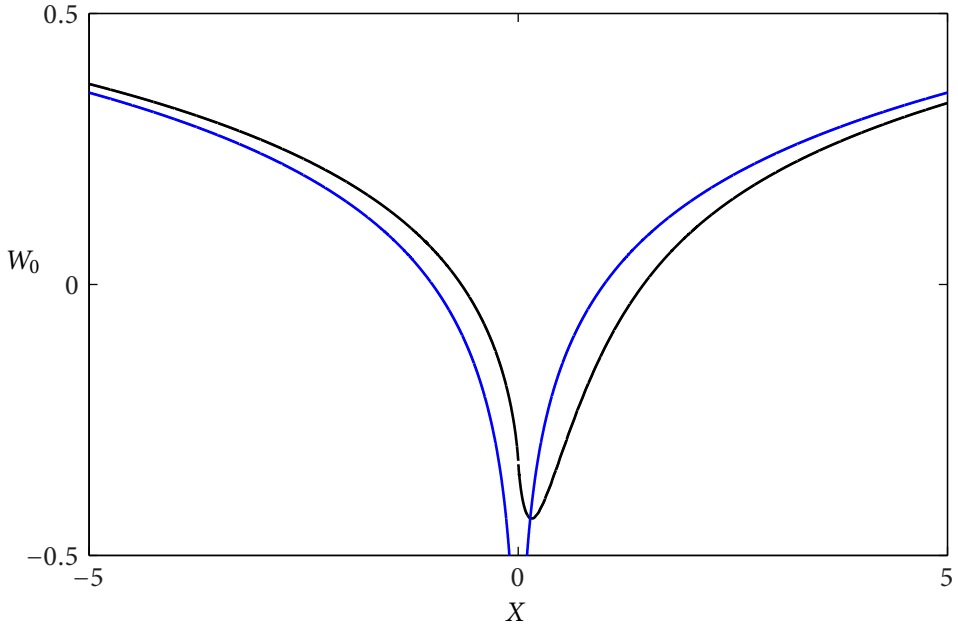

Figure 4.21: The function $W_0(X,0)$ (black) defined by (4.252) for $\eta = 1$, $\mu = 1$ and its leading order, logarithmic, behaviour as $X \to \infty$ (blue) given by $-V(0)\log|X|/\pi$, where $V(X)$ is defined by (4.248).

We would also like to find $W_0(R,\theta) \to 0$ as $R \to \infty$ for $0 \le \theta \le \pi$. Unfortunately, W_0 as just defined has a logarithmic source at $X = 0$, as

$$\int_0^\infty W_{0Y}\,dX = -\frac{1}{2}A_X(0) \tag{4.251}$$

which is non-zero (we also have $V \to 0$ as $X \to \infty$). The version of W_0 that is regular at $X = 0$ has

$$\begin{aligned} W_0(X,0) &= \frac{1}{\pi}\int_0^\infty \log|X-X'|V_X(X')dX' \\ &= -\frac{1}{\pi}V(0)\log|X| - \frac{1}{\pi}\int_0^\infty \frac{V(X')}{X'-X}dX'. \end{aligned} \tag{4.252}$$

Figure 4.21 shows $W_0(X,0)$ for $\eta = 1$ and its leading order logarithmic behaviour for large X. Fortunately, the logarithmic term in (4.252) is exactly cancelled by a logarithmic term with equal magnitude but opposite sign emerging from the far-field of the inner problem, so that with suitable choice of the constant C_1, the composite solutions for $\hat{\Phi}$ defined in (4.245) and (4.247), and plotted in figures 4.22 and 4.23 vanish as $|X| \to \pm\infty$ and are bounded everywhere. Figure 4.24 shows that half-plane solution for $\hat{\Phi}$ for $\lambda = 50$ fits the shape of this envelope, and shows a deviation of the mean of $\hat{\Phi}$ on the scale $X = O(1)$.

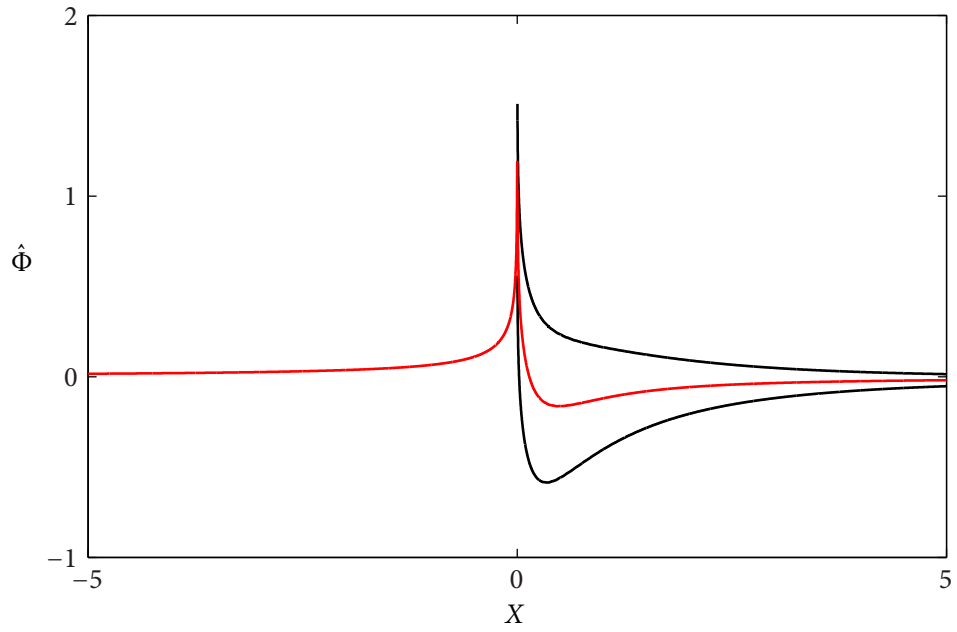

Figure 4.22: The composite solution envelope for $\hat{\Phi}$ for $\eta = 1$, $\mu = 1$. The red line shows the mean value of $\hat{\Phi}$ over a single oscillation. The black lines indicate the maximum and minimum values of $\hat{\Phi}$ in each oscillation. The black and red lines here represent the solution at fixed X as $\epsilon \to 0$. For finite $\hat{\epsilon}$, this 'outer' envelope is inaccurate for $X = O(\epsilon)$, where the inner problem smooths over the singular behaviour at $X = 0$.

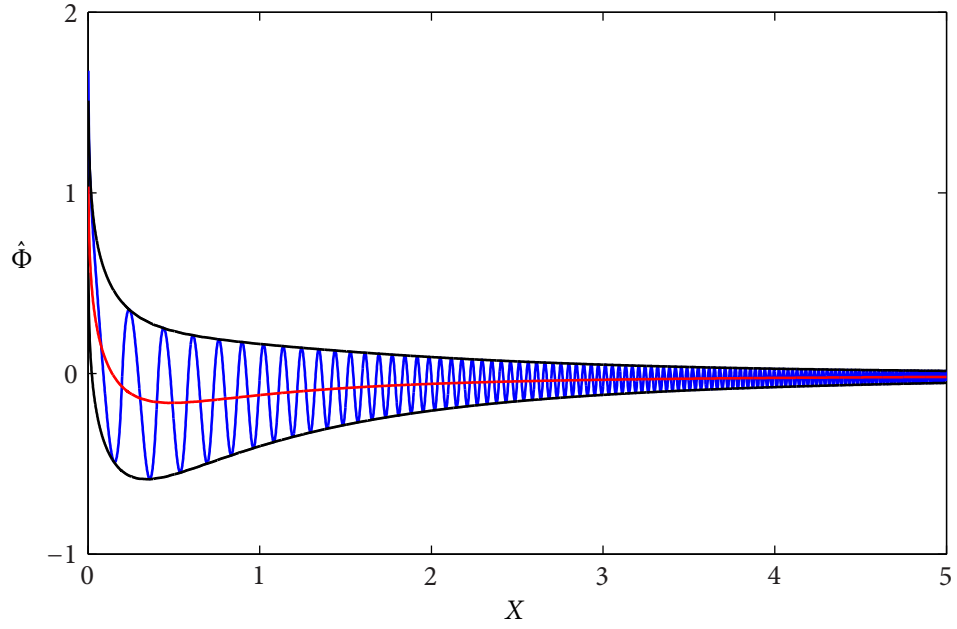

Figure 4.23: An outer composite solution and solution envelope for $\hat{\Phi}$ with $\eta = 1$, $\mu = 1$. Here $\hat{\epsilon} = x_c^{-3} = 0.05$.

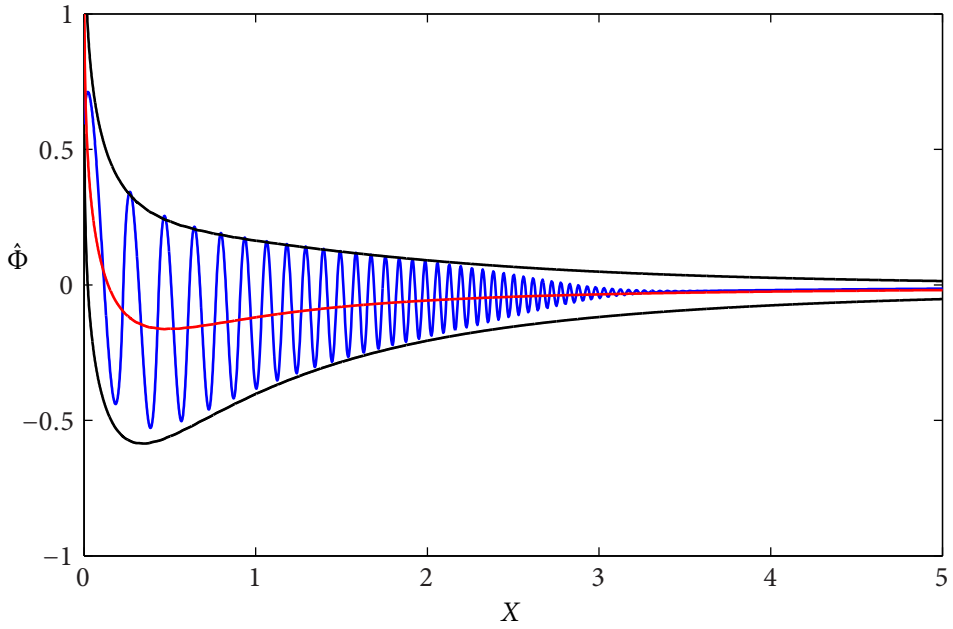

Figure 4.24: A finite-λ solution calculated using the numerical discretisation from section 4.4. This has $\mu = 1$, $\eta = 1$ as in figure 4.23, but with $\lambda = 50$ and $\hat{\epsilon} = x_c^{-3} = 0.535$. The rapid decay of the numerical solution compared to the asymptotic envelope is due to discretisation errors.

4.8 Conclusion

In this chapter we have sought distinguished density ratios for the two fluid problem corresponding to a small change in contact angle for a fat wedge, with far-field wedge angle $\pi - \epsilon$ and contact angle $\pi - \lambda\epsilon$ where $\epsilon \ll 1$. For density ratio $\rho_1/\rho_2 = O(\epsilon)$, we found that for $\epsilon \to 0$ with $\lambda = O(1)$ we obtained a leading order problem where the equations for $\rho_1 = 0$, $\rho_2 = 1$ and for $\rho_1 = 0$, $\rho_2 = 0$ were directly coupled in the Bernoulli equation. This leading order system featured linear PDEs for the velocity potential in fluid 2 coupled to nonlinear ODEs for the velocity potential in fluid 1. We solved the leading order system numerically using a boundary integral method to reduce the equations for Φ_2 to a one-dimensional integro-differential equation, and used parameter continuation to obtain nonlinear solutions.

The numerical solutions to the half-plane problem indicated that pinch-off does not occur for finite λ if the density ratio k, where $\rho_1/\rho_2 = k\epsilon$, is finite as $\lambda \to 0$. Solutions for $k = 1$ shown in figure 4.2(a) have a similar magnitude and frequency to those for $k = 0$ shown in figure 3.10. However, unlike for the solutions for $k = 0$, the solutions for $k = 1$ have local minima approaching but not intersecting the wall as λ increases. A scaling argument suggested that a distinguished limit is obtained for large λ when the density ratio $k = O(\lambda)$, so $\rho_1/\rho_2 = O(\lambda\epsilon)$. Numerical solutions for $k = \mu\lambda$ with $\mu = 1$ shown in figure 4.2(b) have a smaller contact point displacement x_c and also interface height H for fixed values of λ compared to the $k = 0$ and $k = 1$ solutions.

In section 4.5, we derived equations for a large-λ asymptotic solution with density ratio $\rho_1/\rho_2 = \mu\lambda\epsilon$ with $\mu = O(1)$. The free surface equations featured both nonlinear and nonlocal terms, and were able to support rapidly oscillating capillary waves, with slowly varying amplitude and phase. Due to the nonlinearity, the wavelength of the oscillations may depend on the solution amplitude, and had to be determined as part of the solution. The resulting leading order periodic oscillator solutions could not be solved analytically for finite density ratio, but we were able to find numerical solutions to a discretised scheme with a spectral term for the nonlocal effects and continuation for nonlinear elements. We also derived secularity equations for the slow variation of the oscillator equation parameters.

Given reasonable constraints on the behaviour of the oscillator equation parameters

near the contact point, we found that the oscillator solutions became progressively sharper as we approached the contact point along the free surface. For small X, we found that the solution resembled a sequence of upturned parabolas, with 'V' shaped regions connected by highly curved neck regions (figure 4.9). In order to reconcile this periodic solution with a two-dimensional flow in the region of the contact point, we matched to an inner region where the periodicity that defines the oscillator solutions was slightly relaxed in favour of solving a new half-plane problem. We attempted to solve this half-plane problem numerically in appendix A, but were thwarted by evidence of a discretisation-related branch structure, and so cannot be confident that we have found a solution that has a well-behaved non-discretised counterpart. The appearance of this non-periodic inner problem is consistent with the phenomenon of non-homogenisable regions in the vicinity of cracks.

We used a set of inner problem numerical solutions obtained in appendix A to supply the necessary boundary conditions for integration of the secularity conditions. This allowed us to calculate solution envelopes and composite solutions for the interface position and velocity potentials along the free surface. We found that the composite solution for Φ, the velocity potential in fluid 2, features a non-trivial slowly varying mean which arises from a fourth secularity equation that is uncoupled from the oscillator equations. The composite solutions agreed surprisingly well with the numerical solutions to the full finite-λ half-plane-problem, given the uncertainty over the inner problem solutions.

Finally, we note that for finite density ratio μ/η, the capillary wave decay is determined primarily by the flow in fluid 2 once x is large enough. As the density ratio ρ_1/ρ_2 decreases, the critical distance from the contact point decreases, so for large η or small μ, we expect the solution envelope to be largely controlled by fluid 2. However, we find that the terms in the Bernoulli equation corresponding to fluid 1 have a significant effect on the interface position even as $\mu \to 0$, due to a constraint on the average of $1/H^2$, and this constraint is independent of density ratio. We therefore are able to find a large-η asymptotic solution to the secularity equations, with the solution envelope amplitude determined by fluid 2, but its slowly varying mean determined by fluid 1. We rescaled this to provide a solution for $\mu \ll 1$.

The limit $\mu \to 0$ seems very likely to be a singular limit. In chapter 3, we found that the outer limit of the inner problem, solved exactly in terms of the dock problem, involved H oscillating with fixed amplitude about a mean of $O(x^{-1/2})$. The decay of this mean forced the eventual scaling $\lambda = O(x_c^{9/2})$, rather than $O(x_c^3)$ as expected from the initial scaling, and as in the problems for finite μ/η and for $\mu \ll 1$ that we investigated in this chapter. Here, our inner problem is constructed such that the mean of H must tend towards a finite constant as $x \to \infty$, so we must have a different solution to that for $k = 0$.

The strong dependence of the asymptotic results on the solution of this inner problem means that this chapter has a less triumphant conclusion than chapter 3. However, in retrospect, we could have anticipated the crucial role of the inner problem for this two-fluid problem, due to the pivotal role of the dock problem solution in the chapter 3 analysis.

Chapter 5

Conclusion

5.1 Thesis results

In this thesis, we have analysed the surface tension driven recoil of inviscid fluid wedges. We focused on the case where one wedge is very fat, with initial wedge angle $\pi - \epsilon$ where $\epsilon \ll 1$. A second inviscid fluid occupies the slender wedge with angle ϵ between the first wedge and a rigid wall. At time $t = 0$, the tip angle ϵ is suddenly changed to $\lambda\epsilon$, and the fluid recoils. We must determine the subsequent position of the wedge tip, the interface position and the velocity within each fluid.

For this inviscid recoil problem, with all boundary conditions expressed in angles, the solution must be self similar, with all lengthscales proportional to $t^{2/3}$. This removes the time dependence from the problem. For general λ and ϵ, we must solve the Bernoulli equation, which is an ODE involving the interface position and velocity potentials, coupled to kinematic equations for the velocity potentials in the two fluids, which we can write as nonlinear integral equations.

In chapters 3 and 4, we considered recoil problems with $\lambda = O(1)$ as $\epsilon \to 0$, so that the domain for the fluid in the fat wedge becomes a half plane at leading order, while the domain for the other fluid remains slender. As $\epsilon \to 0$, the kinematic equations become a linear PDE for the fluid in the fat wedge, while the flow in the slender wedge is described by nonlinear ODEs.

We began our analysis of this linearised problem by considering the case when the fluid in the slender wedge has zero density. The leading order system as $\epsilon \to 0$ and $\lambda = O(1)$ is then a linear partial differential equation with a single independent parameter, λ. We solved this system numerically using a boundary integral method. We found that

the amplitude of capillary waves increased with λ, and the free surface became self intersecting for $\lambda > 37.8$. In order to improve our understanding of the solution structure, we investigated the behaviour of the linear PDE system for $\lambda \to \infty$.

We found a solution using matched asymptotic expansions, with an inner region where $x = O(x_c^{-2})$ and an outer region where $x = O(x_c)$. In the inner region the equations reduced to the dock problem, which is a PDE describing constant amplitude surface waves incident on a rigid dock. We discussed the calculation of the exact solution of the dock problem by complex variable methods in chapter 2. The dock problem solution gave the amplitude and phase of the free surface waves explicitly, and also a bounded mean velocity potential that decays to zero as $r \to \infty$. We related the dock problem solution to the interface position for the wedge recoil problem. We found that in the outer region, the capillary waves in H have amplitude $O(\lambda/x_c^2)$, while the slowly varying mean of H has magnitude $O(\lambda/x_c^{7/2})$, and so as x_c increases, the interface position H will eventually become negative and hence self intersecting. The slow variation of the mean of Φ in the far field, coupled to the kinematic equation for Φ, gave us an ODE for the mean of H, which we solved to find $\lambda = O(x_c^{9/2})$.

We also considered the recoil of a fat wedge with $|\lambda - 1| \ll 1$ and $\epsilon \ll 1$, so that the contact and wedge angles are both close and small and so we were able to neglect terms corresponding to the contact point displacement in the Bernoulli and kinematic equations. The leading order system was a parameter-free linear PDE. We solved this PDE using Mellin transforms in chapter 3; the method was very similar to the dock problem solution by Mellin transforms in chapter 2. We found that, as for the dock problem, there was a unique bounded solution for the velocity potential that vanishes as $r \to \infty$.

We can calculate the flow induced in the slender wedge for a given interface position $H(x)$. We find that a rapid flow is driven in the negative-x direction in regions where the interface position approaches the rigid wall, which may have a significant effect on whether the solution pinches off or remains valid as $\lambda \to \infty$ for two-fluid problems. The velocity in the slender wedge is $O(1)$ as $\epsilon \to 0$ with $\lambda = O(1)$, while the velocity in the fat wedge is $O(\epsilon)$ in this limit, and so a distinguished density ratio occurs when $\rho_1/\rho_2 = k\epsilon$ where $k = O(1)$. We investigated the resulting leading order problem in chapter 4 and obtained non-intersecting numerical solutions for all λ with $k > 0$. The

solution is again dominated by capillary waves, which have a high curvature in regions where they approach the wall, and so the solutions became harder to resolve as $\lambda \to \infty$.

We then considered the behaviour of this two-fluid half-plane problem in the double limit $1 \ll \lambda \ll \epsilon^{-1}$. We found that maximum coupling between the two fluids occurs if $\rho_1/\rho_2 = O(\lambda\epsilon)$. The leading order equations were nonlinear ODEs for the interface position H and the velocity potential in the slender wedge $P(x)$, coupled to a linear PDE for the velocity potential in the fat wedge $\Phi(x, y)$. The asymptotic analysis of this system via Kuzmak's method featured elements of the $\rho_1 = 0$ solution derived in chapter 3 and the $\rho_2 = 0$ solution found by Billingham [2006]. We derived periodic oscillator equations for capillary waves on the free surface in the two-fluid problem. We solved these equations numerically using a spectral method, and used the solutions to evaluate and solve secularity equations for the slow variation of oscillator parameters.

The determination of the boundary conditions at the contact point for the secularity equations required the solution of another integral equation problem. This two-fluid inner problem incorporated both the discontinuous interface derivative H_x required by Billingham [2006] for the recoil of a slender wedge of fluid, and equations for the half-plane problem that we solved in chapter 3. The resulting PDE is nonlinear in the semi-infinite sequence of 'contact points' at which H_x is discontinuous, which we must determine as part of the solution. We attempted to solve the inner problem numerically in appendix B; however we found that this nonlinearity, together with the inevitable truncation of the contact point sequence, led to the numerical solutions having a discretization related branch structure. We did obtain some plausible solutions to the inner problem, which led to reasonable composite solutions to the large-λ problem, however it is far from clear whether suitable inner problem solutions exist for all density ratios, in the semi-infinite, non-truncated limit.

Assuming that suitable inner problem solutions do exist, we find that the composite solutions for $1 \ll \lambda \ll \epsilon^{-1}$ and $\rho_1/\rho_2 = O(\lambda\epsilon)$ do not pinch off or intersect the wall as $\lambda \to \infty$, and that the contact point displacement $x_c = O(\lambda^{1/3})$. This is in contrast to the zero density surrounding fluid solution where solutions are self-intersecting for $\lambda \gtrapprox 30$, and $x_c = O(\lambda^{2/9})$ as $\lambda \to \infty$.

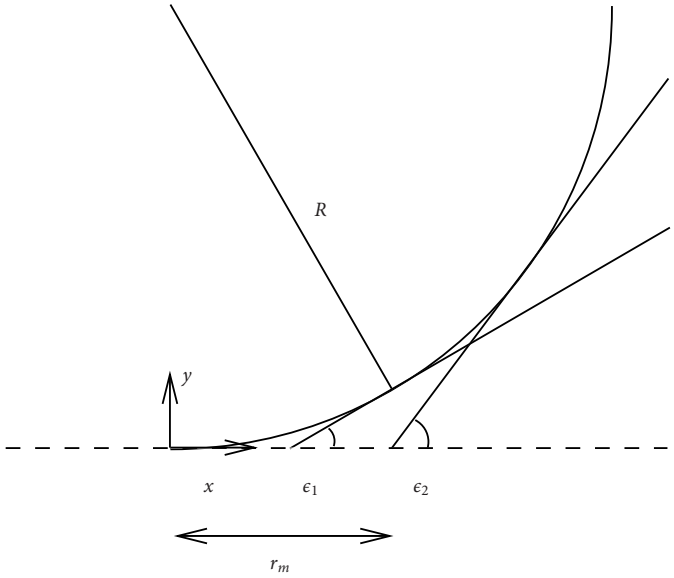

Figure 5.1: To compare coalescence of wedges and spheres, we must relate the tangent angle ϵ to r_m/R. The tangent to the circle at $x = r_m$ makes an angle $\epsilon_1 = \arcsin(r_m/R)$ with the x-axis. The tangent to the circle that goes through $(x, y) = (r_m, 0)$ has angle $\epsilon_2 = 2\arctan(r_m/R)$. As $r_m/R \to 0$, we find $\epsilon_1 \sim r_m/R$ and $\epsilon_2 \sim 2r_m/R$.

5.2 Further work

The relationship between ϵ and x_c for self similar solutions with $\beta = \pi/2$ governs the time dependence of spherical coalescence. Similarity solutions for the inviscid recoil of a wedge have $L \propto t^{2/3}$, while experiments and numerics for spherical coalescence of drops and bubbles agree that $r_m = O(t^{1/2})$. The far field angle ϵ slowly increases throughout coalescence, and we find that if $x_c = O(\epsilon^{-1/3})$ as $\epsilon \to 0$ for the self similar solution, we recover the $t^{1/2}$ time dependence for spherical coalescence.

We suppose that at meniscus radius r_m, the far field angle ϵ is zr_m/R, where z is a constant (figure 5.1). We also suppose that the asymptotic solution for $\epsilon \to 0$ with $\beta = \pi/2$ gives $x_c \sim x_{co}\epsilon^{-a}$. The self similar solution then relates r_m and x_c by

$$r_m = x_c \left(\frac{\gamma}{\rho}\right)^{1/3} t^{2/3} \sim x_{co}\epsilon^{-a} \left(\frac{\gamma}{\rho}\right)^{1/3} t^{2/3} = x_{co} \left(\frac{R}{zr_m}\right)^{a} \left(\frac{\gamma}{\rho}\right)^{1/3} t^{2/3}. \tag{5.1}$$

Solving this equation for r_m we find $r_m \propto t^b$, where $b = 2/(3(1 + a))$. To obtain $b = 1/2$ we must have $a = 1/3$, in which case we find

$$r_m = x_{c0}^{3/4} z^{-1/4} \left(\frac{\gamma R}{\rho}\right)^{1/4} t^{1/2}, \tag{5.2}$$

which has the same dependence on R, γ, ρ and t as equation (1.9). The asymptotic result $x_c = O(\epsilon^{-1/3})$ is exactly that found by Billingham [2006] for a recoiling slender fluid wedge, which is applicable to the coalescence of bubbles surrounded by an inviscid fluid.

In order to compare the prefactor of (1.9) and (5.2), we need to choose the constant z which relates ϵ to r_m/R. Some obvious choices are $z = 1$, which gives the original angle of the sphere at horizontal displacement r_m, and $z = 2$, which gives the angle of the line tangent to the sphere passing through r_m. These tangents and angles are illustrated in figure 5.1. Billingham's calculations suggest $x_{c0} \approx 1.11$, which gives a prefactor of 1.08 if $z = 1$ and 0.909 if $z = 2$, which should be compared to the prefactor 1.39 calculated by Thoroddsen et al. [2005] from experimental observations of the coalescence of bubbles. There is no asymptotic solution for $\epsilon \to 0$ applicable to the coalescence of drops with zero density surrounding fluid, as the similarity solutions do not exist in this limit. It would be interesting to compare asymptotic solutions for other density ratios to experimental observations of coalescence with a surrounding fluid.

Calculation of self similar solutions for the coalescence problem requires solving the recoil problem with $\beta = \pi/2$. In this case, the problem for $\epsilon \to 0$ becomes a fully nonlinear free boundary problem. The interface height need not be a monotonic function of x, so should be parameterised with respect to arc length. The kinematic conditions on the velocity potential can be written as integral equations that depend linearly on $\Phi_{1,2}$ and nonlinearly on the interface position $(X(s), Y(s))$. We derive the equations for this nonlinear free boundary problem in appendix B and show that as $\epsilon \to 0$ the nonlinear integral equations reduce to the kinematic equations for P and Φ found in chapter 4. The integral equations become harder to resolve numerically as the interface approaches the wall, and we again expect to find that the slender wedge velocity and interface curvature increase in neck regions.

Another consideration for coalescence of spherical and cylindrical drops is the influence of the reflected interface (figure 5.2) and of the axisymmetric component of curvature. Both of these effects would be significant if $x_c \ll 1$, but we expect to find that $x_c \gg 1$ for $\epsilon \to 0$. The reflection in $x = 0$, and the axisymmetric curvature, do not have a strong effect in neck regions where $Y \to 0$ away from the contact point, and so these extra terms are unlikely to affect the leading order behaviour as $\epsilon \to 0$. In section B.3 we discuss the effect

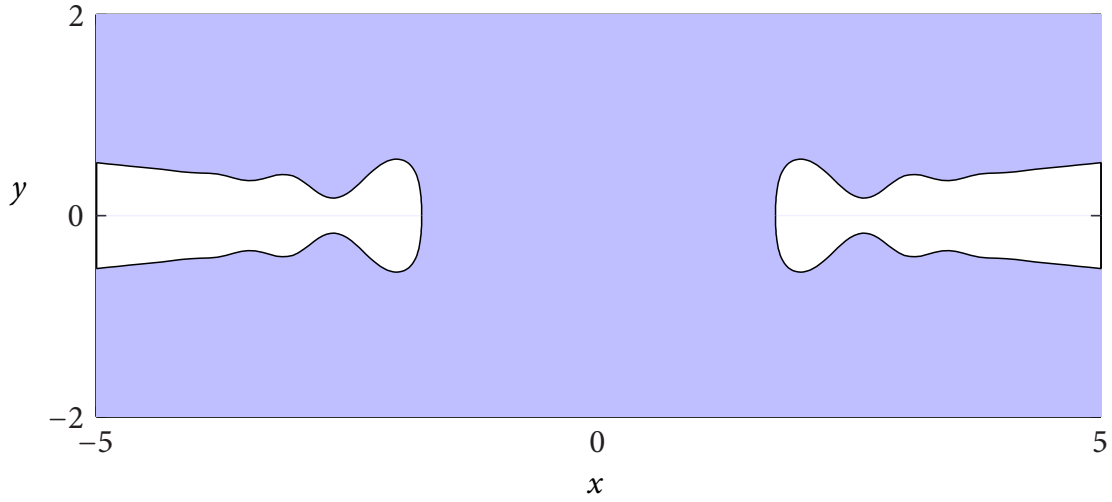

Figure 5.2: The problems analysed in chapters 3 and 4 have a rigid wall along the x-axis but are not symmetric about the x-axis. For the coalescence of cylinders, we should consider the effect of the other half of interface, reflected in the y-axis, as in was implemented by Keller et al. [2002]. Investigation of the integral equations for $\lambda\epsilon \ll 1$ shows that the effect of the reflected free-surface diminishes as the contact-point displacement x_c increases, and so the asymptotic solutions we found for large λ are essentially unchanged.

of the second reflected interface on the asymptotic solutions calculated in this thesis.

The asymptotic analysis of the two-fluid small angle problem led to a distinguished density ratio $\rho_1/\rho_2 = O(\lambda\epsilon)$ for $1 \ll \lambda \ll \epsilon^{-1}$. If this density ratio is still distinguished when $\lambda\epsilon = O(1)$, then we should find a new balance when $\rho_1/\rho_2 = O(1)$ in the nonlinear free boundary problem. Extrapolating from the structure of the two-fluid solution for large λ here, we would expect asymptotic solutions of the nonlinear problem for $\epsilon \to 0$ to require the solution of an integral equation that is also a free-boundary problem, and also to require matching to capillary waves, also described by nonlinear free-boundary problems. For the linearised problem we considered in chapter 4, these elements in the two-fluid problem are considerably more complicated than in the two separate one-fluid problems, and we may expect a further increase in complexity for the two-fluid free boundary problem.

Appendix A

Two-fluid inner problem

For the two-fluid inner problem in chapter 4, we wish to find a solution, in the limit $A \to 0$, of

$$\mu\left[\frac{1}{3}\bar{P} - \frac{2}{9} + \frac{1}{2}\frac{A^2}{\hat{H}_0^2}\right] + \frac{2}{3}\eta\omega\hat{\Phi}_{0\hat{x}}(\hat{x},0) = \omega^2\hat{H}_{0\hat{x}\hat{x}}, \tag{A.1}$$

and

$$\hat{\Phi}_{0\hat{y}}(\hat{x},0) = -\frac{2}{3}\hat{H}_{0\hat{x}}, \tag{A.2}$$

both for $\hat{x} > 0$, with

$$\hat{\Phi}_{0\hat{y}}(\hat{x},0) = 0 \tag{A.3}$$

on $\hat{x} < 0$. The eigenvalue ω will eventually be determined by the new boundary condition

$$\omega\hat{H}_{0\hat{x}}(0,0) = 0. \tag{A.4}$$

For all $\hat{x}$ and $\hat{y}$, we have

$$\hat{\Phi}_{0\hat{x}\hat{x}} + \hat{\Phi}_{0\hat{y}\hat{y}} = 0 \quad \text{for} \quad \hat{y} > 0. \tag{A.5}$$

We seek a solution with $\hat{H}_0(\hat{x})$ tending to a periodic functions with period 1 as $\hat{x} \to \infty$. We expect $\hat{\Phi}_0$ to grow no faster than logarithmically as $\hat{r} \to \infty$ (section 4.7.5).

A.1 Behaviour of Bernoulli equation as $X \to 0$

As $A \to 0$, the term

$$\frac{A^2}{\hat{H}_0^2} \tag{A.6}$$

in (A.1) behaves like a δ-function if $\hat{H}_0$ approaches zero. The oscillator equation solutions for small non-zero A show a solution that looks like a parabola, with a rapid sign change in

$\hat{H}_{0\hat{x}}$ near the minimum of $\hat{H}_0$. For $A \to 0$, we obtain a δ-function in $\hat{H}_{0\hat{x}\hat{x}}$ at any $\hat{x}_n$ where $\hat{H}_0(\hat{x}_n) = 0$. The magnitude of this delta function should be determined by the constraint that $\hat{H}_{0\hat{x}}$ changes sign at $\hat{x} = \hat{x}_n$. The small-A behaviour of the oscillator solutions is discussed further in section 4.6.3.

So now we replace (A.1) by

$$\mu\left[\frac{1}{3}\bar{P} - \frac{2}{9}\right] + \frac{2}{3}\eta\omega\hat{\Phi}_{0\hat{x}}(\hat{x}, 0) = \omega^2\hat{H}_{0\hat{x}\hat{x}}, \tag{A.7}$$

which holds for $x > 0$, $x \neq z_n$. The z_n are points where $\hat{H}_0(\hat{x}) = 0$, and the derivative $\hat{H}_{0\hat{x}}$ changes sign.

A.2 Reduction to the single independent parameter σ

We currently have an eigenvalue problem for ω, with three independent parameters, which are the density ratios η and μ, and also the value of $\bar{P}(0)$. We can rescale our discontinuous inner problem to give only one independent parameter rather than three in the eigenvalue problem. We leave $\hat{x}$ unchanged to keep the far-field period fixed at 1. We let:

$$\omega = \omega_0\tilde{\omega}, \quad \hat{H}_0 = \omega_0^{-1}h, \quad \hat{\Phi}_0 = \frac{2}{3}\omega_0^{-1}\phi, \tag{A.8}$$

where

$$\omega_0 = -\mu\left[\frac{1}{3}\bar{P} - \frac{2}{9}\right], \quad \hat{x} = x, \quad \hat{y} = y. \tag{A.9}$$

The new density parameter σ is defined as

$$\sigma = -\frac{4\eta}{9\mu\left[\frac{1}{3}\bar{P} - \frac{2}{9}\right]}. \tag{A.10}$$

The problem for $\sigma = 0$ corresponds to $\eta = 0$. We expect to find $\bar{P}(0) < 0$, so that we seek solutions for $\sigma \geq 0$.

The rescaled Bernoulli equation is

$$\tilde{\omega}^2 h_{xx} = \tilde{\omega}\sigma\phi_x - 1 \tag{A.11}$$

on $x > 0$, $y = 0$, for $x \neq z_n$. This is coupled to the kinematic boundary conditions

$$\phi_y(x, 0) = \begin{cases} -h_x & \text{for } x > 0, \\ 0 & \text{for } x < 0, \end{cases} \tag{A.12}$$

with

$$\phi_{xx} + \phi_{yy} = 0, \quad \text{for} \quad y > 0, \tag{A.13}$$

with the crucial new pointwise boundary condition

$$\tilde{\omega} h_x = 1 \quad \text{at} \quad x = 0. \tag{A.14}$$

At the 'contact points' at $x = z_n$, we have

$$h(z_n) = 0, \qquad \tilde{\omega} h(z_n+) = -\tilde{\omega} h(z_n-) = \alpha_n. \tag{A.15}$$

We want $z_n - z_{n-1} \to 1$, and α_n to tend to a non-zero constant, as $n \to \infty$. As the whole system is unchanged by the addition of an arbitrary constant to ϕ, we choose to normalise so that $\phi(0,0) = 0$. For large x, we want $h(x)$ to tend to a periodic function with period 1. We find that ϕ must grow logarithmically as $r \to \infty$.

A.3 Logarithmic growth of velocity potential

We begin by considering the velocity potential $\psi_n(x, y)$ driven by h in the single oscillation $z_n < x < z_{n+1}$ We assume that $h(x)$ is finite and differentiable in this region. This velocity potential is bounded, and up to a constant, can be written as

$$\psi_n(x,0) = \frac{1}{\pi} \int_{z_n}^{z_{n+1}} \log|x - x'| \phi_y(x',0) dx' = -\frac{1}{\pi} \int_{z_n}^{z_{n+1}} \log|x - x'| h_x(x') dx'. \tag{A.16}$$

The potential $\psi_n(x,0)$ as defined by (A.16) is bounded everywhere and decays as $O(|x - z_n|^{-1})$ as $|x| \to \infty$ with n fixed, which is the decay rate of a dipole. In order to assemble ϕ, we need to add together a half-line of these dipoles. However, as the far field of each one decays as $O(|x - n|^{-1})$, we find that this sum does not converge for any fixed value of x. For example, with $x = -a$, $a > 0$, we would like to write

$$\phi(-a,0) \sim const. \times \sum_{n=0}^{\infty} \frac{1}{a+n}, \tag{A.17}$$

This sum does not converge for any finite a, but in some sense 'tends to zero' as $a \to \infty$.

By renormalising the flow from an individual oscillation, we can exchange decay at infinity for boundedness for finite x. We do this by choosing the additive constant for ψ_n so that $\psi_n(0,0) \equiv 0$ for all n. The new expression for ϕ converges for finite x, and grows logarithmically for large $|x|$.

We now write the contribution ϕ_n to ϕ from the region $0 \le z_n < x < z_{n+1}$ as

$$\begin{aligned}\phi_n(x,0) &= \frac{1}{\pi}\int_{z_n}^{z_{n+1}} \log|x-x'|\phi_y(x',0)dx' - \frac{1}{\pi}\int_{z_n}^{z_{n+1}} \log|x'|\phi_y(x',0)dx' \\ &= -\frac{1}{\pi}\int_{z_n}^{z_{n+1}} \log|x-x'|h_x(x')dx' + \frac{1}{\pi}\int_{z_n}^{z_{n+1}} \log|x'|h_x(x')dx' \\ &= \frac{1}{\pi}\int_{z_n}^{z_{n+1}} \frac{h(x')}{x'-x}dx' - \frac{1}{\pi}\int_{z_n}^{z_{n+1}} \frac{h(x')}{x'}dx. \end{aligned} \tag{A.18}$$

The cumulative function ϕ can then be expressed as

$$\phi(x,0) = \frac{1}{\pi}\sum_{n=0}^{\infty}\left(\int_{z_n}^{z_{n+1}} \frac{h(x')}{x'-x}dx' - \int_{z_n}^{z_{n+1}} \frac{h(x')}{x'}dx\right). \tag{A.19}$$

We want to determine the behaviour of (A.19) as $|x| \to \infty$. Now suppose that $x = -a$ with $a > 0$, so that $|x - z_n| >> 1$ for all n. If $|x - z_n| \gg 1$ and $z_n \gg 1$, we can estimate ϕ_n as

$$\phi_n(x,0) \sim \frac{1}{\pi}\frac{x}{z_n(z_n-x)}\bar{h}_n \quad \text{as} \quad |z_n - x| \to \infty. \tag{A.20}$$

where

$$\bar{h}_n \equiv \int_{z_n}^{z_{n+1}} h(x')dx'. \tag{A.21}$$

We know that $\bar{h}_n > 0$ for $n \ge 0$, and $\bar{h}_n \to \bar{h}_\infty$ as $n \to \infty$. In order to determine the leading order behaviour of ϕ as $r \to \infty$, we can take $z_n = n$ and $\bar{h}_n = \bar{h}_\infty$ for $n \ge 0$. Corrections to this do not affect the logarithmic growth of ϕ but would alter the constant term.

At leading order for $|x| \gg 1$, we find

$$\phi(x,0) \sim \frac{1}{\pi}\bar{h}_\infty \sum_{n=1}^{\infty}\frac{x}{n(n-x)} + O(1). \tag{A.22}$$

Now, it happens that

$$\sum_{n=1}^{\infty}\frac{1}{n(n-x)} = \frac{1}{\pi}\left(-\gamma - \psi_0(1-x)\right) \tag{A.23}$$

where γ is the Euler-Mascheroni constant, and ψ_0 is the digamma function [NIST, 2011], defined by

$$\psi_0(z) = \frac{d}{dz}\log\Gamma(z). \tag{A.24}$$

If z does not lie on the negative real axis, we find

$$\psi_0(z) \sim \log z + O(1/z), \tag{A.25}$$

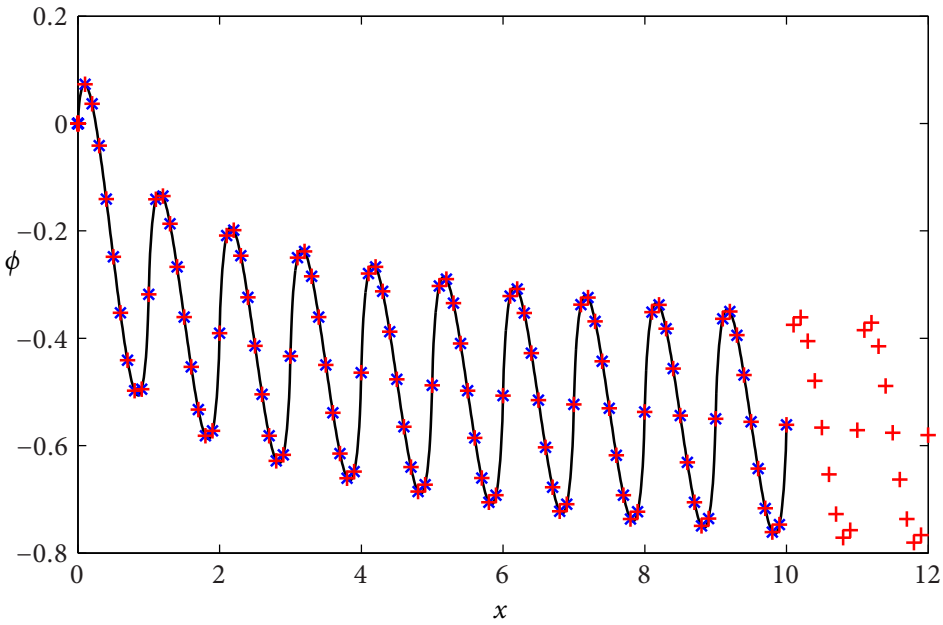

Figure A.1: $\phi(x, y)$ calculated for $\sigma = 0$, in which case h is a sequence of parabolas, all of width 1. This plot tests the Gaussian quadrature rule. We should get perfect agreement for $\sigma = 0$, as in this case H is a parabola for each oscillation and H_x varies linearly between grid points. The solutions shown here are for $N = 10$, $k = 100$, $M = 100$ (black solid line), $N = 10$, $k = 10$, $M = 100$, (blue crosses) and $N = 100$, $k = 10$, $M = 100$ (red plusses).

so that

$$\phi(x, 0) \sim -\frac{\bar{h}_\infty}{\pi} \log x + O(1), \tag{A.26}$$

for $|x| \gg 1$ with $x < 0$, and by analytic continuation we find

$$\phi \sim -\frac{\bar{h}_\infty}{\pi} \log r + O(1) \tag{A.27}$$

for all $r \gg 1$. This logarithmic growth does not appear in the composite solution for $\hat{\Phi}$ in the secularity calculations of chapter 4, as it is exactly cancelled by a singularity as $R \to 0$ in the slow variation of the velocity potential $W_0(X, Y)$. The composite solution is discussed in section 4.7.5.

A.4 Piecewise integration of Bernoulli equation

We can integrate (A.11) to reach

$$\tilde{\omega}^2 h_x = \tilde{\omega} + \tilde{\omega}\sigma\phi(x,0) - x + \sum_{m=1}^{\infty} B_m \theta(x - z_m), \tag{A.28}$$

where θ is the Heaviside step function. We know $\phi(x,0)$ is continuous at $x = z_n$, and $\tilde{\omega} h_x(z_n\pm) = \pm\tilde{\omega}\alpha_n$. Evaluating (A.28) at $x = z_n\pm$, we find

$$\tilde{\omega}^2 h_x(z_n+) = \tilde{\omega}\alpha_n = \tilde{\omega} + \tilde{\omega}\sigma\phi(z_n,0) + \sum_{m=1}^{n} B_m \tag{A.29}$$

and

$$\tilde{\omega}^2 h_x(z_n-) = -\tilde{\omega}\alpha_n = \tilde{\omega} + \tilde{\omega}\sigma\phi(z_n,0) + \sum_{m=1}^{n-1} B_m. \tag{A.30}$$

Subtracting (A.30) from (A.29), we find that $B_n = 2\tilde{\omega}\alpha_n$ for $n \geq 1$, and so we can write (A.28) as

$$\tilde{\omega}^2 h_x = \tilde{\omega} + \tilde{\omega}\sigma\phi(x,0) - x + 2\tilde{\omega}\sum_{m=1}^{\infty} \alpha_m \theta(x - z_m). \tag{A.31}$$

We can rearrange (A.31) to give $\phi(z_m)$:

$$\tilde{\omega}\sigma\phi(z_n,0) = \tilde{\omega}\alpha_n - \tilde{\omega} + z_n - 2\tilde{\omega}\sum_{m=1}^{n} \alpha_m. \tag{A.32}$$

We know from the previous section that $\phi(x,0)$ should grow no faster than logarithmically with x for large x. We can use this to find a constraint on the behaviour of α as $n \to \infty$. For large n, we require $z_n - z_{n-1} \to 1$ and α to tend to a constant, so suppose

$$z_n = n + \bar{z} + o(1), \qquad \alpha_n = \bar{\alpha} + \frac{b_0}{n} + o(n^{-1}). \tag{A.33}$$

Then (A.32) becomes

$$\tilde{\omega}\sigma\phi(z_n) = n(1 - 2\tilde{\omega}\bar{\alpha}) - 2\tilde{\omega}b_0 \sum_{j=1}^{n} \frac{1}{j} + O(1). \tag{A.34}$$

Here the $O(1)$ term includes anything that is bounded as $n \to \infty$. Kinematically, we expect ϕ_n to grow logarithmically as $x \to \infty$. However, linear growth in n is not permitted, so

$$\bar{\alpha} = \lim_{n\to\infty} \alpha_n = \frac{1}{2\tilde{\omega}}. \tag{A.35}$$

A.5 Formulation of integral equation

Given a trial solution h, σ, $\tilde{\omega}$, α_n and z_n for $1 \le n \le N$, we want to find a harmonic function $\phi(x,y)$ with $\phi(0,0) = 0$ such that

$$\phi_y(x,0) = \begin{cases} -h_x, & \text{for } 0 < x < z_N \\ 0, & \text{for } x < 0 \end{cases} \tag{A.36}$$

and

$$\phi(x,y) = -\sum_{m=1}^{\infty} a_m \sin(2\pi m(x - z_N)) e^{-2\pi m y} + \frac{C_1}{2}\log(x^2 + y^2) + C_2 \tag{A.37}$$

for $x > z_N \equiv X$. In terms of σ and $\tilde{\omega}$, the Fourier coefficients are

$$a_m = \frac{1}{\pi m \tilde{\omega}(\sigma - 2\pi m \tilde{\omega})}. \tag{A.38}$$

For the integral equation, we use the Green's function $G(\mathbf{x},\mathbf{x}') = \log|\mathbf{x} - \mathbf{x}'|/2\pi$, on the semicircle of radius $R = X$, centred at the origin. We know that

$$\int_V \phi(\mathbf{x}')\nabla'^2 G(\mathbf{x},\mathbf{x}')d\mathbf{x}' = \int_{\partial V} \phi(\mathbf{x}')\mathbf{n}'\cdot\nabla' G(\mathbf{x},\mathbf{x}')d\mathbf{x}' - G(\mathbf{x},\mathbf{x}')\mathbf{n}'\cdot\nabla'\phi(\mathbf{x}')d\mathbf{x}', \tag{A.39}$$

where $\mathbf{n}$ is outwards-pointing unit normal. For $\mathbf{x} = (x,0)$, with the normalisation $\phi(0,0) = 0$, this becomes

$$\begin{aligned} \frac{1}{2}\phi(x,0) = &\int_0^X \frac{1}{2\pi}\log\left|\frac{x - x'}{x'}\right| \phi_y(x',0) \\ &+ \int_{|\mathbf{x}'|=X} \phi(\mathbf{x}')\mathbf{n}'\cdot\nabla' G(\mathbf{x},\mathbf{x}')d\mathbf{x}' - G(\mathbf{x},\mathbf{x}')\mathbf{n}'\cdot\nabla'\phi(\mathbf{x}')d\mathbf{x}' \\ &- \int_{|\mathbf{x}'|=X} \phi(\mathbf{x}')\mathbf{n}'\cdot\nabla' G(\mathbf{0},\mathbf{x}')d\mathbf{x}' - G(\mathbf{0},\mathbf{x}')\mathbf{n}'\cdot\nabla'\phi(\mathbf{x}')d\mathbf{x}'. \end{aligned} \tag{A.40}$$

There are two components of the far field contribution to the velocity potential ϕ. The sequence of oscillations corresponding to a_m gives a flux across the line $x = R$. Also, the slow, smooth decay of ϕ could give a contribution across the whole semicircle arc $r = R$. On this semicircle, we have

$$G(\mathbf{x},\mathbf{x}') = \frac{1}{4\pi}\log\left[R^2 - 2xR\cos\theta + x^2\right] \tag{A.41}$$

and

$$\mathbf{n}' = (\cos\theta, \sin\theta), \tag{A.42}$$

so

$$\mathbf{n}' \cdot \nabla' G(\mathbf{x}, \mathbf{x}') = \frac{\partial G}{\partial R} = \frac{1}{2\pi} \frac{R - x\cos\theta}{R^2 - 2xR\cos\theta + x^2}. \tag{A.43}$$

We begin by considering the slow growth of ϕ as $r \to \infty$. Suppose that for large r, we have

$$\phi = C_1 \log r + C_2 \tag{A.44}$$

where C_1 and C_2 are constants. Then

$$\begin{aligned}
\phi_{outer}(x) = &\int_{|\mathbf{x}'|=R} \phi(\mathbf{x}')\mathbf{n}' \cdot \nabla' G(\mathbf{x}, \mathbf{x}')d\mathbf{x}' - G(\mathbf{x}, \mathbf{x}')\mathbf{n}' \cdot \nabla' \phi(\mathbf{x}')d\mathbf{x}' \\
&- \int_{|\mathbf{x}'|=R} \phi(\mathbf{x}')\mathbf{n}' \cdot \nabla' G(\mathbf{0}, \mathbf{x}')d\mathbf{x}' - G(\mathbf{0}, \mathbf{x}')\mathbf{n}' \cdot \nabla' \phi(\mathbf{x}')d\mathbf{x}' \\
= &\int_0^\pi \left\{ (C_1 \log R + C_2) \frac{1}{2\pi} \left(\frac{R - x\cos\theta}{R^2 - 2xR\cos\theta + x^2} - \frac{1}{R} \right) \right. \\
&\left. -C_1 \frac{1}{4\pi} \left(\log\left[R^2 - 2xR\cos\theta + x^2\right] - 2\log R \right) \right\} R d\theta.
\end{aligned} \tag{A.45}$$

Let $u = x/R$. Then

$$\begin{aligned}
\phi_{outer}(x) = &(C_1 \log R + C_2) \frac{1}{2\pi} \int_0^\pi \left(\frac{1 - u\cos\theta}{1 - 2u\cos\theta + u^2} - 1 \right) d\theta \\
&-C_1 \frac{1}{4\pi} \int_0^\pi \log\left[1 - 2u\cos\theta + u^2\right] d\theta.
\end{aligned} \tag{A.46}$$

However we find that

$$\int_0^\pi \frac{1 - u\cos\theta}{1 - 2u\cos\theta + u^2} d\theta = \pi, \qquad \int_0^\pi \log\left[1 - 2u\cos\theta + u^2\right] d\theta = 0 \tag{A.47}$$

so

$$\phi_{outer}(x) = 0 \tag{A.48}$$

So with the normalisation $\phi(0, 0) = 0$, the slow growth from $\phi \sim C_1 \log r + C_2$ gives no contribution to the boundary integral expression for ϕ.

However, we do obtain a non-trivial contribution from the oscillations for $x > X$. In the far field,

$$h_{osc} = \sum_{m=1}^{\infty} a_m [\cos\{2\pi m(x - X)\} - 1], \tag{A.49}$$

so

$$\frac{\partial \phi_{osc}}{\partial y}(x, 0) = -h_x(x) = \sum_{m=1}^{\infty} a_m 2\pi m \sin\{2\pi m(x - X)\}, \tag{A.50}$$

and

$$\phi_{osc}(x,y) = -\sum_{m=1}^{\infty} a_m \sin\{2\pi m(x-X)\}\, e^{-2\pi m y}. \tag{A.51}$$

Along the line $x = X$, the Fourier expansion (A.51) gives $\phi_{osc}(X,y) = 0$, but

$$\frac{\partial \phi_{osc}}{\partial x}(X,y) = -\sum_{m=1}^{\infty} 2\pi m a_m e^{-2\pi m y}. \tag{A.52}$$

Substituting (A.51) for ϕ in the integrals over $\mathbf{x}' = X$ in (A.40), we obtain

$$\begin{aligned}\phi(x,0) = &-\frac{1}{\pi}\int_0^X \log\frac{|x-x'|}{|x'|} h_x(x')dx' \\ &+\frac{1}{2\pi}\sum_{m=1}^{\infty} a_m 2\pi m \int_0^{\infty} \log\left(\frac{(X-x)^2+y^2}{X^2+y^2}\right) e^{-2\pi m y} dy.\end{aligned} \tag{A.53}$$

We can transform the variable of integration, letting $Y = 2\pi m y$. Then

$$\begin{aligned}\phi(x,0) = &-\frac{1}{\pi}\int_0^X \log\frac{|x-x'|}{|x'|} h_x(x')dx' \\ &+\frac{1}{2\pi}\sum_{m=1}^{\infty} a_m \int_0^{\infty} \log\left(\frac{(2\pi m(X-x))^2+Y^2}{(2\pi m X)^2+Y^2}\right) e^{-Y} dY.\end{aligned} \tag{A.54}$$

For the numerical evaluation, we define a function:

$$S(Z) := \int_0^{\infty} \log(Z^2+Y^2) e^{-Y} dY. \tag{A.55}$$

$S(Z)$ is defined for all real Z, with $S(0) = -2\gamma$, where $\gamma = 0.577\ldots$ is the Euler-Mascheroni constant. For large Z, $S(Z) \sim 2\log Z$. Plots of $S(Z)$ against Z and $\log(1+Z)$ are shown in figures A.2 and A.3.

We can rewrite (A.54) in terms of S as

$$\begin{aligned}\phi(x,0) = &-\frac{1}{\pi}\int_0^X \log\frac{|x-x'|}{|x'|} h_x(x')dx' \\ &+\frac{1}{2\pi}\sum_{m=1}^{M} a_m \left[S(2\pi m(X-x)) - S(2\pi m X)\right] \\ &+\frac{1}{2\pi}\sum_{m=M+1}^{\infty} a_m \left[2\log\left(\frac{X-x}{X}\right)\right].\end{aligned} \tag{A.56}$$

Here we evaluate $S(Z)$ explicitly for the first M Fourier modes, and use the large-Z

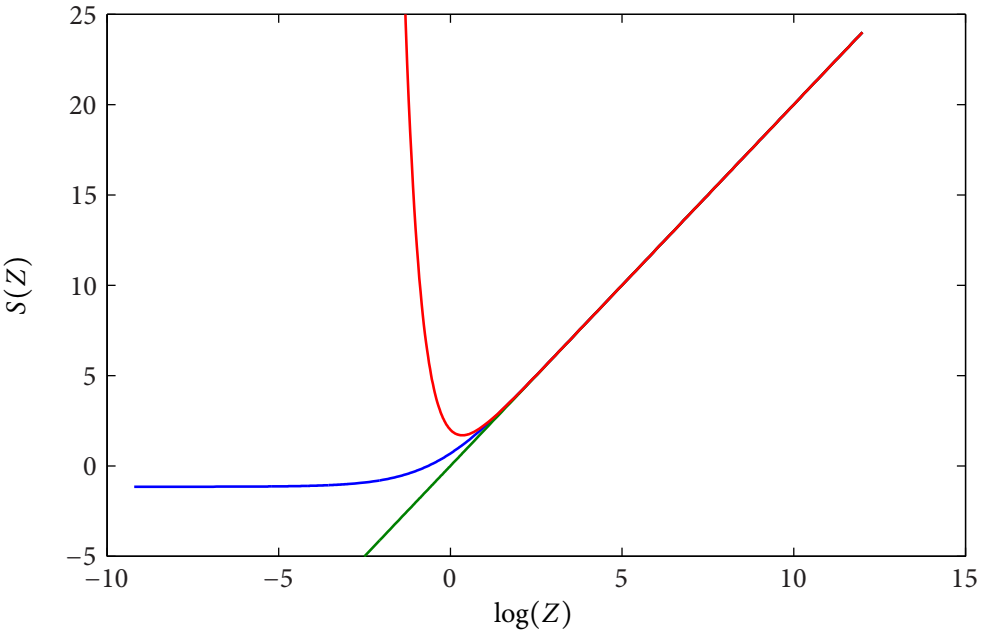

Figure A.2: A semi-logarithmic plot of the function $S(Z)$ defined by (A.55). The blue line shows $S(Z)$ calculated using Matlab's quadgk routine. The green line shows the leading-order large Z approximation $S \sim 2\log(Z)$. The red line shows the next correction: $S \sim 2\log(Z) + 2/Z^2$. This correction improves convergence for large Z, but has a large deviation for small Z.

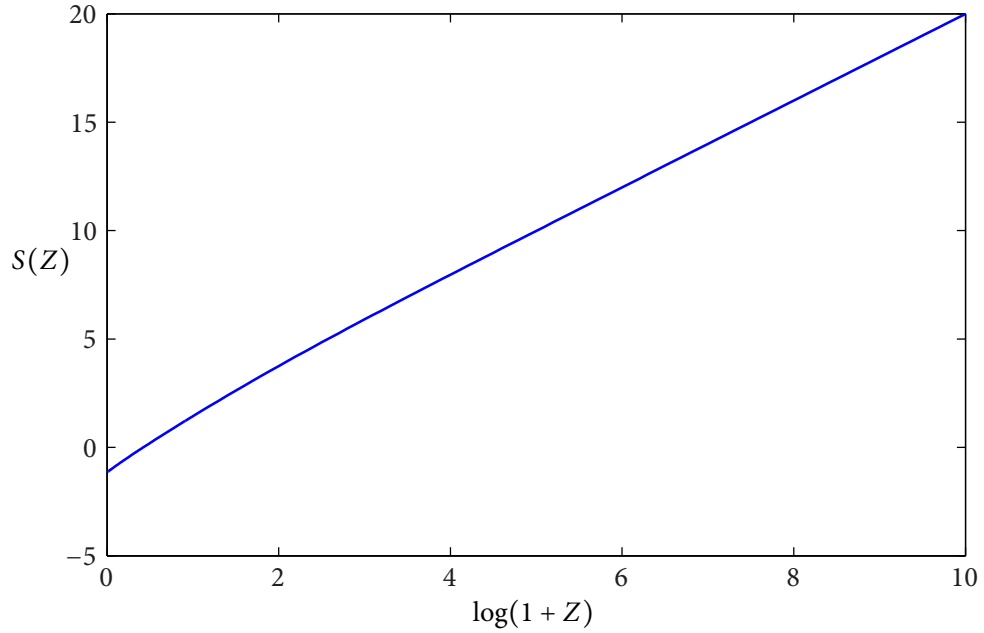

Figure A.3: For the purposes of interpolating S, we use linear interpolation based on $S(Z)$ vs. $\log(1+Z)$, which gives a close-to-linear plot, compared to figure A.2.

approximation $S(Z) \sim 2\log(Z)$ for $m > M$. This simplifies to become

$$\begin{aligned}\phi(x,0) = &-\frac{1}{\pi}\int_0^X \log\frac{|x-x'|}{|x'|}h_x(x')dx' \\ &+\frac{1}{2\pi}\sum_{m=1}^{M} a_m\left[S(2\pi m(X-x)) - S(2\pi mX)\right] \\ &+\frac{1}{\pi}\log\left(\frac{X-x}{X}\right)\left(\sum_{m=M+1}^{\infty} a_m\right).\end{aligned} \tag{A.57}$$

The use of the large Z expansion for the higher terms of $S(Z)$ should be a good approximation provided $2\pi M(X-x) \gg 1$.

Clearly this approximation will fail when $x = X$, in which case we can make use of the exact result $S(0) = -2\gamma$. Then we can write

$$\begin{aligned}\phi(X,0) = &-\frac{1}{\pi}\int_0^X \log\frac{|X-x'|}{|x'|}h_x(x')dx' \\ &+\frac{1}{2\pi}\sum_{m=1}^{M} a_m\left[-2\gamma - S(2\pi mX)\right] \\ &+\frac{1}{2\pi}\sum_{m=M+1}^{\infty} a_m\left[-2\gamma - 2\log(2\pi mX)\right],\end{aligned} \tag{A.58}$$

or

$$\begin{aligned}\phi(X,0) = &-\frac{1}{\pi}\int_0^X \log\frac{|X-x'|}{|x'|}h_x(x')dx' \\ &+\frac{1}{2\pi}\sum_{m=1}^{M} a_m\left[-2\gamma - S(2\pi mX)\right] \\ &+\frac{1}{2\pi}\left[-2\gamma - 2\log(2\pi X)\right]\sum_{m=M+1}^{\infty} a_m, \\ &-\frac{1}{2\pi}\sum_{m=M+1}^{\infty} a_m \log m.\end{aligned} \tag{A.59}$$

In order to evaluate the integrals involving h_x in (A.57) and (A.59) we use Gaussian quadrature with a logarithmic weight function, and a single collocation point, so that the integrals are exact if h_x varies linearly between grid points. The Gaussian weight functions and abscissa will be different for every subinterval and value of x'.

We want to find weight functions W and collocation points q so that:

$$\int_a^b f(x')\log|x-x'|dx' = W[qf(a) + (1-q)f(b)], \tag{A.60}$$

where W and q are constants, that give exact results for $f(x) = Ax + B$, for arbitrary values of the constants A and B. Then

$$\int_a^b (Ax' + B) \log|x - x'| dx' = W[q(Aa + B) + (1 - q)(Ab + B)], \tag{A.61}$$

so

$$F_1 = \int_a^b x' \log|x - x'| dx' = W[qa + (1 - q)b]. \tag{A.62}$$

and

$$F_2 = \int_a^b \log|x - x'| dx' = W. \tag{A.63}$$

Thus

$$q = \frac{1 - F_1/F_2}{b - a}, \qquad W = F_2. \tag{A.64}$$

F_1 and F_2 both depend on a, b and x'. We use integration by parts to find exact expressions for F_1 and F_2.

When $\sigma = 0$, the solution for h is a sequence of parabolas, so h_x varies exactly linearly between grid points. We find that for $\sigma = 0$, the grid points for $\phi(x, 0)$ for using $k = 10$ points per subinterval lie directly on top of those calculated using $k = 80$ points per subinterval (figure A.1). As σ increases, the solution will deviate from the initial sequence of parabolas, and so discretisation errors will be introduced.

A.6 Numerical continuation scheme

We discretise x with k points per oscillation and a total of N free oscillations. The grid points are equally spaced within each oscillation. We use finite difference formulae to discretise the Bernoulli equation (A.31), taking care that difference formulae do not cross the points $x = z_n$ where h_x is discontinuous. We interpolate S for the first M Fourier modes in (A.57) and (A.59). We would like to solve for the eigenvalue $\tilde{\omega}(\sigma)$ as the discretisation parameters N, k and M tend to infinity.

For given values of z_n, the problem is linear in h, ϕ and α_n, and depends nonlinearly on $\tilde{\omega}$. We also need to find z_n as part of the solution, which provides a significant source of nonlinearity. The integral equation can be expressed as a dense matrix equation linking ϕ and h. However, the coefficients of this matrix depend on the x distribution and hence the choice of z_n, so whenever z_n is altered, the matrix must be recalculated. The Jacobian for

the relationship between the integral equation and z_n is determined by finite differencing, which is the most time consuming component of the computation.

A.7 Solutions for general σ

We use Newton iteration and continuation in σ to obtain solutions, starting from the known solution at $\sigma = 0$, $\tilde{\omega} = 1/2$. The system is linear in α_n, h and ϕ, but nonlinear in $\tilde{\omega}$ and z_n. Discretised solutions of this problem show a branch structure, illustrated in A.4 for some attainable values of N, k and M. We are interested in the solution in the limit of each of these three discretisation parameters tending to infinity.

We expect the 'true' branch to be connected to $\sigma = 0$, $\tilde{\omega} = 1/2$, and to satisfy $\tilde{\omega} > \sigma/2\pi$, as crossing this line would give a singularity in the Fourier coefficients (A.38). In figure A.4, we note that as N increases, the two branches above this line move closer together, and are almost touching when $N = 30$, however there is still a small kink near $\sigma = 6.86$. It is not clear whether for $\sigma > 6.86$, the true solution should follow the upper branch (passing through $\sigma = 20$, $\tilde{\omega} \approx 4$) or the lower branch (passing through $\sigma = 20$, $\tilde{\omega} \approx 3.5$), or some other path.

Figures A.5 and A.6 show individual solutions on the upper and lower branches that are above the line $\tilde{\omega} = \sigma/2\pi$. It seems the upper branch is the correct one for $\sigma < 6.86$ and the lower branch is correct for $\sigma > 6.86$. This path corresponds to the one taken by the red line (for $N = 30$, $k = 30$, $M = 100$) in figure A.4, though this red line cannot represent the true behaviour in the kink area itself. We use the red branch, smoothing over the kink, to calculate boundary conditions for the multiple scales analysis in section 4.7.1.

A.8 Conclusion

In this appendix, we discussed numerical solutions to the two-fluid inner problem. This is a half-plane problem, corresponding to two-dimensional flow around a sequence of constant pressure regions. The length and position of these regions is unknown, which causes significant nonlinearities in the discretised equations, and the solutions to the eigenvalue problem for $\tilde{\omega}(\sigma)$ show a complicated branch structure which seems to be related to the discretisation parameters. We can choose a path of plausible branches through this branch structure in order to calculate boundary conditions for the secularity

integration in section 4.7.1, however it is not clear whether this path corresponds to valid solutions of the non-discretised problem.

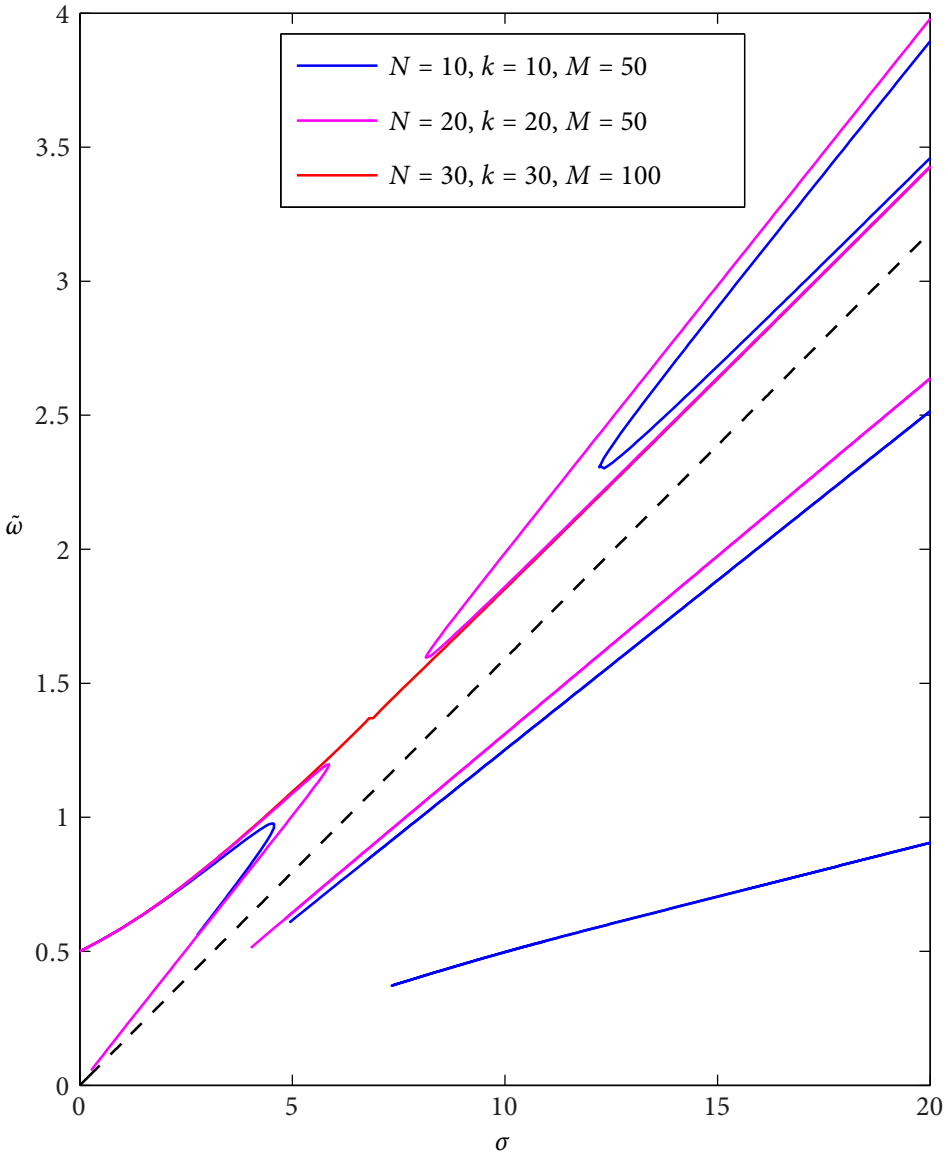

Figure A.4: The dependence of the eigenvalue $\tilde{\omega}$ as calculated by solution of the discretised problem shows a complicated branch structure with respect to density parameter σ. We are looking for a branch connected to $\sigma = 0$, $\tilde{\omega} = 1/2$. There is a singularity in the far-field Fourier coefficients if $\sigma = 2\pi n\tilde{\omega}$ for any integer n, and so we expect the true eigenvalue to remain above the dashed line which indicates $\tilde{\omega} = \sigma/2\pi$. Figures A.5 and A.6 shows solutions for $\sigma = 4$ and $\sigma = 12$ for the two branches above this line. An examination of the behaviour of these solutions near $x = z_N$ suggests that we should choose the upper of the two branches for $\sigma = 4$ and the lower of the two branches for $\sigma = 12$.

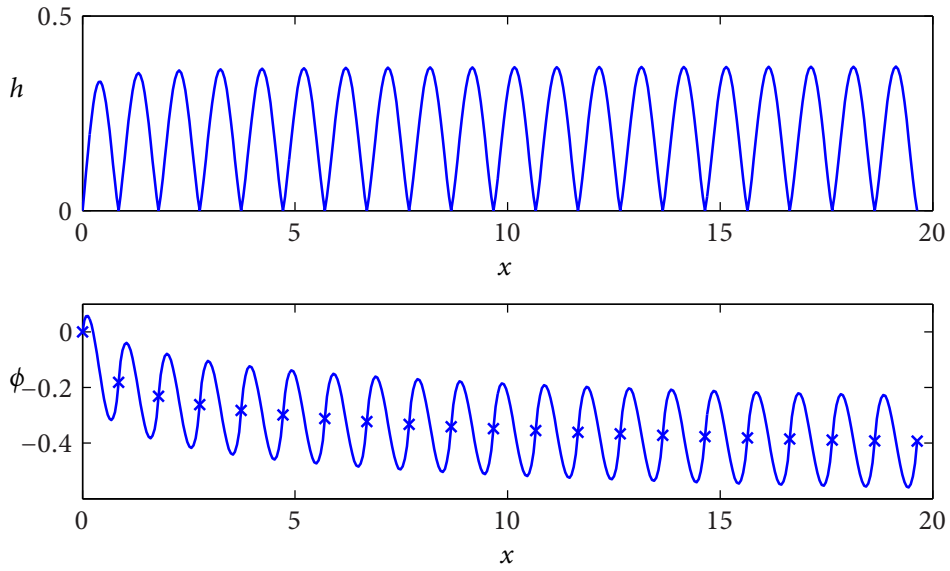

(a) Upper branch solution: $\tilde{\omega} = 0.9500$

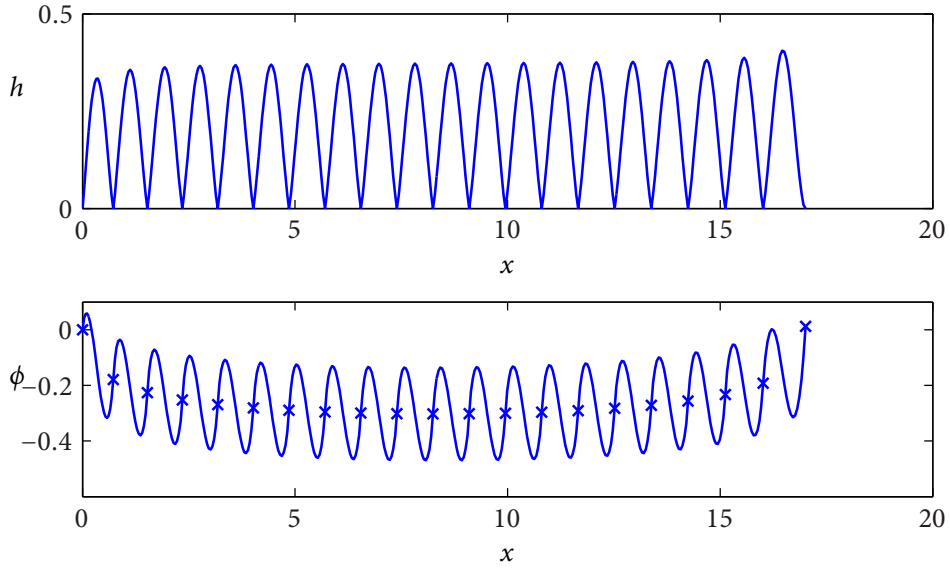

(b) Lower branch solution: $\tilde{\omega} = 0.8046$

Figure A.5: Two solutions for $N = 20$, $k = 20$, $M = 100$ at $\sigma = 4$. The upper branch solution appears to be periodic for $x > 5$. The lower branch solution has non-periodic behaviour in h for the last oscillation, and $O(1)$ growth in ϕ; this solution is probably invalid. The crosses mark the value $\phi(z_n, 0)$.

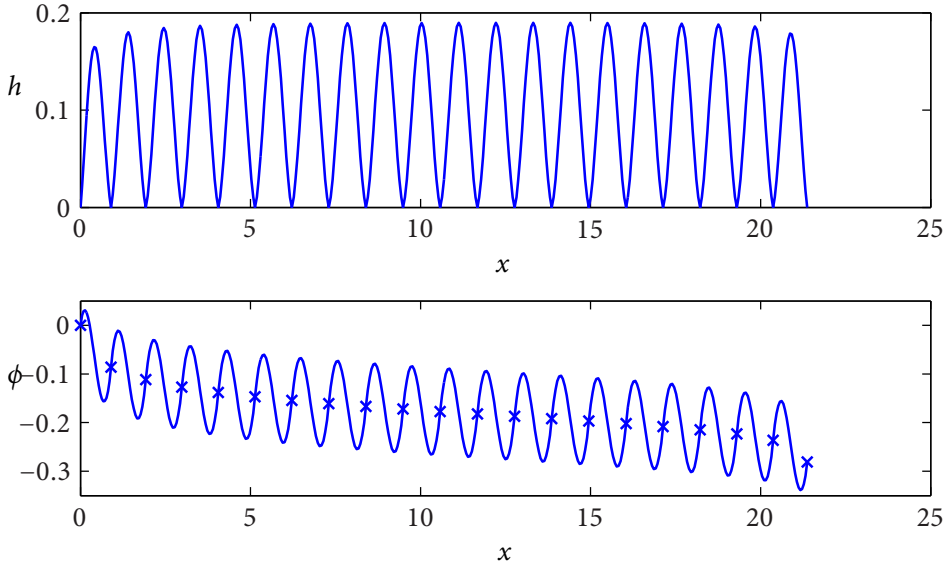

(a) Upper branch solution: $\tilde{\omega} = 2.3858$

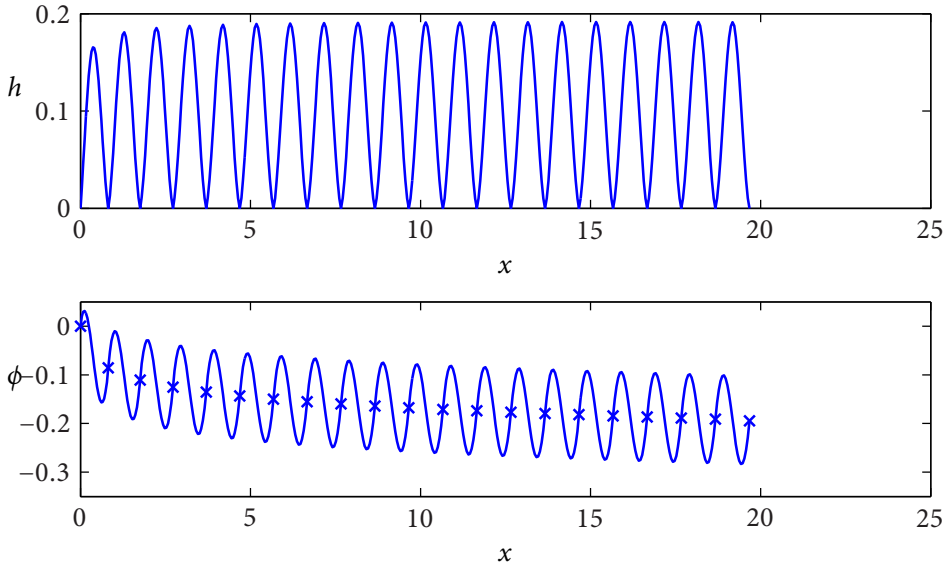

(b) Lower branch solution: $\tilde{\omega} = 2.1700$

Figure A.6: Two solutions for $N = 20$, $k = 20$, $M = 100$ at $\sigma = 12$. The difference between these two solutions is much more subtle than for those in figure A.5. The crosses mark the values of $\phi(z_n, 0)$. Neither sequence $\phi(z_n)$ is completely smooth near $n = N$, but the upper branch solution shows a much larger kink. For this value of σ it seem that the lower branch solution is better converged to a periodic solution as $x \to \infty$, and so we take the lower branch of this pair for the secularity calculations in section 4.7.1.

Appendix B

Nonlinear free-boundary problem

B.1 Nonlinear free-boundary problem

In chapters 3 and 4 we analysed wedge recoil problems with wedge angle ϵ and contact angle $\lambda\epsilon$ in the limit $1 \ll \lambda \ll \epsilon^{-1}$. The interface height tends to zero as $\epsilon \to 0$, and we can write the interface position as $(x, y) = (x, \epsilon H(x))$, where H is a single-valued differentiable function of x. However, for coalescence problems with $\beta = \pi/2$, H_x is not defined at the contact point, and the interface height y need not be a single-valued function of x. It is therefore sensible to parametrize the interface with respect to arc-length for problems which have $O(1)$ contact angles.

The interface is located at $(x, y) = (X(s), Y(s)) = \mathbf{R}$, where s is arc-length and so

$$X'^2 + Y'^2 = 1. \tag{B.1}$$

where a $'$ to indicate d/ds. We need to solve for $X(s)$, $Y(s)$, $\Phi_1(s) \equiv \Phi_1(X(s), Y(s))$ and $\Phi_2(s) \equiv \Phi_2(X(s), Y(s))$.

The nonlinear, dimensional Bernoulli equation can be written as

$$\rho_1 \left(\frac{\partial \phi_1}{\partial t} + \frac{1}{2} |\nabla \phi_1|^2 \right) - \rho_2 \left(\frac{\partial \phi_2}{\partial t} + \frac{1}{2} |\nabla \phi_2|^2 \right) = \sigma \kappa, \tag{B.2}$$

where ϕ_1 and ϕ_2 are the dimensional velocity potentials, and κ is the dimensional curvature. In similarity variables this becomes

$$\frac{\rho_1}{\rho} \left(\frac{1}{3}\Phi_1 - \frac{2}{3}\mathbf{R} \cdot \nabla \Phi_1 + \frac{1}{2} |\nabla \Phi_1|^2 \right) - \frac{\rho_2}{\rho} \left(\frac{1}{3}\Phi_2 - \frac{2}{3}\mathbf{R} \cdot \nabla \Phi_2 + \frac{1}{2} |\nabla \Phi_2|^2 \right) = X'Y'' - Y'X'', \tag{B.3}$$

where ρ is the reference density used in the nondimensionalisation, and the expression for curvature has been simplified using the arc-length equation.

The kinematic boundary condition is that the normal velocities of the interface and the fluid on either side match, so dimensionally we have

$$\mathbf{n} \cdot \frac{\partial \mathbf{R}}{dt} = \mathbf{n} \cdot \nabla \phi_1 = \mathbf{n} \cdot \nabla \phi_2, \tag{B.4}$$

which becomes

$$\frac{2}{3}\mathbf{n} \cdot \mathbf{R} = \mathbf{n} \cdot \nabla \Phi_1 = \mathbf{n} \cdot \nabla \Phi_2 \tag{B.5}$$

in similarity variables, where $\mathbf{n}$ and $\mathbf{t}$ are unit normal and tangential vectors to the interface respectively.

The Bernoulli equation currently involves derivatives of $\Phi_{1,2}$ with respect to both x and y. However, the kinematic boundary condition gave the normal components of $\nabla\Phi$ at the boundary in terms of the interface position directly, and so it is helpful to write $\nabla\Phi$ in (B.3) as

$$\nabla \Phi_{1,2} = \mathbf{t}(\mathbf{t} \cdot \nabla \Phi_{1,2}) + \mathbf{n}(\mathbf{n} \cdot \nabla \Phi_{1,2}) = \Phi'_{1,2}\mathbf{t} + \frac{2}{3}(\mathbf{n} \cdot \mathbf{R})\mathbf{n}. \tag{B.6}$$

As the interface is parametrized by arc-length, the normal and tangential vectors can be written as $\mathbf{n} = (-Y', X')$ and $\mathbf{t} = (X', Y')$, where $\mathbf{n}$ points into fluid 2. The Bernoulli equation (B.3) now becomes

$$\begin{aligned} &\frac{\rho_1}{\rho}\left[\frac{1}{3}\Phi_1 - \frac{2}{9}(X'Y - XY')^2 + \frac{1}{2}\Phi'_1\left(\Phi'_1 - \frac{4}{3}(XX' + YY')\right)\right] \\ &-\frac{\rho_2}{\rho}\left[\frac{1}{3}\Phi_2 - \frac{2}{9}(X'Y - XY')^2 + \frac{1}{2}\Phi'_2\left(\Phi'_2 - \frac{4}{3}(XX' + YY')\right)\right] \\ &\qquad = X'Y'' - Y'X'', \end{aligned} \tag{B.7}$$

which requires only tangential derivatives of Φ_1 and Φ_2.

We would also like to write the kinematic boundary conditions in terms of Φ_1 and Φ_2 and their tangential derivatives. We do this by using a boundary integral method, with the Green's function $G(\mathbf{x}, \mathbf{x}') = \log|\mathbf{x} - \mathbf{x}'|/2\pi$. In order to avoid explicit contributions from the line of symmetry at $y = 0$, we reflect the interface in this line, so the integral is over both parts of the interface. The vector $\mathbf{n}$ is an outwards pointing normal to fluid 1, and so we obtain

$$\begin{aligned} -\Phi_1(s_0) =& \frac{2}{3\pi}\int_0^\infty \mathbf{n}(s) \cdot \mathbf{R}(s)\left\{\log|\mathbf{R}(s) - \mathbf{R}(s_0)| + \log|\mathbf{R}_-(s) - \mathbf{R}(s_0)|\right\} ds \\ &+ \frac{1}{\pi}\int_0^\infty \Phi_1(s)\left\{\frac{\mathbf{n}(s) \cdot (\mathbf{R}(s_0) - \mathbf{R}(s))}{|\mathbf{R}(s_0) - \mathbf{R}(s)|^2} + \frac{\mathbf{n}_-(s) \cdot (\mathbf{R}(s_0) - \mathbf{R}_-(s))}{|\mathbf{R}(s_0) - \mathbf{R}_-(s)|^2}\right\} ds. \end{aligned} \tag{B.8}$$

n is an inwards pointing normal to fluid 2, and so the integral equation for fluid 2 differs only by a sign from (B.8), specifically

$$\begin{aligned}\Phi_2(s_0) =& \frac{2}{3\pi}\int_0^\infty \mathbf{n}(s)\cdot\mathbf{R}(s)\left\{\log|\mathbf{R}(s)-\mathbf{R}(s_0)|+\log|\mathbf{R}_-(s)-\mathbf{R}(s_0)|\right\}ds\\ &+\frac{1}{\pi}\int_0^\infty \Phi_2(s)\left\{\frac{\mathbf{n}(s)\cdot(\mathbf{R}(s_0)-\mathbf{R}(s))}{|\mathbf{R}(s_0)-\mathbf{R}(s)|^2}+\frac{\mathbf{n}_-(s)\cdot(\mathbf{R}(s_0)-\mathbf{R}_-(s))}{|\mathbf{R}(s_0)-\mathbf{R}_-(s)|^2}\right\}ds.\end{aligned} \tag{B.9}$$

Here $\mathbf{R}=(X,Y)$, $\mathbf{R}_-=(X,-Y)$, $\mathbf{n}=(-Y',X')$ and $\mathbf{n}_-=(-Y',-X')$. $\mathbf{R}_-$ is the position of the reflected part of the interface, and $\mathbf{n}_-$ is the reflected normal.

B.2 Recovery of linearised kinematic equations

We can obtain the leading order kinematic conditions on Φ_1 and Φ_2, that is (4.28) and (4.29), by manipulating the boundary integral equations (B.8) and (B.9)

We begin by scaling X and Y as $\epsilon\to 0$. We write

$$X(s)=X_c+s+O(\epsilon^2),\qquad Y(s)=\epsilon H(s)+O(\epsilon^2). \tag{B.10}$$

We find

$$\begin{aligned}&\frac{2}{3\pi}\int_0^\infty \mathbf{n}(s)\cdot\mathbf{R}(s)\left\{\log|\mathbf{R}(s)-\mathbf{R}(s_0)|+\log|\mathbf{R}_-(s)-\mathbf{R}(s_0)|\right\}ds\\ &\qquad=\frac{4\epsilon}{3\pi}\int_0^\infty [H(s)-(X_c+s)H'(s)]\log|s-s_0|ds+O(\epsilon^2).\end{aligned} \tag{B.11}$$

The kernel integral coming from the non-reflected part of the interface gives a term which is $O(\epsilon\Phi_{1,2})$ respectively as $\epsilon\to 0$. We have

$$\begin{aligned}&\frac{1}{\pi}\int_0^\infty \Phi_{1,2}(s)\left\{\frac{\mathbf{n}(s)\cdot(\mathbf{R}(s_0)-\mathbf{R}(s))}{|\mathbf{R}(s_0)-\mathbf{R}(s)|^2}\right\}ds\\ &\qquad=\frac{\epsilon}{\pi}\int_0^\infty \Phi_{1,2}(s)\left\{\frac{H(s_0)-H(s)-(s_0-s)H'}{|s_0-s|^2}\right\}ds+O(\epsilon^2).\end{aligned} \tag{B.12}$$

The integrand in (B.12) is finite at $s=s_0$, taking the value

$$-\Phi_{1,2}(s_0)\frac{H''(s_0)}{2}.$$

Determining the behaviour of the kernel integral coming from the reflected free surface as $\epsilon\to 0$ is more problematic. The approximation

$$\frac{1}{|\mathbf{R}(s_0)-\mathbf{R}_-(s)|^2}\equiv\frac{1}{|X(s)-X(s_0)|^2+|H(s)+H(s_0)|^2}\sim\frac{1}{|s-s_0|^2}+O(\epsilon) \tag{B.13}$$

fails when $|s - s_0| = O(\epsilon)$. We therefore split this integral into regions for $|s - s_0| \gg \epsilon$ and $|s - s_0| = O(\epsilon)$, writing

$$\begin{aligned}\frac{1}{\pi}\int_0^\infty \Phi_{1,2}(s)\left\{\frac{\mathbf{n}_-(s)\cdot(\mathbf{R}(s_0)-\mathbf{R}_-(s))}{|\mathbf{R}(s_0)-\mathbf{R}_-(s)|^2}\right\}ds \\ = \text{P.V.}\frac{\epsilon}{\pi}\int_0^\infty \Phi_{1,2}(s)\left\{\frac{-H(s_0)-H(s)-(s_0-s)H'(s)}{|s_0-s|^2}\right\}ds \\ + \frac{\epsilon}{\pi}\int_{s_0-\epsilon}^{s_0+\epsilon} \Phi_{1,2}(s)\left\{\frac{-H(s_0)-H(s)-(s_0-s)H'(s)}{|s_0-s|^2+\epsilon^2|H(s)+H(s_0)|^2}\right\}ds\end{aligned} \tag{B.14}$$

The final integral in (B.14) may be approximated by

$$-\frac{2\epsilon}{\pi}\Phi_{1,2}(s_0)H(s_0)\int_{-\infty}^{\infty}\left\{\frac{1}{|s_0-s|^2+4\epsilon^2H(s_0)^2}\right\}ds = -\Phi_{1,2}(s_0). \tag{B.15}$$

This term exactly cancels the left-hand-side of (B.8), and has the opposite sign to the left-hand-side of (B.9), and so we reach very different leading order equations from the two integral equations.

Rearranging the integral equation (B.8) for $\Phi_1(s)$ gives an equation which is independent of ϵ:

$$\begin{aligned}\frac{4}{3\pi}\int_0^\infty (H(s)-(X_c+s)H'(s))\log|s-s_0|ds \\ = \text{P.V.}\frac{2}{\pi}\int_0^\infty \Phi_1(s)\left\{\frac{H(s)+(s_0-s)H'(s)}{|s_0-s|^2}\right\}ds,\end{aligned} \tag{B.16}$$

while the leading order version of (B.9) gives Φ_2 explicitly as

$$\Phi_2(s_0) = \frac{2\epsilon}{3\pi}\int_0^\infty (H(s)-(X_c+s)H'(s))\log|s-s_0|ds, \tag{B.17}$$

which is the desired leading order equation for $\Phi_2(s)$.

We can rearrange (B.16) to give an ODE for Φ_1. We observe that

$$\frac{H(s)+(s_0-s)H'(s)}{|s_0-s|^2} = \frac{d}{ds}\left(\frac{H(s)}{s_0-s}\right), \tag{B.18}$$

We then differentiate (B.16) with respect to s_0, and make use of the identity

$$\int_0^\infty \frac{g'(s)}{t-s}ds = \left[\frac{g(s)}{t-s}\right]_0^\infty + \frac{d}{dt}\int_0^\infty \frac{g(s)}{t-s}ds, \tag{B.19}$$

so that the integral equation (B.16) becomes

$$0 = \text{P.V.}\int_0^\infty \left[\frac{2}{3}(H(s)-(X_c+s)H'(s)) + (\Phi_1'(s)H(s))'\right]\frac{1}{s_0-s}ds \tag{B.20}$$

and hence

$$\frac{d}{ds}[H(s)\Phi_1'(s)] = \frac{2}{3}[\tilde{H}(s) - (X_c + s)\tilde{H}'(s)] \tag{B.21}$$

which is the desired leading order equation for $\Phi_1(s)$.

B.3 Influence of reflected interface

Figure 5.2 shows a coalescence problem with fluid 2 bounded by two free-surfaces, with the interface for $x > X_c$ reflected in the line $x = 0$. This interface does not affect the integral equation for fluid 1, as it does not change the boundary for this fluid, but will change the integral equation for fluid 2. In terms of the interface position $(X(s), Y(s))$, where $X(0) = X_c$, $Y(0) = Y$, the integral equation for Φ_2 with only the free-surface for $x > 0$ can be written as

$$\begin{aligned}\Phi_2(s_0) =& \frac{1}{3\pi}\int_0^\infty (X'Y - Y'X)\left\{\log|(X - X_0)^2 + (Y - Y_0)^2| + \log|(X - X_0)^2 + (Y + Y_0)^2|\right\} ds \\ &+ \frac{1}{\pi}\int_0^\infty \Phi_2(s)\left\{\frac{-Y'(X_0 - X) + X'(Y_0 - Y)}{(X - X_0)^2 + (Y - Y_0)^2} + \frac{-Y'(X_0 - X) - X'(Y_0 + Y)}{(X - X_0)^2 + (Y + Y_0)^2}\right\} ds.\end{aligned} \tag{B.22}$$

With two free-surfaces, the integral equation becomes

$$\begin{aligned}\Phi_2(s_0) =& \frac{1}{3\pi}\int_0^\infty (X'Y - Y'X)\,\{ \\ &\log[(X - X_0)^2 + (Y - Y_0)^2] + \log[(X - X_0)^2 + (Y + Y_0)^2] \\ &+ \log[(X + X_0)^2 + (Y - Y_0)^2] + \log[(X + X_0)^2 + (Y + Y_0)^2]\Big\}\, ds \\ &+ \frac{1}{\pi}\int_0^\infty \Phi_2(s)\left\{\frac{-Y'(X_0 - X) + X'(Y_0 - Y)}{(X - X_0)^2 + (Y - Y_0)^2} + \frac{-Y'(X_0 - X) - X'(Y_0 + Y)}{(X - X_0)^2 + (Y + Y_0)^2}\right\} ds \\ &+ \frac{1}{\pi}\int_0^\infty \Phi_2(s)\left\{\frac{Y'(X_0 + X) + X'(Y_0 - Y)}{(X + X_0)^2 + (Y - Y_0)^2} + \frac{Y'(X_0 + X) - X'(Y_0 + Y)}{(X + X_0)^2 + (Y + Y_0)^2}\right\} ds.\end{aligned} \tag{B.23}$$

At leading order as $\epsilon \to 0$, we reach

$$\Phi_2(s_0) = \frac{2\epsilon}{3\pi}\int_0^\infty (H(s) - (X_c + s)H'(s))[\log|s - s_0| + \log|s + s_0 + 2X_c|]ds. \tag{B.24}$$

However, there is no source in the flow, so we can write this as

$$\Phi_2(s_0) = \frac{2\epsilon}{3\pi}\int_0^\infty (H(s) - (X_c + s)H'(s))\left[\log|s - s_0| + \log\left|1 + \frac{s}{s_0 + 2X_c}\right|\right] ds. \tag{B.25}$$

and the effect of the new reflected term on Φ_2 diminishes as X_c increases.

We can consider the effect of this new term on the asymptotic solutions we found in chapters 3 and 4. A new line of symmetry at $x = 0$ would change the leading order problem for $|\lambda - 1| \ll 1$ with $\rho_1 = 0$, which is sensible as $x_c \ll 1$ for this solution. The reflected interface would not change the leading order capillary wave equations for the two large-λ analyses, as these are derived for a lengthscale $x = O(x_c^{-2})$. However, the next order equations are for variation on the lengthscale $x = x_c$, which is exactly the separation of the two interfaces. The reflected interface significantly changes the leading order problem for Φ outer problem for $\rho_1 = 0$. The far-field solution for Φ was important in determining the mean of H in the far-field, and hence the contact-point displacement. However, for the two-fluid problem, the slow variation of Φ in W_0 has no effect on the interface. The new terms do not affect the short-lengthscale inner region near the contact point.

It is important to note that for any contact angle, the new terms in (B.23) compared to (B.9) add no extra sensitivity to interfacial neck formation, and so the reflected interface will not have an effect on the leading order flow in the neck regions.

Bibliography

D. G. A. L. Aarts and H. N. W. Lekkerkerker. Droplet coalescence: drainage, film rupture and neck growth in ultralow interfacial tension systems. *Journal of Fluid Mechanics*, 606:275–294, 2008.

D. G. A. L. Aarts, H. N. W. Lekkerkerker, H. Guo, G. H. Wegdam, and D. Bonn. Hydrodynamics of droplet coalescence. *Physical review letters*, 95:164503, 2005.

A. V. Anilkumar, C. P. Lee, and T. G. Wang. Surface-tension-induced mixing following coalescence of initially stationary drops. *Physics of Fluids A*, 3:2587–2591, 1991.

E. W. Barnes. The genesis of the double gamma functions. *Proceedings of the London Mathematical Society*, 31:358–381, 1899.

A.-L. Biance, C. Clanet, and D. Quéré. First steps in the spreading of a liquid droplet. *Physical Review E*, 69:016301, 2004.

J. Billingham. Surface-tension-driven flow in fat fluid wedges and cones. *Journal of Fluid Mechanics*, 397:45–71, 1999.

J. Billingham. The initial surface tension-driven flow of a wedge of viscous fluid. *SIAM Journal on Applied Mathematics*, 66:510–532, 2005.

J. Billingham. Surface tension-driven flow in a slender wedge. *SIAM Journal on Applied Mathematics*, 66:1949–1977, 2006.

J. Billingham and A. C. King. The interaction of a moving fluid/fluid interface with a flat plate. *Journal of Fluid Mechanics*, 296:325–351, 1995.

J. Billingham and A. C. King. Uniform asymptotic expansions for the Barnes double gamma function. *Proc. R. Soc. Lond. A*, 453:1817–1829, 1997.

J. Billingham and A. C. King. Surface tension-driven flow outside a slender wedge with an application to the inviscid coalescence of drops. *Journal of Fluid Mechanics*, 533: 193–221, 2005.

Y.-J. Chen and P. H. Steen. Dynamics of inviscid capillary breakup: collapse and pinchoff of a film bridge. *Journal of Fluid Mechanics*, 341:245–267, 1997.

D. G. Crighton, A. P. Dowling, J. E. Ffowcs Williams, M. Heckl, and F. G. Leppington. *Modern Methods in Analytical Acoustics*. Springer-Verlag, 1992.

R. F. Day, E. J. Hinch, and J. R. Lister. Self-similar capillary pinchoff of an inviscid fluid. *Physical Review Letters*, 80:704–707, 1998.

S. P. Decent and A. C. King. The recoil of a broken liquid bridge. *Proceedings of the IUTAM Symposium on Free-Surface Flows, Birmingham*, pages 81–88, 2001.

S. P. Decent and A. C. King. Surface-tension-driven flow in a slender cone. *IMA Journal of Applied Mathematics*, 73:37–68, 2008.

L. Duchemin, J. Eggers, and C. Josserand. Inviscid coalescence of drops. *Journal of Fluid Mechanics*, 487:167–178, 2003.

E. B. Dussan V. On the spreading of liquids on solid surfaces: static and dynamics contact lines. *Ann. Rev. Fluid. Mech.*, 11:371–400, 1979.

J. Eggers, J. R. Lister, and H. A. Stone. Coalescence of liquid drops. *Journal of Fluid Mechanics*, 401:293–310, 1999.

K. O. Friedrichs and H. Lewy. The dock problem. *Communications on Pure & Applied Mathematics*, 1:135–148, 1948.

A. E. Heins. The scope and limitations of the method of Wiener and Hopf. *Communications on Pure & Applied Mathematics*, 9:447–466, 1956.

R. W. Hopper. Plane Stokes flow driven by capillarity on a free surface. *Journal of Fluid Mechanics.*, 213:349–375, 1990.

C. Huh and L. E. Scriven. Hydrodynamic model of steady movement of a solid/liquid/fluid contact line. *Journal of Colloid and Interface Science*, 35:85–101, 1971.

J. B. Keller and M. J. Miksis. Surface tension driven flows. *SIAM Journal on Applied Mathematics*, 43:268–276, 1983.

J. B. Keller, A. King, and L. Ting. Blob formation. *Physics of Fluids*, 7:226–228, 1995.

J. B. Keller, P. A. Milewski, and J.-M. Vanden-Broeck. Merging and wetting driven by surface tension. *European Journal of Mechanics B - Fluids*, 19:491–502, 2000.

J. B. Keller, P. A. Milewski, and J.-M. Vanden-Broeck. Breaking and merging of liquid sheets and filaments. *Journal of Engineering Mathematics*, 42:283–290, 2002.

A. C. King. Moving contact lines in slender fluid wedges. *Quarterly Journal of Mechanics and Applied Mathematics*, 44:173–192, 1991.

A. C. King, J. Billingham, and D. F. Popple. The moving contact line between two wedges of fluid on a flat plate. *Quarterly Journal of Mechanics and Applied Mathematics*, 53: 453–468, 1999.

J. B. Lawrie. Surface-tension-driven flow in a wedge. *Quarterly Journal of Mechanics and Applied Mathematics*, 43:251–273, 1990.

J. B. Lawrie and A. C. King. Exact solution to a class of functional difference equations with application to a moving contact line flow. *European Journal of Applied Mathematics*, 5:131–157, 1994.

D. Leppinen and J. R. Lister. Capillary pinch-off in inviscid fluids. *Physics of Fluids*, 15: 568–578, 2003.

A. Menchaca-Rocha, A. Martínez-Dávalos, R. Núñez, S. Popinet, and S. Zaleski. Coalescence of liquid drops by surface tension. *Physical Review E*, 63:046309, 2001.

M. J. Miksis and J.-M. Vanden-Broeck. Self-similar dynamics of a viscous wedge of fluid. *Physics of Fluids*, 11:3227–3231, 1999.

NIST. *Digital Library of Mathematical Functions.* National Institute of Standards and Technology from http://dlmf.nist.gov/. Release date 2011-08-29, 2011.

B. Noble. *Methods based on the Wiener-Hopf technique for the solution of partial differential equations*. Pergamon Press, 1958.

D. H. Peregrine, G. Shoker, and A. Symon. The bifurcation of liquid bridges. *Journal of Fluid Mechanics*, 212:25–39, 1990.

R. S. M. Schulkes. The evolution and bifurcation of a pendant drop. *Journal of Fluid Mechanics*, 278:83–100, 1994.

A. Sierou and J. R. Lister. Self-similar recoil of inviscid drops. *Physics of Fluids*, 16: 1379–1394, 2004.

I. N. Sneddon. *The use of integral transforms*. McGraw-Hill, 1972.

J. J. Thomson and H. F. Newall. On the formation of vortex rings by drops falling into liquids, and some allied phenomena. *Proceedings of the Royal Society of London*, 39: 417–436, 1885.

S. T. Thoroddsen, T. G. Etoh, K. Takehara, and N. Ootsuka. On the coalescence speed of bubbles. *Physics of Fluids*, 17:071703, 2005.

S. T. Thoroddsen, B. Qian, T. G. Etoh, and K. Takehara. The initial coalescence of miscible drops. *Physics of Fluids*, 19:072110, 2007.

M. Van Dyke. *Perturbation methods in fluid mechanics*. Parabolic Press, 1975.

M. Wu, T. Cubaud, and C.-M. Ho. Scaling law in liquid drop coalescence driven by surface tension. *Physics of Fluids*, 16:L51, 2004.

W. Yao, H. J. Maris, P. Pennington, and G. M. Seidel. Coalescence of viscous liquid drops. *Physical Review E*, 71:016309, 2005.